SCUOLA DI DOTTORATO
UNIVERSITÀ DEGLI STUDI DI MILANO-BICOCCA

# Regional and local scale analysis of very slow rock slope deformations integrating InSAR and morphostructural data

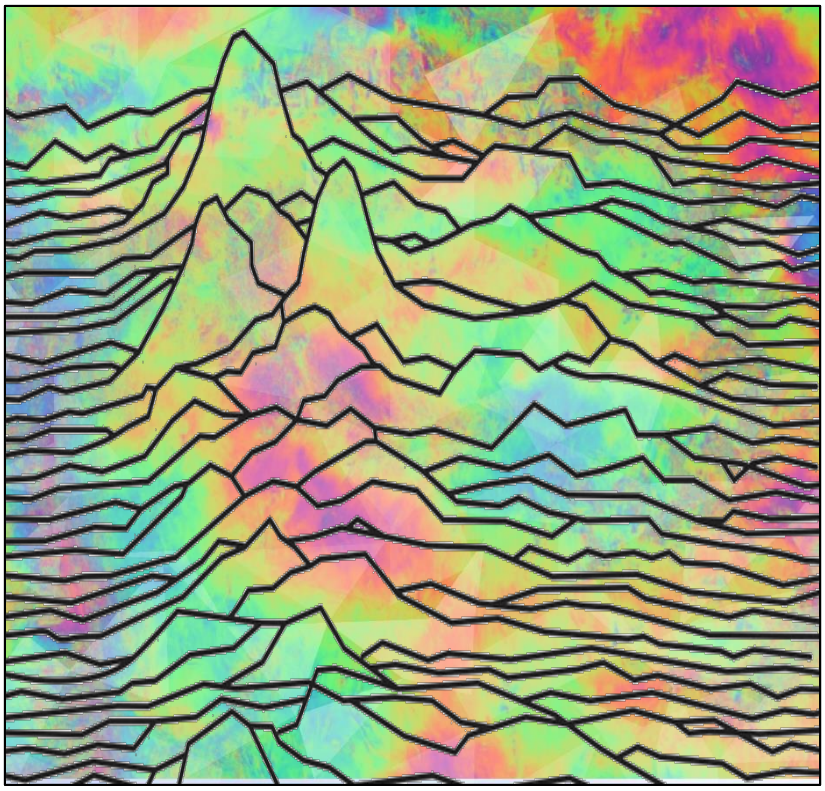

Chiara Crippa

SCUOLA DI DOTTORATO
UNIVERSITÀ DEGLI STUDI DI MILANO-BICOCCA

Department of Earth and Environmental Sciences

PhD program in Chemical, Geological and Environmental Sciences, Cycle XXXIII

Geological Sciences curriculum

# REGIONAL AND LOCAL SCALE ANALYSIS OF VERY SLOW ROCK SLOPE DEFORMATIONS INTEGRATING INSAR AND MORPHOSTRUCTURAL DATA

Crippa Chiara

Registration number:763185

Supervisor: Prof. Federico Agliardi

Tutor: Prof. Giovanni B. Crosta

Coordinator: Prof.ssa. Maria Luce Frezzotti

**ACADEMIC YEAR 2020/2021**

# Contents

# List of figures

# List of tables



# List of equations

# Abstract

Slow rock slope deformations (DSGSDs and large landslides) are widespread, affect entire hillslopes and displace volumes up to billions of cubic meters. They evolve over long time by progressive failure processes, under variable climatic and hydro-mechanical coupling conditions mirrored by a complex creep behaviour. Although characterized by low displacement rates (up to few cm/yr), these slope instabilities damage sensitive structures and host nested sectors potentially undergoing rockslide differentiation and collapse. A robust characterization of the style of activity of slow rock slope deformations is required to predict their interaction with elements at risk and anticipate possible failure, yet a comprehensive methodology to this aim is still lacking. In this perspective, we developed a multi-scale methodology integrating geomorphological mapping, field data and different DInSAR techniques, using an inventory of 208 slow rock slope deformations in Lombardia (Italian Central Alps), for which we performed a geomorphological and morpho-structural mapping on aerial images and DEMs. On the regional scale, we developed an objective workflow for the inventory-scale screening of slow-moving landslides. The approach is based on a refined definition of activity that integrates the displacement rate, kinematics and degree of internal damage for each landslide.

Using PS-InSAR and SqueeSAR$^{TM}$ datasets, we developed an original peak analysis of InSAR displacement rates to characterize the degree of segmentation and heterogeneity of mapped phenomena, highlight the occurrence of sectors with differential activity and derive their characteristic displacement rates. Using 2DInSAR velocity decomposition and machine learning classification, we set up an original automatic approach to characterize the kinematics of each landslides. Then, we sequentially combine PCA and K-medoid cluster analysis to identify groups of landslides characterized by consistent styles of activity, accounting for all the relevant aspects including velocity, kinematics, segmentation, and internal damage. Starting from the results of regional-scale classification, we focused on the Corna Rossa, Mt. Mater and Saline DSGSDs, that are emblematic case studies on which apply DInSAR analysis to investigate typical issues in large landslide studies (spatial segmentation, heterogeneous activity, sensitivity to hydrological triggers). We applied a targeted DInSAR technique on multiple temporal baselines to unravel the spatial heterogeneities of complex DSGSDs and through a novel stacking approach on raw long temporal baseline interferograms we outlined the permanent displacement signals and sectors with differential evolution as well as individual active structures.

We then used DInSAR to investigate the possible sensitivity of slow rock slope deformations to hydrological triggers. Comparison between seasonal displacement rates, derived by interferograms with targeted temporal baselines, and time series of precipitation and snowmelt at the Mt. Mater and Saline ridge outlined complex temporally shifted seasonal displacement trends. These trends, more evident for shallower nested sectors, outline dominant controls by prolonged precipitation periods modulated by the effects of snowmelt. This suggests that DSGSDs, often considered insensitive to short-term (pluri-annual)

climatic forcing, may respond to hydrological triggering, with key implication in the interpretation of their progressive failure.

Our results demonstrated the effectiveness of the proposed multi-scale methodology that exploits DInSAR products and targeted processing to identify, classify and characterize the activity of slow rock slope deformation at different levels of details by including geological data in all the analysis stages. Our approach, readily applicable to different settings and datasets, provides the tools to solve key scientific issues in a geohazard-oriented study of slow rock slope deformations.

# Preface

Slow rock slope deformations are fairly common phenomena in the Alps. They are processes induced by gravity and affect entire hillslopes, displacing volumes of rock up to billions of cubic meters. Consequently, even if their displacement rates are low (mm/year or cm/year), they may damage local infrastructures or host secondary and more active rock slope failures. The evolution towards failure of these phenomena is complex, due to the occurrence of progressive failure processes with increasing hydro-mechanical coupling mirrored by creep behaviour. Furthermore, they are usually characterized by heterogeneous styles of activity associated to slope sectors with different kinematics, displacement rates and strain partitioning into morpho/structural features.
Their study is thus very challenging since they are widespread, and need to be characterized in an extensive way, they have a complex style of activity, evolve during different stages of evolution and are usually recognized when they differentiate in rockslides that are sensitive to hydromechanical forcing. In addition, they often threaten infrastructures damaging sensitive elements (pipelines, roads, buildings) with their slow movements, but can also represent important geohazard for human lives in the case of catastrophic collapse.
Among all the available in-situ and remote-sensing monitoring techniques, differential synthetic aperture radar interferometry (DInSAR) and the related processing approaches provide a useful tool for the quantitative measurement of slow slope displacement rate, making possible long-term monitoring of surface deformations maximizing the spatial and temporal coverage at a relatively low cost.

This study contributed in the project "Slow2Fast: Long-term activity, damage and collapse potential of large slow-moving landslides in rock in Lombardia" funded by Fondazione Cariplo. Some analyses were also carried out in collaboration with the ETH Zurich's Engineering Geology group.
It aims at studying alpine slow rock slope deformations both at the regional and local scale in order to analyse their style of activity, understand the main geological structures that control their onset and achieve a long term evolution of their movement in a geohazard perspective. To gather a sound regional scale analysis, we developed an innovative approach to exploit data provided by Persistent Scatterers Interferometry techniques integrated with mapping derived information extracted from an ad hoc processed inventory over Lombardia region (North Italy). Our processing workflow allows to characterize in a semi-automated and replicable way the activity, kinematics and heterogeneity of very slow rock slope deformations and provide a classification of these phenomena using multivariate statistical techniques.
We then took advantage of this regional screening to focus on three critical case studies emerging from the regional scale classification and with peculiar issues in an applied perspective, refining the analysis to unravel their spatial and temporal heterogeneities. To this aim, we integrated a targeted, local-scale DInSAR processing with monitoring and field

data to retrieve a deep characterization of their displacement pattern and possible evolutive style.

Our analyses and classification workflow (regional) provide targeted methodology to maximize the use of InSAR processing techniques for further site specific activity analyses. We highlight the potential and limits of DInSAR approach in the study of complex phenomena such as slow rock slope deformations and stress the importance of a detailed geological and morpho-structural study for a complete definition of their style of activity in an evolutive perspective.

# 1 Slow rock slope deformations

## 1.1 Definition, classification and terminology

Slow deep seated rock slope deformations consist of gravity-induced processes that affect entire hillslopes, displacing volumes of rock up to hundreds of millions of cubic meters (Bovis, 1990; Chigira, 1992; Saroli et al., 2005; Audemard et al., 2010; Crosta et al., 2013; Lin et al., 2013), that deform slowly (mm-cm/year) over long periods ($10^3$-$10^4$ years) through creep processes.

The first documented accounts of these mass movements date back to 1930s (Dal Piaz, 1936; Ampferer, 1939). Since them, several definitions were proposed in the literature including "deep-seated large-scale rock slides" (Terzaghi, 1962); "depth creep" (Ter-Stepanian and Goldstein, 1969); "deep-seated creep" (Nemcok, 1972);"deep-seated continuous creep" (Hutchinson, 1968); and "mass creep"(Terzaghi, 1953; Skempton and Hutchinson, 1969).

However, only from 1970s, the study of these slope instabilities increased in response to the rising interest in understanding their mechanisms and impact (Nemcok, 1972;Mahr, 1977; Radbruch-Hall et al., 1977; Radbruch-Hall, 1978; Sorriso-Valvo, 1979; Savage and Varnes, 1987; Varnes et al., 1989; Durville, 1992; Dramis and Sorriso-Valvo, 1994). In this context, their study was also facilitated by new geomorphological and engineering geology insights and improved monitoring systems that could effectively demonstrate creep processes ongoing in large slopes (Emery, 1978).

However, until then, all the studies did not define a unique mechanism driving the slow deep seated mass movements, but identified several possible ones, thus supporting a complex link between the phenomenon and the driving mechanism itself.

In the most popular landslide classification, Varnes (1978) identified and grouped different landslide types according to specific attributes such as: "the *type of movement, kind of material, the rate of movement, geometry of the area of failure and the resulting deposit, age, causes, degree of disruption of the displaced mass, relation or lack of relation of slide geometry to geologic structure, degree of development, geographic location of type examples, and state of activity",* thus considering as main criteria the kinematic mechanism at the onset and type of material involved (Table 1; Varnes, 1978; Cruden and Varnes, 1996).

Based on these criteria, slow rock slope deformations could thus fall in different classes of Varnes classification and were framed in the *rock flow* class (Nemcok, 1972; Nemčok et al., 1972; Tabor, 1971; Zischinsky, 1966) only according to a rheological assumption. The slow creep movement was in fact assimilated to the behaviour of a viscous fluid in which creep was distributed in the entire mass instead of being associated to a progressive brittle failure

mechanism inducing the localization and evolution of a defined basal shear zone. Therefore, a boundary still persisted between slow deep seated rock slope deformations and the common definition of landslide (Crescenti et al., 1994; Dramis and Sorriso-Valvo, 1994; Sorriso-Valvo, 1995) and this difference was supported by the huge dimensions, the lack of a continuous sliding surface and the complex deformation style of the phenomenon.

*Table 1: Abbreviated Classification of Slope Movements (Cruden and Varnes, 1996)*

Abbreviated Classification of Slope Movements

| Type of Movement | Type of Material | | |
|---|---|---|---|
| | Bedrock | Engineering Soils | |
| | | Predominantly Coarse | Predominantly Fine |
| Fall | Rock fall | Debris fall | Earth fall |
| Topple | Rock topple | Debris topple | Earth topple |
| Slide | Rock slide | Debris slide | Earth slide |
| Spread | Rock spread | Debris spread | Earth spread |
| Flow | Rock flow | Debris flow | Earth flow |

However, successive studies revealed that many gravitational slope deformations have a more or less evolved basal shear zone as observed from boreholes, geophysical investigations and models interpretations, that extend hundreds of meters below the surface (Gignoux and Barbier, 1955; Desio, 1961; Barla et al., 2010; Agliardi et al., 2012). The lack of a macroscopically clear shear zone can' t be thus considered a key classification criterion and the term "slow rock slope deformations" should effectively refer to landslides phenomena.
This is also supported by the area-frequency distributions of slow rock slope deformations that, for landslides above a certain size threshold, follow a power-law with exponent values similar to those reported in the landslide literature (Stark and Hovius, 2001; Malamud et al., 2004; Agliardi et al., 2012;), and then deviate from the power law over the threshold (*roll-over*, Figure 1.1; Agliardi et al., 2012).

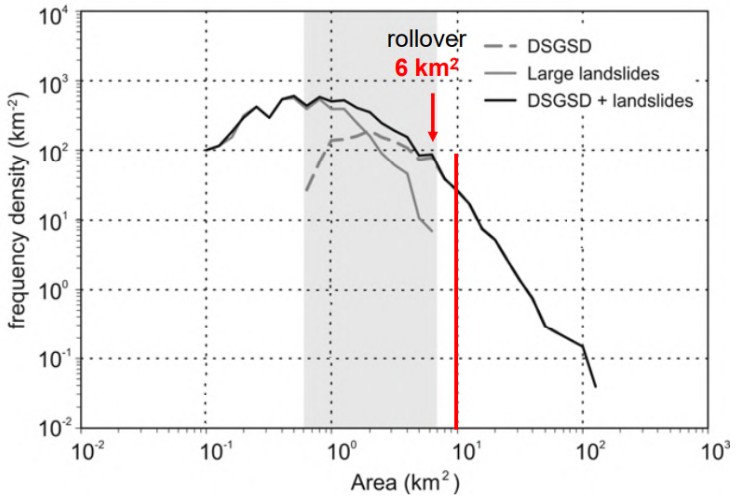


*Figure 1.1: Frequency distribution of DSGSD and LL in the Alpine inventory (Agliardi et al., 2012).*

A simple classification and characterization of these phenomena based on the kinematic behavior is thus incomplete since the rock mass strength, structural features and preexisting tectonic elements condition a variety of failure geometries (Figure 1.2; Agliardi et al., 2012).

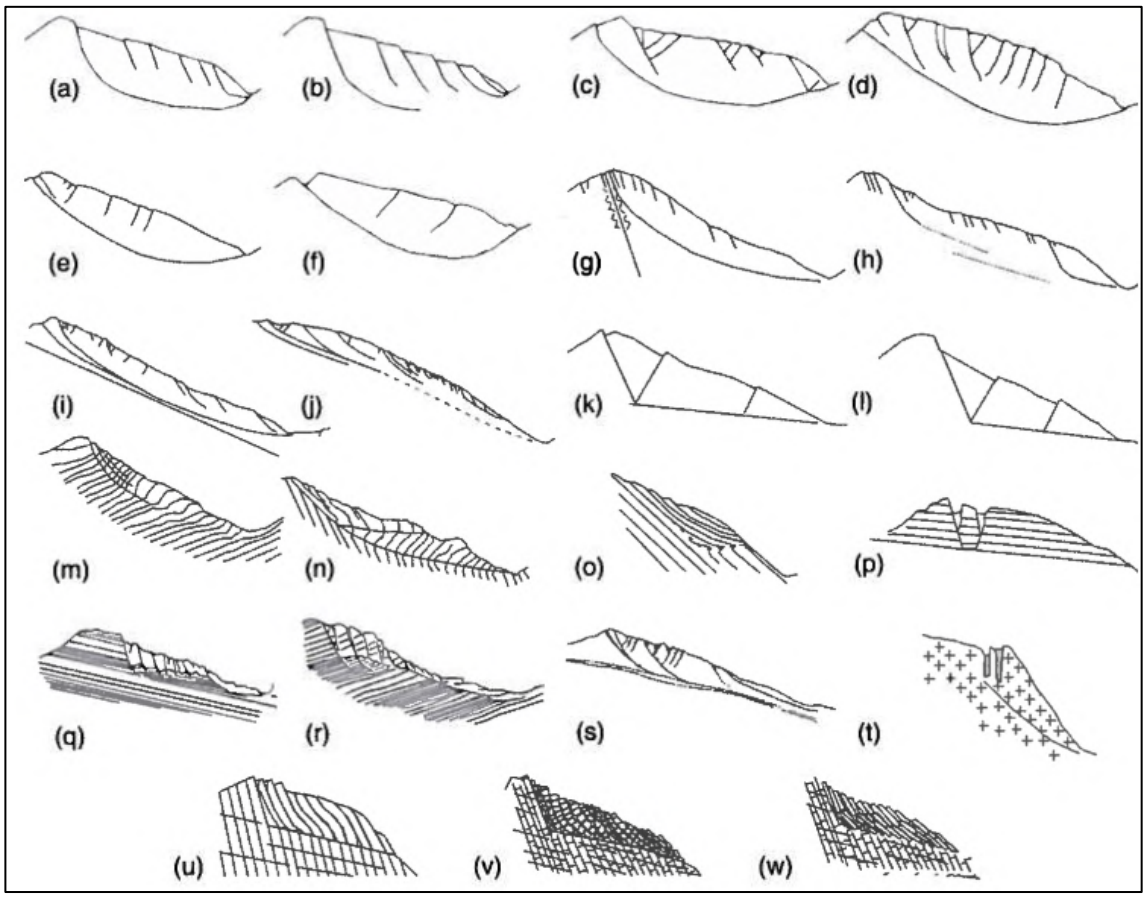


*Figure 1.2: mechanisms of large scale slope failures proposed in the literature according to different structural settings (Agliardi et al., 2012).*

In this work we refer to the terminology proposed by Agliardi er al., 2012,2013 and Crosta et al., 2013 who distinguished slow rock slope deformations in two main classes: deep-seated gravitational slope deformations (DSGSD) and large landslides (hereafter LL) according to their areal extent, surface expression and strain accumulation.

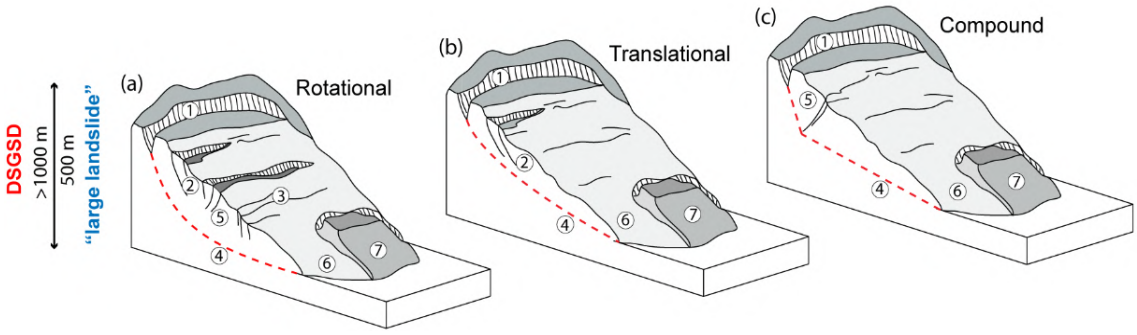


*Figure 1.3: Schematic sketches depicting the surface morpho-structural features commonly associated, to different extents, to DSGSD and large landsldies (see text for explanation): a) rotational b)translational c)compound; 1) head scarp , 2) scarps, 3) trenches; 4) basal shear surface, 5) counterscarp, 6) toe, 7) nested landslide.*

These two classes of phenomena are similar and form a continuum in the global spectrum of slow rock slope deformations(Figure 1.1) with major difference related to their areal change: DSGSDs involve entire slope flanks even beyond the ridge crest, while LL have smaller extent, but always major than 1 $Km^2$ (Figure 1.1).

In detail:

- DSGSDs affect high relief slopes (Figure 1.3) (>1000m) up to and beyond the ridge over areas exceeding 6-10 $km^2$ (Agliardi et al., 2012). They are characterized by large involved volumes (>0.5 $km^3$), ill-defined lateral boundaries and deep basal shear zones (200-300m deep and more). The style of activity is complex and characterized by variable kinematics and heterogeneous strain fields strongly constrained by inherited structures (Agliardi et al., 2001; 2012), resulting in remarkable internal segmentation and damage localized within typical morpho-structural features (Agliardi et al., 2001) and the development of nested secondary landslides. These often consist of active rockslides differentiated from the main landslide mass and capable of catastrophic evolution, thus representing an important issue for anthropic activities and close infrastructures. Some examples can be found in Ruinon (Agliardi et al., 2001; Crosta and Agliardi, 2003a), La Saxe (Crosta et al., 2013) and La Clapière (Guglielmi et al., 2005)rockslides, all nucleated inside bigger DSGSDs.
- Large landslides (Figure 1.3Figure 1.) are commonly smaller than DSGSDs with a more elongated shape (higher length/width ratio) and affect the middle-lower slope sectors. They usually involve areas less than 6 $km^2$ wide (Figure 1.1; Agliardi et al. 2012) and show evidence of greater internal strain with more pronounced landslide scarps, rock mass damage and past and ongoing instability with respect to DSGSDs, to which they can be associated or not (Agliardi et al., 2012; Crosta et al. 2013). Large landslides can evolve faster and progress more easily towards catastrophic collapse than DSGSDs, thus becoming important geohazard for towns and infrastructures they involve.

Both of them are widespread in the European Alps (Figure 1.4; Crosta and Agliardi, 2003b) as well as in other mountain ranges, and evolve by progressive failure processes testified by slope creep (Emery, 1978; Riva et al., 2018).

They are characterized by strong heterogeneity and segmentation with differential deformations that affect both superficial elements (e.g. buildings, roads, pipelines) and underground structures (tunnels), as result of the interplay of the type of building, position on the slope and relative to landslide sectors, extent of the infrastructure and its response to variable movements within the landslide mass (Frattini et al., 2013).They evolve with low displacement rates, that over the long term can result in high cumulative displacements (Agliardi et al., 2012; Crosta et al., 2013; Pánek and Klimeš, 2016) damaging local infrastructures or triggering secondary failures, and eventually accelerate until catastrophic collapse of entire slope sectors posing major risks for human lives and sensitive infrastructures. Due to the damage of rock masses, resulting in the decay of mechanical properties, the pattern and rate of progressive failure, relief, loading history and fluid circulation, both DSGSDs and large landslides can host differentiated and potentially

catastrophic nested landslides (Agliardi et al., 2018) that nucleate inside the main landslide body (Figure 1.5).

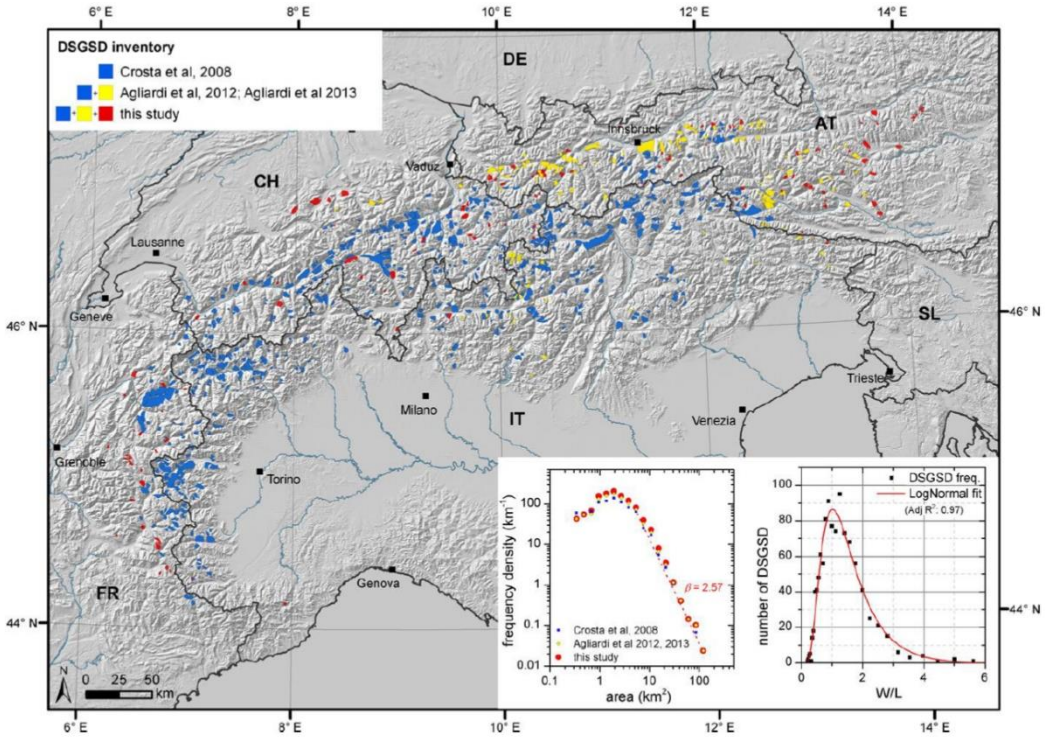


*Figure 1.4: Alpine DSGSD inventory. Size frequency distribution and Width/downslope length ratio are also reported (from Crosta et al., 2013).*

These account for large rockslides, falls, topples and shallower instabilities which evolution is linked to the bigger slow rock slope deformation, but usually result more active and sensitive to external perturbations (e.g. rainfall, snowmelt, etc.).

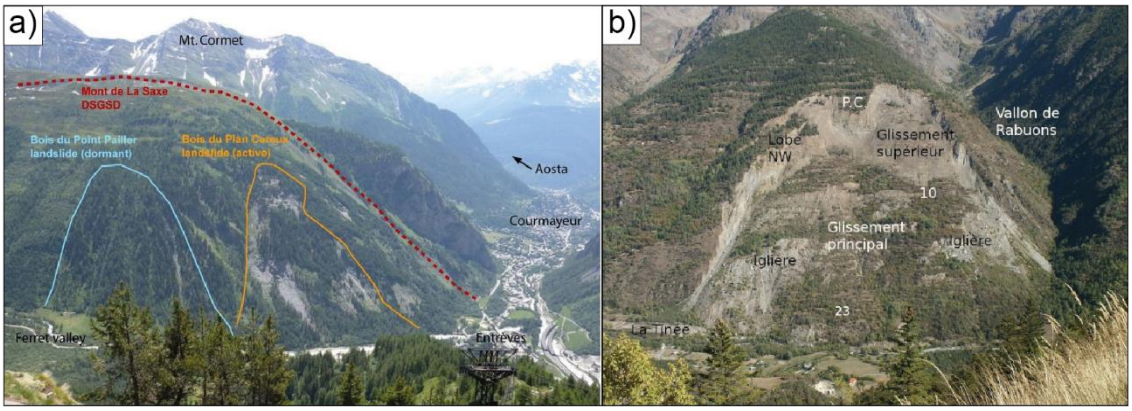


*Figure 1.5: examples of DSGSDs with nested landslides: a) Mt. de La Saxe landslide (Hölbling et al. 2012); b) La Clapière landslide (https://www.encyclopedie-environnement.org/en/soil/la-clapiere-largest-french-landslide-major-risk/).*

## 1.2 Evidence, distribution and controls

The long term evolution of these giant slow rock slope deformations strongly imprints the mountain settings, leaving important geomorphic signatures in the shape of valleys (Brocklehurst and Whipple, 2004; Sternai et al., 2011). This is evident both in the case that the deformation eventually stabilizes, or it continues to creep, or evolves in a slow to fast fashion towards catastrophic collapse. Whatever the evolutive pattern, slow rock slope deformations are recognized through their typical morpho-structural evidence (Zischinsky, 1966; Radbruch-Hall et al., 1976; Massart, 1983; Agliardi et al., 2001; Bovis, 2013), including both extensional and compressional features that mirror the deep deformation pattern and degree of strain localization.

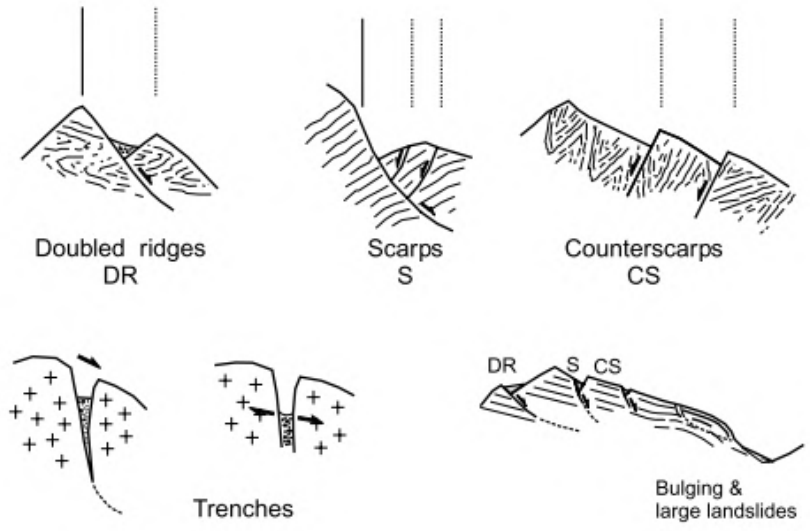


*Figure 1.6: Morpho-structural expression of slow rock slope deformations (Agliardi et. Al. 2001).*

Extensional features are characteristic of the upper part of the deformed rock mass and include double-crested ridges, trenches, tension cracks, scarps and counterscarps, also associated in half-grabens structures (Figure 1.6; Radbruch-Hall et al., 1976; Chigira, 1992; Agliardi et al., 2009; Jarman and Ballantyne, 2002; Bovis, 2013;).
Uphill-facing scarp depressions can often host ephemeral or permanent ponds (Bovis, 2013; Agliardi et al.,2009) which control the local water infiltration and groundwater flow (Jaboyedoff et al., 2013). Compressional features are related to tectonic structures affecting the slope and interplaying with the gravitational movement or associated with internal deformation that causes local thrusting and folding. Folds can occur at different scale (Chigira, 1992) and their wavelength and geometry are controlled by the density of discontinuities in the rock mass, the competence and strength of the rock and the applied stress, the layering of the rock mass and the depth at which they develop (Figure 1.7).
They often develop also in the lowest portion of the slope, which is the sector that mainly experiences shortening/compression of the rock mass as response of the extension produced

at the top. Here, common structures comprise folds and toe bulging (local uplift) deformation, due to the push of the rock mass towards the valley floor.

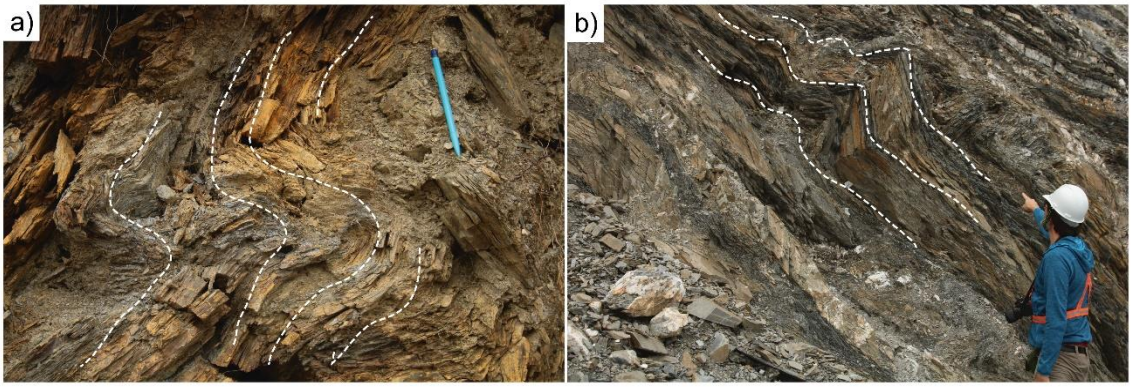


*Figure 1.7: slope tectonic evidence. Folds in pelitic and arenaceous shists a) in the headscarp sector and b) close to the sliding plane.*

A reconnaissance study combining an assessment of morpho-structural evidence and surface displacement measures becomes fundamental to identify the ongoing displacement pattern and characterize the phenomena. Since surface deformations mirror the geometry and kinematics at depth, different morpho-structures and their associations are witnesses of different deformation mechanisms and provide a first insight into the kinematic behavior of the landslide.

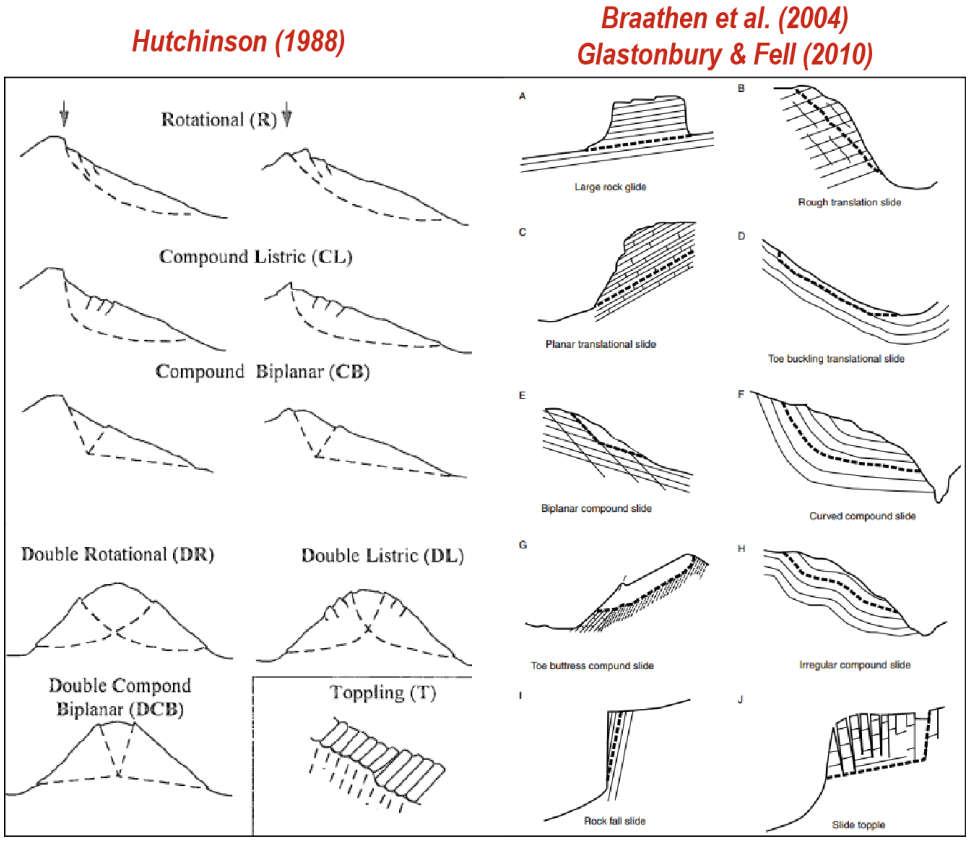


*Figure 1.8: Schematic cross sections showing different deformation patterns of large rock slope failures (after Hutchinson, 1988; Braathen et al., 2004; Glastonbury and Fell, 2010, Hermanns and Longva 2012).*

Several orders of scarps that dissect the slope from the edge to the toe associated to few minor counterscarps suggest a translational sliding mechanism characterized by synthetic structures developing at different depth levels. On the contrary, major counterscarps association points out a more rotational movement accommodating a higher portion of vertical displacement rate along slope through internal shearing.
Hutchinson (1988), Glastonbury and Fell (2010) defined, using schematic cross-sections (Figure 1.8), possible structural set up in which catastrophic slope failures occurred in the past or are prone to develop (Hermanns and Longva, 2012). In general, deformation mechanisms can be ascribed to fall, toppling, slide (rotational, translational, compound sliding), or complex interactions (Braathen et al., 2004) according to slope morphometry and the interplay of structural elements.
Slide commonly occurs in moderate slope gradients (<45°) while fall and toppling usually occur on steep slopes (60-75°) with vertically oriented discontinuities (Braathen et al., 2004). Slow rock slope deformations considered in this work belong to the alpine and prealpine chain of Lombardy region (North of Italy) and all of them have a mean slope gradient lower than 45° (Figure 1.9). Therefore, the driving deformation mechanism is sliding and the associated kinematics are translation, with sliding parallel to the slope, rotation, characterized by inward displacement at the headscarp and possible outward at the toe, and rototranslation that refers to a hybrid compound displacement pattern both showing a strong inward displacement component and along slope sliding.

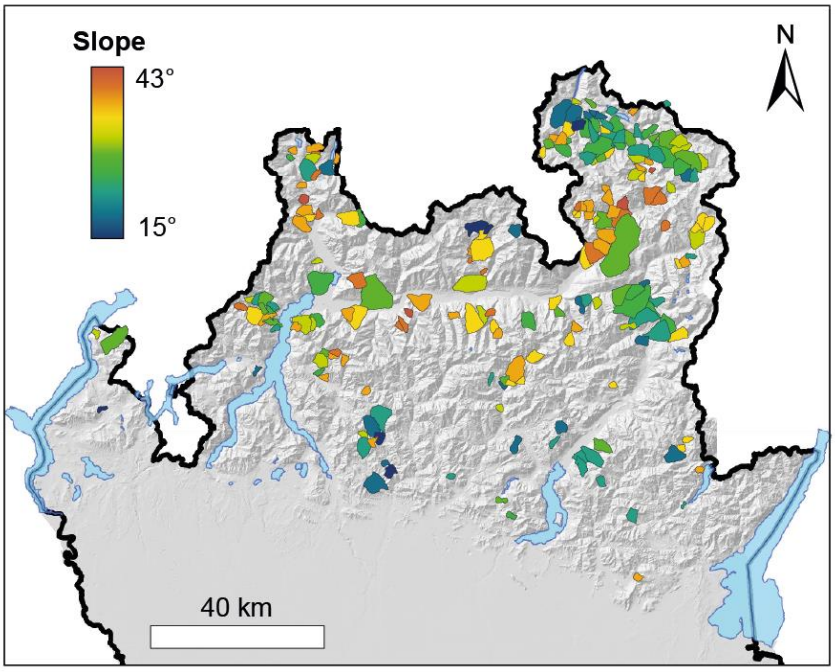


*Figure 1.9: Mean slope gradient of the mapped slow rock slope deformantions in Lombardia (North Italy).*

Slow rock slope deformations are now recognized in different mountain ranges worldwide and are particularly diffused in the Alpine setting where more than 1000 have been mapped (Figure 1.4; Agliardi et al., 2013; Crosta et al., 2013).

They mainly nucleate in anisotropic rocks with moderate strength (Figure 1.10; i.e. metapelites, paragneiss and flysch-type rocks; Agliardi et al., 2013; Crosta et al. 2013b), different geomechanical behavior and heterogeneities in rock masses with contrasting strength and deformability (Figure 1.10, Poisel and Eppensteiner 1988).

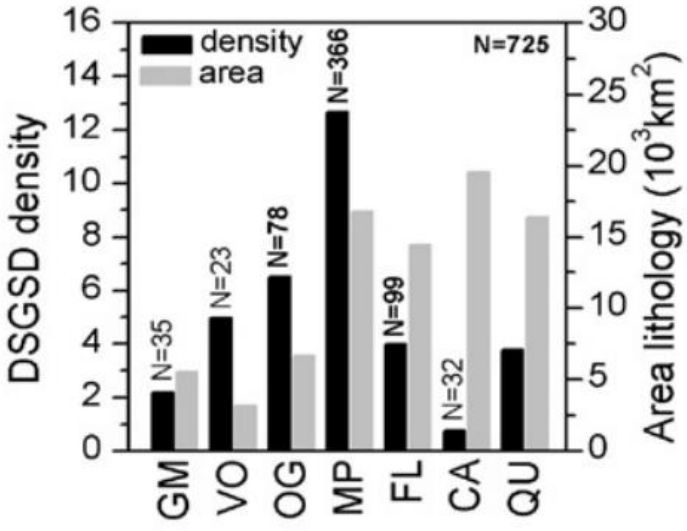


*Figure 1.10: rock type controls on DSGSD distribution in the Alpine chain expressed by areal density. Rock types are grouped according to their expected geomechanical behavior (i.e. average rock mass properties and anisotropy): GM: granitoid/metabasite; VO: volcanics; OG: orthogneiss; MP: metapelite; FL: bedded sandstones and marls, including flysch; CA: carbonate rocks (Agliardi et al., 2013).*

Inherited tectonic features also control slow rock slope deformations on three different scales (Agliardi et al., 2013). At regional scale, major features (regional faults, thrusts, nappe boundaries etc.; Ambrosi and Crosta, 2006; Agliardi et al., 2009) control their distribution with clusters of slow rock slope deformations frequently developed around them and rock mass damage and properties degradation induced by such regional-scale lineaments. Steep faults or master fractures constrain the localization and geometry of the landslide (Agliardi et al., 2001; Hippolyte et al., 2006), while gently dipping features (i.e. low angle faults, tectonic boundaries) more likely control the localization of basal shear planes and the pattern of surface features (Agliardi et al., 2009, 2012). In addition, together with brittle structures (i.e. faults and fractures), that have been extensively documented (Agliardi et al., 2001; Hippolyte et al., 2006; Stead and Wolter, 2015), also inherited stratigraphic and tectonic features such as large-scale folds (Figure 1.11; Badger, 2002; Humair et al., 2013; Agliardi et al., 2019;) influence the slope structures and the instabilities nucleation.

At slope scale, master fractures constrain the occurrence, type, and geometry of major morpho-structures, and condition the onset and kinematics of the slope instabilities (Agliardi et al., 2001, 2013).

At the outcrop scale, rock fabric and structure influence rock mass strength, deformability and degrees of freedom (Agliardi et al., 2013).

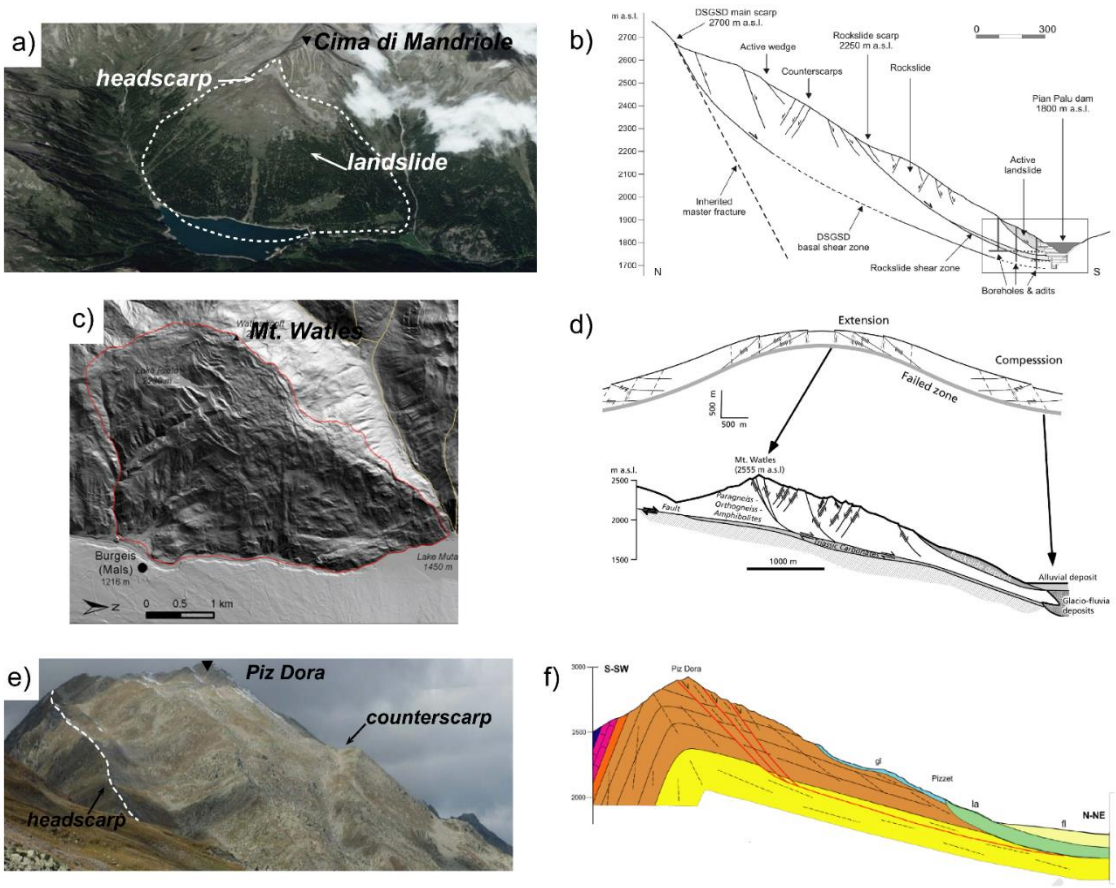


*Figure 1.11: Structural controls on slow rock slope deformations. a)Cima di Mandriole DSGSD controlled by the presence of an inherited master fracture at the top of the slope (Agliardi et al., 2012) b) Mt. Watles DSGSD influenced by the presence of extensional structures and a less competent layers (carbonate) at the base (Agliardi et al., 2009) c) Piz Dora DSGSD influenced by the presence of a major fold affecting the slope (Agliardi et., al 2o19).*

The interaction between mountain slopes, geometry, strength and morpho-climatic forcing are the primary controls on the onset of gravitational slope instabilities. In alpine (i.e. formerly glaciated) areas, glacial and paraglacial processing also play an important role in the destabilization of large rock slopes.

## 1.3 Mechanisms and driving factors

The driving factors that condition and control the evolution of the slow rock slope deformations are not easily defined because they act differently according to the maturity degree of the progressive failure process (Bjerrum, 1967; Chigira 1992; Eberhardt et al., 2004; Amitrano and Helmstetter, 2006;), that refers to mechanical properties degradation in sub-critical stress conditions and progressive increase of fracture intensity.

Deglaciation (Figure 1.12, Figure 1.13; i.e. slope debuttressing and stress release; Augustinus, 1995; Agliardi et al., 2001; Ambrosi and Crosta, 2006; Riva et al., 2018), fluvial erosion and active tectonics (i.e. seismicity), can favor rock mass damage and perturbations of slope hydrology contributing to the development of progressive rock failure processes (Agliardi et al., 2019) which control the slope evolution in the long-term period in a complex interaction of causes and triggers that interplay in the slope deformation. Moreover, different geomorphological settings (i.e. glacial Vs fluvial erosion) define different triggering factors that, in other environments, may condition the bulk characteristics of the topography more than modifying the stress distribution in the slopes directly affecting on the landslide destabilization.

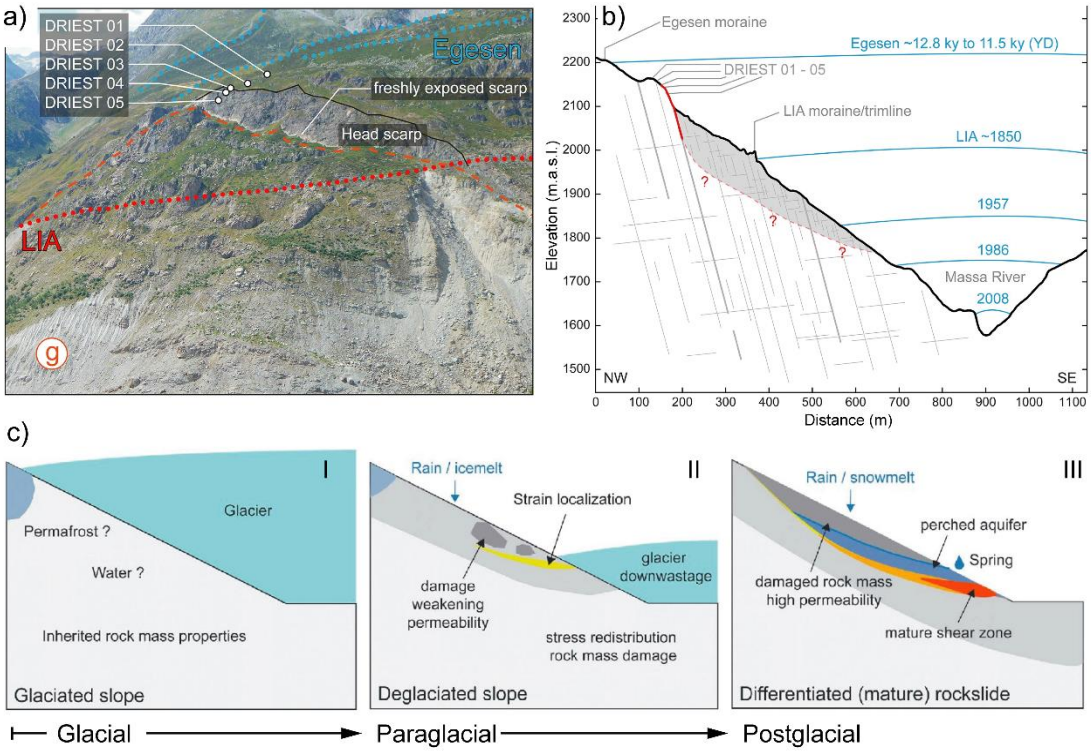


*Figure 1.12: Deglaciation effect on stress release and nucleation of slow rock slope deformations. a) Driest DSGSD (Aletsch Valley, Switzerland) showing an important headscarp with evidences of several activations (Gramiger et al., 2017). b) scheme of Driest DSGSD during different glacial stages (Gramiger et al., 2017). c) evolution of rock mass damage induced by Glacier retreat (Riva et., al 2018).*

Here, we focus on the Alpine environment in which slow rock slope deformations onset is set within the paraglacial stage and deglaciation can be considered the main triggering factor. This is in accordance with literature data resulting from morphostructures dating through CRE (Agliardi et al., 2009; Hippolyte et al., 2012) which date the activation of Alpine DSGSDs back to the Lateglacial.

While rockfall activity can occur on the steepest slopes right after the deglaciation and during successive events due to unloading and stress redistribution, weathering and erosion processes (Riva, 2017), the onset of huge slope deformations generally occurs with a certain

time span after the deglaciation, with the nucleation of a potential instability that supports the mechanism of a progressive damage in subcritical state (Figure 1.13 a; Agliardi et al., 2020; Eberhardt et al., 2004; Riva et al., 2018). Starting from glacial conditions where rock masses are poorly damaged and hydraulically interconnected, progressive slope debuttressing (Figure 1.12) in paraglacial conditions induces brittle damage and permeability increase (Figure 1.13 b) (Riva et al., 2018), causing slope destabilization and rockslides differentiation as result of stress and hydrological perturbations (Figure 1.13 c) (Broadbent and Zavodni, 1982; Crosta et al., 2017; Riva et al., 2018; Agliardi et al., 2020).

Moreover, despite deglaciation is the principal trigger, some instabilities need further factors to develop. One can be found in the active tectonic setting and seismic condition of the region (Lenti and Martino, 2013; Gischig et al., 2016; Wolter et al., 2016; Agliardi, et al., 2019;) where repeated seismic events can promote deformation and collapse of large rock slopes through progressive damage. In absence of deglaciation, a rapid valley erosion (fluvial incision) on high energy slopes may also induce destabilization and influence the overall stability (Crosta and Zanchi, 2000) especially in layered sedimentary or weak rocks.

The typical creep deformation curve consists of three distinct stages in a strain versus time diagram: (I) primary or decelerating stage, (II) secondary or steady-state stage, (III) tertiary or accelerating stage (Figure 1.13 b) (Riva et al., 2018).

Primary creep is the period characterized by transient creep in which creep occurs at a constant rate under loading. It is correlated with variations in the fracture density and structure rearrangements (Amitrano and Helmstetter, 2006; Bonora and Esposito, 2011). After the primary creep regime, the strain and the damage rate increase due to internal elements interactions (Amitrano and Helmstetter, 2006) leading to the secondary creep regime. This stage is characterized by almost constant strain rate with fluctuations due to the influence of external factors that induce differential stresses and control the timing of macroscopic failure (Brantut et al., 2014; Riva et al., 2018). However, the secondary creep is not always clearly observed and in some cases it can be interpreted as a crossover between primary creep and accelerating tertiary creep more than a steadily stationary regime (Lockner, 1993; Amitrano and Helmstetter, 2006).

Tertiary creep is characterized by a rapid acceleration of displacement until final failure (Dai et al., 2020) and catastrophic collapse (Figure 1.13 b). The failure occurs when the mobilized stress in subcritical conditions exceeds the material instantaneous strength (Figure 1.13 a), which is described by a Mohr-Coulomb failure criterion with tensile cutoff.

During the long term creep process, sub-critical crack nucleation and growth may be catalyzed by increase in pore water pressure and a consequent voids coalescence in a defined shear band, that differentiates from the intact rock mass ( Figure 1.13 c,d; Carlà et al., 2019; Agliardi et al., 2020). This induces a transition from peak to residual strength conditions and the kinematic release of the unstable mass that is explicated by a phase of progressive deformation (i.e. accelerating or tertiary creep) during which it is recorded a strain increment on the slope surface and an exponential increasing velocity until failure is observed (Figure 1.13 b,c,d; slow to fast transition).

During the progressive failure (Figure 1.13 b), hydrological inputs and external perturbations (seismic events, cycles of loading and unloading) drive the long term evolution modulating and amplifying the development of the shear zone (Figure 1.13 d) that evolves according to cataclastic processes, with a progressive transition from permeable localized damage zones to sealing cataclastic layers.

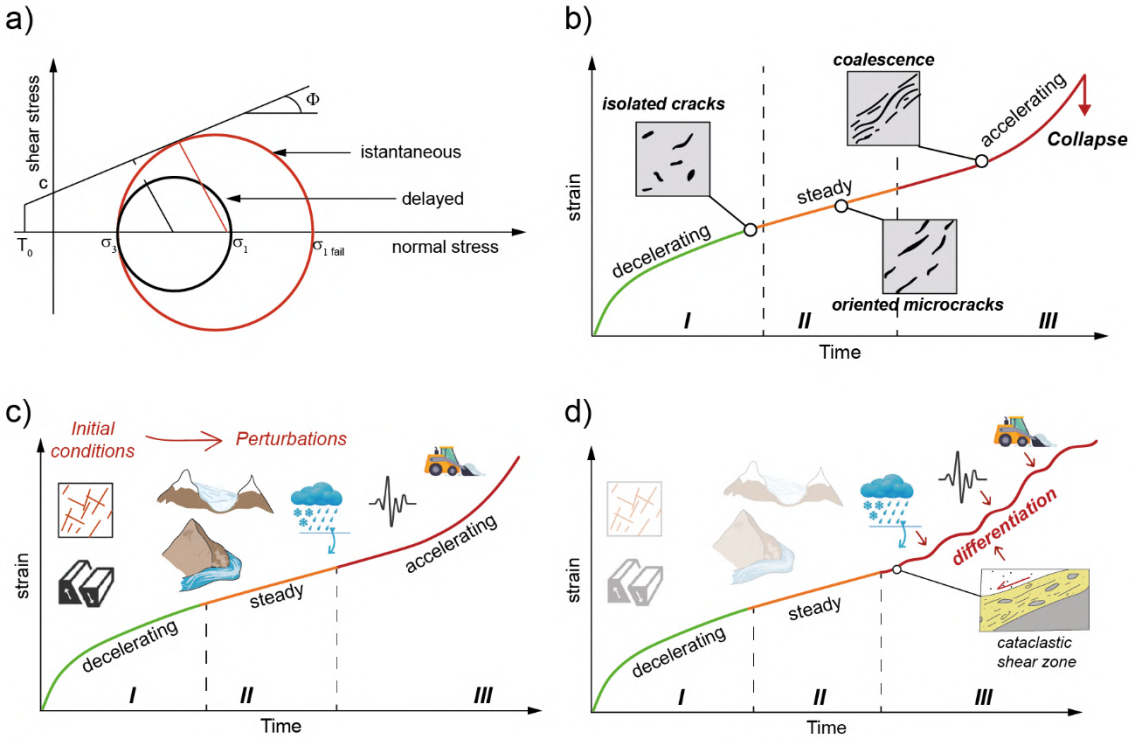


*Figure 1.13: Progressive damage induced by brittle creep processes in a large rock slope deformation. a) instantaneous failure (red circle) versus progressive failure occurring in subcritical stress conditions (black circle) (after Riva et al., 2018); b) progressive long-term slope evolution steps with main stages involved in microcracks initiation, growth and coalescence; c) initial rock mass properties and conditions (fracturing, topography, tectonic elements etc.) and main factors driving the creep process: deglaciation, fluvial incision, rainfall and snowmelt, seismic events, loading and unloading (also anthropic); d) evolution of a sealing cataclastic shear zone that differentiates the landslide from the stable slope. Frictional processes, hydrological inputs and external forces control the seasonal response.*

Such layers are formed by granular material with texture similar to fault rocks and geotechnical properties similar to a soil (Figure 1.13 d; Agliardi et al., 2020) and have low permeability that favors the formation of perched water table that condition the onset of differentiated rockslides. These latter are highly sensitive to hydrological forcing and external inputs that induce non-linear displacement trends and seasonal response (Figure 1.13 d). While giant slow rock slope deformations creep slowly for years in drained hydraulic conditions (Agliardi et al., 2020), differentiated mature rockslides are dominated by shear zone frictional processes and hydromechanical coupling and may undergo acceleration pulses or periods of high displacement rates towards catastrophic collapse. Agliardi et al. (2020) proved how rockslide shear zones respond to pore pressure increments by impulsive acceleration and dilatancy, causing spontaneous deceleration (Creep I) followed by sustained steady-rate creep (CreepII). This is due to the evolution of the loading conditions from

undrained to semi-drained, favored by fabric rearrangement and fluid diffusion (Agliardi et al., 2020). Further increase in pore pressure results in high creep rates (Creep III) and eventual collapse.
The overall evolution of the slope is thus influenced by different activation and stabilization phases which finally result in long-term stability or catastrophic collapse (Broadbent and Zavodni, 1982; Bovis, 2013; Zerathe et al., 2014).
Despite their slow deformation rate, large deep seated rock slope deformations are important geohazard, since they can cause the deformation on structures and infrastructures nearby (i.e. dams, tunnels, railway tracks, buildings) (Ambrosi and Crosta, 2006) and, because of the damage of rock masses and consequent decay of the mechanical properties, trigger secondary landslides or catastrophically collapse themselves.
In addition, because of the difficulty in identifying reliable precursory clues of tertiary creep, many slope failures still occur with few notice, posing major risks for human lives.
Understanding the diverse creep style is thus key to capture a possible slow to fast transition from slow moving rock slope deformations to mature and differentiated rockslides affecting limited slope sectors, but highly unstable and sensitive to hydrological contribution changes.

## 1.4 Challenges in defining the activity of slow rock slope deformation

According to Cruden and Varnes (1996), landslide activity can be defined considering three major headings describing the state, the distribution and the style of activity.
Despite the apparent simplicity of this definition and its implications, a comprehensive and useful definition of the "activity" of complex, slow-moving landslides remains challenging. A definition of activity only based on a representative displacement rate (e.g. mean velocity) can be unsuitable to capture the behaviour of slow rock slope deformations evolving over long periods in a time depending behaviour (up to $10^4$ yr; Agliardi et al., 2013; Pánek and Klimeš, 2016; Agliardi et al., 2019) of which present-day displacement rates are just a snapshot of longer and variable trends (Riva et al., 2018).
In addition, slow rock slope deformations are usually characterized by: (a) strongly heterogeneous displacement patterns, associated with complex mechanisms (strain partitioning, damage localization and/or secondary landslides nested at different depths); (b) variable and often unknown trends of activity and sensitivity to external forcing. To investigate these points, displacements must be characterized in a spatially distributed fashion and with a sufficiently high rate of temporal sampling, able to catch the different internal deformation patterns.
A complete assessment of the activity of large slow rocks slope must therefore incorporate and integrate different aspects, namely: displacement rate, segmentation / heterogeneity, kinematics (translational, rotational, compound), as well as information on internal damage and accumulated strain.
However, because of the huge volumes involved, a major difficulty in assessing the activity of large slow moving rock slope instabilities is the impossibility to extensively use

conventional geotechnical and geophysical methods, which may only provide punctual or local information of discrete sectors of the entire body.

To face this issues, spaceborne differential radar interferometry (DInSAR) has proved to be a powerful tool to characterize ground deformation rates from a few millimetres to centimetres per year, maximizing the spatial and temporal coverage at a relatively low cost (Saroli et al., 2005; Ambrosi and Crosta, 2006; Colesanti and Wasowski, 2006; Frattini et al., 2018; Crippa et al., 2020)

The integration of DInSAR data, which provides clues on the ongoing displacement pattern, with morphological evidence and long term constraints (e.g. absolute datings) is then needed to unravel the complex style of activity of the studied phenomena.

# 2 Spaceborne radar interferometry

## 2.1 SAR basics

### 2.1.1 SAR technology

Remote sensing radar (acronym for Radio Detection And Ranging) technologies have been developed since the beginning of the 20th century to detect and investigate a broad spectrum of surface deformations with a high level of detail. Radar systems use radio-waves (Figure 2.1) which are electromagnetic waves with wavelength from 1 mm to 1 m, emitted by an antenna to determine the position, velocity and distance of moving objects.

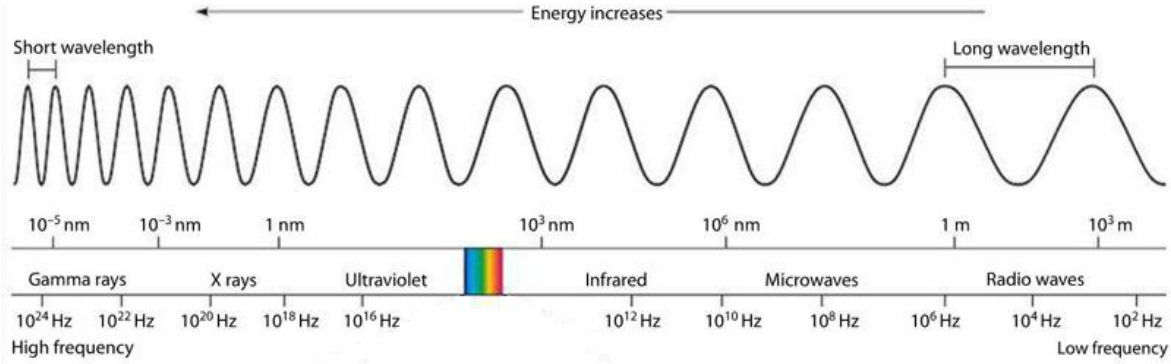


*Figure 2.1: Eelectromagnetic spectrum with of frequencies electromagnetic radiation and their respective wavelengths (source: www.miniphysics.com).*

Real aperture radar systems (RAR) only measure and process the amplitude of returning signal and the image resolution is controlled by the physical length of the antenna with typical resolutions in the order of several kilometers. Since the dimensions of the antenna footprint on the ground is inversely proportional to the antenna dimension, the longest is the antenna, the more limited is its footprint, allowing to identify smaller targets.
SAR (Synthetic Aperture Radar) system exploits the classical radar acquisition improving the spatial resolution of imaging by synthesizing a long antenna through the movement on a platform or orbit of a small physical one operating in different frequency bands (Table 2; Mccandless and Jackson, 1978; Richards et al., 2010).

*Table 2: Radar frequency bands. Spaceborne SAR missions commonly operates in L, S and C band.*

| Frequency band | Frequency range (GHz) | Wavelength range (cm) |
|---|---|---|
| L band | 1–2 | 15–30 |
| S band | 2–4 | 7.5–15 |
| C band | 4–8 | 3.75–7.5 |
| X band | 8–12 | 2.5–3.75 |
| Ku band | 12–18 | 1.67–2.5 |
| K band | 18–27 | 1.11–1.67 |
| Ka band | 27–40 | 0.75–1.11 |
| V band | 40–75 | 0.4–0.75 |
| W band | 75–110 | 0.27–0.4 |

These different physical properties have direct impact on the application of each frequency in different conditions and scenarios (Figure 2.2). In addition, frequency conditions the microwave propagation and thus its choice (i.e. wavelength) depends on the application requirements.

Since radar waves strongly interact with structures similar in size to the radar wavelength, surfaces appear rougher in images acquired using shorter wavelengths (X, C bands). Longer wavelengths (L band) tend to penetrate more the vegetation, dry soils, and ice; but phase measurements from longer wavelengths tend to be less sensitive to small changes in the surface conditions over time (Wempen and McCarter, 2017). Thanks to these advantages and sensing capability, SAR technique has been thus widely applied to geomorphological, volcanic and oceanographic studies to catch small surface displacements that can't be detected by conventional approaches.

It shows great potential also for detecting instabilities across wide areas and can monitor surface displacement inside a single landslide.

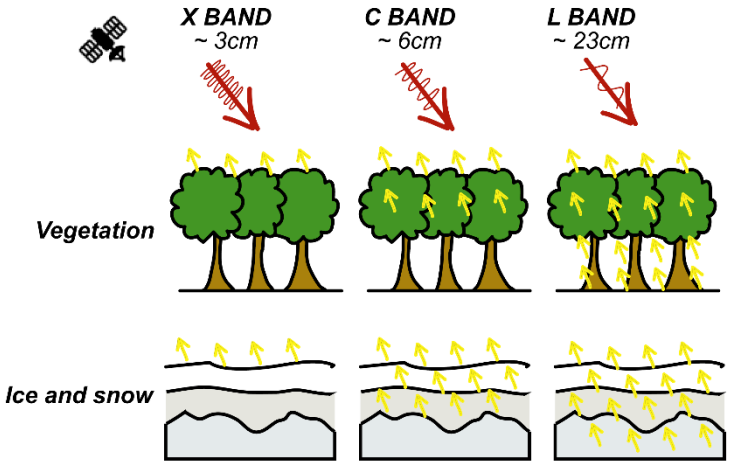


*Figure 2.2: Penetration of different radar frequency bands trhough vegeation and dry ice snow and ice.*

The transmitted microwaves consist of electric and magnetic field perpendicular to the propagation direction of the wave. This field can be polarized so to transmit only the wave propagating in the horizontal (H) or vertical plane (V).
HH or VV polarizations (single-polarization) indicate that the transmitted and received signal only propagate in the horizontal or vertical plane. HV or VH polarizations (dual-polarization) on the contrary indicate that the transmitted signal is respectively horizontal and vertical and the received one is the opposite (the first designation is the transmit direction and the second is receive).
According to the polarization of the transmitted and receiving signal SAR system emphasizes different details (structures, orientations etc.) of the ground surface depending on its backscattering properties (Table 3) (Richards, 2009). Dual-polarization systems cause a greater dispersion of the backscattered signal resulting weaker than single-polarization systems, but on the other hand single-polarization may present limitations analysing heterogeneous targets which could be misclassified because of the speckled backscatter response (Irwin et al., 2018).

*Table 3: Polarization modes*

| Polarization mode | Applications |
|---|---|
| HH | Soil moisture, crops, ice and water, urban areas, flooded vegetation |
| VV | Small scale roughness, sea waves detection, bare soils |
| HV-VH | Ice deformations, bare ground, soil moisture, vegetation covers |

## 2.1.2 Basics of SAR acquisition

SAR satellites operate along sun-synchronous, near polar orbits, that sense the earth surface in all weather and light conditions with a selected radar wavelength and specified revisiting time over the same area (Figure 2.3 a).

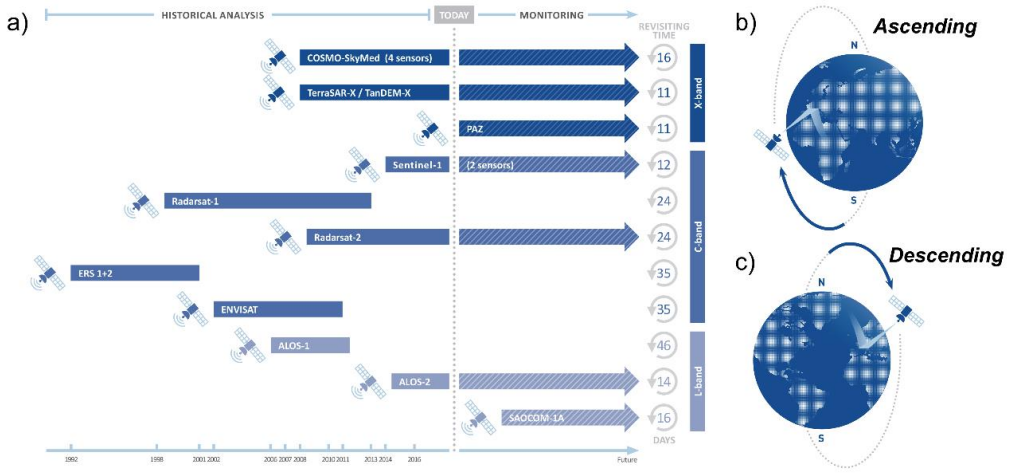


*Figure 2.3: SAR satellites with corresponding wavelength and revisiting time. Ascending and descending geometry. (Images by TRE Altamira https://site.tre-altamira.com/insar/).*

Because of the combination of the near polar-orbit and the Earth rotation, SAR satellites sense the ground in two possible "geometries": ascending (from South to North) and descending (from North to South) (Figure 2.3 b,c).
The radar sensor mounted on the satellite platform follows its azimuth or "along track" direction (Mccandless and Jackson, 1978; Richards et al., 2010). The perpendicular direction on the ground to the trajectory is called ground range or across track (Figure 2.4 a). The distance between the sensor and the target is defined as slant range (Figure 2.4 b) and corresponds to the line of sight vector (LOS) of the satellite. LOS angle or incident angle is the angle between the LOS direction and the nadir direction and corresponds to the look angle of the satellite. Each pixel in a radar image is identified by a couple of range (R)-Azimuth (Az) values that define the radar coordinate system and are related to the satellite geometry acquisition.
Since satellite SAR sensors have a side looking configuration, in the ascending geometry they better sense east facing slopes, while in the descending geometry west facing slopes are more favourable.
SAR operates as a coherent pulsed waveform transmitter emitting a sequence of chirps (finite duration pulses) separate by times during which the sensor works as a receiver of complex signals, as they carry both an amplitude and phase component (Hanssen, 2001).The radiation is transmitted from the antenna to the ground where it hits objects and part of the radiation is backscattered to the receiver on the SAR-platform.
Compared to RAR, SAR synthetically increases the antenna's size to increase the azimuth resolution (Sarmap, 2009). At each position, a pulse is transmitted, the return echoes stored echo store and processed as if the data came from a physically long antenna. Result of this processing is a high-resolution image.
The product of a single acquisition is a radar image, which is a complex matrix including an amplitude and a phase component. The amplitude is a map of the (microwave) ground reflectivity while SAR phase depends both on the local reflectivity and on the sensor-target distance (Colesanti and Wasowski, 2006).

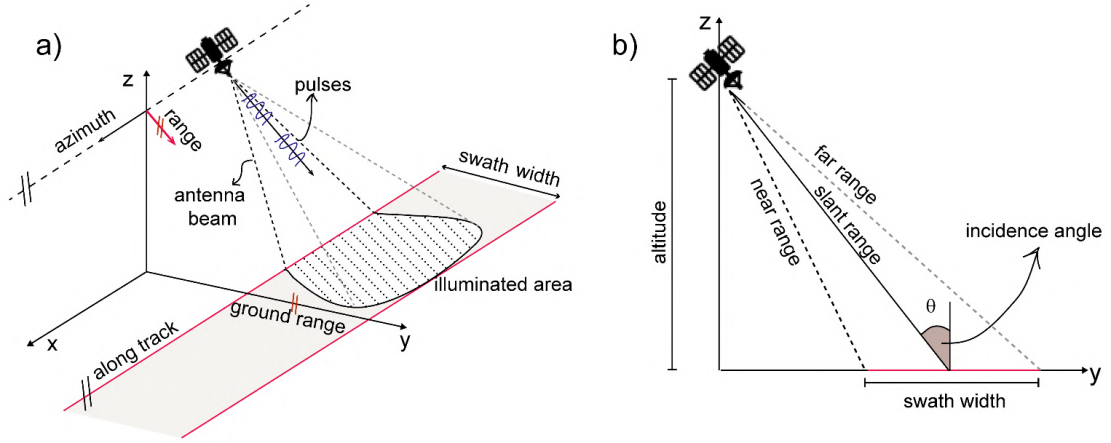


*Figure 2.4: Radar acquisition geometry (modified after Baumgartner and Kriege 2014).*

However, interpreting a SAR image is not a straightforward task as it can be affected by several sources of noise and distortions that must be considered in the exploitation of SAR data in engineering geological investigations, especially in those concerning slope stability and ground displacements.

### 2.1.3 SAR image resolution

Spatial ground resolution of RADAR systems is directly correlated to the antenna characteristics and the pulse wavelength. The antenna dimensions determine the azimuth resolution, the pulse length defines the range resolution.

- Range resolution

The maximum unambiguous range (Rmax) of any radar pulse occurs when the transmitted and return pulse from the target to the sensor are adjoining (Figure 2.5 c). If the two pulses are separated more than Rmax in the range direction, then the two scatterers are considered to be resolved in range (Figure 2.5 a; Sireci, 2005). If on the contrary the two pulses overlap (Figure 2.5 b), they form a mixed echo and the scatterers can't be solved (Richards et al., 2010).

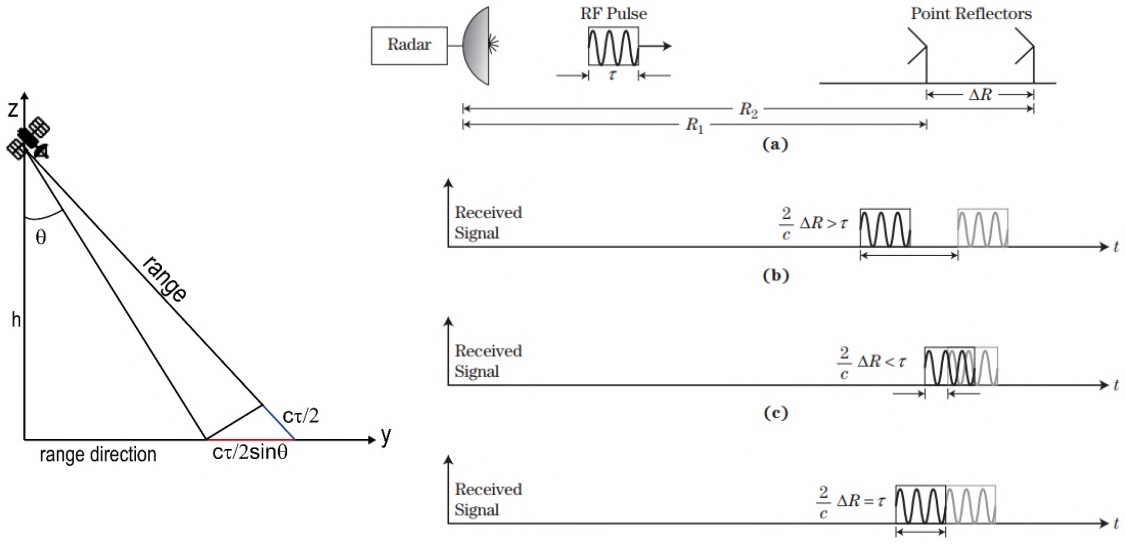


*Figure 2.5: Range resolution (Richards et al.2010).*

The maximum unambiguous range can be computed with the formula:

$$R_{max} = \frac{c\tau}{2} \qquad \textit{Eq. 1}$$

or equally

$$R_{max} = \frac{c}{2PRF} \qquad \textit{Eq. 2}$$

where τ is the pulse length, c is the speed of light ($3x10^8$ m/s) and PRF the pulse repetition frequency corresponding to the measured pulse per second.
The ground range projection of Rmax can be computed considering the LOS angle (ϑ) as follows:

$$R_{max} = \frac{c\tau}{2sin\theta} \qquad Eq.\ 3$$

If finer resolution is needed, shorter pulses can be used, but too short pulses may produce a *range ambiguity* situation. If the period between successive pulses is too short, a returning echo from the target may come back before the emission of a new one, making impossible to distinguish between the two pulses.

- Azimuth (cross range) resolution

The azimuth resolution ($r_{az}$) corresponds to the minimum distance measured along the azimuth direction (Figure 2.6) to see two scatterers as separate objects.

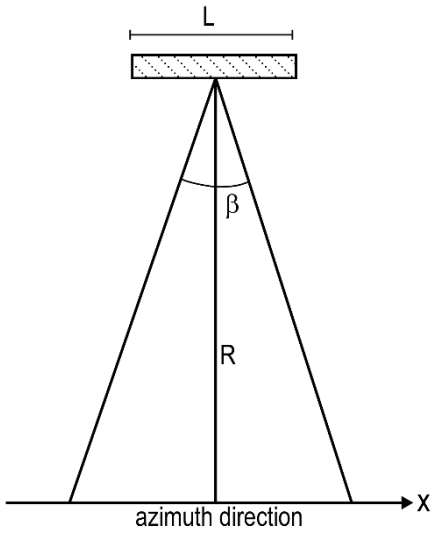


*Figure 2.6:Azimuth resolution.*

In a general radar acquisition system it depends on the real antenna length (L), the radar beam aperture (beamwitdh, β), the altitude of flight (h) and the wavelength (λ) according to this relation:

$$r_{az} = \beta \cdot R \qquad Eq.\ 4$$

where $\beta = \frac{\lambda}{L}$ and R= $\frac{h}{cos\theta}$

These same equations are valid for SAR systems, in which the synthetic antenna length ($L_S$) is expressed in terms of velocity (v) and time period of observation for the same target (T) (Chan and Koo, 2008):

$$Ls = v \cdot T = \frac{R \cdot \lambda}{L} \qquad Eq.\ 5$$

In addition, because of the two-way path from transmission to reception, the beamwidth β of a SAR system (Mccandless and Jackson, 1978; Ulaby et al., 1986; Chan and Koo, 2008; Ager, 2013) corresponds to:

$$\beta_{SAR} = \frac{\lambda}{2L_S} \qquad Eq.\ 6$$

And the corresponding azimuth resolution is simply the product of the effective horizontal beam width and the slant-range distance to the target (Budge, 2011):

$$r_{az} = \beta_{SAR} \cdot R = \frac{R\lambda}{2L_S} \qquad Eq.\ 7$$

It turns out that if the maximum aperture length ($L_s$) is used, combining *Eq. 5* and *Eq. 7*, in first approximation, the smallest azimuth resolution corresponds to half of the radar antenna in the azimuth direction (L/2).
This result shows that the azimuth resolution is independent on the distance between the sensor and the scene and inversely proportional to the size of the antenna.
This can be explained in the following way: the smaller the physical antenna (L) is, the larger its footprint and the longer the observation time of each point on the surface (T). This means that a longer array can be synthesized, allowing a narrow bandwidth (*Eq. 6*) and, hence, a finer surface resolution (Van Zyl and Kim, 2011).

### 2.1.4 Geometrical distortions

The main factors influencing the quality of a SAR image are related in first instance to geometrical distortions that locally hamper the exploitation of amplitude and phase information (Lillesand et al., 1987).
The principal geometrical distortions are referred to as *foreshortening, layover and shadowing.*

- *Foreshortening*: it happens in the case of slopes facing the sensor. Point 2 (Figure 2.7) is sensed shortly after point 1 in time. This causes a compression of the object that appears, with a thin bright "edge" on the SAR image. The real slope length is shortened on the radar imagery and compressed in a few pixels with bright reflectivity ( Colesanti and Wasowski, 2006; Chen et al., 2018). The sensor's incident affects foreshortening; a larger look angle will decrease the effect.
- *Layover:* it is an extreme case of foreshortening where the object is so steep that the radar signal reaches point 4 before it reaches point 3 (Figure 2.7).

- *Shadowing*: it occurs in SAR images because of the particular side-looking viewing geometry of SAR systems .Shadow regions appear as dark (zero signal) since they can't be reached by any radar pulse (sector 5 and points 6 and 7), because higher objects interpose between the SAR antenna and the area affected by shadowing. (Colesanti and Wasowski, 2006; Bouvet et al., 2018) For these regions, phase changes are caused only by system noise, and other less important contributions.

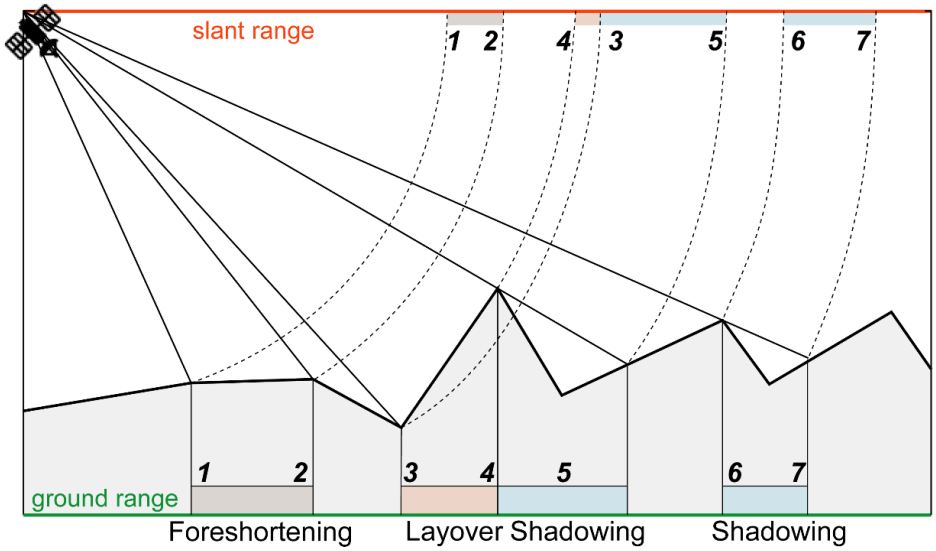


*Figure 2.7: Geometrical distorsions associated to slopes configurations (Modified from Lillesand et al. 1987).*

A quantification of the pixel compression in slant and range direction is given by the $R$ index (Eq. 8) (Notti et al., 2010; Cigna et al., 2014;) which takes into account the acquisition geometry of the radar and the geometry of the ground surface (slope and aspect derived from a DEM) (Notti et al., 2010) and provide a first indication of areas that are more easily sensed by the sensor.

$$R = \sin(\theta - \alpha \cdot \sin(A)) \qquad \textit{Eq. 8}$$

where $\alpha$ =terrain slope
a= aspect
$\gamma$= satellite's orbit heading angle
A= $\gamma$+ a+180 (ascending geometry) ; A= a- $\gamma$ (descending geometry)

Areas facing away from the sensor are characterized by sizes in ground range higher than in slant range and favorable orientation expressed by positive R values ranging from $R_0$ to 1, which is the maximum value of the R-index and it occurs when the topography is parallel to the LOS (Cigna et al. 2014, Figure 2.8Figure 2.8).
On the contrary, the smaller the R-index, the more difficult it is to detect ground targets on the slope. When R tends to 0 we enter in a foreshortening condition, while the layover effect and the shadow effects occur when the R-index is negative (Figure 2.8).

R-index reaches its minimum value ($R_{min}$) when the terrain is perpendicular to the LOS direction (90° for the descending geometry, 270° for the ascending geometry) and layover effects are stronger (Figure 2.8). However, in good visibility conditions it can happen that active shadow occurs, despite having high R index (0.75-1). This happens on steep slopes ($\beta > 90° - \vartheta$) and is represented by the folding back of the curve to lower values as $\beta$ increases (Cigna et al., 2014). The sole use of R index thus doesn't allow to discriminate between shadow and good visibility areas, but still provides a first assessment of possible slope configurations preventing a reliable SAR acquisition.

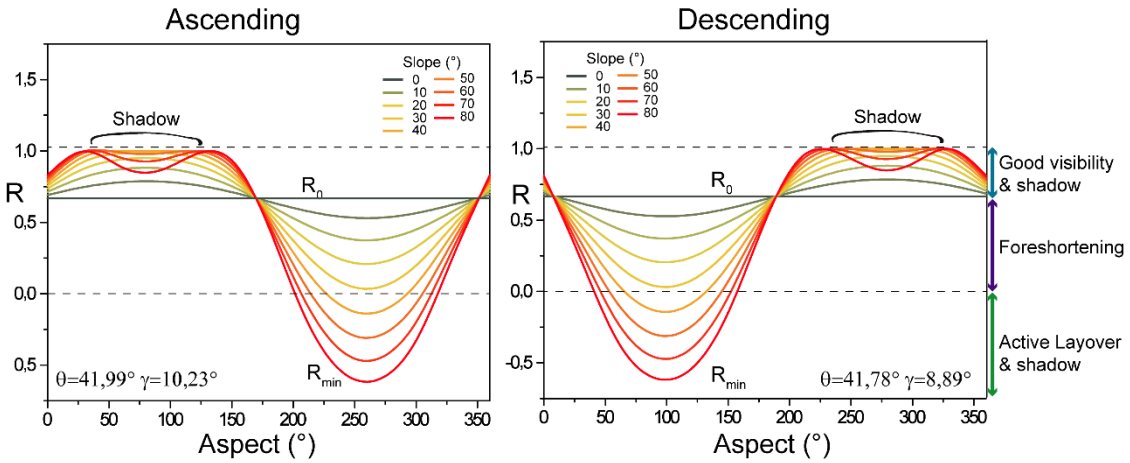


*Figure 2.8: geometric effects caused by morphometric and orbital parameters combination of Sentinel 1 A/B (modified after Cigna et al., 2014).*

## 2.1.5 Speckle

Another phenomenon influencing the quality of SAR imagery is the so called "speckle", a direct consequence of the scattering properties of the ground objects depending on the roughness of the scene and the resolution the radar signal. Depending on the terrain

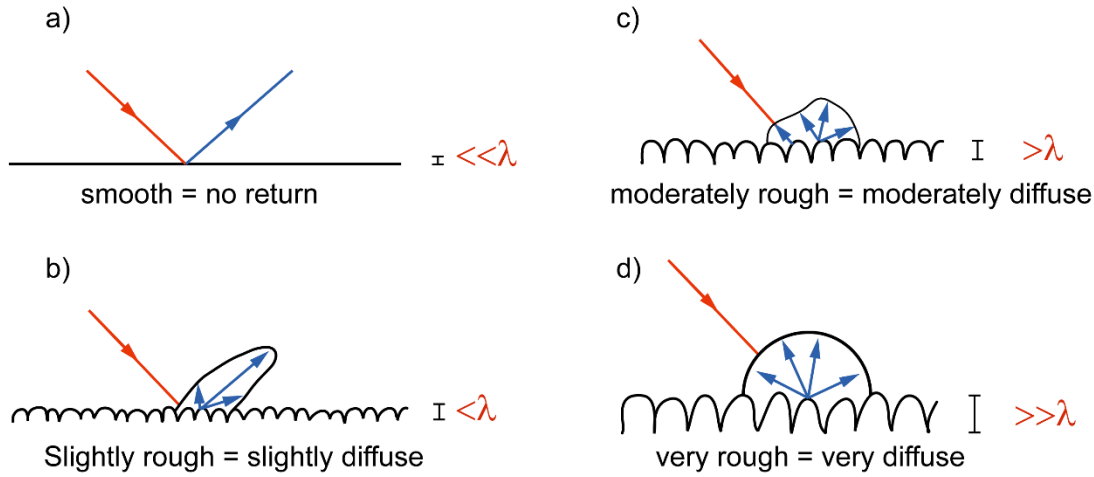


*Figure 2.9: dependence of scattering response to different surface roughness.*

roughness, the backscattered RADAR signal shows different patterns (Sabins, 1997) with positive or negative interference. This results in sprinkled light and dark signal mixed in and a "salt and pepper" pattern.
Radar backscattering is dependent on the relative height (or roughness) of the incident surface, on the wavelength (Figure 2.9) and on the incident angle: as incident angle increases backscatter decreases.
In general, speckle effects can be reduced by two methods: SAR image multi-look processing (see annex A) and filtering techniques in which moving window filters smooth the reflectivity of the central pixel considering all the intensity of the surroundings pixels inside the window. In both cases speckle is reduced at the expenses of the spatial resolution.

## 2.2 SAR Interferometry

### 2.2.1 Interferometric phase contributions

SAR interferometry (InSAR) is a set of techniques aimed at reconstructing the ground surface or its changes in time (i.e. deformations) by combining SAR images acquired at different times. InSAR can be exploited for the generation of digital elevation models (DEMs) ( Zebker et al., 1994; Gabriel et al., 1989a; Colesanti and Wasowski, 2006;) and for the detection of ground deformation phenomena. The phase information φ associated to each pixel of a single radar image doesn't provide meaningful information on the factors contributing to its value, and it is not very useful if independently considered. On the contrary, it gains importance if compared (i.e. differentiated) in radar images acquired at different time. The difference in phase between two SAR images, (i.e. a "master" and as "slave"), is called *interferogram.* Comparing phase differences from repeat-pass it is possible to accurately measure ground deformations.

The phase difference $\Delta\varphi$ between the two acquisitions is expressed in radians from 0 to $2\pi$ and it is the result of different contributions, namely: the displacement $\Delta r$ of the ground targets alon the radar Line Of Signt (LOS), difference in atmospheric path delay ($\Delta\phi_{atmo}$), topography ($\Delta\phi_{topo}$) and other noise sources ($\Delta\phi_{noise}$).

$$\Delta\varphi = \Delta\varphi_{disp} + \Delta\varphi_{topo} + \Delta\varphi_{atmo} + \Delta\varphi_{orb} + \Delta\varphi_{noise} \qquad \textit{Eq. 9}$$

- $\Delta\varphi_{disp}$ accounts for ground displacements of the scatterers between the two observations.

$$\Delta\varphi_{disp} = \frac{\Delta r \cdot 4\pi}{\lambda} \qquad \textit{Eq. 10}$$

  Where $\Delta_r$ is the ground displacement between the same target in the two acquisitions.
- $\Delta\varphi_{topo}$ represents the topography-induced phase due to a non-perfect removal of the of the effective height model (i.e., the DEM errors: z) (Pepe and Calò, 2017).

$$\Delta\varphi_{topo} = \frac{4\pi B_{\perp} z}{\lambda r_1 sin\theta} \qquad \textit{Eq. 11}$$

  Where $B_{\perp}$ is the spatial perpendicular baseline, $\lambda$ is the satellite wavelength, $\vartheta$ the incident angle and $r_1$ the slant range distance between the sensor and the target.
  Topography contribution is proportional to the spatial perpendicular baseline $B_{\perp}$ that corresponds to the distance between the two satellites positions (or orbits) projected perpendicular to the slant range. Increasing $B_{\perp}$, InSAR technique catches smaller height changes, but as drawback if the spatial baseline becomes too big decorrelation effects will arise. On the contrary, interferograms with small perpendicular baselines are more suitable to minimize sensitivity to topography (Eriksen, 2013; Pepe and Calò, 2017)

The perpendicular baseline thus also condition the *altitude of ambiguity* ($h_a$) that is the elevation change correspondent to a $2\pi$ phase shift (Pepe and Calò, 2017) .

$$h_a = \frac{\lambda r_1 sin\theta}{2\, B_\perp} \qquad \textit{Eq. 12}$$

The smaller the height of ambiguity is, the lower are the errors caused by the instrument and the decorrelation effects.

- $\Delta\varphi_{atmo}$ refers to phase variations caused by changes in atmospheric humidity, temperature and pressure between the master and slave acquisition (Zebker et al., 1997) between the master and slave acquisition. It can be partially corrected with specific algorithms and atmospheric models (Colesanti et al., 2003)
- $\Delta\varphi_{orb}$ due to residual fringes resulting from inaccurate orbital information in the synthesis of the topographic phase (Pepe and Calò, 2017) resulting in velocity gradients in range and azimuth directions (Fattahi and Amelung, 2014).
- $\Delta\varphi_{noise}$ derives from changes of geometrical or scattering properties of surface cover and decorrelation effects caused by difference in spatial and temporal baseline (Lauknes et al., 2010; Pepe and Calò, 2017).

### 2.2.2 Differential SAR Interferometry (D-InSAR)

If the phase shifts related to topography, atmosphere and other contributions are removed from the interferograms, the final result will be directly related to the surface deformation patterns occurred between the two acquisition dates. The displacement is indicated by a sequence of colored fringes that thicken toward the center of the deforming features.
For example, emblematic interferograms result from permanent co-seismic or volcanic deformations (i.e. inflation/deflation or flank collapse), with evident repeating cycles of fringes that can be easily related to the corresponding displacement fields (Figure 2.10).

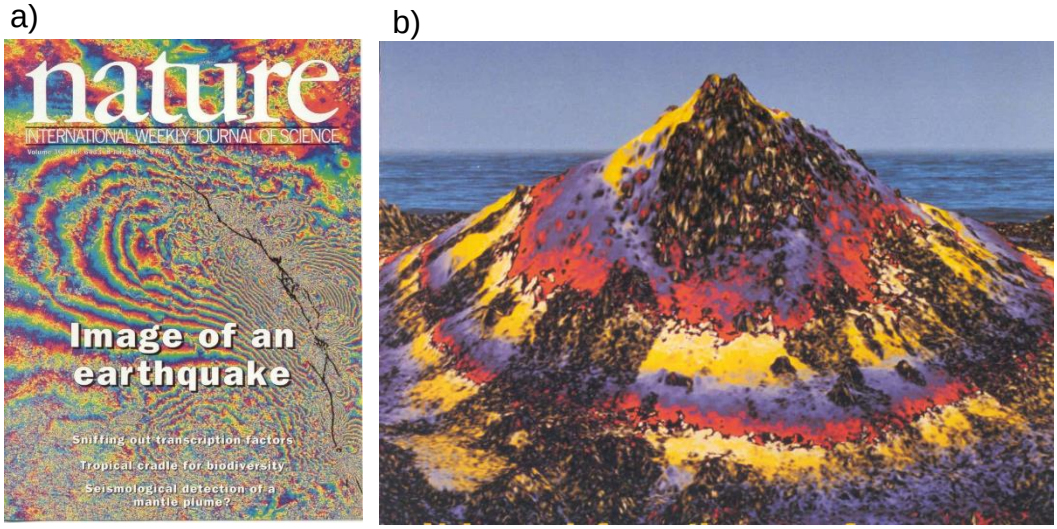


*Figure 2.10:: First DINSAR maps computed for a) Landers earthquake b) deflation of Mount Eta(Massonet et al., 1993, 1995).*

This methodology is called Differential Interferometry (DInSAR).
The topographic effects are compensated by using a Digital Elevation Model of the area of interest that is subtracted from the original interferogram simplifying the phase equation as follows:

$$\Delta\Phi_{(DInSAR)} = \frac{4\pi\Delta r}{\lambda} \qquad \textit{Eq. 13}$$

where $\Delta$r is sensor to target distance variation in the slant range direction, and $\lambda$ is the radar wavelength. Since the wavelength is inversely proportional to the displacement sensitivity, short wavelengths are advisable in measuring very slow movements
It is always better to use a DEM which is closer to the spatial resolution of the sensor. If a DEM of higher resolution is subtracted (e.g. 1m), it will be down sampled to the pixel size of the sensor and this might introduce artifacts.
Thus, if nothing has changed between the master and slave images, if the backscattered properties have remained stable, no atmospheric fluctuations have occurred and there are almost no orbital errors, the range variations can be simply computed considering the sensor to target distance changes and the radar wavelength, highlighting any possible deformation phenomena occurred between the master and slave acquisitions (Ferretti, 2014).
More precisely each pixel (p) in the resulting interferogram will be computed as the product between the complex values of the master ($I_m$), by the complex conjugate of the slave ($I_s$):

$$p_j = I_{m,j} \cdot I^*_{s,j} = \left|I_{m,j} \cdot I^*_{s,j}\right| \cdot e^{,j(\varphi_m - \varphi_s)} \qquad \textit{Eq. 14}$$

where $\phi$ is the interferometric phase (Ferretti, 2014; Pepe and Calò, 2017) and is calculated as:

$$\phi = arctan\frac{Imm(p_j)}{Real\ (p_j)} \qquad \textit{Eq. 15}$$

where the numerator corresponds to the imaginary part and the denominator the real part of the pixel value.
In an interferogram the phase information measures the distance between the radar antenna and a target (Rott, 2009; Tessari et al., 2017) while amplitude values give an indication of the power of the backscattered signal and depend on the reflectivity properties of the target.
The accuracy on the mean displacement rates depends on the wavelength, the spatial resolution (which influences the phase noise) and the number of acquisition in the observation time-span (revisit time) (Bovenga et al., 2018)introducing limitations in the DInSAR capability to detect certain ranges of ground movements.
One of the major limit of the technique is the identification of movements that exceed the so called velocity of ambiguity between the two acquisition, and that can introduce errors in the phase unwrapping procedure, necessary to convert phase displacement to metric scale.

### 2.2.3 Phase aliasing and velocity of ambiguity

Sensor to target distance can always be expressed as an integer number of wavelength plus a fraction of λ (Ferretti, 2014). The interferometric phase in a SAR interferogram can be thus represented as fraction of a cycle in the range 0-2π (Figure 2.11).

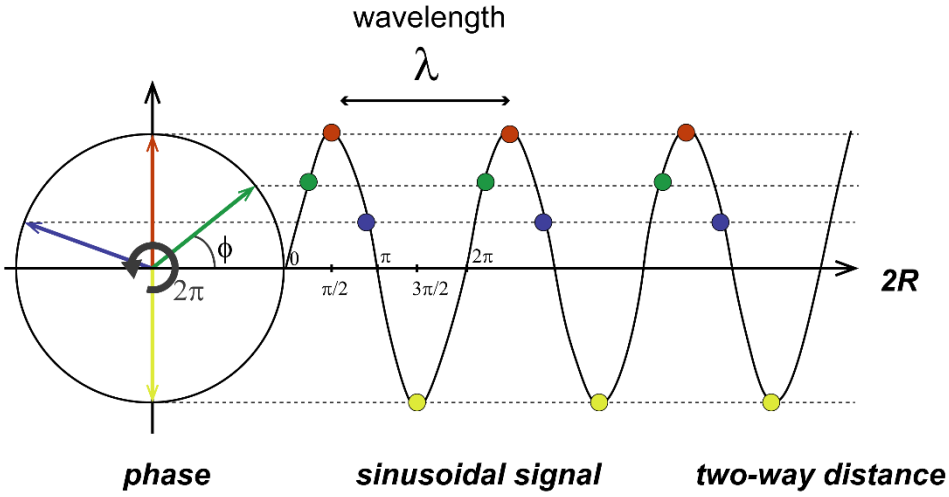


*Figure 2.11: Interferometric phase expressed as fraction of a cycle 0-2π and as sinusoidal function sin φ with a 2π radian period. The transmitted signal can be assimilated to a pure sinusoid whose angle or phase φ depends on the slant range coordinate R and wavelength λ. Assuming 0 the phase of the transmitted signal, the received signal that covers the distance 2R shows a phase φ = 4πR/λ radians (eq.14) (Ferretti et al., 2007).*

Taking into account the two way travel path of the radar pulse, from the sensor to the target and back, an object appears steady if its distance from the radar is changed by multiples of λ/2, which is the "effective wavelength" of the system. This becomes clear considering the signal as a sinusoidal wave.

When the target moves exactly of λ/2 the transmitted sinusoidal wave and the return one wipe out with Δφ=0 (Figure 2.12 E). Measuring phase values in this case doesn't allow to know if and how much the ground has moved, since the result will always be an integer number of λ.

If on the contrary the target moves less than λ/2 (Figure 2.12 A, B, C, D) the radar system can measure without ambiguity its displacement. If it moves of (λ/2+ ΔR) the system will measure only the ΔR portion, with no information on the effective numbers of cycles (i.e. number of λ/2) covered by the displacement.

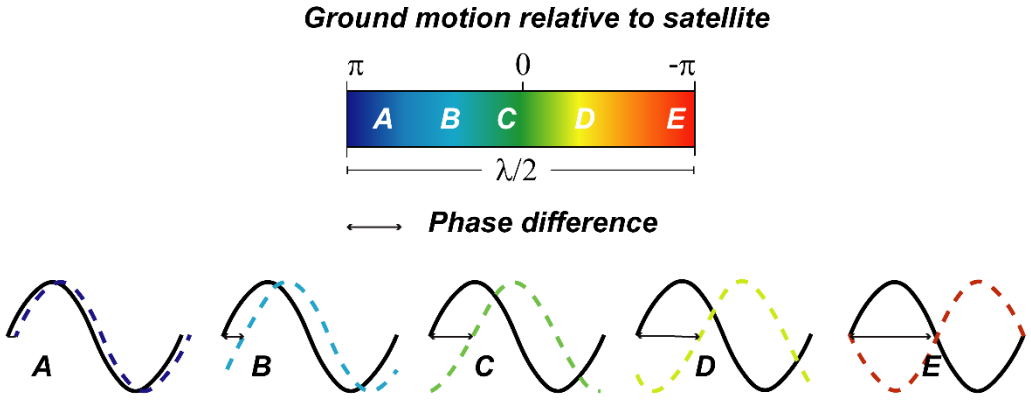


*Figure 2.12: Increasing of phase differences to a maximum λ/2 displacement (modified from www.volcano.si.edu).*

So, in order to unambiguously measure the ground deformation, the maximum displacement between the two following acquisitions must be less than λ/2. More precisely, to measure not only the displacement magnitude, but also the direction of movement (i.e. towards or away from the satellite) displacement must be less than λ/4 (Colesanti and Wasowski, 2006; Ferretti et al., 2007; Manconi, 2019).

This ambiguity hampers to univocally track the relative LOS displacement between two scatterers exceeding λ/4 (1,4 cm for Sentinel 1) within one revisiting time interval (6 days): in practice it is extremely difficult to detect unambiguous LOS displacement rates exceeding 0.23cm/day (i.e. 85 cm/year)

$$v_{ambiguity} = \frac{\lambda}{4\,RT} \qquad \textit{Eq. 16}$$

where RT is the revisiting time.

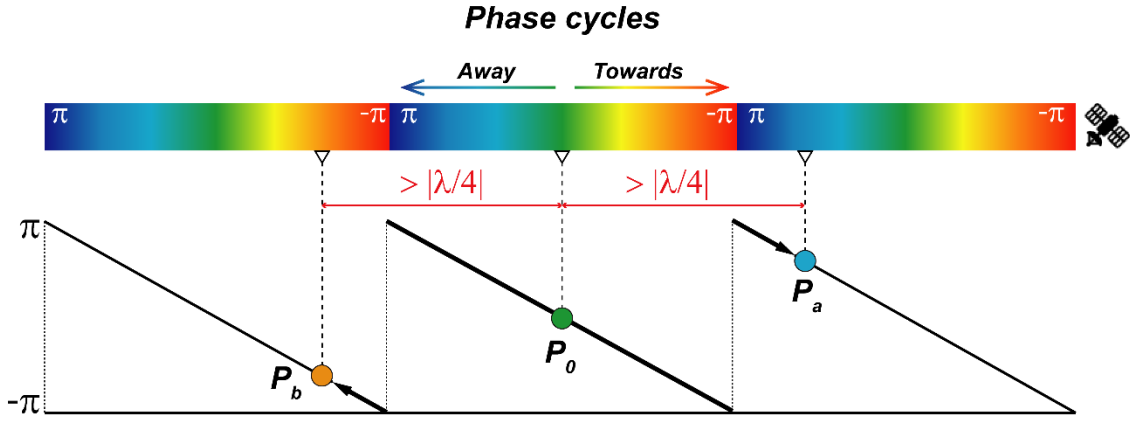


*Figure 2.13:Displacements exceeding λ/4*

This can be graphically visualized as follows: if a point $P_0$ moves more than $\lambda/4$ in modulus, in the color bar representing phase cycles (Figure 2.13) it shifts from a stable position (green) to a blue fringe ($P_a$ displacement toward the sensor), but it can also move away from the satellite of the same $\lambda/4$ quantity ending in a red fringe ($P_b$).
Therefore, even if the displacement is less than $\lambda/2$, there is still ambiguity in the measure: in general deformations that are n times greater than the $\lambda/4$ threshold can be underestimated as they produce similar observed phase signals (Tzouvaras et al., 2020).
On the contrary, if the movement is less than $\lambda/4$ in modulus (Figure 2.14), there is no ambiguity in the displacement direction. If $P_0$ shifts from a green fringe to a red one ($P_a$), then it is moving towards the satellite, if it moves on a blue fringe it is getting away from the sensor.
An "a priori" knowledge of the analyzed phenomenon and its possible range of displacement values is thus required to complete a sound interpretation of the DInSAR data to avoid misinterpretations of the resulting signals.

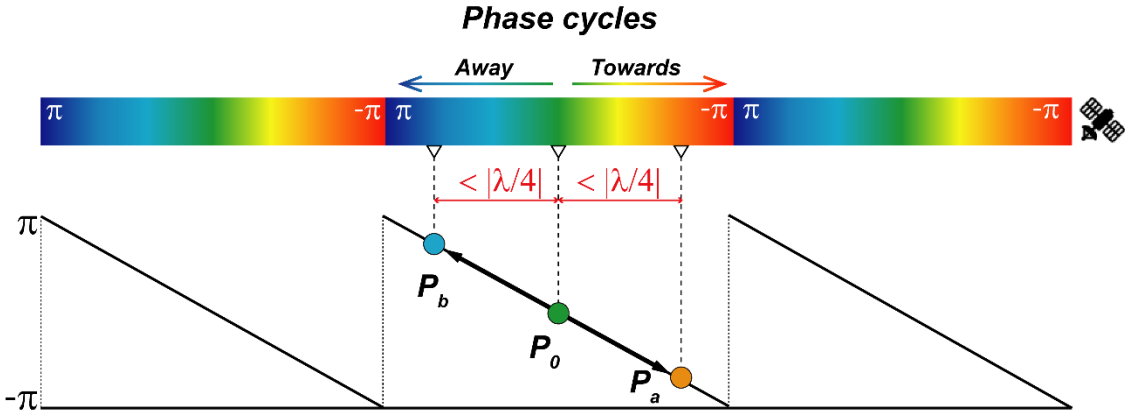


*Figure 2.14 Displacements lower than λ/4*

This qualitative observation can be better explained considering the *unambiguous Doppler shift measurement.*
The relative motion between the radar and the target can be expressed as frequency changes of the EM wave emitted and received by the radar. This is Doppler effect: as target moves toward the radar, frequency is increased, if the target is moving away from the radar, the frequency is reduced. Given phase shifts in a certain interval of time correspond to frequency shifts, which the radar can measure (Turkish State Meteorological Service, 2005; Scheer and Holm, 2010).
The Doppler frequency shift is approximately given by:

$$f_d = \frac{2v_r}{\lambda} \qquad \textit{Eq. 17}$$

Where $v_r$ is the radial velocity (i.e.towards the radar or away from it) and $\lambda$ the radar wavelength.
From Eq. 17, maximum radial velocity can be expressed as:

$$v_{r\_max} = \frac{f_{max}\,\lambda}{2} \qquad \textit{Eq. 18}$$

Where $f_{max}$ is function of the pulse repetition frequency (PRF) of the radar (Figure 2.5: Range resolution (Richards et al.2010). and, for the Nyquist theorem, it is given by:

$$f_{max} = \frac{PRF}{2} \qquad \textit{Eq. 19}$$

Combining these equations the $v_{r\_max}$ becomes:

$$v_{r\_max} = \frac{f_{max}\,\lambda}{2} = \frac{\frac{PRF}{2}\,\lambda}{2} = \frac{PRF\,\lambda}{4} \qquad \textit{Eq. 20}$$

This explains why the maximum velocity that can be unambiguously measured is function of $\lambda/4$.

To detect high velocity displacements, small revisit times, large PRF, long wavelengths or all of them must be used.to avoid aliasing and to perform reliable phase unwrapping (Turkish State Meteorological Service, 2005; Scheer and Holm, 2010; Manconi, 2019;).

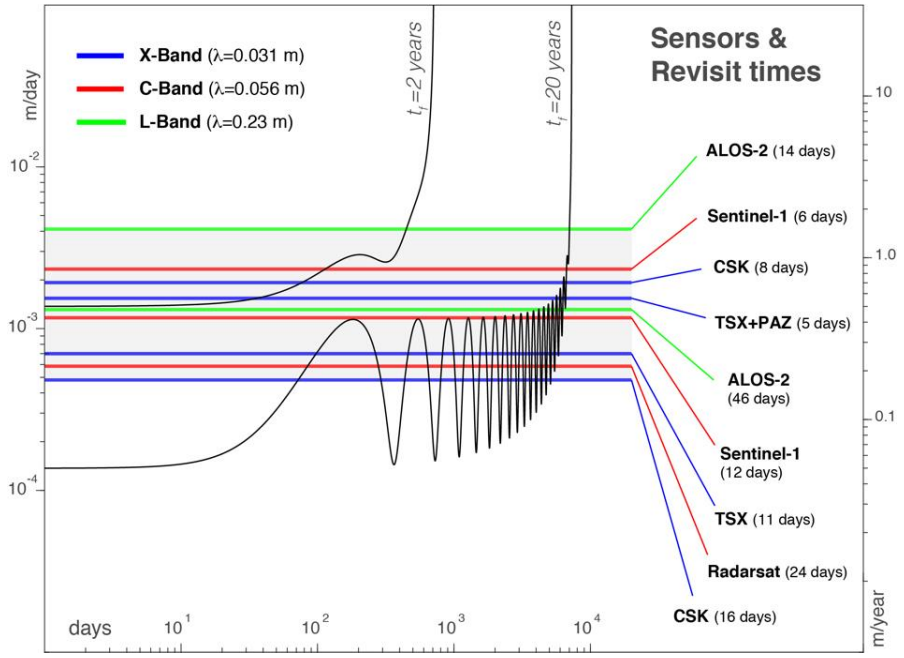


*Figure 2.15: maximum detection velocity for different satellite missions. (Manconi, 2019).*

Therefore, the use of different frequency bands and revisiting time impacts on the monitoring of surface phenomena, subsidence and landslides in particular (Figure 2.15 and Table 4) (Bovenga et al., 2018). In fact, when the surface velocities exceed the velocity of ambiguity threshold defined for a given satellite, the DInSAR measure is intrinsically underestimated

due to aliasing affecting the phase unwrapping step (Manconi, 2019; Rabus and Pichierri, 2018).

*Table 4:Selected characteristics of principal Synthetic Aperture Radar (SAR) sensors (Wasowsky and Bovenga, 2014).*

| Satellite mission | Wave-length (cm) | Life status | Resolution az./range (m) | Repeat cycle (days) | Swath width (km) | Max. vel. (cm/yr) | Incident Angle(°) |
|---|---|---|---|---|---|---|---|
| | | | C-band | | | | |
| ERS-1/2 | 5.6 | 1992–2001 | ≈6/24 | 35 | 100 | 14.6 | 23 |
| ENVISAT | 5.6 | 2003–2010 | ≈6/24 | 35 | 100 | 14.6 | 19–44 |
| RADARSAT-1 | 5.5 | 1995– | ≈8–30 | 24 | 45 (fine)<br>100 (strip)<br>200 (scan) | 20.4 | 20–50 |
| RADARSAT-2 | 5.5 | 2007– | ≈3/3<br>≈8/8<br>≈26/25 | 24 | 10 (spot)<br>40 (strip)<br>200 (scan) | 20.4 | 20–50 |
| Sentinel-1 | 5.6 | 2014–2024 | 5–20 | 6, 12 | 250 | 85 | 30–46 |
| RADARSAT Constellation Mission (3 Sat) | 5.5 | 2018–2026 | 5–50 | 3, 12 | 30–350 | 163.2 | 20–55 |
| | | | L-band | | | | |
| J-ERS | 23.5 | 1992–1998 | 18 | 44 | 75 | 48.7 | 35 |
| ALOS PALSAR | 23.6 | 2006–2011 | ≈5/7–88 | 46 | 40–70 | 46.8 | 8–60 |
| ALOS PALSAR-2 | 22.9 | 2013–2017 | 1/3<br>3–10/3–10<br>100/100 | 14 | 25 (spot)<br>50–70 (strip)<br>350 (scan) | 149.2 | 8–70 |
| SAOCOM (2 Sat) | 23.5 | 2014–2021 | 10–50 | 8, 16 | 20–150 | 268 | 20–50 |
| | | | X-band | | | | |
| COSMO-SkyMED (4 Sat) | 3.1 | 2007–2014 | ≈2.5/2.5<br>1.0/1.0 | 2, 4, 8, 16 | 10 (spot)<br>40 (strip)<br>200 (scan) | 17.7<br>35.4<br>70.7<br>141.4 | 20–60 |
| TerraSAR-X | 3.1 | 2007–2018 | ≈3.3/2.8<br>1.0/1.0 | 11 | 10 (spot)<br>30 (strip)<br>100 (scan) | 25.7 | 20–55 |
| COSMO-SkyMED-2 (2 Sat) | 3.1 | 2015–2023 | 1–3 | | 10–40 | | |
| TerraSAR-X-2 | 3.1 | 2015–2018 | 0.5–4 | | 10–40 | | |

### 2.2.4 Phase Unwrapping and displacement maps

Any interferogram is displayed in the phase domain as repetition of cycles of fringes, each one corresponding to a $2\pi$ or $\lambda/2$ interval. Phase values are thus ambiguous, as they are wrapped (i.e. constrained) in the interval $(-\pi, \pi]$ or $[0, 2\pi)$ (Figure 2.16Figure 2.16: Wrapped and unwrapped phase.). To obtain a correct map and attributing the correct number of cycles to each pixel, the phase unwrapping procedure must be applied (Chen et al., 2000; Ferretti, 2014).

Phase unwrapping consists in a series of target algorithms that aim to recover the integer number of cycles ($k$) to be added to the original wrapped phase ($\varphi$) in order to obtain for each pixel the unambiguous phase value $\psi$ (Figure 2.16).

$$\psi_{unw} = \phi_{wrapped} + 2\pi \cdot k \qquad \textit{Eq. 21}$$

Unwrapping procedures provide an infinite number of different solutions, and a priori information must be added to get the most appropriate one.

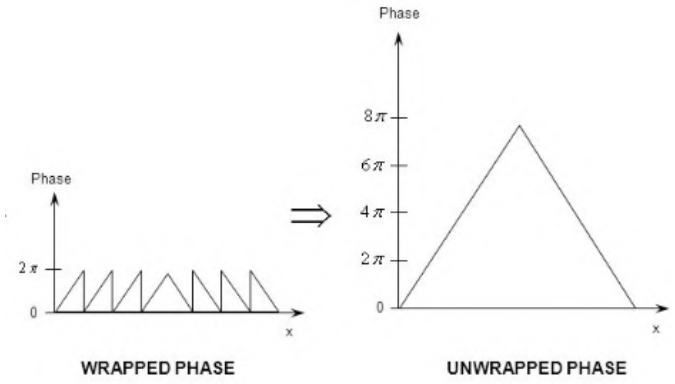


*Figure 2.16: Wrapped and unwrapped phase.*

Several algorithms have been proposed: Branch cuts, Region Growing, Minimum Cost Flow, minimum Least Square etc., but none of them gives an overall correct result and they must be chosen according to the specific case.

Basically, all the phase unwrapping algorithms are based on the main assumption that the unwrapped phase field varies smoothly between neighboring pixels (i.e. slow variation between close phase values) remaining within one half cycle of one another. (Ferretti, 2014). In terms of topographic height, the difference between two successive pixels must be less than half the height of ambiguity ($h_a$, *Eq. 12*).

However, it is hard to assume that an interferogram doesn't present any noise effects and there are no inconsistencies due to phase discontinuities. As consequence the abovementioned conditions are not always satisfied.

Discontinuities are always present and mainly due to low SNR values caused by temporal or geometrical decorrelation and possible fast phase variation of the signal of interest (local topography or surface deformation) (Ferretti, 2014).

So, if between two points (i,j) and (i,j+1) or (i+1,j) the following conditions are verified (Small, 1998):

$$|\phi(i,j) - \phi(i,j+1)| \geq \pi$$
$$|\phi(i,j) - \phi(i+1,j)| \geq \pi \qquad \textit{Eq. 22}$$

an ambiguity of 2πk arises, and it is impossible to analytically compute the value of k, that points out a univocal correspondence between $\Delta\varphi$ in slant range and the real height or displacement between the two points.

Phase unwrapping algorithms try to reach a solution optimizing the error and making the unwrapped gradient equal to the wrapped one (i.e.$\Delta\varphi$=$\Delta\psi$) almost everywhere, minimizing the cost function C (Carballo and Fieguth, 2000):

$$C = \left\{ \sum_{i,j} w_{i,j}^{(r)} |\Delta^{(r)}\psi_{i,j} - \Delta^{(r)}\phi_{i,j}|^p + \sum_{i,j} w_{i,j}^{(a)} |\Delta^{(a)}\psi_{i,j} - \Delta^{(a)}\phi_{i,j}|^p \right\} \qquad \textit{Eq. 23}$$

Where $0 \leq p \leq 2$

w= weights defined by the user according to coherence values, since they help to identify areas where phase values are noisy and the assumption of the smooth phase variation isn't appropriate.

(r), (a) = range and azimuth direction

Different p values lead to different solving algorithms (for a specific description of the single algorithms and their application please refer to the relative following references).

p=0 → Least Mean Squares (Weike and Goulin, 2012)

p=1 → Minimum Cost Flow (Mario Costantini, 1998)

p=0 → Branch Cut (Goldstein et al., 1988)

The more the interferometric fringes are concentric and the more the coherence is high, the more the unwrapping procedure will be successful. That is why DInSAR interferograms are generally filtered before the unwrapping stage, to reduce phase discontinuities and make phase variation smoother (Ferretti, 2014).

The reliability of the unwrapped result is thus highly variable and it is inappropriate and risky to rely only on a single interferogram. Results must be always integrated with in situ observations or a priori knowledge of the area analyzed and the processing of more than one interferogram is suggested to quantitative increase the precision assessment.

Once computed the unwrapped maps, they provide information on the relative height/displacement between two pixels. To obtain absolute estimates a tie point (i.e. known height, zero displacement) can be used to rescale the values. Finally, since the raw values are still presented in radians (π), to convert them from phase to meters it is necessary to multiply their values for the wavelength λ according to Eq. 10.

### 2.2.5 Interferometric coherence

Interferometric coherence γ is a measure of degree of reflectivity associated to the scatterers or to the entire sensed area between the two acquisitions (Bamler and Just, 1993)
The coherence associated to each pixel is computed as the cross-correlation coefficient of the SAR image pair estimated over a small window (few pixels in range and azimuth) and its values range from 0 (the interferometric phase is just noise) to 1 (complete absence of phase noise) (Ferretti et al., 2007).

$$\gamma = \frac{|E[\mu_1 \mu_2^*]|}{\sqrt{E[|\mu_1|^2]E[|\mu_2|^2]}} \qquad \textit{Eq. 24}$$

where $\mu_1$ and $\mu_2$ represent the master and slave complex data respectively. * indicate complex conjugate, $E[\cdot]$ represents mathematical expectation (Qiu et al., 2016).
Coherence value depends on the spatial (i.e. distance between the two antennas) and temporal decorrelation (changes in the physical and geometric properties of the scatterers, Ma et al. 2018) between the master and slave images, on the scattering properties of the ground, which change according to its cover and dielectric properties, and on the displacement rate of the surface, since high surface deformation rates negatively affect the quality and the coherence of the interferogram (see section 2.2.3). For example, water and vegetated areas (grass, trees with leaves etc.) usually show high decorrelation effects even on short temporal baselines (minutes, hours), while other scatterers (bedrock, outcrops, buildings, infrastructures etc.) keep a more stable electromagnetic signature over the time and remain coherent also with longer temporal baselines between the master and slave acquisitions (Barboux et al., 2014; Monserrat et al., 2014; Eriksen, 2017). These are defined permanent scatterers (Ferretti et al., 2001).
The time interval inducing decorrelation depends on the SAR-instrument's wavelength, and surface properties in the scene(Eriksen, 2017). Therefore, the process inducing ground deformation, surface cover and range of displacement must be considered when selecting sensor and temporal baseline.
The higher is the coherence, the sharper is the quality of the interferometric fringes, while low coherence points out an unreliable measurement. However, having a high coherent interferogram doesn't necessarily mean high accuracy in the displacement measure as this can be affected by the above-mentioned source of noise and phase contributions.

### 2.2.6 Atmospheric effects

Atmospheric phase screening (APS) also influence the exact measure of ground displacement rates. Turbulence phenomena, vertical stratification of the atmosphere, local temperature and density anomalies affect the EM propagation velocity, introducing different indexes of refraction (Ferretti, 2014). EM electromagnetic waves are delayed (slowed down) when they travel through the troposphere while the ionosphere tends to accelerate the phases of electromagnetic waves travelling through it (Ding et al., 2008).

However, more than the atmospheric stratification, an important role in then the mountainous regions is played by the water vapor content that is strongly correlated to the local topography.
Water vapor mainly concentrates in the near-ground surface troposphere (Ding et al., 2008)(up to about 2 km above ground), where a turbulent mixing process occurs resulting in three-dimensional (3D) spatial heterogeneity in the refractivity.
Due to the propagation delay of radar signals the phase measurements $\Delta\varphi$ of Eq. 10 becomes:

$$\Delta\varphi_{master} = \frac{4\pi}{\lambda}(r_m + \Delta r_m), \qquad \Delta\varphi_{slave} = \frac{4\pi}{\lambda}(r_s + \Delta r_s) \qquad \textit{Eq. 25}$$

where $\Delta r_m$ and $\Delta r_s$ are atmospheric propagation delays of radar signals corresponding to the master and slave acquisitions.
The difference between the two atmospheric contributions gives the relative tropospheric delay ($\Delta r_m$-$\Delta r_s$). If there are no changes in the atmospheric profiles in the two acquisitions, the relative tropospheric delay disappears, however this is almost impossible in practice, leaving an almost constant atmospheric disturb.

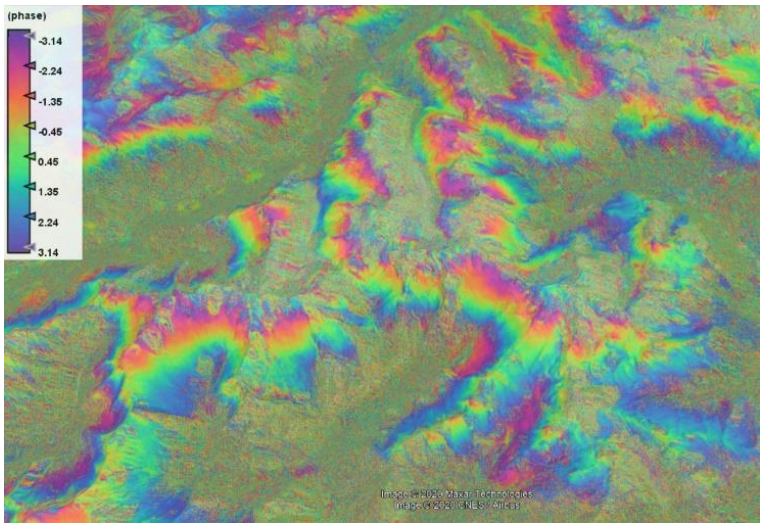


*Figure 2.17: Example of atmospheric artefacts in a mountainous area (Central Alps, Lombardia).*

One of the most effective ways to correct atmospheric artifacts is to generate an atmospheric delay map for both the acquisition dates from external data and then subtract it from the SAR interferogram or deformation map (Li, 2005; Li et al., 2007; Ding et al., 2008).
The atmospheric contribution is generally less than a phase cycle ($2\pi$) and results in the image as a gradual color change or, where it is particularly strong, as a series or fringes masking the topographic similarly to contour lines (Figure 2.17).

### 2.2.7 Slope and aspect bias on velocity measure

Displacement perpendicular to the LOS direction cannot be detected as they lay on a *blind plane* (Figure 2.18 a, b). Considering a natural slope favourably oriented with respect to a given orbital direction (ascending or descending), a movement can be completely registered only if occurs parallel along the relative LOS (Figure 2.18 c). Other configurations induce underestimation of the displacement vector which is projected on the LOS plane returning only a part of the real displacement vector.

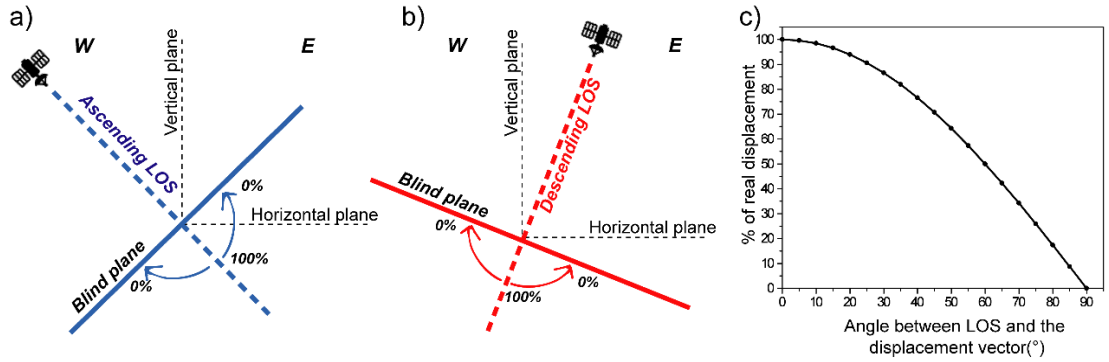


*Figure 2.18: Satellite detection capability in a) ascending and b) descending geometry and c) percentage of real displacement read according to differnet angles between displacement vector and LOS movement on a fictitious slope oriented as the LOS direction.*

A knowledge of the LOS direction parameters and of the slope topography (slope, aspect etc) (Eriksen et al., 2017) is thus necessary to estimate how much of the true three-dimensional (3D) displacement can be observed.

Some studies tried to overcome this issue approximating the movement to a surface-parallel displacement, as in the case of ice flows analysis (Joughin et al., 1998), projecting the LOS velocity along slope ($v_{slope}$; Notti et al., 2012, 2014; Aslan et al., 2020) This facilitate the interpretation of $v_{LOS}$ data, but since it assumes a global translational sliding, it hampers any unconstrained interpretation of the landslide kinematics (Frattini et al., 2018; Meisina et al., 2008). This is especially true for phenomena such as complex landslides, in which the internal displacement pattern can be variable and differ from the simple downward movement. $v_{slope}$ is computed as the ratio between $v_{LOS}$ and a coefficient C that refers to the percentage of movement detected along the slope (Colesanti and Wasowski, 2006; Notti et al., 2012; Plank et al., 2012).

The coefficient "C" derives from the integration of satellite geometry and slope and aspect configuration according to the formula (Notti et al., 2012):

$$C = [\cos(\alpha) \cdot \sin(\gamma - 90) \cdot N] + \{[-1 \cdot \cos(\alpha) \cdot \cos(\gamma - 90)] \cdot E\} + [\cos(\alpha) * H] \qquad \text{Eq. 26}$$

where:

H= sin (ϑ)

N= cos(90-ϑ)*cos(n)

E=cos(90-ϑ)*cos(e)

ϑ= LOS incident angle

n= angle of LOS with North

α= slope

γ=aspect

C coefficient can be intended also as the percentage of movement that can be registered by a SAR sensor. Where it shows negative values the movement is more suitable registered by the opposite acquisition geometry (Figure 2.19 a)

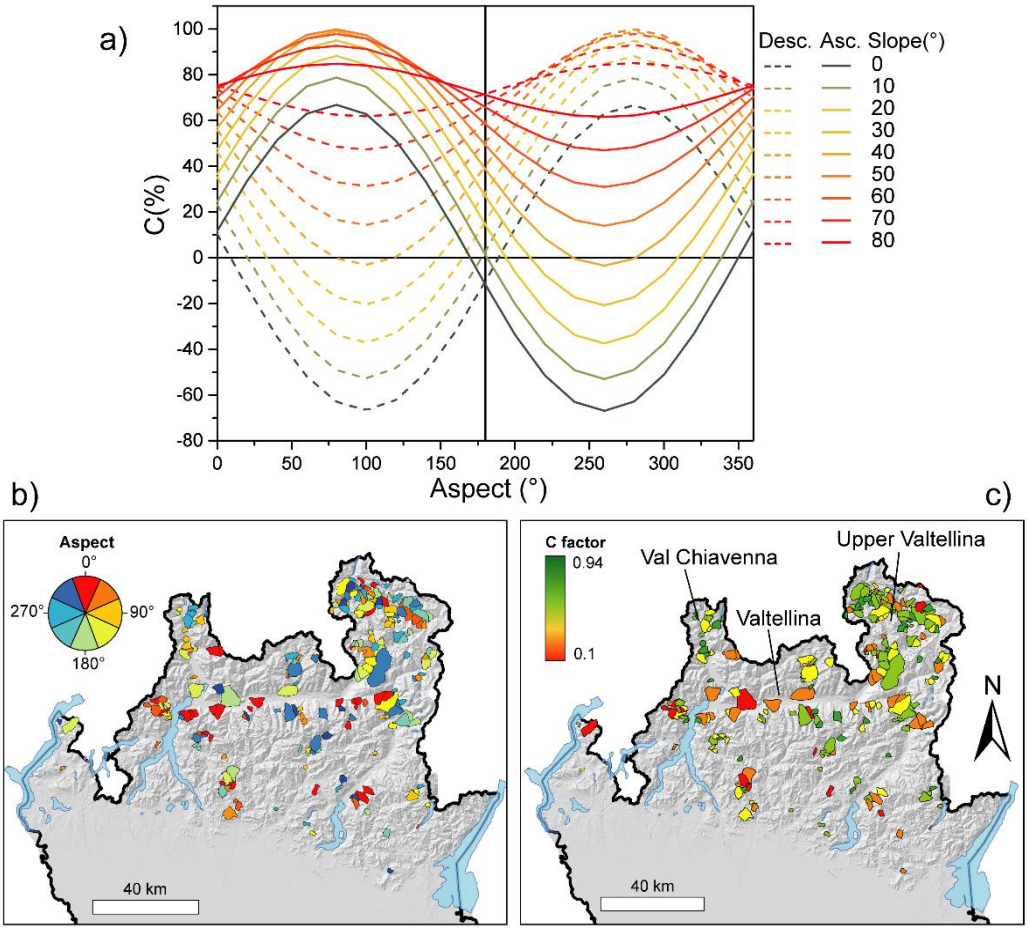


*Figure 2.19: influence of topographic orientation on LOS displacements measurement a) percentage of detected movement according to orbital parameters and slope morphometry. b) aspect orientation of slow rock slope deformations in the study area (Lomabardy region, North Italy) c) C index computed for the mapped phenomena.*

It is evident as North-South facing slopes and E-W trending valleys (i.e. Valtellina, Lombardy, North Italy) display low C values, while N-S trending ones (i.e. Val Chiavenna, upper Valtellina), have higher C coefficients resulting favorable oriented towards the sensor.

It is thus fundamental to assess the most suitable LOS geometry to ensure that the target area is visible to the employed sensor mode.

The integration of InSAR displacement data from ascending and descending satellite orbits can help increasing the sensitivity for displacements close to the blind plane spanned by the two los vectors (Figure 2.18). However, as the azimuth displacement components can't be retrieved by the sensor, the ascending and descending radar LOS directions are simplified as both belonging to the East-West plane.

This multi-geometry technique (2DInSAR, Figure 2.20, Manzo et al., 2006; Dalla Via et al., 2012; Eriksen et al., 2017) extracts a 2D displacement vector (T) lying on the EW vertical plane and allows to compute the real vertical ($V_v$) and horizontal ($V_e$, east-west) components, thus obtaining kinematic diagnostic parameters that can be used as tools for the interpretation of displacement patterns.

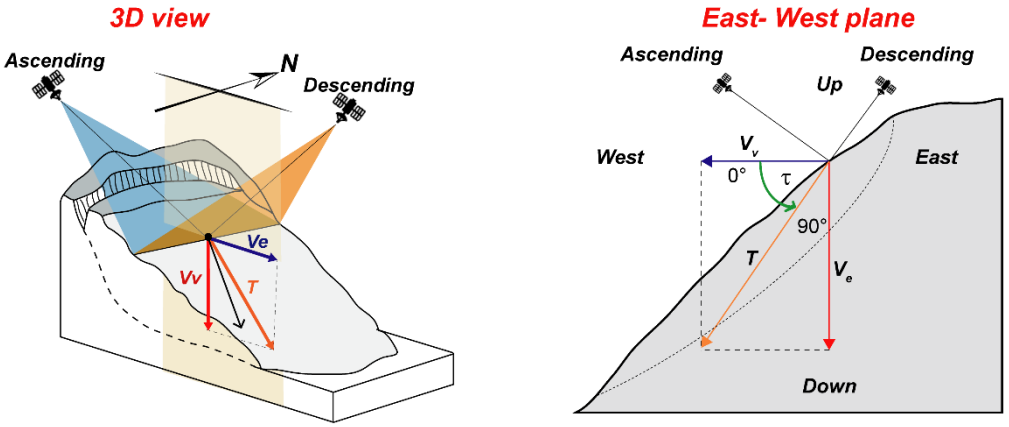


*Figure 2.20: 2DInSAR technique. Ascending and descending satellite data are combined to extract displacement components in a grid of regular points (PseudoPS) on the ground.*

$$V_e = \frac{V_d \cos\theta_a - V_a \cos\theta_d}{\sin(\theta_a + \theta_d)} \quad \text{Eq. 27}$$

$$V_v = \frac{V_d \sin\theta_a + V_a \sin\theta_d}{\sin(\theta_a + \theta_d)} \quad \text{Eq. 28}$$

$$V_T = \sqrt{{V_V}^2 + {V_e}^2} \quad \text{Eq. 29}$$

$$\tau = \cos^{-1}\frac{V_e}{V_T} \quad \text{Eq. 30}$$

where: $V_a$ and $V_d$ are the ascending and descending LOS velocities (mm/year), and $\vartheta_a$ and $\vartheta_d$ are the incidence LOS angles for the considered satellite platform in the two acquisitions geometries.

## 2.3 Multi-interferogram techniques

The atmospheric and decorrelation effects are the two major sources of noise affecting SAR interferograms. These contributions are often many times larger than the expected movement from slow slope deformations making difficult for an individual interferogram to cover a sufficiently long-time period such that the accumulated slope deformation is greater than the noise. Several methods, the so called "*Multi-interferogram techniques*", have been used to combine multiple interferograms to overcome this problem (Ferretti et al., 2007) and further decrease temporal and spatial decorrelation due to long revisit time.

Since the first description of DInSAR technique (Gabriel et al., 1989b) several algorithms have been developed to improve the degree of the measurement accuracy (i.e. small displacement rates, higher SNR) : Permanent Scatterers (PS) technique (Ferretti et al., 2000, 2001), SqueeSAR technique (Ferretti et al., 2011), Small Baseline Subset (SBAS) technique (Berardino et al., 2002) Multiple Aperture SAR Interferometry (MAI) (Bechor and Zebker, 2006) etc.

Although these techniques implement different assumptions and procedures, their main goal is always to reduce the atmospheric effects in SAR interferograms extracting "good pixels" out of an incoherent background (Ferretti et al., 2007) by averaging data within multiple interferograms (Lyons and Sandwell, 2003; Sandwell and Price, 1998; Strozzi et al., 2000; Wright et al., 2001) The main assumption is that atmospheric phase is rarely constant or correlated between different acquisitions and can thus be removed by averaging its contribution through multi temporal interferograms.

The stack of $n$ independent interferograms with different acquisition time intervals results in a total acquisition time interval $t_{cum}$ and the sum of all the unwrapped phase $\varphi_j$ in a cumulative unwrapped phase $\varphi_{cum}$. (Strozzi et al., 2000).

$$v_{disp} = \frac{\lambda \varphi_{cum}}{4\pi\, t_{cum}} \qquad \text{Eq. 31}$$

Considering a constant noise level in each interferogram, if noise or atmospheric effects induce spurious phase components and if the displacement rate is constant in time (stationary displacement velocities), the velocity estimation error is reduced by a factor of $\frac{n}{t^{2}_{cum}}$ respect to the single interferogram (Ferretti et al., 2007), thus enhancing the SNR that would emerge from a single interferogram

Despite increasing the accuracy of InSAR analyses, interferogram stacking still suffers of some limitations due to important assumptions on which the methodology itself is based on. First of all the velocity is assumed to be constant, thus losing information on the temporal dynamic of the displacement and resulting less effective if applied to landslides or volcanoes that commonly have seasonal or periodical responses and variations.

Moreover, atmospheric contributions are only averaged, in order to mitigate their impact on the final result, but not completely removed.

Usually small geometrical baselines are selected in the stacking procedure, reducing geometrical decorrelation and DEM errors, but hampering the extraction of information from all the other possible interferograms (Ferretti et al., 2007).

### 2.3.1 Permanent Scatterers technique: PSInSAR

The so-called Persistent Scatterers technique, that was developed by the SAR group of Politecnico di Milano (POLIMI)(Ferretti et al., 2000, 2001; Colesanti et al., 2003), can be considered one of the most representative stacking approach. A more detailed description is here reported since all the PS datasets that we use in our analysis come from this processing algorithm.

This technique is based on the concept that in order to limit the number of phase contribution in the interferogram stack and emphasize the SNR, the analysis should focus only on coherent targets. These are the so called Permanent Scatterers (PS) and correspond to stable points on the ground that have a constant electromagnetic backscattered signal. Usually they correspond to infrastructures (pillars, buildings etc.) and natural elements like bare rock outcrops.

In the PS technique, data are co-registered on a master image, selected to minimize artefacts due to the temporal and geometrical values and maximize the average coherence. Then $n$ differential interferograms are computed between all the SAR images and the chosen master one (Figure 2.21 a).

Once unwrapped all the interferograms and after the atmospheric correction (statistically calculated with low polynomial approach), possible PS points are selected (Figure 2.21 b) and only those providing useful (i.e. respecting velocity, stability or amplitude threshold) information are kept.

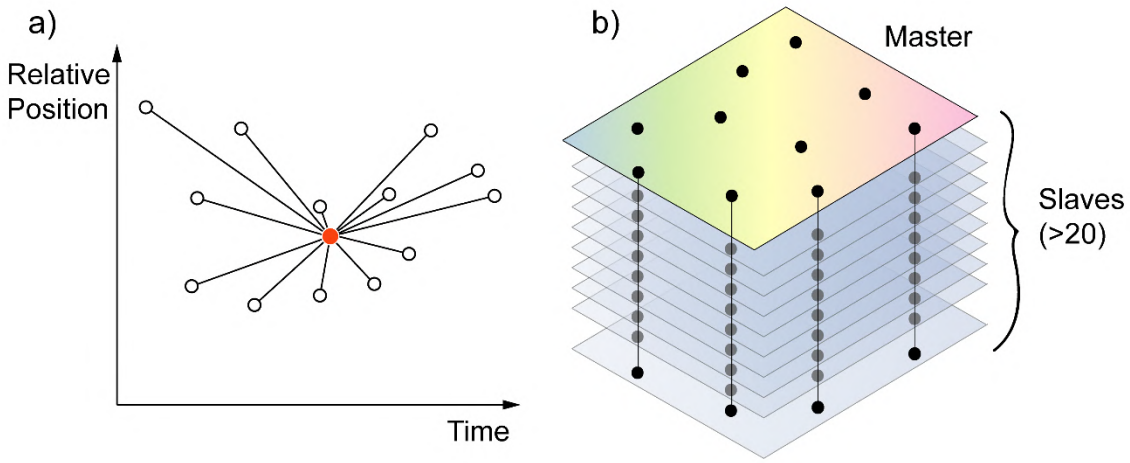


*Figure 2.21: Basic concepts of PSI algorithm: a) PS stacking approach b) PS selection.*

An implementation of the PS technique called SqueeSAR™, was presented in 2010 by (Ferretti et al. 2011). This improved approach increases the density of the scatterers introducing also distributed scatteres (DS) which identify more spatially dense measurement

points in non-urban areas. A DS corresponds to a homogeneous area with similar electromagnetic response spread over a group of pixels in a radar image (e.g. a debris covered area, crop fields etc., Figure 2.22).
All of the measurements are relative to a reference point chosen a priori in an area assumed to be stable.

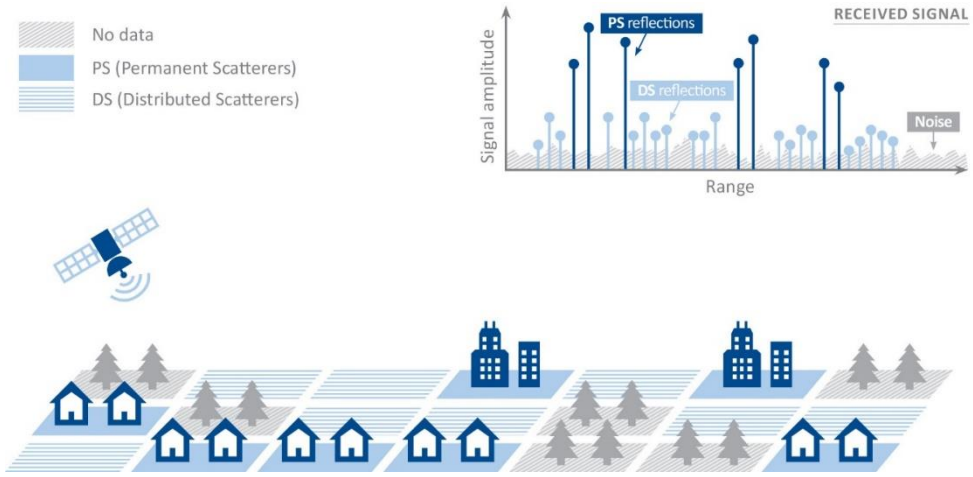


*Figure 2.22: PS and DS identification (TRE Altamira https://site.tre-altamira.com/insar/).*

### 2.3.2 Application of PSI to slow rock slope deformation study

Due to the limits of conventional geotechnical and geophysical investigations (Brückl *et al.*, 2006, 2013) in reaching the deep expression of slow rock slope deformations, the analysis of these complex phenomena pose major challenges. In the past, their study was limited by the low spatial coverage and resolution of monitoring techniques, either unable to detect very small displacement rates (Bovis, 1990) or to capture displacement patterns over space and time.
In this context, InSAR became the primary tool to characterize ground deformation rates from few millimetres to centimetres per year along the satellite line-of-sight (LOS; Goldstein and Zebker, 1989a). In particular, PSI techniques, including the PS-InSAR™ (Ferretti et al., 2001) and SqueeSAR™ technique (Ferretti et al., 2011) proved their capability to measure small ground deformations with millimetric precision, making them suitable for regional-scale landslide mapping and inventory studies (Colesanti et al., 2003; Colesanti and Wasowski, 2006; Rosi et al., 2014; Wasowski and Bovenga, 2014; Frattini et al., 2018).
Despite the improvements and refinements introduced by these methods, several limitations, some of which already presented in the previous paragraphs and widely discussed in the scientific literature, (i.e. Colesanti and Wasowski, 2006) still affect the application of DInSAR to the landslide investigation.
A first major limit of the technique applied to landslide characterization is the inability of the satellite sensor to record the real 3D components of ground displacement, catching only the LOS projection of any possible 3D ground deformation. Moreover, the system has no

sensitivity along the sensor orbit (due to the near polar orbit) and any deformation occurring along the north– south direction results in a very small LOS projection.
Two components play an important role in the landslide characterization: (a) slope orientation (i.e. North-South facing landslides result almost blind to the sensor) and ground displacement direction respect to the LOS, (b) downslope Vs vertical displacement components. This implies that DInSAR displacement data can be fully exploited and correctly interpreted only when field evidence or ground truthing information provides clues on the kinematic style of the landslide (i.e. translational with main downslope movement Vs rotational with important vertical components), otherwise fictitious or biased displacement components may be derived. The application to slow rock slope deformations is then further complicated because of low signal to noise ratio, presence of vegetation that can reduce the number of coherent scatterers and ambiguities related to the complexity and heterogeneity of landslide mechanisms (Notti et al., 2012). Landslides evolving in alpine and mountainous settings also suffer from atmospheric artefacts that, in the multi interferogram technique, are usually corrected according to regional scale mean delay maps, thus losing the local scale complexity and negatively affecting the velocity measurements.
Finally, since PS velocity is computed relative to a reference point (Figure 2.23), it is important to take into account the propagation of the measure uncertainty moving away from this point.

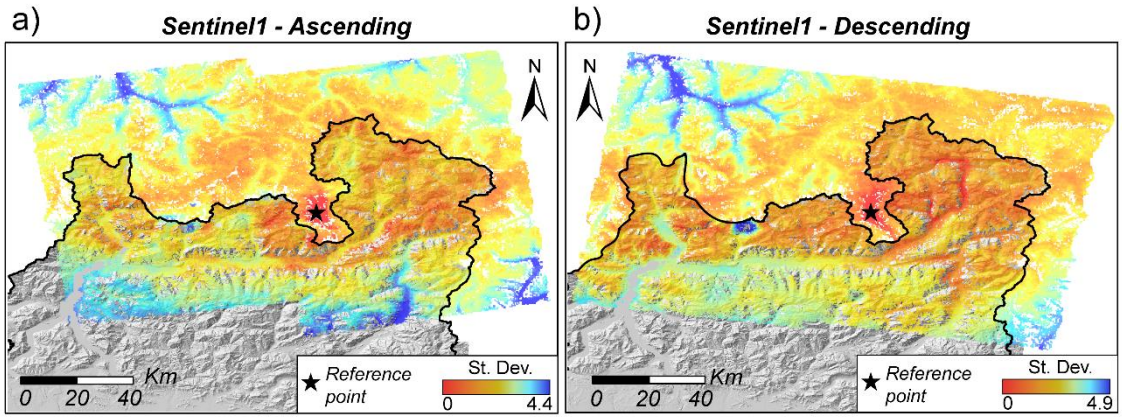


*Figure 2.23: Standard deviation map associated to Sentinel 1 SqueeSAR datasets.*

The reference point is selected as a radiometric stable target that keeps high coherence in the entire sensed period and isn't affected by ground movements (subsidence, landslide area etc.). Standard deviation (Figure 2.23), highlights the shift between the reference point and all the other PS. For instance, a standard deviation of +0.5 mm/yr means that a PS velocity measure of -4mm/y has a real velocity value between -3.5 and 4.5 mm/yr with a probability of 68% (1 sigma). So, the standard deviation also conditions the capability to detect slow movements. Also topography conditions the propagation of the error of the standard deviation that negatively affects the velocity measure getting far from the reference point and in high relief areas (topographic peaks).

Because of these limitations, a blind analysis of PSI data isn't effective in the study of complex landslides, but targeted analysis and combined studies integrating InSAR data and mapping observations must be always adopted.

# 3 Style of activity of slow rock slope deformations

## 3.1 Definition

Slow rock-slope deformations can be characterized by different kinematics and internal deformation, depending on structural controls and damage accumulation mechanisms, with major implications on the spatial-temporal distribution of displacements (Crippa et al., 2020) and the collapse potential of main or nested landslide masses.
Moreover, different landslides with similar displacement rates can have different practical impacts, depending on their size, mechanisms, maturity and predisposition to collapse (Agliardi et al., 2020) and modes of interaction with elements at risk (Peduto et al., 2017; Nappo et al., 2019).
The classical definition of landslides activity, also adopted for slow rock slope deformations, is based on the mean slope displacement rate but, because of the abovementioned issues, this is ineffective in capturing the behaviour of slow rock slope deformations evolving over long periods. A complete characterization of their style of activity must therefore consider the complex combinations of their displacement rates (degree of activity), kinematics, and complexity (e.g. segmentation, heterogeneity, internal damage, structural controls).
We propose an integrated approach to the definition of the style of activity of large slow rocks slope deformations combining different aspects, namely: displacement rate, segmentation/heterogeneity, kinematics, internal damage and accumulated strain and set up targeted procedures in Matlab and GIS environment to account for each of them in a fast and cost effective way (Figure 3.1).
To this aim, we produced an original geomorphological inventory of slow rock slope deformations for the alpine and prealpine area in Lombardia (Northern Italy) through DEM, ortophotos and morphometric analysis, and exploited PS datasets covering the area to extract sound descriptors of their state of activity and kinematics.

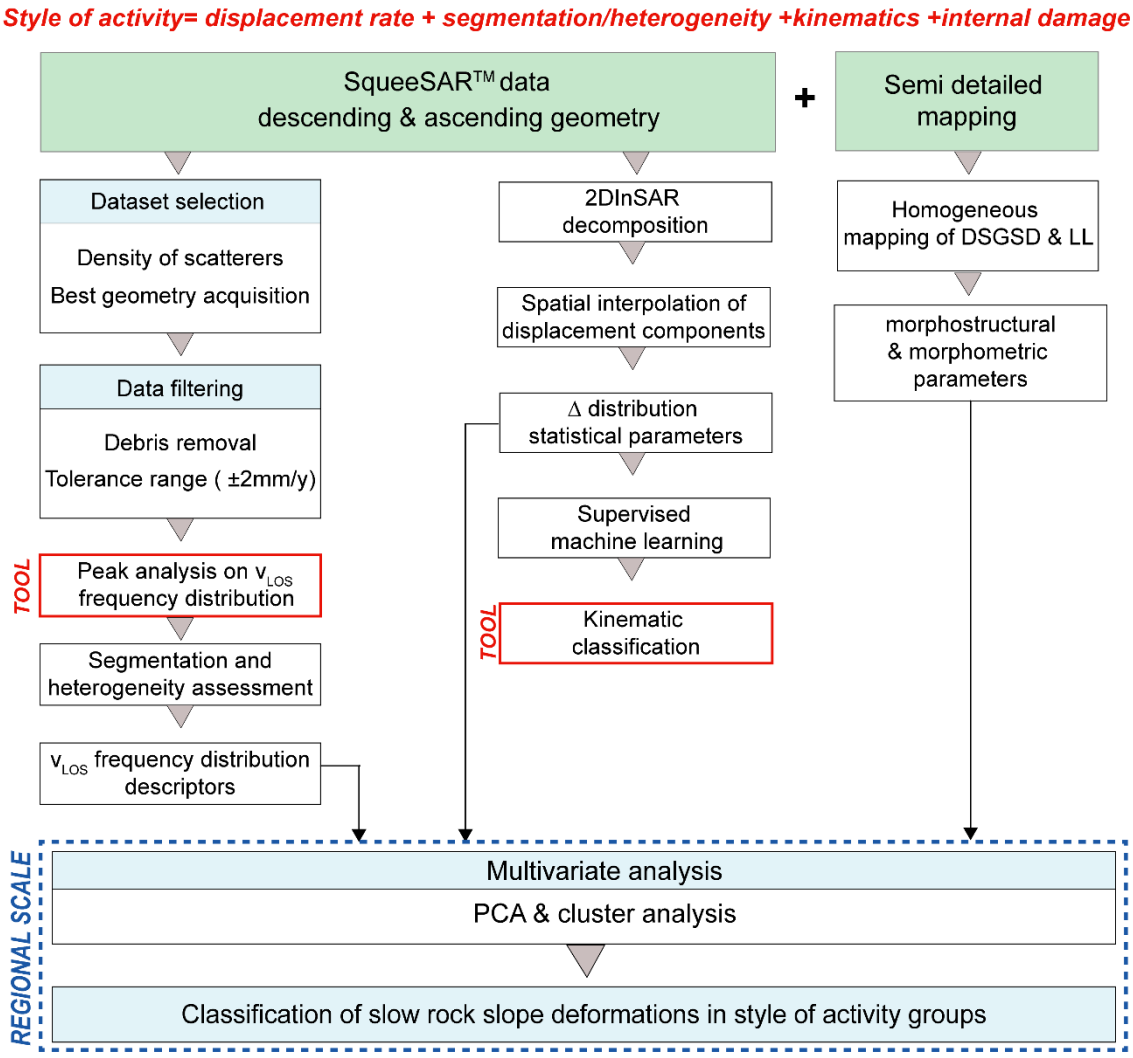


*Figure 3.1: Parameters interplaying in the definition of the style of activity of slow rock slope deformations and relative analytical workflow. Red boxes highlight the original standalone tool developed in Matlab™ environment.*

## 3.2 Study area

The study area (Figure 3.2) includes the alpine and pre-alpine sectors of Lombardia region, that belong to three major domains, namely the Austroalpine, Penninic and Southalpine domains. N-verging Austroalpine and Penninic units are separated from the S-verging Southalpine units by the Insubric Line, a steeply dipping E-W trending fault zone active during the latest orogenic stages in Oligocene to Miocene times (Schmid, 2017).

These three tectonic domains include a wide variety of rock types with different paleogeographic provenance. In particular, Penninic units were once located between the European and the Apulian margins and mainly include remnants of oceanic lithosphere (e.g. Malenco-Forno units) and portions of the European margin (e.g. Adula, Tambò and Suretta nappe). They outcrop in western Lombardia between Valchiavenna and Valmalenco (Figure 3.2). Austroalpine units overlie Penninic nappes and are mainly composed of continental lithosphere derived from the former Apulian margin. These units include metamorphic

basement rocks, intrusive rocks and Mesozoic sedimentary successions (Florineth and Froitzheim, 1994; Schmid, 2017).

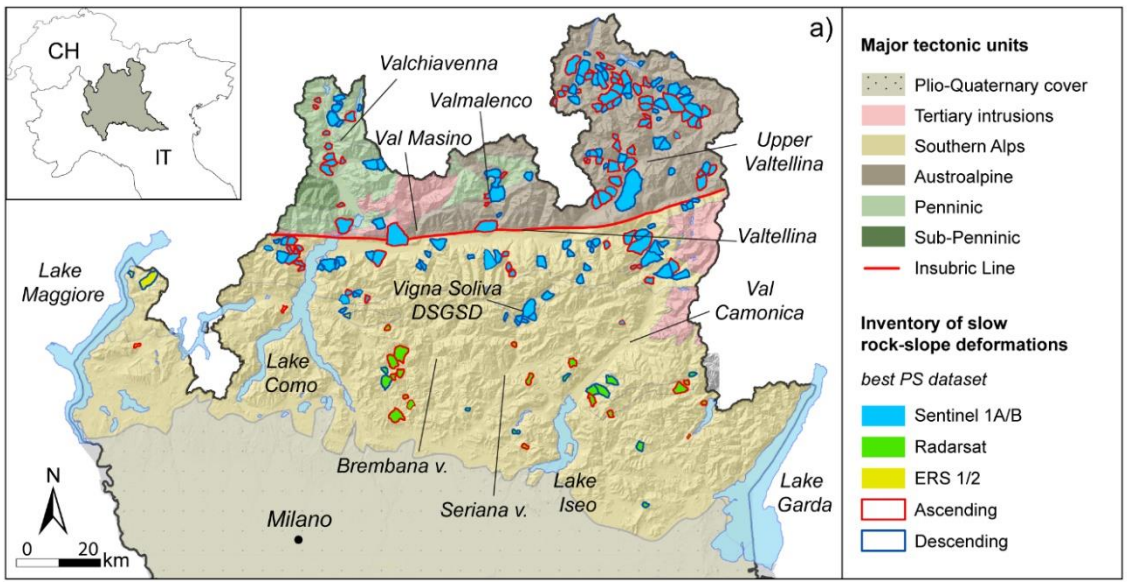


*Figure 3.2: Slow rock slope deformations inventory and corresponding best InSAR dataset.*

They extend from Valmalenco to the easternmost part of Valtellina (Figure 3.2). These units are intruded by two major Tertiary tonalitic and granodioritic bodies outcropping in Valchiavenna-Val Masino (Masino-Bregaglia) and Val Camonica (Adamello). The Southalpine domain includes the Prealps south of the Insubric Line, characterized by a fold-and-thrust belt made, from north to south, of Variscan metamorphic basement rocks, Permian volcaniclastic and sedimentary successions, and Mesozoic sedimentary succession including carbonate and terrigenous rocks (Figure 3.2).

The alpine sector of the study area is characterized by high elevation (up to 4000 m a.s.l.), high local relief and a relatively steep topography, all progressively decreasing moving to the south across the Southalpine sector up to the foothills (Agliardi et al., 2013).This topographic setting is the result of the complex interplay between the rock type, Cenozoic tectonic forcing, and Quaternary exhumation history in alternating fluvial and glacial environments (Sternai et al., 2012). During the Last Glacial Maximum (LGM; Ivy-Ochs et al. 2008; Grämiger et al. 2017) a thick ice cap covered the alpine valleys with ice stages reaching 2800 m a.s.l. (Bini et al., 2009) feeding major valley glacier systems (e.g. Adda, Oglio and Adige glaciers) that carved the topography and reached the Po Plain to the south. LGM collapse and the subsequent deglaciation resulted in significant stress and hydrological perturbations that triggered the paraglacial response of slopes and their progressive failure (Grämiger et al., 2017; Riva et al., 2018). Fluvial incision then reshaped the valleys especially in the prealpine and foothill areas. The lithological, structural and topographic settings resulting from this long-term evolution strongly controlled the onset and spatial distribution of large, slow rock slope deformation (Ambrosi and Crosta, 2006; Agliardi et al., 2013; Pánek et al., 2019). These are more frequent in axial alpine areas characterized by medium strength

foliated metamorphics, high local relief and degree of valley incision and tend to cluster along major tectonic structures. In Southalpine areas with sedimentary rocks and relative low relief, giant slow rock slope deformations are less favored and often controlled by local stratigraphic and structural features (Crosta and Zanchi, 2000; Agliardi et al., 2013;).

## 3.3 Semi-detailed geomorphological mapping

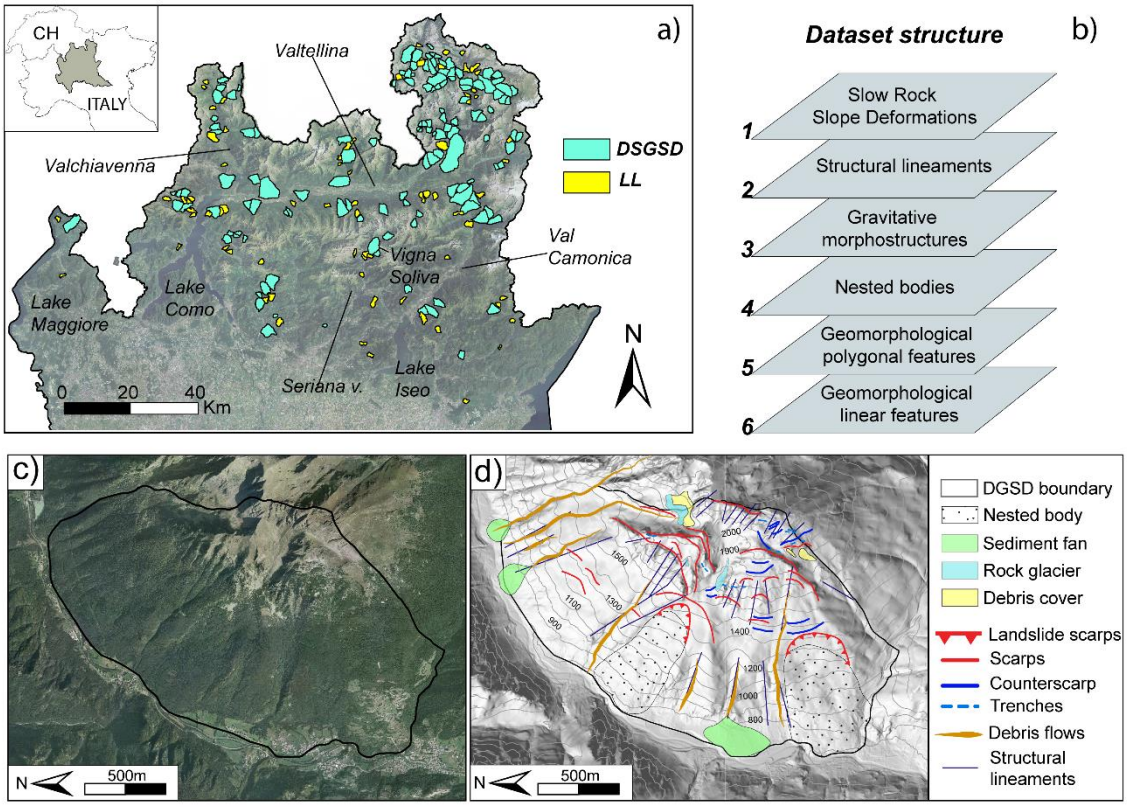


*Figure 3.3: Regional scale semi-detailed mapping. a)slow rock slope deformations mapped in Lombardia region; b) layers forming the final dataset; c) Vigna Soliva DSGSD (BG) and d) example of semi detailed mapping over Vigna Soliva DSGSD.*

A systematic mapping approach focused on the recognition of unstable slopes has been applied in different countries (Jaboyedoff et al., 2012; Hermanns et al., 2013; Oppikofer et al., 2015). Commonly, three main approaches can be adopted to this aim.
The first consists in the application of InSAR data directly as mapping tool (Rosi et al., 2018; Aslan et al., 2020). The second one uses morphological observations, field data and local scale measurements integrated with InSAR data for an initial screening of unstable rock slopes (Lauknes et al., 2010; Henderson et al., 2011; Hermanns et al., 2013;) to provide a mapping of each phenomenon. All slopes found with this first overview are then systematically mapped using air photos and, where available, further local information (Hermanns et al., 2013). The third one, that we adopted, integrates regional scale morphostructural mapping, aerial photo interpretation and, where available, existing inventories to map each landslide at the regional scale and eventually integrates InSAR data

that are here aimed at providing a characterization of the style of activity of each landslide, and are not used as a mapping tool.

To implement this mapping strategy and speed up the feature recognition at the regional scale, we carried out an original geomorphological mapping of 208 slow rock-slope deformations in Lombardia region selected from different published inventories (GeoIFFI landslide inventory: Ceriani and Fossati 2006; DSGSD inventory). In particular, we considered all the 134 deep-seated gravitational slope deformations (DSGSDs) recognized in Lombardia and 74 large landslides (Figure 3.3 a) (here LL), extracted from the GeoIFFI database according to their areal extent (area >1.5 $km^2$ or >1 $km^2$ when interacting with elements at risk) and practical relevance (e.g. actively monitored landslides or areas that underwent structural remediation works).

For the selected cases, we performed a new geomorphological mapping by means of detailed stereoscopic photo-interpretation of aerial imagery (Regione Lombardia TEM1 series, 1981-1983; nominal scale 1:20000), digital orthophotos (2000; resolution 1m, 2007, 2012, 2015; resolution 0.5m), GoogleEarth$^{TM}$ imagery and Digital Elevation Models (Regione Lombardia, cell size: 5m), locally validated by field visits and information from published literature where available.

We adopted a "semi-detailed" mapping strategy, considering major slope-scale features allowing the rapid mapping of hundreds of cases, yet providing site-specific information. The main goal of this mapping is to maximize the information at the slope scale thus providing a consistent dataset to be used as support for a regional scale kinematic and long-term activity analysis and give clues on the deformation and damage degree of each phenomenon. The final inventory is made of six information layers, including (Figure 3.3 b,c,d): 1) landslide boundaries (polygons), 2) nested landslides (immature or deformed; polygons); 3) areal geomorphological features (e.g. debris fans, shallow landslide deposits, sediment fans, periglacial features; polygons); 4) linear geomorphological features (e.g. debris flow channels, erosion gullies; polylines); 5) gravitational morpho-structures (e.g. scarps, counterscarps, trenches; polylines); 6) tectonic lineaments (considered as persistent structures long more than few tens of+ meters; polylines).

All the mapped elements, both polygonal and linear, are discriminated by a code corresponding to the landslide ID they are associated and each landslide polygon reports the "class" of the represented slow rock slope deformation, thus DSGSD or LL.

This distinction comes from an a priori classification originally made in the initial inventories according to criteria exposed in chapter 1. However, this distinction wasn't used as constraint on the geomorphological mapping, which was carried out according to homogenous criteria regardless of the slow rock slope deformation class.

For each slow rock-slope deformation, we also extracted the dominant lithology from a 1:250.000 digital geological map of Lombardia (Montrasio et al., 1990). Lithostratigraphic units were grouped into 9 rock type classes based on their expected, typical geomechanical behaviour (Agliardi et al., 2013), namely: carbonate rocks (C), metamorphic foliated (MF), massive metamorphic (M), clastic sedimentary rocks (S), quarzite (Q), orthogneiss (OT), flysch-type rocks (FL), granitoid/metabasite (IT), and volcanic rocks (V).

Considering the so extracted features, we computed morphometric and morpho-structural variables (Table 5) that can be used as descriptors of the degree of internal damage and evolution of each landslide (e.g. density of morphostructures, density of nested bodies etc.) as well as a quantification of the slope predisposition to induce slow rock slope deformations (e.g. relief, slope inclination etc.).

*Table 5: Parameters computed from the semi detailed mapping*

| rock type | Description | |
|---|---|---|
| C | Carbonate rocks (both massive and layered) | |
| S | Sedimentary clastic rocks | |
| FL | Flysch-type rocks | |
| M | Massive metamorphic rocks | |
| MF | Phyllosilicate-rich foliated metamorphic rocks | |
| OT | Quartz-rich foliated metamorphic rocks | |
| IT | Intrusive rocks | |
| Q | Quartzite | |
| morpho-structure | Definition | Description |
| ensity of immature nested landslide (NB) | (nested area / total landslide area)*100 | areal density of nested bodies in an embryonic stage of evolution |
| density of deformed nested landslide (DB) | (nested area/ total landslide area)*100 | areal density of nested bodies in an advanced stage of evolution |
| landslide scarps (LS) | (scarp area/ total landslide area)*100 | proxy of total accumulated landslide strain |
| density of linear morpho-structures (DM) | total morpho-structure length / landslide area | proxy of internal damage |
| morphometry | Definition | Description |
| elongation ratio (L/W) | landslide length (L) / width (W) | form factor assuming an elliptical landslide area with axes L and W |
| shape factor (A/2p) | landslide area (A) / landslide perimeter (2p) | form factor based on the ratio of landslide spatial and linear extent |
| relief (Δh) | Δh= Maximum elevation – Minimum elevation | relief energy in the landslide area |
| hypsometric integral (Hi) | $\text{Hi} = \frac{\text{Mean elevation} - \text{minimum elevation}}{\text{Maximum elevation} - \text{minimum elevatior}}$ | proxy of the morphological maturity of the landslide area |
| mean aspect | mean azimuth (dip direction) of the landslide area | mean aspect calculated as circular mean of each pixel |

## 3.4 Activity, representative velocities and segmentation

As first step to determine the state of activity of each landslide, we identified the most suitable reference InSAR dataset (i.e. the dataset that optimizes the spatial density of permanent scatterers, PS, and distributed scatterers, DS), and chose the most suitable acquisition geometry from 3 different PS-InSAR™ and SqueeSAR™ datasets (TRE Altamira) derived by ERS 1-2, Radarsat and Sentinel 1A/B C-band radar imagery. Images were acquired between 1992 and 2017 in both ascending and descending modes (Table 6) and processed over the alpine sector of Lombardia region.

*Table 6: InSAR PSI datasets used in the analysis. Θ= LOS inclination; δ=azimuth heading.*

| tellite | PSI technique | Mode | Θ (°) | δ (°) | Revisit time (days) | Time interval (years) |
|---|---|---|---|---|---|---|
| ERS 1/2 | PSInSAR™ | Ascending | 23.20 | ~13.00 | 35 | 1992-2003 |
| ERS 1/2 | PSInSAR™ | Descending | 23.09 | ~12.00 | | 1992-2000 |
| RADARSAT-S3 | SqueeSAR™ | Ascending | 32.49 | 12.12 | 24 | 2003-2007 |
| RADARSAT-S3 | SqueeSAR™ | Descending | 36.27 | 9.60 | | 2003-2007 |
| Sentinel 1A/B | SqueeSAR™ | Ascending | 41.99 | 10.23 | 12 (6 after 2016) | 2015-2017 |
| Sentinel 1A/B | SqueeSAR™ | Descending | 41.78 | 8.89 | | 2015-2017 |

The best acquisition geometry was selected depending on data density, landslide morphometric parameters as slope and aspect and satellite orbit parameters (LOS and azimuth angle), according to the C index proposed by Notti et al. 2012, 2014. A basic definition of degree of activity can be attained considering the mean LOS velocity of active scatterers (PS or DS) inside each landslide area. Here we considered as "active" all the PS and DS with coherence $> 0.7$ and associated (mean) velocity values outside the uncertainty/noise range of $\pm 2$ mm/yr.

Moreover, since movement associated to PS and DS point-like data can be related to shallow movements within slope deposits (e.g. scree deposits, periglacial features), not directly related to DSGSD or large landslide deformations (Meisina *et al.*, 2008; Frattini *et al.*, 2018;) we removed PS inside slope deposit. To this aim, we used geomorphological maps produced during the realization of the GeoIFFI inventory (courtesy of Regione Lombardia) and refined by further interpretation of Google Earth™ imagery and recent orthophotos.

The detail of the InSAR analysis of slow moving landslides is strongly influenced by the number and density of active PS or DS detected within individual landslides (Frattini et al., 2018). This depends on slope orientation (aspect and inclination; see section 2.2.7 and Figure 2.19) and vegetation cover, which negatively affects the number of detected PS limiting the possibility to obtain robust samples of InSAR-derived velocity values (annex D). Fewer PS and DS result in a more uncertain definition of landslide segmentation and representative velocities.

The simplest and most commonly used definition of "landslide activity" is based on estimates of mean displacement rate as a representative descriptor of the state of activity. However, the mean LOS velocity evaluated over the entire landslide area may be not representative of the actual activity of the landslide (Frattini et al., 2018), or even misleading. In fact, slow rock slope deformations frequently host nested (secondary) phenomena that move faster than the main body, resulting in a domain segmentation of activity, as well as heterogeneities related to rock mass damage and active morpho-structures (Crippa et al., 2020), that induce a larger LOS velocity variability. Sparse PS and DS point-like data can be ineffective in capturing the internal segmentation and heterogeneity of slow rocks slope deformations, thus a simple mean velocity can fail to correctly represent their degree of activity (Ferretti, 2014; Crippa et al., 2020).

In order to fill this gap, we developed an original Matlab$^{TM}$ script to perform an objective, automatic characterization of internal segmentation based on a peak analysis of the frequency distribution of LOS velocity within each landslide (Figure 3.4). This routine can be run as a stand-alone tool to characterize the state of activity and segmentation of each landslide both for local scale investigation or integrated in a regional scale analysis, to extract a quantification of segmentation and heterogeneity for each mapped landslide in a fast and cost-effective way.

In general, rigid landslide bodies with little internal damage are characterized by homogeneous displacement fields and velocity distributions that tend to be unimodal (Figure 3.4 a,b). On the opposite, landslides with segmented activity in nested bodies are characterized by multimodal velocity distributions (Figure 3.4 c, d, and Figure 3.5).

In our analysis, peaks of the probability density distribution of velocity are defined as local maxima exceeding a certain probability density threshold. This threshold can be arbitrarily set to allow the detection of peaks with different relevance. Here, we set its value to 1/10 of the maximum probability density. Each detected peak represents the distribution of a specific cluster of velocity values, but does not provide direct clues on their spatial distribution. Distinct peaks emerging from the threshold indicate the occurrence of clearly segmented domains, each characterized by a given mean velocity and dispersion. Minor peaks (frequency $<$ threshold) are usually related to outliers or noise. The highest peak (i.e. most frequent) corresponds to the modal velocity value and can be considered as the representative velocity of the major landslide mass, while the secondary ones account for further velocities that may either be related to a single nested sector or outline heterogeneities in the velocity distribution.

Depending on the statistical dispersion of velocity values, some peaks can mask additional clusters that are not readily recognized as local maxima (Figure 3.4 e,f) by the algorithm, but still represent conspicuous bunches of high displacements values.

Therefore, we introduced a specific spatial criterion to outline the presence of these additional clusters (Figure 3.4 e, f, Figure 3.5).

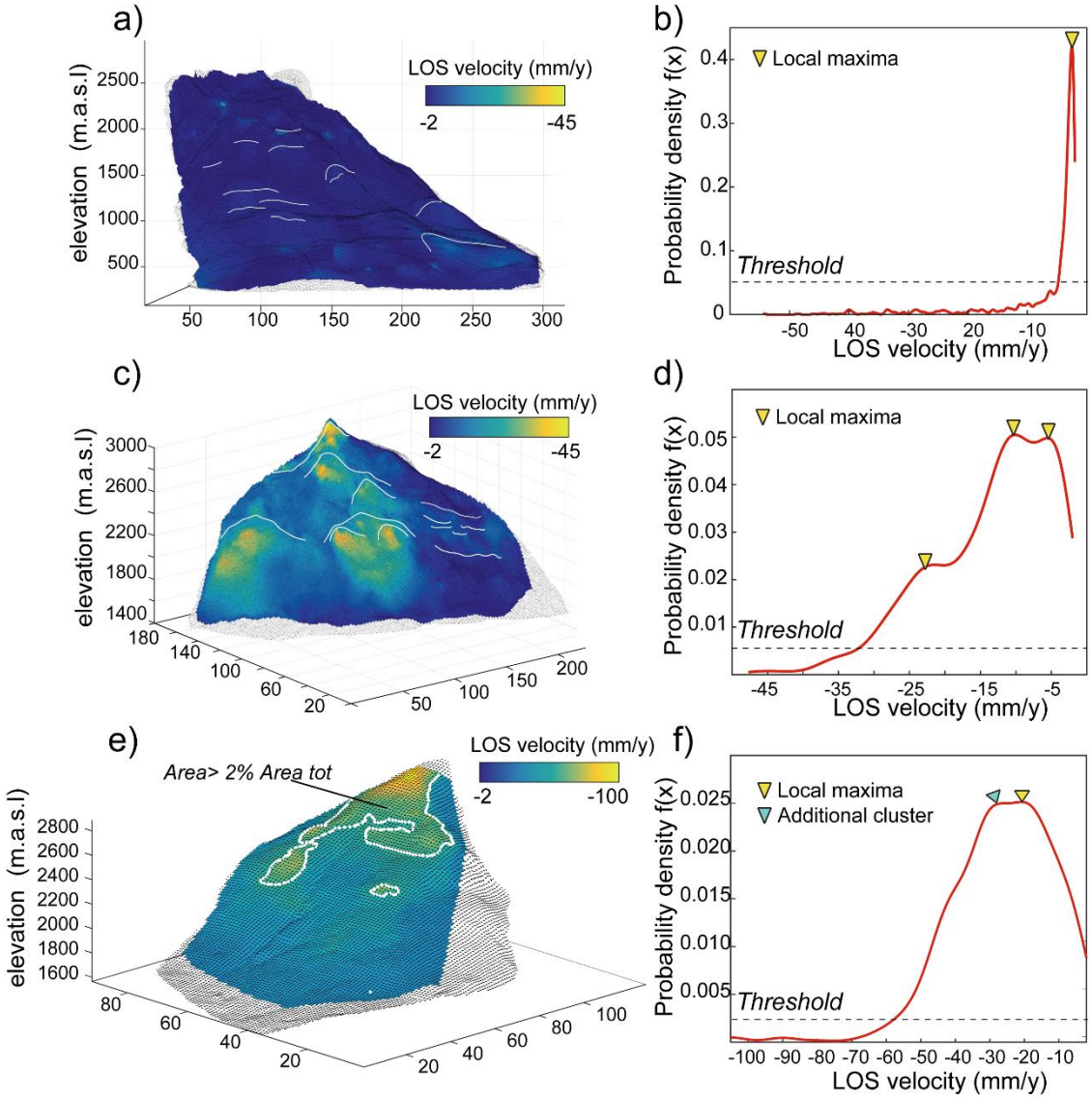


*Figure 3.4: Segmentation assessment through PSI analysis. 3 cases of different degree of segmentation are shown: a) homogeneous DSGSD with corresponding b) unimodal velocity distribution with only a major peak exceeding the threshold value. c) segmented DSGSD with corresponding d) plurimodal velocity distributions. More peaks exceeding the threshold value are found. e) segmented DSGSD with f) almost unimodal velocity distribution hiding a major peak representative of a conspicuous cluster of pixels (corresponding to a nested slope sector).*

We interpolated PS and DS velocity values (natural neighbour interpolation) over the landslide area and obtained a raster map of interpolated velocity. Then, using a raster binarization algorithm we checked for the occurrence of clusters of adjoining pixels with velocity that exceeds a selected value (e.g. modal velocity or another arbitrary value), covering a continuous area above a user-defined threshold, indicating additional segmented domains.

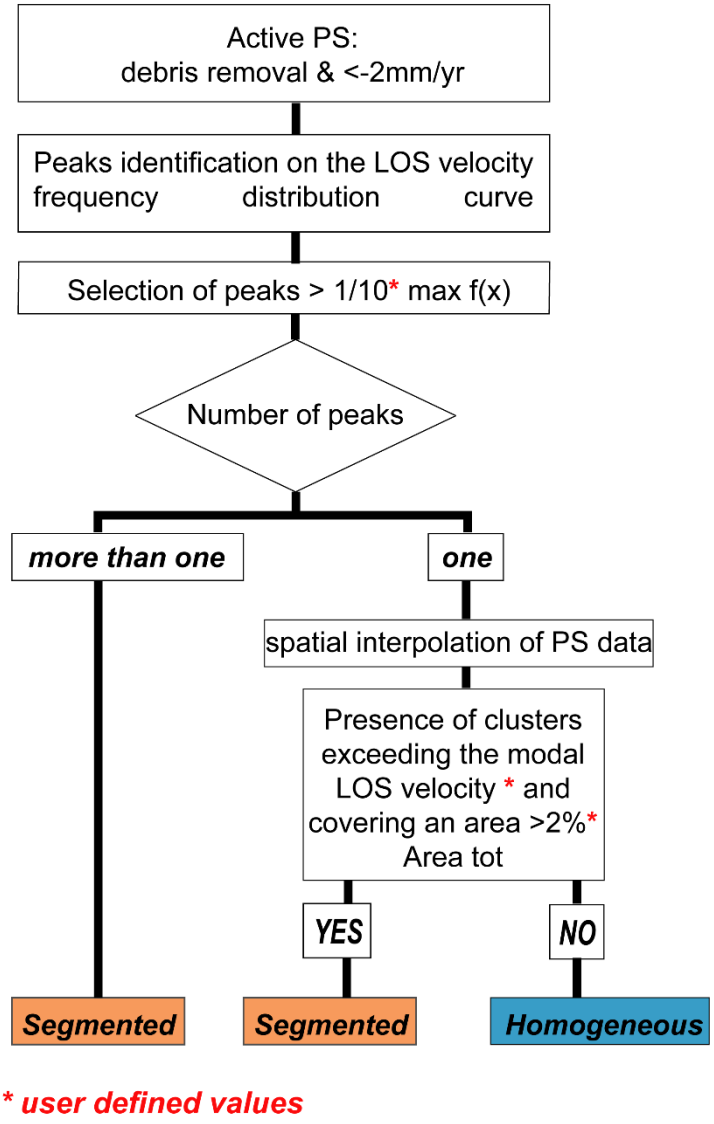


*Figure 3.5: Workflow to identify segmented and homogeneous phenomena.*

We further quantified landslide heterogeneity (i.e. dispersion of velocity values) over the entire area of each mapped landslide considering the coefficient of quartile deviation Q_Dev=(Q3-Q1) / (Q3+Q1), where Q1 and Q3 are the 25th and 75th percentiles the landslide velocity distribution, respectively. Larger velocity heterogeneity is mirrored by a larger value of Q_Dev.

## 3.5 Landslide kinematics

### 3.5.1 Kinematic indicators

In addition to spatial variation of LOS velocity values, changes in displacement components extracted from 2DInSAR analysis result very useful in the kinematic interpretation too.
Landslides with the same displacement rate may in fact behave in different ways both in an evolutive and risk perspective according to the involved rock mass volumes, interaction with at risk elements and collapse potential (Peduto et al., 2017; Agliardi et al., 2020). Moreover the kinematic style also influences the percentage of movement that can be sensed along the LOS thus resulting in different representative LOS velocities.
To operate a fast 2DInSAR decomposition we developed an original Matlab™ script that discretizes the study areas (i.e. multiple landslide polygons) into regular square grids and, for each cell, averages the LOS velocity values of PS/DS belonging to the same acquisition geometry. The average LOS velocity value computed at each cell for the two geometries is then assigned to the cell centroids referred to as "pseudo-PS". For each pseudo-PS, the script extracts the Ve and Vv displacement rate components (Eq. 27, Eq. 28), as well as the magnitude ($V_T$ Eq. 29) and inclination ($\tau$, Eq. 30) of the 2D displacement rate vector T (Figure 2.20). In our analysis we selected a 25x25m grid in order to optimize the number of pseudo-PS yet returning realistic mean LOS velocity values and avoid mixing up distant scatterers.
Depending on the failure geometry, the superficial slope movement has different components along the landslide body and consequently the displacement components (vertical, horizontal, dip angle) change too. Close to the main headscarp, the displacement vectors have a downward movement (Frattini et al., 2018) and T plunges at high angle into the slope. In the middle and lower part, the horizontal component tends to become dominant and T vector usually becomes parallel to the slope or points upward in response of the toe uplifting. A first assessment of the local (i.e. cell-scale) slope kinematics can be thus inferred by observing the difference between $\tau$ and the local slope dip ($\alpha$) in each square cell, namely $\Delta$ (Figure 3.6 a).

$$\Delta = \tau - \alpha \qquad \textit{Eq. 32}$$

Values of $\Delta$ close to zero indicate slope-parallel sliding (Figure 3.6 b, d), negative values indicate daylighting or bulging movements (Figure 3.6 b, c) while where $\Delta$ is positive, the movement is mainly downward dipping in the slope (Figure 3.6 c, e).
To evaluate the effectiveness of different descriptors in the interpretation of the global kinematics of slow rock slope deformations, we extracted along slope profiles comparing the different distribution of LOS, vertical and horizontal displacements and $\Delta$ angle for selected

case studies. In addition, we tested 3 different methods to extract along slope profiles in order to highlight the main issues possibly arising from each different approach.

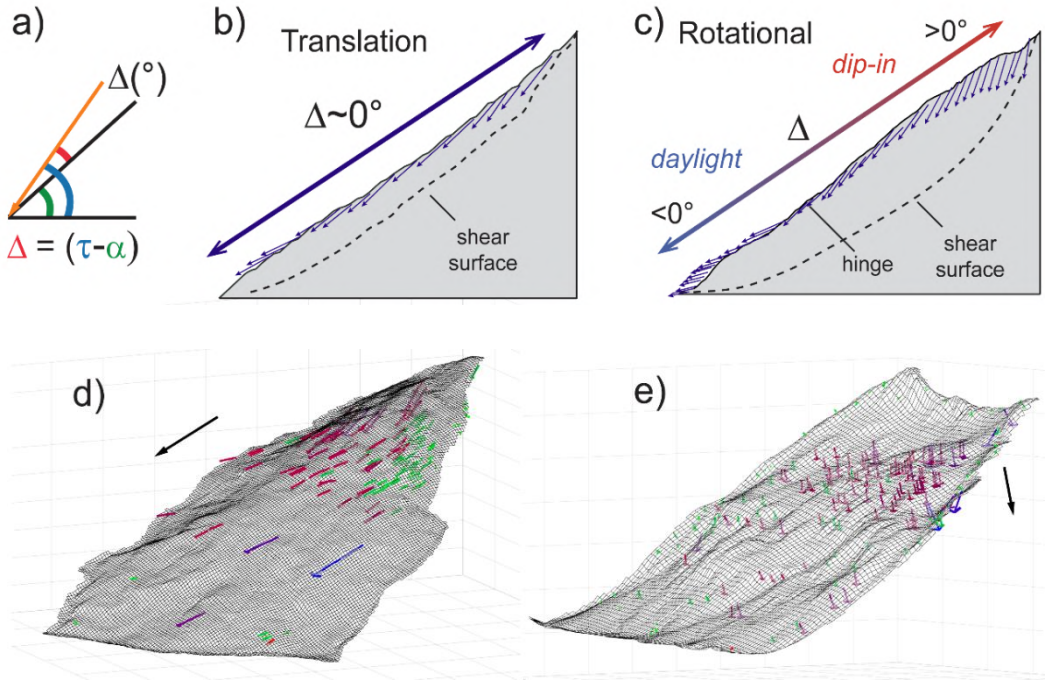


*Figure 3.6: Kinematics extracted from 2DInSAR geometrical components. a) definition of Δ value. Tis the 2D displacement vector inclination, a the local dip of the slope. b)simplified 2D geometry of a translational sliding. c) simplified 2D geometry of a rotational slow rock slope deformation and relative Δvalues. 2D displacement vectors are displacyed in 3D views on real case studies with d) translational and e) rotationl kinematics.*

### 3.5.2 Testing kinematic indicators along slope profiles

- Step 1: spatial interpolation methods

As first approach, through an original Matlab™ tool we generated longitudinal swath profiles of displacement rate (i.e. segments. perpendicular to the down-slope direction in which the statistics of the displacement rate are calculated). Frattini et al. (2018) already used a similar method considering swaths extending up to the lateral boundary of the DSGSD. However, lateral variations due to changes in displacement vector direction with respect to the LOS, presence of secondary landslides or active structures, the geometry of the failure surface and the physical mechanical characteristics of the material (Frattini et al., 2018) can significantly affect the summary interpretation of global kinematics along the central (reference) slope profile.

To overcome this limitation and maximize the accuracy of the data we implemented a handy and interactive Matlab™ tool that allows to set both the orientation and geometrical parameters of the swath (width, sampling step size). The profile trace can be arbitrarily drawn inside the landslide polygon, it is then subdivided in stripes perpendicular to the trace

direction with variable length and width and inside each of them the mean value of PS data is calculated (Figure 3.7 a,d).

As second interpolation method, using the ArcGIS "Point Statistics" tool, we extracted for each PS the average of the values within a specified neighborhood. The final output is a raster where the value of each cell is function of the surrounding ones around that location (Figure 3.7 b,e).

The neighbourhoods can overlap so that cells in one may also be included in the neighbourhood of another processing cell. This is the most restrained spatial interpolator as it considers only the displacement values averaged on the PS itself and its closest neighbours. However, if points are too scattered, the raster map results discontinuous and the derived profile contains gaps due to the lack of data, thus compromising a correct interpretation.

As third method we tested a Natural-neighbour interpolation. This latter finds the closest subset of input samples to a query point and applies weights to them based on proportionate areas to interpolate a value (Sibson, 1981) This method preserves input data values and produces a continuous surface except at the sample points. We computed a 20x20m grid and interpolated a surface bounded between PS locations. No extrapolation was used to approximate values outside the convex hull (Figure 3.7 c,f).

If the number of input PS is too small (<3) no interpolation can be produced and therefore it is impossible to extrude LOS and 2DInSAR profiles. Therefore, those landslides with few PS due to unfavourable slope orientation toward satellite orbit, thick vegetation cover or lack of reflectors will be hardly analysed.

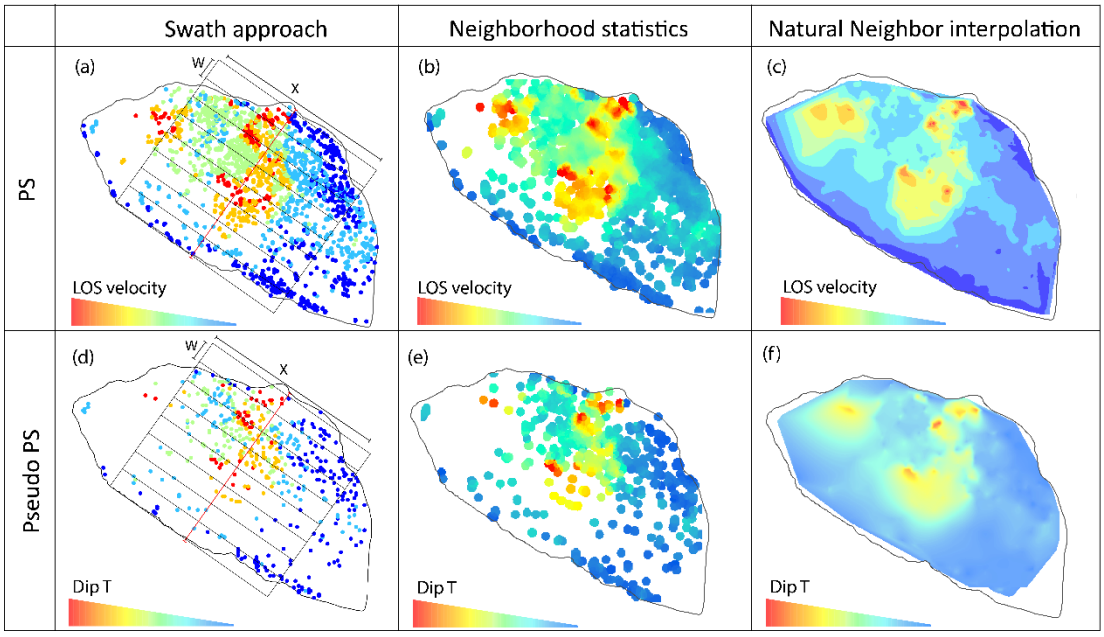


*Figure 3.7: Dataset (Sentinel 1) and spatial interpolation methods applied on Corna Rossa DSGSD to extract LOS and 2DInSAR profiles. PS data always result more spatially dense than Pseudo PS that comes from the integration of ascending and descending datasets. The 3 considered interpolation methods are a, d) swath approach; b,e)Arcgis Point statistics interpolator; c,f) natural neighbor interpolation. See text for details.*

- Step 2: profiles extraction

Because of internal segmentation and strain partitioning, LOS velocity values aren't usually costant through the slope and as consequence the derived kinematic interpretation varies from sector to sector. In this case, swath approach must be carefully applied, choosing an appropriate dimension of the strips.

Variable dimensions (Figure 3.8 a, d) highlight either the local movement of the sector close to the profile trace (narrow swath) or a mean displacement trend of a broader area (wide swath).

Keeping constant the longitudinal length of the swaths (100m), a short lateral width (50m) gives a more precise response than a longer one (2000m) as it emphasizes local changes in velocity with sharp peaks, possibly corresponding to active morphostructures. A wide swath on the contary averages a larger number of points that belong, as in this case, to sectors with different kinematics and, as result, returns a smoother trend with lower mean velocities.

If the landslide has a complex behaviour and an internal segmentation, the use of wide swaths can be misleading for the analysis of the landslide activity and kinematics, whereas if the landslide is homogeneous and without strong strain partitioning a wide swath (Frattini et al., 2018) may be used to interpret the general deformation pattern.

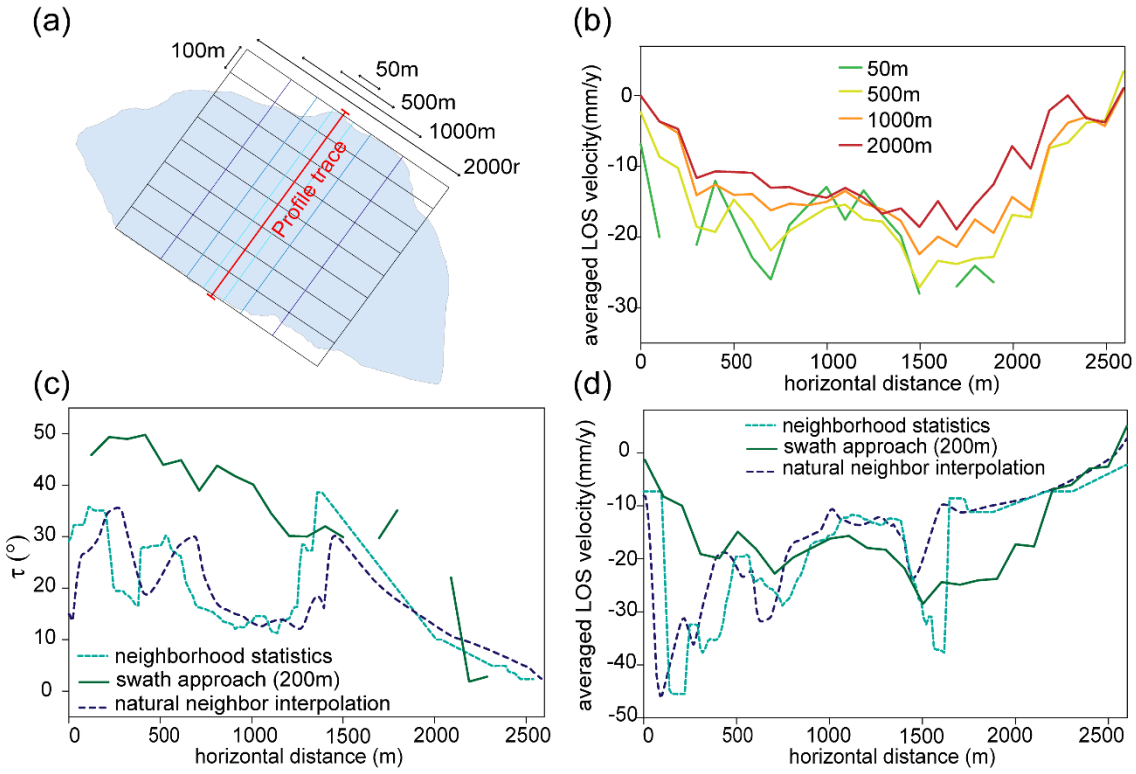


*Figure 3.8: a,b) comparison between profiles extracted using different swath width on Corna Rossa DSGSD. Wider swaths have smoother trend and a smaller velocity ranges; c,d ) comparison of dipT profiles and LOS profiles extracted using point statistics, swath, and natural neighbor approach; see text for discussion.*

Geological and structural observations should therefore come first in order to select the most suitable slope sector and the dimension of the swaths for a consistent analysis of the phenomenon.
Other differences arise from the comparison of profiles extracted using swath approach and the other two methods (Figure 3.8 c,d): neighbourhood statistics and natural neighbour interpolation. Using swath profile a mean value is extracted inside each strip and its value can be very different from the one obtained through neighbourhood statistics or natural neighbour interpolation in which weighted values are computed starting from the given interpolation points. Neighbourhood statistics (Point statistics) in addition results strongly influenced by points distribution emphasizing local response of isolated points and sharpening the values changes along slope resulting in a more accentuate and pointy profile than that provided by Natural Neighbour interpolation.
The outcomes of the profiles were compared and validated with general aspecific constraints considering representative kinematics of synthetic 2D finite elements models and analyzing the response of three case studies with known kinematic.

### 3.5.3 Interpretation: 2DFEM templates

We based our general kinematic interpretation of profiles on the comparison with the results of 2D simple Finite Element numerical simulations run with the commercial code RS2 (Rocscience Inc.), thus providing aspecific interpretation templates (Figure 3.9).

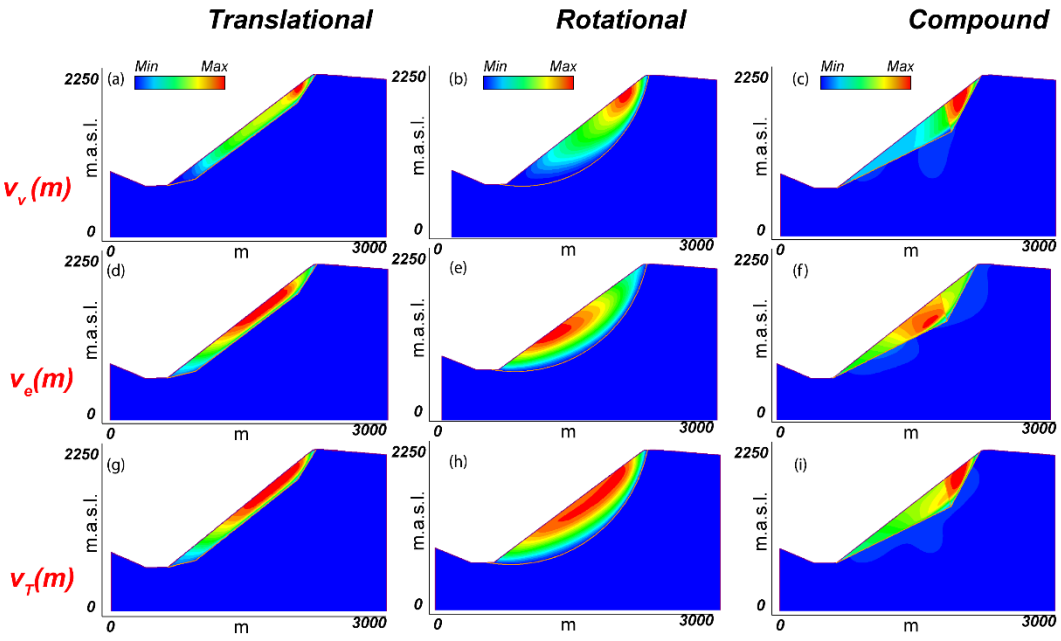


*Figure 3.9: 2D finite element models computed with imposed sliding surfaces in RS2. $V_v$ refers to the vertical component of the displacement vector, $V_e$ to the horizontal one and $V_T$ is the modulus of the total displacement vector.*

Although based on a continuum small-strain formulation, the adopted code is able to account for deformation and failure mechanisms in both continuum and discontinuum rock masses (Hammah et al., 2008; Riahi et al., 2010).
For the simulations, we considered simplified slope geometries with constant slope gradient (30°) and characterized by imposed failure surfaces with different shape (translational, rotational, and compound) introduced as a Goodman joint elements (pseudo-joints in continuum-based modelling; Riahi et al., 2010) to constrain landslide kinematics. Slope height was set to 1200m and failure surfaces traced at depth comprised between 200 and 400 m of depth to simulate large rock slope deformations.
These models do not cover the wide range of possible geometrical and mechanical conditions but are simply meant to extract the distribution of displacement components on simple failure surfaces.
We attributed to the sliding mass values of strength and deformability parameters representative of common rock types (Table 7) as gneiss, schists, granitoids, plus idealized "very stiff" and "soft" rocks in order to extract a generic displacement signature for each kinematics. The non-deformed stable slope was constrained imposing an elastic behaviour and high strength parameters.
We considered homogeneous materials characterized by an elasto-plastic behavior according to a Mohr–Coulomb failure criterion and we ran the simulations using the SSR (Shear Strength Reduction) technique, which enables to evaluate the Strength Reduction Factor associated to computed stress-displacement fields and failure mechanisms (Dawson et al., 1999). We then considered for each model the best SRF stage displaying the most evident kinematic deformation style and critical stability conditions.

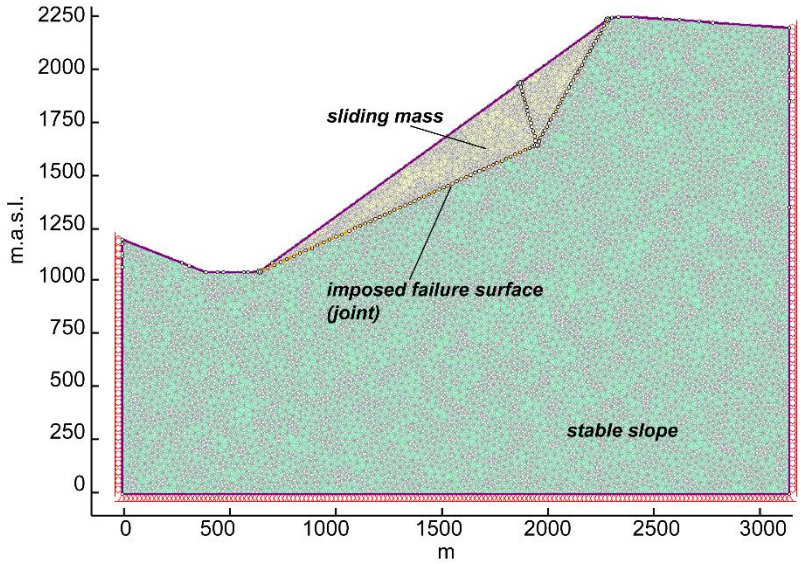


*Figure 3.10: Model setup and mesh discretization.*

The model domain was discretized into six noded triangular finite elements (Figure 3.10). Boundary conditions were assigned in terms of displacements (i.e. fixed bottom and side displacements), and a gravitational stress field was initialized.

*Table 7: Models parameters*

| | stable slope | very stiff | weak | schist | gneiss | granitoid |
|---|---|---|---|---|---|---|
| Unit weight ($MN/m^3$) | 0.027 | 0.027 | 0.027 | 0.027 | 0.027 | 0.027 |
| Stiffness | isotropic | isotropic | isotropic | isotropic | isotropic | isotropic |
| Poisson's ratio | 0.3 | 0.3 | 0.3 | 0.3 | 0.3 | 0.3 |
| Young's modulus | 100000 | 100000 | 10000 | 19000 | 31000 | 41000 |
| Material type | elastic | plastic | plastic | plastic | plastic | plastic |
| Peak tensile strength (MPa) | 5 | 0.4 | 0.4 | 0.1 | 0.15 | 0.2 |
| Peak cohesion (MPa) | 5 | 0.75 | 0.3 | 0.4 | 0.5 | 0.7 |
| Peak friction angle | 35 | 35 | 30 | 36 | 47 | 50 |

For each model, vertical ($v_v$), horizontal ($v_e$) and 2D total displacement inclination ($\tau$) values were extracted along slope and plotted in normalized distance-displacement graphs providing valid templates for the interpretation of real case results (Figure 3.11).

A constant decreasing in vertical values from the top to the toe of the slope is typical of rotational kinematics as the sliding surface is steep in the upper slope sector and then becomes progressively parallel or gently dipping into the slope. A perfect rotational kinematics may also present daylight $\tau$ values at the toe, corresponding to bulging induced by rock mass push.

On the contrary, translational and compound mechanisms are characterized by almost constant vertical values that tend to stabilize in a plateau that becomes more evident for rigid rocks. Localized higher vertical components correspond to the headscarp sector as clearly shown in the compound mechanism where the most of the deformation is accommodated in an active wedge at the top of the slope connected through antithetic structures to a sliding sector.

Horizontal component $v_e$ isn't instead meaningful as it is strongly biased by the geometry of the model and doesn't provide clear signatures of different kinematic styles.

$\tau$ angle, on the contrary, gives clear geometric information also in complex and heterogeneous conditions and can be considered a valid indicator of both local and global kinematics.

A flat pattern, corresponding to a constant dip angle, is typical of translational landslides where the sliding movement is manly parallel to the slope, while for rotational kinematics it presents a highly decreasing angle going from the main headscarp to the toe. Compound mechanism is a combination of the previous two, as it shows highly plunging vectors in the

headscarp sector, followed by translational movement along slope, mirrored by almost constant τ values.

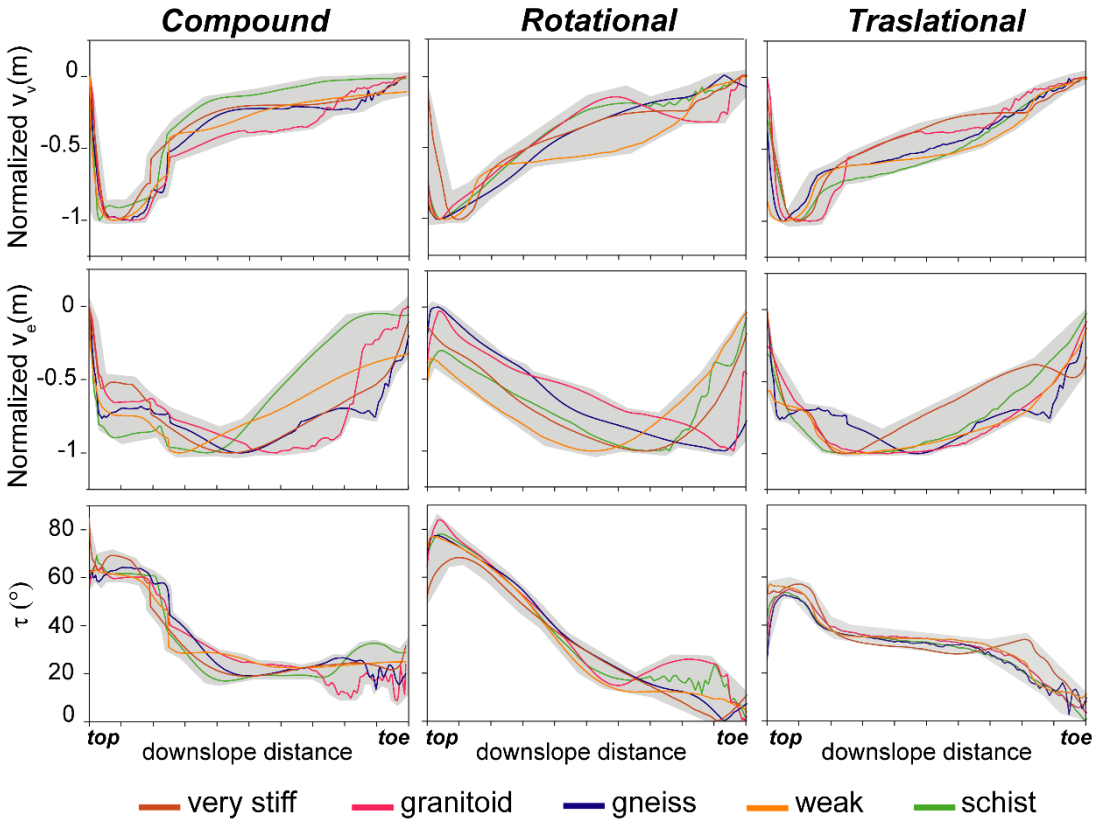


*Figure 3.11: Displacement curves obtained from simplified 2DFEM of rotational, translational and compound mechanisms. Vertical and horizontal components are normalized to be better compared. Dip of total vector represents the inclination of the 2D SAR total vector along slope.*

### 3.5.4 Testing kinematic descriptors on real slow rock slope deformations

We evaluate the applicability and robustness of kinematic profiles to the analysis of slow rock slope deformations at three selected case studies: Mt. Solena large landslide, Farinaccio (Agliardi et al., 2012; Frattini et al., 2018) and Corna Rossa DSGSDs (Agliardi et al., 2018; Agliardi et al., 2019) and for each of them we extracted Δ profiles (i.e. best geometric indicator, see above section 3.5.3) integrating the kinematic analysis with morpho-structural observations derived from semi-detailed mapping (see section 3.3).

In the first case, Monte Solena large landslide (Figure 3.12 a), we observe highly plunging Δ in the headscarp sector and constant Δ values along the profile trace, where it remains almost parallel to the slope (Figure 3.12 b), as in the case of a simple planar surface in which the type of movement is strongly limited (Figure 3.12 c).

Changes in the profile trend correspond to mapped areas of debris accumulation and nested shallower phenomena. A different scenario can be depicted for Mt. Farinaccio DSGSD (Figure 3.12 d). Δ shows highly dipping angles in the upper sector (Figure 3.12 e) of the

slope corresponding to the main headscarp and then decreases downslope, but always remaining steeply plunging into the slope. This trend is typical of rotational phenomena (Figure 3.12 f) and local fluctuations are due to the presence of active morphostructures, as highlighted by the mapping.
Corna Rossa DSGSD (Figure 3.12 g) is a more complex phenomenon (Agliardi et al., 2018; Frattini et al., 2018; Agliardi et al., 2019) with a strong internal segmentation. In the westernmost sector, Δ profile shows a double trend: first decreasing in the headscarp sector and then stabilizing along slope (Figure 3.12 h). Comparing this trend to the 2DFEM template we can describe the kinematic as compound with a rotational uppermost sector followed by a mainly sliding part (Figure 3.12 i).

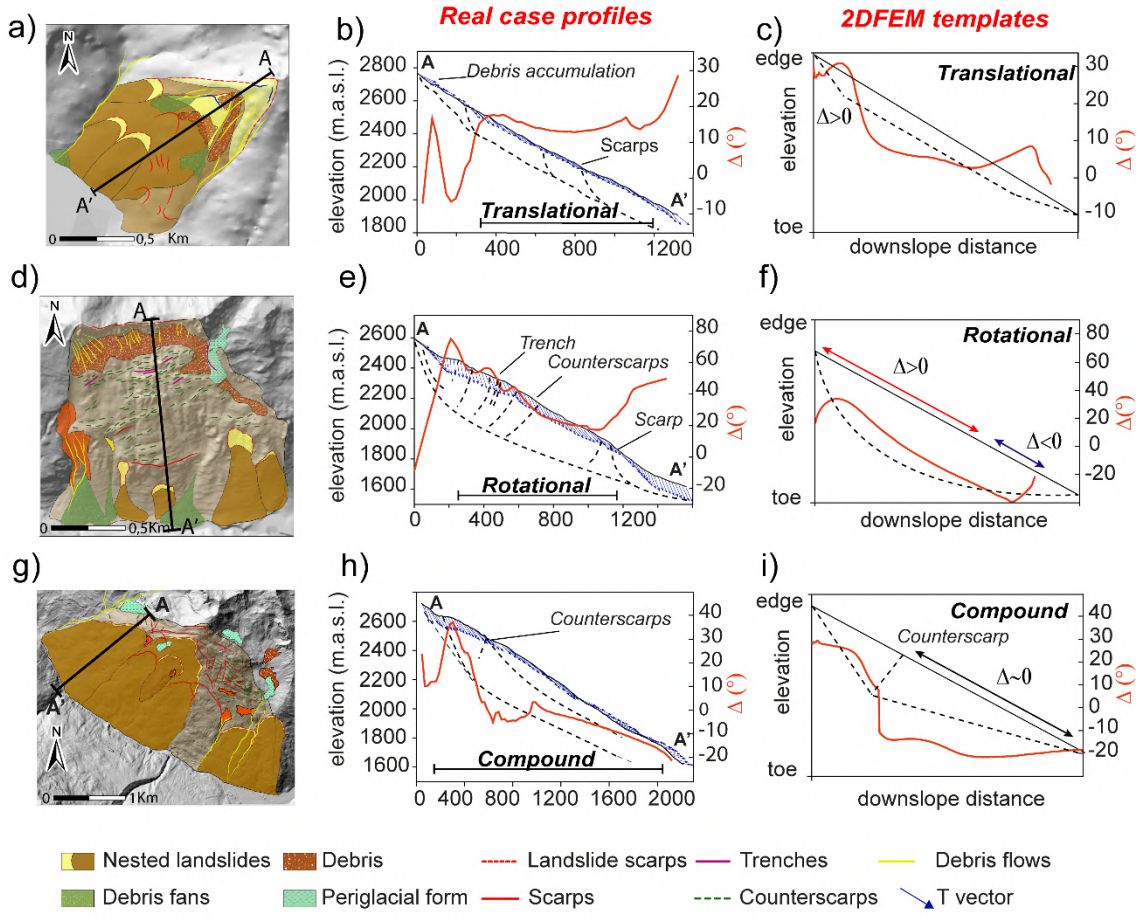


*Figure 3.12: Comparison between morpho-structural mapping, Δ profiles extracted along (a,b ) Mt.Solena (d,e) Mt. Farinaccio and (g,h) Corna Rossa DSGSD and (c,f,i) Δ profiles extracted from 2DFEM assuming a constant slope of 30°.*

### 3.5.5 Comparison of kinematic descriptors

To select the most suitable kinematic descriptor we compared LOS velocity values (Figure 3.13 a, d) with vertical displacement components (Figure 3.13 c, d) and τ angles (Figure 3.13 b, e). We did not consider the horizontal displacement rate $v_e$ since it represents the horizontal movement on a 2D E-W plane and its values can be highly biased on slope with

unfavorable orientation. On the contrary the vertical velocity represents the real upward/downward displacement rate and gives more significant information on the landslide gravitational movement.

Considering these parameters, translational movement is characterized by almost flat $V_v$ and $\tau$ profiles, as shown in Mt. Solena plots (Figure 3.13 g). After a drop in vertical displacement velocity corresponding to the main headscarp, $V_v$ stabilizes around a steady value of about -3.5mm/y suggesting that there are no active structures that induce important vertical movements and the deformation remains almost homogeneous (Figure 3.13 c,g). Similarly, $\tau$ profile confirms this observation with only few local fluctuations (Figure 3.13 b, g).

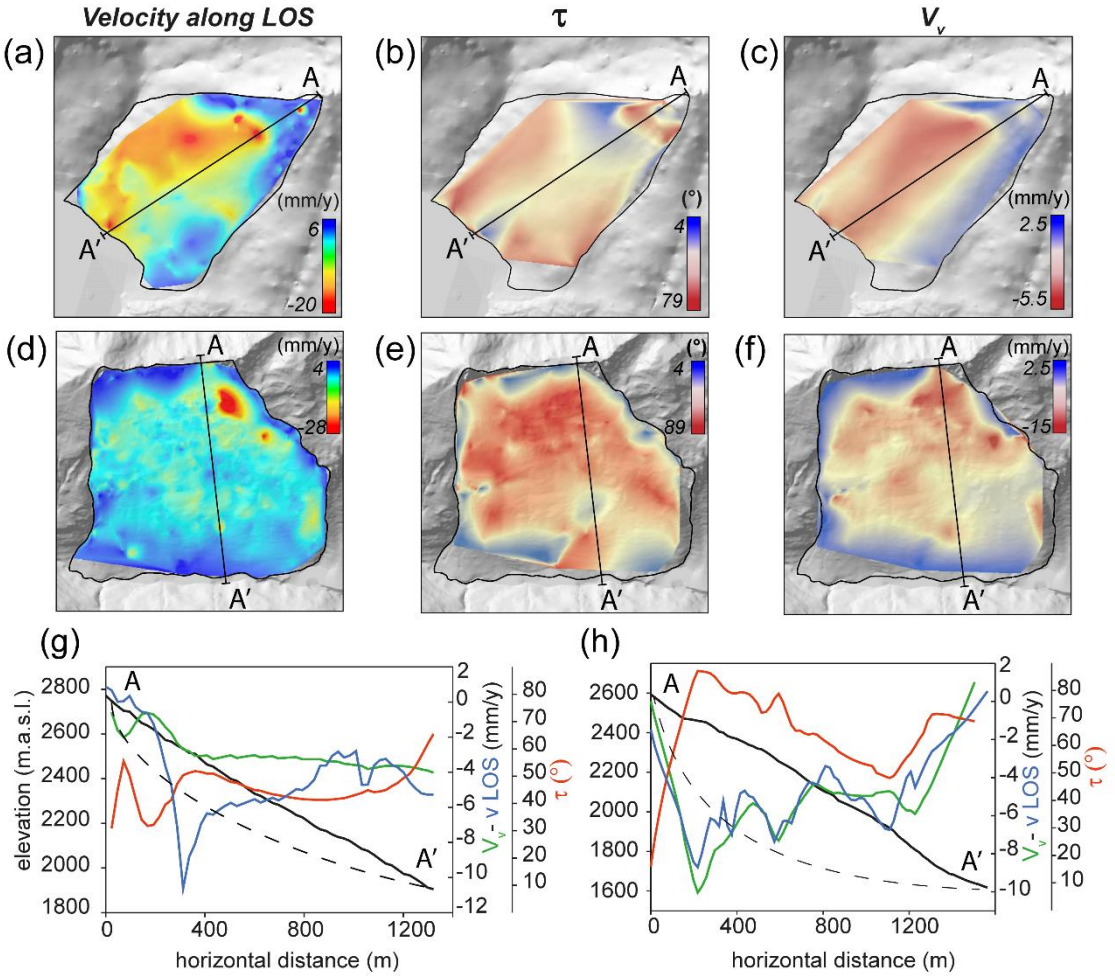


*Figure 3.13: Example of LOS and 2DInSAR profiles extracted along a translational (Mt. Solena) and a rotational (Mt. Farinaccio) DSGSD using natural neighbor approach. a,d) map of LOS values distribution b,e) map of total displament vector dip distribution c,f) map of vertical component distribution distribution g,h) LOS and 2DInSAR profiles along slope.*

Rotational kinematics (Mt Farinaccio DSGSD, Figure 3.13), on the contrary is characterized by highly dipping displacement vectors in the upper sector of the slope (Figure 3.13 b, c, h), corresponding to the main headscarp, and then decreasing downslope as the movement becomes less steep.

The interpretation of these trends is consistent with the results obtained from the 2DFEM analysis and integration with morpho-structural mapping, thus supporting the effectiveness of $v_v$ and $\tau$ parameters as kinematic descriptors.

As consequence, they can also be used as valid tool to assess the kinematics of different sectors in more complex phenomena, outlining the internal slope segmentation and linking the surface expression with deeper deformation mechanisms.

In this perspective, we adopted this approach to analyse different slope sectors of Corna Rossa DSGSD (Figure 3.14), that is strongly segmented and characterized by different morpho-structural expressions such as scarps, in the NW sector, and several orders of steep scarps and counterscarps arranged in a graben system in the SE area (Agliardi et al., 2018; Agliardi et al., 2019). Different features are ascribable to different deformation mechanisms and outline a transition from a mainly sliding sector to a "spreading" one, characterized by dominant extension accommodated by symmetric and asymmetric graben structures.

This change in kinematic behaviour, inferred from morpho-structural observations, is confirmed by $\Delta$ plots. From NW to SE we can recognize a transition from a compound

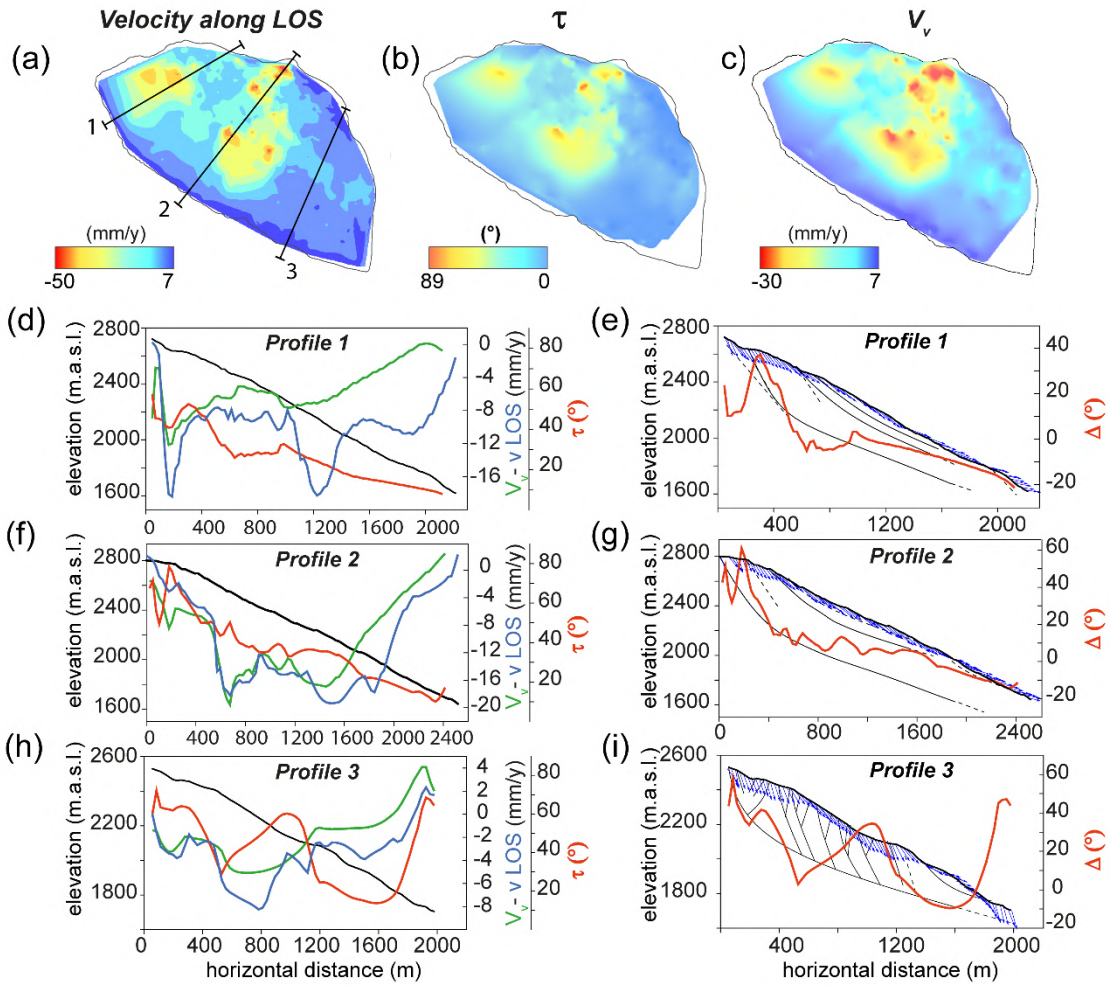


*Figure 3.14: Profiles extracted using natural neighbor interpolation from 3 different sectors of Corna Rossa DSGSD. Their trends suggest a strong internal partitioning that causes changes in kinematics along slope, as reflected by the presence of different mapped morphostructures.*

sliding (Figure 3.14 d, e) to a dominant rotation (Figure 3.14 f, g) and a more complex kinematic (Figure 3.14 h, i) strongly influenced by the presence of deep scarps and counterscarps arranged in a graben system.

$\tau$ and $\Delta$ profiles well reflect the deep deformation style because they are velocity independent parameters. In fact, even if the LOS velocity is underestimated or biased, the combination of two different points of view provides a true angle of the 2D displacement on the E-W vertical plane. On the contrary, the interpretation of 1D LOS profiles is not always straightforward in the assessment of kinematics because they can present peaks and fluctuations linked to heterogeneous velocity and isolated high values more than true kinematic transitions. Negative or positive peaks can outline active structures or nested phenomena that, despite having different displacement rates, keep the same deformation style (e.g. fast or slow sliding sectors). Moreover, 1D LOS velocity values are strongly influenced by the orientation and inclination of the slope and can be highly underestimated. To unravel the complex kinematic pattern of slow rock slope deformations a single velocity analysis based on 1D LOS values is thus not sufficient since it is biased by slope orientation and can report spurious information of the real ongoing displacement. A 2DInSAR analysis, that combines data from ascending and descending satellite orbits, allows to partially overcome this limitation since it increases the sensitivity to displacement (Eriksen et al., 2017) on the vertical E-W plane and provides consistent geometric information on the ongoing deformation pattern. The analysis of geometric profiles, extracted using a natural neighbour interpolation on 2D InSAR values, proved to be a valid approach to assess the local scale kinematics of slow rock slope deformations, since it allows to highlight geometrical variations of different slope sectors.

However some considerations must be taken into account.

If on one hand multi-geometry SAR processing is a valid tool to investigate the slope kinematics, on the other hand the density of extracted Pseudo PS available within the DSGSD gives a first idea on the effectiveness of the analysis (Annex D).

Taking note of this limitations, 2DInSAR decomposition can be generally applied and has proved to give suitable parameters to define the deformation kinematics, but it must be always integrated with other geological data such as morphological and morpho-structural mapping or field observations in order to have a consistent overview of the phenomenon. A further comparison between 2DInSAR profiles and finite elements models is finally a simple but useful tool for the validation of the conceptual ground displacement distributions as it gives a preliminary idea on the expected deformation style.

# 4 Regional Scale analysis

Slow rock slope deformations are extremely widespread in alpine environments (Crosta et al., 2013), thus they can diffusely interact with different types of elements at risk (i.e. transportation corridors, lifelines, settlements) or pose risks related to rockslide differentiation and evolution towards catastrophic failure (Agliardi et al., 2012, 2020; Frattini et al., 2013, 2018). However, due to their variety of mechanisms and internal complexity, slow rock slope deformations are characterized by very diverse styles of activity, here defined as the interplay of the degree of activity (i.e. displacement rate), kinematics and internal segmentation (Agliardi et al., 2012; Frattini et al., 2018). For example, phenomena with translational kinematics potentially pose higher hazards, since they are intrinsically more unstable and characterized by higher initial mobility than phenomena with rotational kinematics. Moreover, slope deformations evolving at same speed and with similar kinematics can evolve as coherent masses or break up in smaller sectors, depending on their structural segmentation and internal damage.
This complexity, associated to the low displacement rates, makes these phenomena difficult to tackle in a risk management perspective. Thus, a regional scale classification is needed to gather a preliminary characterization of recognized phenomena.

By combining PS-InSAR™ and SqueeSAR™ products (TRE Altamira), acquired over the alpine sectors of Lombardia region we develop a novel approach to characterize and classify slow rock-slope deformations according to their style of activity, with support of an original inventory mapping, performed on regional scale yet accounting for key local-scale information. We developed algorithms and implemented Matlab™ and GIS tools to quantify the kinematics and degree of activity of slow rock-slope deformations. These algorithms capture the internal segmentation of each considered phenomenon, still being suitable for a rapid regional-scale analysis. We use multivariate statistical analysis to identify variables associated to a robust definition of the style of activity and implemented the procedures in a semi-automated workflow that can be readily applied to other landslide datasets in a fast and cost-effective way.

## 4.1 Style of activity analysis at the regional scale

### 4.1.1 Segmentation, heterogeneity and velocity assessment

Between the 208 slow rock-slope deformations mapped in Lombardia, only 166 of them (117 DSGSDs and 49 LL) are covered by InSAR data. 42 of them lack of InSAR data, due to absence of active PS, considered as PS with mean LOS velocity <-2mm/yr or >+2mm/yr, PseudoPS or complete data missing (Table 8).

To classify the state of activity ad kinematics we used the PS-InSAR™ and SqueeSAR™ datasets presented in section 3.4. PS and DS datasets derived from Sentinel 1A-B imagery always resulted the best in terms of total number of PS and coverage of the area and, when available, were preferred in the analysis to datasets derived from Radarsat and ERS images.

*Table 8: number of slow rock slope deformations coevered and missing InSAR data.*

| | SAR covered | Lack of InSAR data | | |
|---|---|---|---|---|
| | | *No active PS** | *No PseudoPS* | *No Data* |
| DGPV | 117 | 3 | 13 | 1 |
| LL | 49 | 3 | 12 | 10 |
| Tot. | *166* | *6* | *25* | *11* |

**active PS are considered in the range -2 >LOSvel (mm/yr) >+2*

As a limiting condition, less than three PS or pseudo-PS hamper the extraction of distribution of LOS velocity values to retrieve information on the segmentation, degree of activity and kinematics of landslides.

To assess the degree of activity of each mapped landslide at the regional scale we applied the peak analysis classification (see section 3.4) and extracted for each landslide representative indexes namely: the number of peaks (i.e. degree of segmentation, Figure 4.1 b), the modal and the smallest peak velocity (i.e. respectively the main mass velocity and the fastest velocity, Figure 4.1 a,c) and the quartile deviation (i.e index of heterogeneity).

Our results, validated by comparison with field data, show that 57 slow rock slope deformations move as coherent blocks ("homogenous" class, Figure 4.1 b), while most mapped cases undergo a variable degree of internal segmentation (Figure 4.1 b). Segmented landslides are usually characterized by one (55 cases) or two (81 cases) distinct nested sectors with different LOS velocity with respect to the background (e.g. Mt. Padrio Varadega DSGSD (Ambrosi and Crosta, 2006) Mt. Mater (Crippa et al., 2020). 15 cases are extremely segmented, with more than three nested sectors (Figure 4.1 b).

Our method's ability to outline segmentation is influenced by the abundance and homogeneity of PS and DS in nested sectors, and by the frequency threshold values used in the peak analysis. Thus, the number of sectors in Figure 4.1 b must be regarded as a lower-bound estimate. At the same time, our analysis is unable to detect fast-moving landslides within slow rock slope deformation, due to the temporal baselines of PS-InSAR™ and SqueeSAR™ analyses processed on the regional scale.

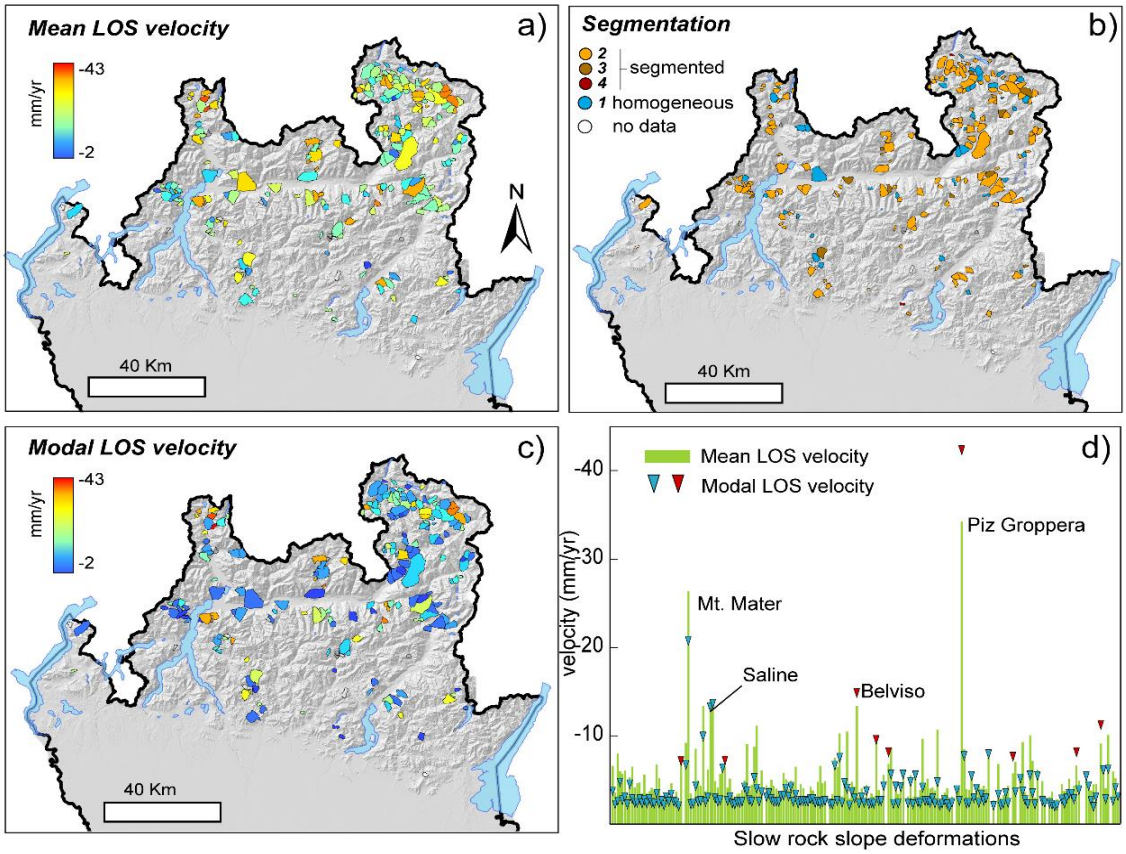


*Figure 4.1: Maps showing distribution of activityand segmentation over the entire inventory. (a) Mean LOS velocity computed for each landslide considering active PS (faster than -2mm/yr). (b) Distribution of segmented and homogeneous phenomena with associated indicative number of internal sectors outlined by the peak analysis. (c) Modal LOS velocity resulting from the peak analysis on active PS distribution for each landslide. (d) plot representing the mean LOS velocity and the peak LOS velocity for each element. Red triangles correspond to some evident cases in which the peak velocity exceeds the mean value.*

Modal values of LOS velocity, representing the state of activity of main landslide bodies are generally in the range of -5÷-3mm/yr. When landslide movements are homogeneous, mean and modal velocities tend to converge. Mean landslide velocity usually (Figure 4.1 a) exceeds the modal one (Figure 4.1c) when the main landslide body hosts smaller and faster nested sectors. On opposite, modal velocity exceeds the mean one (Figure 4.1 d) when faster nested sectors, with abundant PS and DS, involve a high percentage of the total landslide extent (e.g. Piz Groppera large landslide, n°4 in Figure 4.17). Differences between modal and mean velocity are usually in the range of few mm/yr, but can reach several mm/yr (e.g. Belviso n°12 in Figure 4.17, mean velocity ~ 13mm/yr, modal velocity ~ 15mm/yr) and up to 1cm (e.g Piz Groppera: mean velocity ~ 33mm/yr, modal velocity ~ 42 mm/yr).

### 4.1.2 Global landslide kinematics

We then implemented the kinematic analysis at the regional scale by analysing the statistical distribution of the parameter $\Delta$ (Eq. 32) within each entire landslide area.
The local (i.e. cell-scale) slope kinematics can be readily inferred (Agliardi et al., 2019) by observing the difference between the 2D velocity vector inclination ($\tau$) and the local slope dip ($\alpha$) in each square cell, namely $\Delta=\tau-\alpha$ .Where $\Delta$ is positive, we have a dominant downward movement dipping in the slope. Values of $\Delta$ close to zero indicate slope-parallel sliding, while negative values indicate daylighting or bulging movements. We characterize the global (i.e. slope-scale) landslide kinematic by analysing the statistical distribution of the parameter $\Delta$ within each entire landslide area.

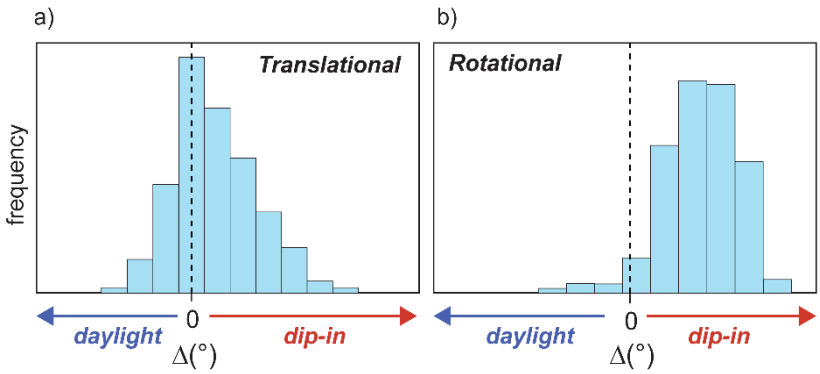


*Figure 4.2: $\Delta$ value distribution over a landslide area provides an indicator of its main deformation style: (a) translational; (b) rotational.*

In particular, the frequency distribution of $\Delta$ values of translational landslides tends to be symmetrical and centred around 0 or slightly shifted towards positive ("dip-in") values (Figure 4.2 a), accounting for the local kinematics of scarp areas. Instead, rotational landslides have either bi-modal distributions or distributions skewed towards positive values (Figure 4.2 b), as the displacement vector becomes steeper within the entire mass and daylights (negative $\Delta$) at the toe.
In order to exploit this assumption in a regional-scale analysis, we used $\Delta$ descriptive statistics (i.e. mean, mode, median, skewness, kurtosis) as input values of a supervised machine learning through the Matlab$^{TM}$ "classification learner" app (Figure 4.3).
The classification learner app works according to a three main steps procedure:

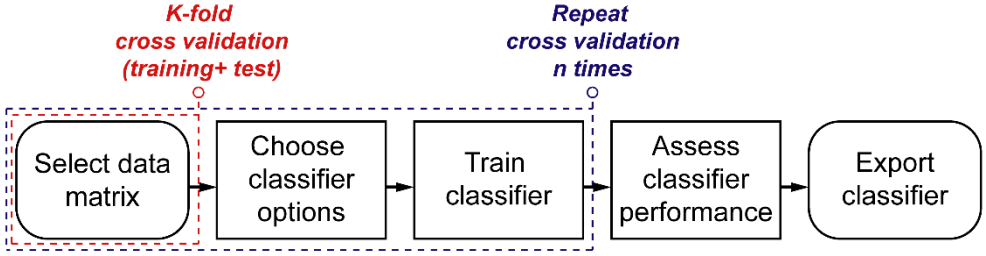


*Figure 4.3: Common classification learner workflow.*

Step 1: Selection of a matrix with input data

Step2: Definition of predictors (in our case $\Delta$ statistics) and responses (kinematic definition).

Step 3: Training of different predictive models and definition of the classifier

To avoid overfitting of the data, we applied a 5-fold cross validation on the input dataset subdividing the same in a training and test subsets.

The app trains in parallel different classification models (e.g. decision trees, discriminant analysis, support vector machines, logistic regression, nearest neighbours, naïve Bayes, and ensemble classification) and selects the best ones (i.e. with the highest accuracy).

Due to the paucity of supporting literature and field data, we calibrated our analysis on a limited number of well-characterized case studies (16) with known kinematics (Agliardi et al., 2001; Allievi et al., 2003; Ambrosi and Crosta, 2006; Frattini et al., 2018) and iterated this procedure more than 20 times to get a sound predictive model.

Linear discriminant (Fisher, 1936) proved to be the best classifier, with a mean accuracy higher than 80% over the iterations.

Discriminant analysis assumes that different classes gather data based on different Gaussian distributions. In the classification training step, the fitting function estimates the parameters of the Gaussian distribution of each class and creates linear boundaries between them.

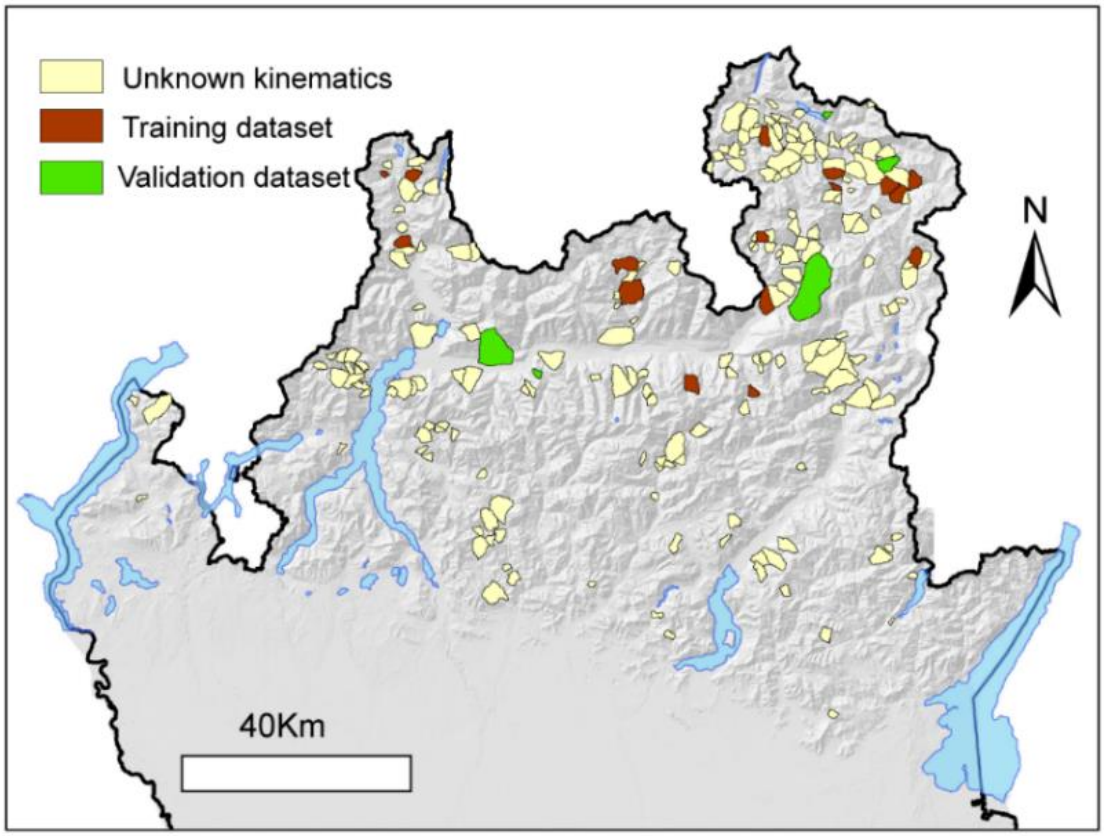


*Figure 4.4: Partition of the inventory for the machine learning kinematics analysis: landslides used as training and validation datasets are highlighted in brown and green. Whitish polygons correspond to the rest of the inventory landslides with no kinematic attribution.*

We then exported the classifier to generate predictions for the remaining data. Finally, we further validated the outcome using a subset of 6 selected case studies with known kinematics (Figure 4.4). Our results (Figure 4.5) show that the median (Δ_M) and in minor portion skewness (Δ_SK) of the frequency distribution of Δ values are good predictors of global landslide kinematics.

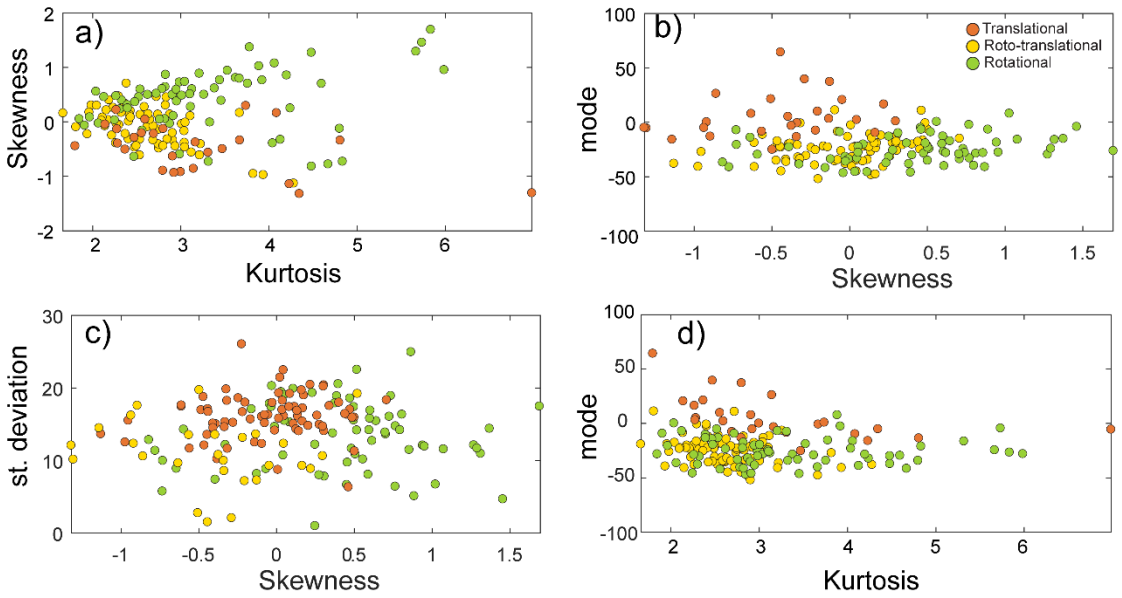


*Figure 4.5: Combinations of descriptive statistical descriptors of Δ distributions.*

Median is a particularly strong controlling factor in the distinction between different kinematic groups, while skewness, which refers to the asymmetry of the data distribution from the normal distribution plays a minor control (Figure 4.6).

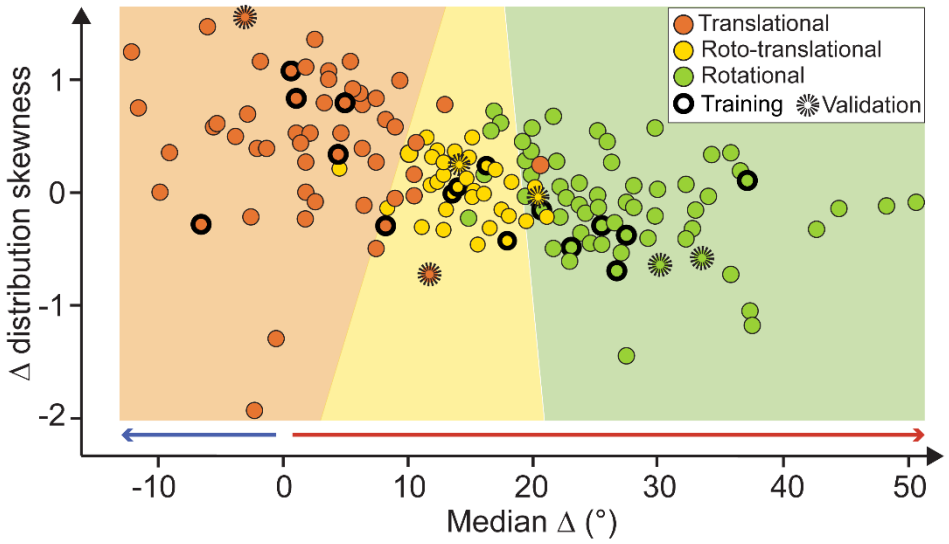


*Figure 4.6: Machine learning classification of mapped landslide kinematics according to Δ distribution skewness and median. The background coloured fields correspond to the kinematic groups signature (R, RT, T) and are defined using linear discriminant decision surface.*

Its value is less influent in the classification, but provides information on the dispersion of $\Delta$ data towards more positive values (negative skew) or negative ones (positive skew).
Figure 4.6 reports the final classification graph resulting from the supervised machine learning analysis. The background coloured fields correspond to the predicted kinematics signature (R, RT, T) and are defined using linear discriminant decision surfaces.
Mapped slow rock slope deformations have dominant rotational (72 cases) or roto-translational kinematics (42 cases), while 57 cases exhibit translational kinematics (Figure 4.7 ).

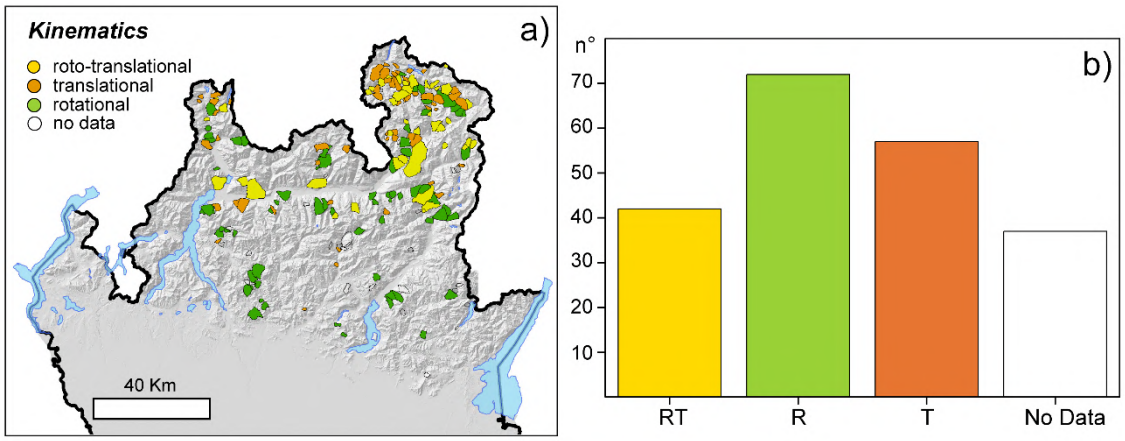


*Figure 4.7: Regional scale kinematics a) kinematic signature of mapped landslides b) frequency distribution of kinematics.*

### 4.1.3 Morpho-structural and morphometric analysis

To define the long term activity state and degree of evolution of all the mapped phenomena we took into account 9 morpho-structural and morphometric variables computed from the semi detailed mapping (section 3.3 and Table 5).
Morpho-structural variables such as density of deformed nested landslides (DB), immature nested landslide (NB), landslide scarp sector density (LS) and the density of morphostructures (DM) represent a first index of the slope style of activity. A high percentage of deformed bodies suggests an intense past evolution and predisposition to develop inner instabilities and failures. On the contrary, a higher percentage of nested bodies points out those phenomena with a minor past activity, but possibly prone to a future evolution of some sectors.
The morphostructures density distribution (DM) which comprises scarps, counterscarps and trenches, provides clues on the internal degree of rock mass damage. Generally, highly fractured rock masses (i.e. high DM density) are the result of intense stress rates, but, since they deform in a plastic way, they tend to accommodate the deformation and less likely evolve towards catastrophic collapse. Intact rock masses with few localized morphostructures on the contrary behave in a more brittle way and when triggered towards failure they may catastrophically collapse as entire blocks.

Morphometric parameters are useful too in the description of the style of activity of slow rock slope deformations, since they control the onset of the phenomena and at the same time provide a quantification of the impact of the landslides on the slopes.
We considered as main morphometric variable the length to width ratio (L/W), elevation ($\Delta$h), area to perimeter ratio (A/2p); hypsometric integral (Hi), mean northerness (aspect), and mean slope angle (slope).
These parameters describe the relief energy and give indication on the slopes shape and topography, which are important predisposing factors for the stability analysis. In fact, since the morphology of the slopes varies widely, (Lebuis et al., 1983) the form factors, relief energy and hypsometry can condition or outline the development and evolution of gravitational phenomena (Lebuis et al., 1983; Mansour et al., 2015). Moreover, the aspect also conditions the visibility of the slopes. East or west facing slopes are better captured by the satellite LOS, either ascending or descending, preventing the underestimation of the displacement pattern because of geometrical artefacts.
We didn't consider lithological variables because, although rock type is a well-recognized major control on the regional occurrence of slow rock slope deformations (Agliardi et al., 2013; Crosta et al., 2013; Pedrazzini et al., 2016), on regional scale it appears uncorrelated with activity and kinematics.
As reported by Agliardi et al (2013), the lithology and structure are the major local controlling factor and foliated metamorphic rocks are more prone to the onset of slow rock slope deformations.

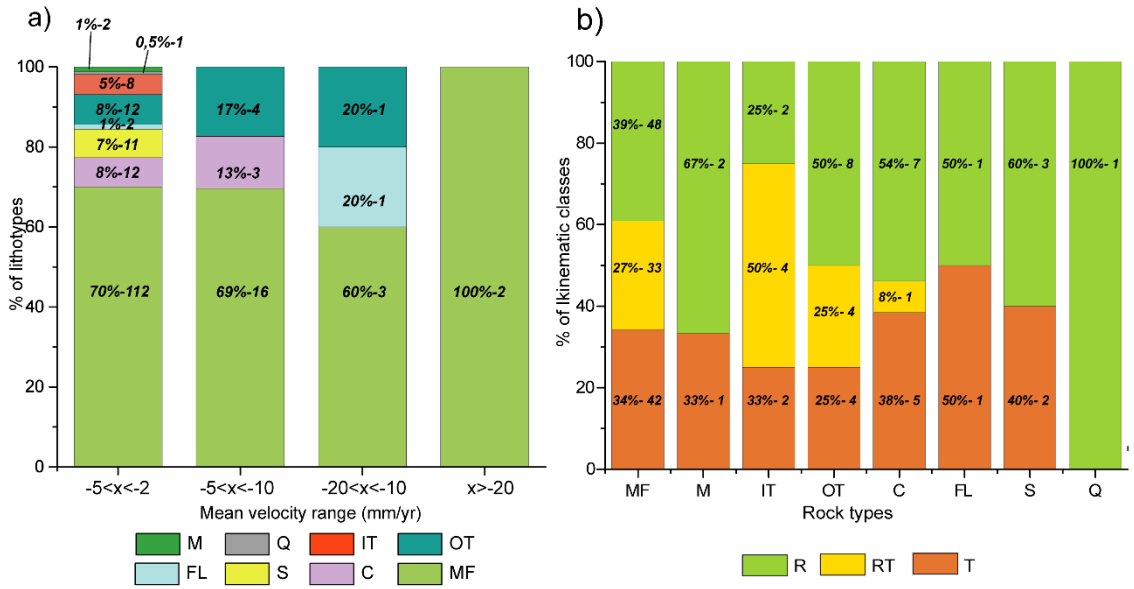


*Figure 4.8: 100% stacked bar coloumns reporting the activity and kinematic distributions according to rock types classes. Percentages are associated to the corresponding number of elements they account for. (a) Shows how main lithologies are distributed in velocity classes. (b) Distribution of kinematics in each rock type class. Also in this case there isn't an evident control, at the regional scale, of the lithology on the kinematic style.*

However the relation between lithology, velocity and kinematics isn't straightforward. Bar charts in Figure 4.8 outline how a sharp correlation between lithotypes and velocity (Figure 4.8 a) and lithotypes and kinematics (Figure 4.8b) can't be attained at the regional scale. We thus excluded lithological variable form the subsequent analyses (Table 9).

*Table 9: Mapping and InSAR-derived variables considered for multivariate statistical analysis*

| Variable type | Label | Variable name |
|---|---|---|
| Morpho-structural | DB | Deformed nested landslides density |
| | NB | Immature nested landslide density |
| | LS | Landslide scarp sector density |
| | DM | Morpho-structures density |
| Morphometric | Hi | Hypsometric integral |
| | L/W | Elongation ratio |
| | A/2p | Shape factor |
| | $\Delta$h | Relief |
| | Aspect | Mean direction toward N |
| InSAR derived | v_PM | Velocity of major peak |
| | v_Pm | Velocity of minor peak |
| | Q_dev | Quartile deviation |
| | $\Delta$_SK | Skewness of $\Delta$ distribution |
| | $\Delta$_M | Median of $\Delta$ distribution |

## 4.2 Classification: multivariate statistical analysis

A complete characterization of the style of activity of slow rock slope deformations must combine all the so extracted indexes explaining the degree of activity, the kinematics and morphometry. In order to classify the mapped phenomena according to their style of activity, we performed multivariate statistical analysis considering 14 variables (5 morphometric, 4 morpho-structural and 5 related to activity and kinematics (Table 9); and combined them in a. PCA and cluster analysis.

### 4.2.1 PCA and cluster analysis

PCA allows the datasets exploration and interpretation reducing dimension and keeping the variation in the data (Ballabio, 2015). It is used for reducing the dimensionality of large datasets described by different variable, increasing the interpretability but at the same time minimizing information loss (Jolliffe and Cadima, 2016). The basic idea of PCA analysis is to maximize the variability (i.e. statistical information) between the variables finding new variables that are linearly related to the original ones and that are uncorrelated to each other (Ballabio, 2015; Jolliffe and Cadima, 2016). These are the so called Principal Components.

In the different analysis steps, we retained the principal components with eigenvalues (amount of variance explained by a given principal component) $> 1$. Cases missing values of some variables, e.g. due to lack of PS, DS or pseudo-PS, were automatically excluded from the PCA according to a listwise deletion procedure.
Since PCA produces synthetic variables each one accounting for a bunch of original variables, we used its results (principal components) as input for an unsupervised Cluster Analysis, aimed at detecting similarities among cases and classifying them into few groups (Massart, 1983; Ballabio and Consonni, 2013; Ballabio, 2015), representative of different styles of activity.
Traditionally clustering is regarded as unsupervised learning since it lacks of a class label or a quantitative response variable (Pan et al., 2013).
For the Cluster Analysis we used the K-medoids method instead of the traditional K-means or a different hierarchical clustering algorithm because K-medoids uses actual sample points as cluster centres (Kaufman and Rousseeuw, 1990; Jin and Han, 2010;) to form n clusters, and remaining data objects are grouped to minimize the sum of dissimilarities of the surrounding points, making the approach more robust to noises and outliers (Arora and Varshney, 2016).
Hierarchical clustering on the contrary produces a dendrogram which organizes clusters with a predominant ordering from top to bottom. So, while non-hierarchical methods (K-means and K-medoids) split the elements in groups so that each one belongs to an independent cluster, hierarchical classification orders elements according to their similarity and clustering becomes strongly controlled by the kind of linkage (Complete Linkage, Simple Average, Centroid, Median, Ward's Minimum Variance) selected between groups and the best cut height of the dendrogram. This latter can be cut where the difference is most significant, selecting a number of clusters, using the square root of the number of individuals, selecting at least 70% of the distance between the two groups etc. The classification thus results less stable in our analysis since it is influenced by setting conditions and user decisions that strongly change the final outcome.

### 4.2.2 Classification steps

We performed the following multivariate (MV) analyses:
MV1: PCA and cluster analysis for rock-slope deformations (DSGSDs + large landslides) covered by InSAR data (166 cases out of 208), considering 14 variables: 5 morphometric, 4 morpho-structural and 5 InSAR-derived, related to activity and kinematics (Table 9);
MV2: PCA and cluster analysis for all the mapped rock-slope deformations (DSGSDs + large landslides, 208 cases), considering 9 variables: 5 morphometric, 4 morpho-structural (no InSAR variables, Table 9);
MV3: PCA and cluster analysis for DSGSDs covered by InSAR data (117 cases), considering 14 variables: 5 morphometric, 4 morpho-structural and 5 InSAR-derived, related to activity and kinematics (Table 9);

MV4: PCA and cluster analysis for large landslides covered by InSAR data (49 cases), considering 14 variables: 5 morphometric, 4 morpho-structural and 5 InSAR-derived, related to activity and kinematics (Table 9);
MV5: proximity analysis on rock-slope deformations (DSGSDs + large landslides) not covered by InSAR data (42 cases).

#### 4.2.2.1 MV1: DSGSD and large landslides covered by InSAR data, all variables

PCA on the bulk inventory (including both DSGSDs and large landslides) allows characterizing only 166 landslides out of 208. In fact, 42 cases with less than 3 active PS or lacking pseudo-PS are automatically discarded from PCA by listwise deletion.

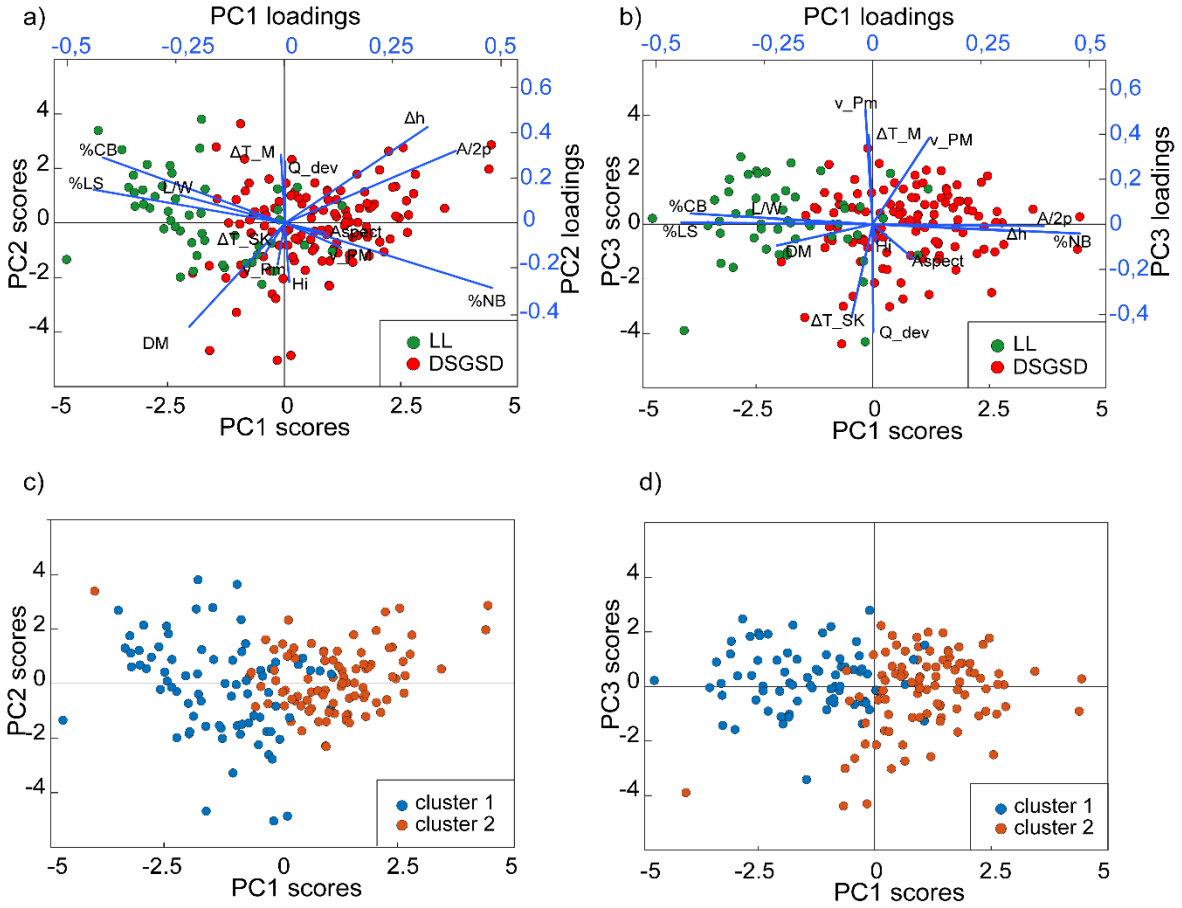


*Figure 4.9: MV1: PCA and cluster analysis on the SAR covered bulk dataset of rock-slope deformations (DSGSD + large landslides, 166 cases) (a) PC1-PC2 biplot with the result of the PCA and the distribution of DSGSDs (red dots) and Large Landslides (green dots). Blue lines are the eigenvectors corresponding to the input variables. (b) PC1-PC2 classification plot resulting from a K-medoids analysis run on the PCs scores. The two clusters almost correspond to DSGSD and LL distribution, confirming the distinction between the two groups. (c) PC1-PC3 biplot resulting from the PCA (d) PC1-PC3 classification graph resulting from the K-medoids cluster analysis on the PCs scores. The distinction between DSGSDs and LL is evident in both the plots.*

In this analysis, we select the first 6 principal components (PCs), accounting for about 70% of the entire multivariate space variance, and focus on the relationships between the first three principal components (PC1, PC2 and PC3 Figure 4.9), that explain about 49% of the variance.
PC1 and PC2 loadings (Figure 4.9 a) are mainly related to morphometric and morpho-structural variables. The strongest control on PC1 is exerted by the density of immature nested landslides (NB) and deformed nested landslides (DB), which distribution is complementary as suggested by their opposite direction along PC1. PC2 is mainly related to the hypsometric integral (Hi), the relief energy ($\Delta$h) and the density of morphostructures (DM). PC3 (Figure 4.9 b) accounts for InSAR-derived parameters such as modal LOS velocity (v_PM), quartile deviation (Q_dev) and kinematics statistics ($\Delta$_SK, $\Delta$_M), providing a figure of the style of activity.
The PC1/PC2 biplot (Figure 4.9 a) shows a clear trend along PC1, corresponding to different distributions of cases pre-classified as "DSGSD" and "large landslide" in the inventory. The distinction between the two classes is dominated by their morphological features, such as a different L/W (i.e. more elongated shape for large landslides), and the abundance of deformed nested bodies (DB) in large landslides with respect to DSGSDs, the latter hosting abundant immature nested bodies (NB). The same distinction between DSGSD and large landslide groups is evident in the PC1/PC3 plot (Figure 4.9 b). We checked the statistical consistency of the inventory pre-classification into these 2 classes by performing a K-medoids cluster analysis on the first 3 PCs (Figure 4.9 c,d), repeating the analysis 20 times to improve the robustness of the classification. The resulting two clusters displayed in PC1/PC2 (Figure 4.9 c) and PC1/PC3 (Figure 4.9 d) plots are in very good agreement with inventory-based classification into large landslides and DSGSDs.

#### 4.2.2.2 MV2: all DSGSD and large landslides, morphometric and morpho-structural variables

The second bulk-dataset PCA, considering only morphometric and morpho-structural variables, allows characterizing all the 208 landslides with respect to the first 3 PCs, that account for the 67% of the multivariate space variance.
Most morphometric variables (CB, NB, LS, $\Delta$h, A/2p, DM) are related to PC1 and PC2 (Figure 4.10 a), while elongation ratio (L/W) and hypsometry (Hi) mainly influence PC3 (Figure 4.10 b)

A cluster analysis with PC1, PC2 and PC3 as input variables and a 3-cluster partition of the dataset defines three main groups, namely: gm1, gm2 and gm3. The first cluster (gm1, Figure 4.10 c,d) includes landslides with high density of deformed nested bodies (DB) and well-developed scarp areas (LS), testifying significant accumulated deformation. The cluster gm2 (Figure 4.10 c,d) includes both large landslides and DSGSD with high values of elongation ratio L/W and affecting a relatively immature topography (high Hi). The third cluster (gm3) mainly includes DSGSDs affecting entire high-relief slopes and characterized by high density of immature nested bodies (NB). These clusters are mainly classified according to PC1, as their boundaries are almost parallel to PC3 axis in the PC1-PC3 plot (Figure 4.10 c,d).

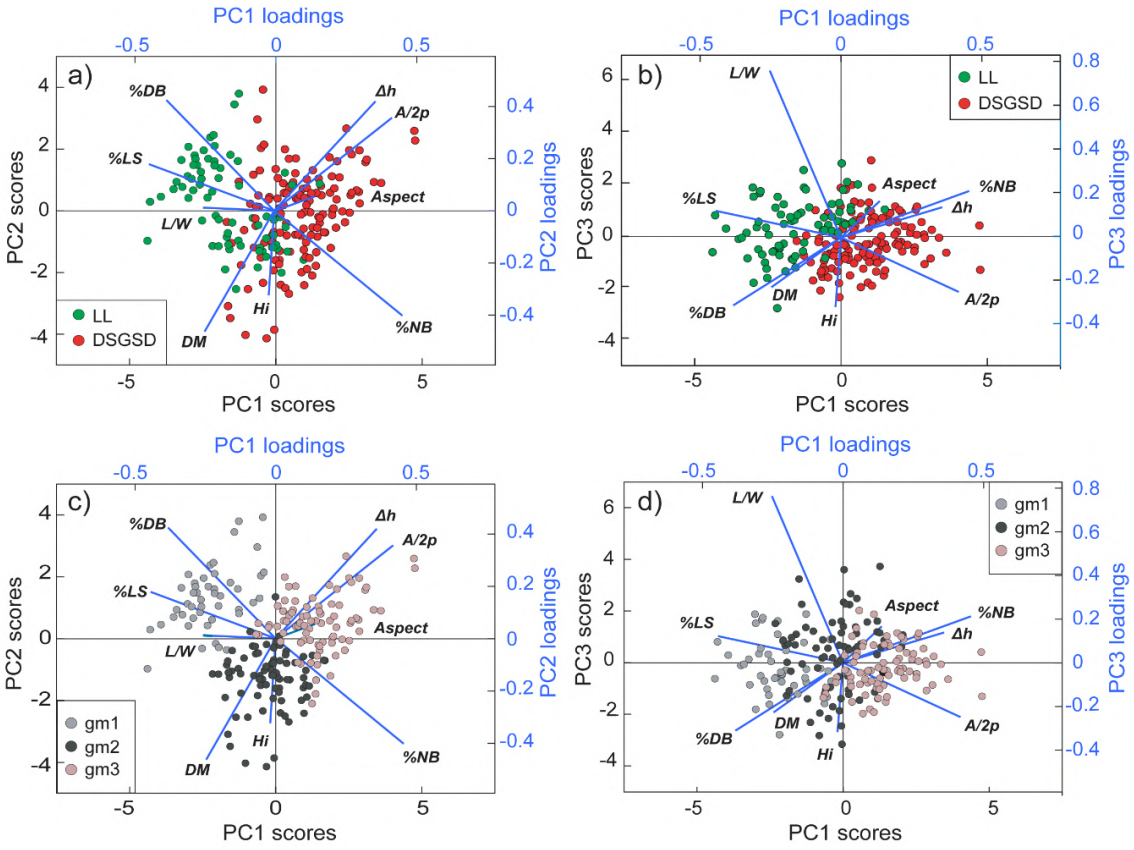


*Figure 4.10: MV2 :PCA and cluster analysis on the entire bulk dataset (208 elements) considering 5 morphometric and 4 morpho-structural variables. (a) and (b) are the PC1-PC2 and PC1-PC3 biplots deriving from a PCA on the whole dataset considering only morphometric and morpho-structural variables. A distinction between inventory based DSGSDs and LL is still evident. (c) and (d) are the result of a 3 clusters K-medoids analysis on the PCs scores. gm1, gm2 and gm3 are the resulting groups and all the 208 mapped slow rock slope deformations can be classified in one of them.*

#### 4.2.2.3 MV3: DSGSD covered by InSAR data, all variables

This PCA allows establishing links between morphometric, morpho-structural and activity characteristics in DSGSD areas covered by Sentinel InSAR data. These are characterized by fairly high areal PS and pseudo-PS (Figure 4.11, mean density 43 PS/Km$^2$), with a maximum of 259/Km$^2$ in a single DSGSD. We analyse PCA results considering the first three PCs, that account for 50.2% of variance.

Again, PC1 and PC2 are related to morpho-structural and morphometric information (Figure 4.12 a). When cases are classified according to their kinematics, the PC1/PC2 plot (Figure 4.12 b) shows a clear trend from the left to the right hand, corresponding to a shift from translational to roto-translational and rotational mechanisms, in agreement with the orientation of Δ skewness (Δ_SK) and Δ median (Δ_M) eigenvectors. A trend in the PC space can be also found by classifying cases by their modal velocity, respectful of segmentation effects and ranging from -2 mm/yr to -21mm/yr towards the upper left of the PC1/PC2 plot (Figure 4.12 c). In general, translational DSGSDs move faster than rotational and roto-translational ones.

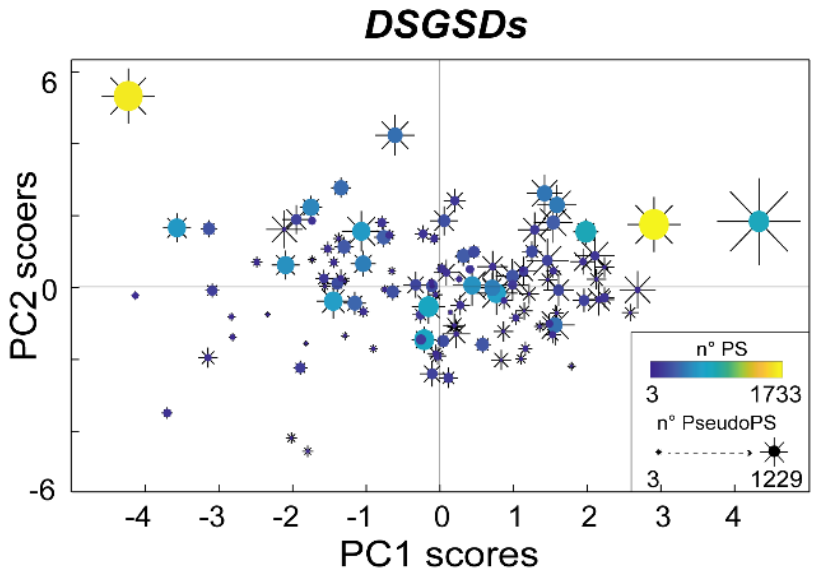


*Figure 4.11: PS and Pseudo-PS density in the DSGSDs. Symbols dimensions and colours report the number of points in each DSGSD.*

These relationships are outlined in a five-class K-medoids classification, based on PCs as input variables in which the resulting groups (gc1 to gc5) have consistent morphometric and morpho-structural characteristics and represent different styles of activity, illustrated by the arrows in Figure 4.12 d, which are oriented as the corresponding variables eigenvectors. Cluster gc1 includes the fastest landslides, characterized by translational kinematics and hosting deformed nested bodies undergoing differential evolution. Clusters gc2 and gc3 include slower landslides, significantly segmented but with different kinematics (gc2 mainly translational, gc3 mainly rotational) and internal deformation (gc2 characterized by distributed damage, gc3 hosting deformed nested sectors). Finally, clusters gc4 and gc5

include slow-moving landslides with mainly roto-translational to rotational kinematics, limited internal damage and immature nested bodies.

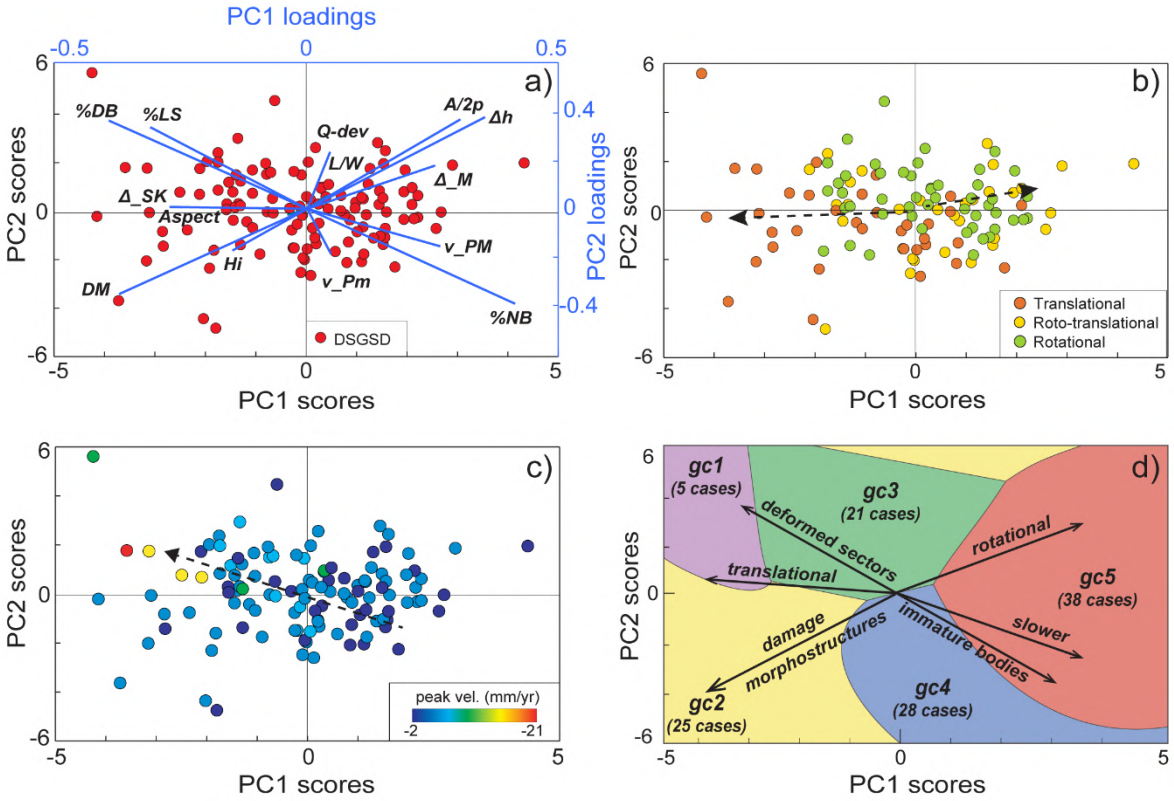


*Figure 4.12: MV3: combined PCA and cluster analysis for DSGSD covered by InSAR data (117 cases), (a) PC1-PC2 biplot resulting from a PCA on morphometric, morpho-structural and InSAR-derived variables. (b) kinematics distribution in the PC1-PC2 plot showing a trend from rotational to translational style from the right to the left side. (c) velocity distribution in the PC1-PC2 plot outlining an increasing velocity trend from the bottom right corner to the upper left one. (d) classification graph in which the coloured fields correspond to the groups identified by a 5 cluster K-medoids analysis on the PCs scores. Boundaries between groups are set according to quadratic discriminant analysis surfaces. Arrows cosrrespond to the direction of representative eigenvectors.*

#### 4.2.2.4 MV4: large landslides covered by InSAR data, all variables

The same procedure used in MV3 allows classifying large landslides. These usually affect densely vegetated middle-lower slope sectors, therefore, the areal density of PS and pseudo-PS in these areas is quite low (Figure 4.13; 35 PS/ $Km^2$ on average), with a maximum of 163 PS/$Km^2$ in a single landslide. PCA interpretation is based on the first three PCs accounting for the 47.2% of variance (Figure 4.14 a).

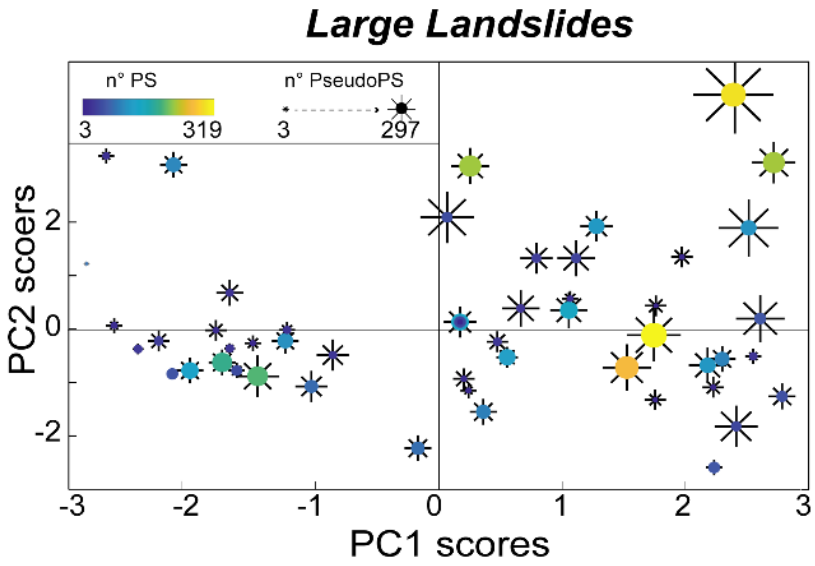


*Figure 4.13: PS and DS density in Large Landslides. Symbols dimensions and colours report the number of points in each DSGSD.*

The PC1-PC2 plot shows a weak trend with respect to landslide kinematics, with a dominantly translational behaviour on the left and a mainly rotational/roto-translational one to the right (Figure 4.14 b). Similar distribution is found for other variables suche as the densities of immature nested bodies (NB) and deformed nested bodies (DB), mainly related to PC1. Activity-related variables, like velocity quartile deviation (Q_dev) and modal LOS velocity (v_PM) are oriented almost perpendicular to PC1 (Figure 4.14 a) without any clear velocity trend (Figure 4.14 c). Because of the small number of input variables, K-medoids cluster classification only considers two groups, in order to avoid over splitting the sparse dataset. The two groups (Figure 4.14 d) are mainly discriminated by PC1 values, and strongly influenced by density of immature nested bodies (NB) and deformed nested bodies (DB).

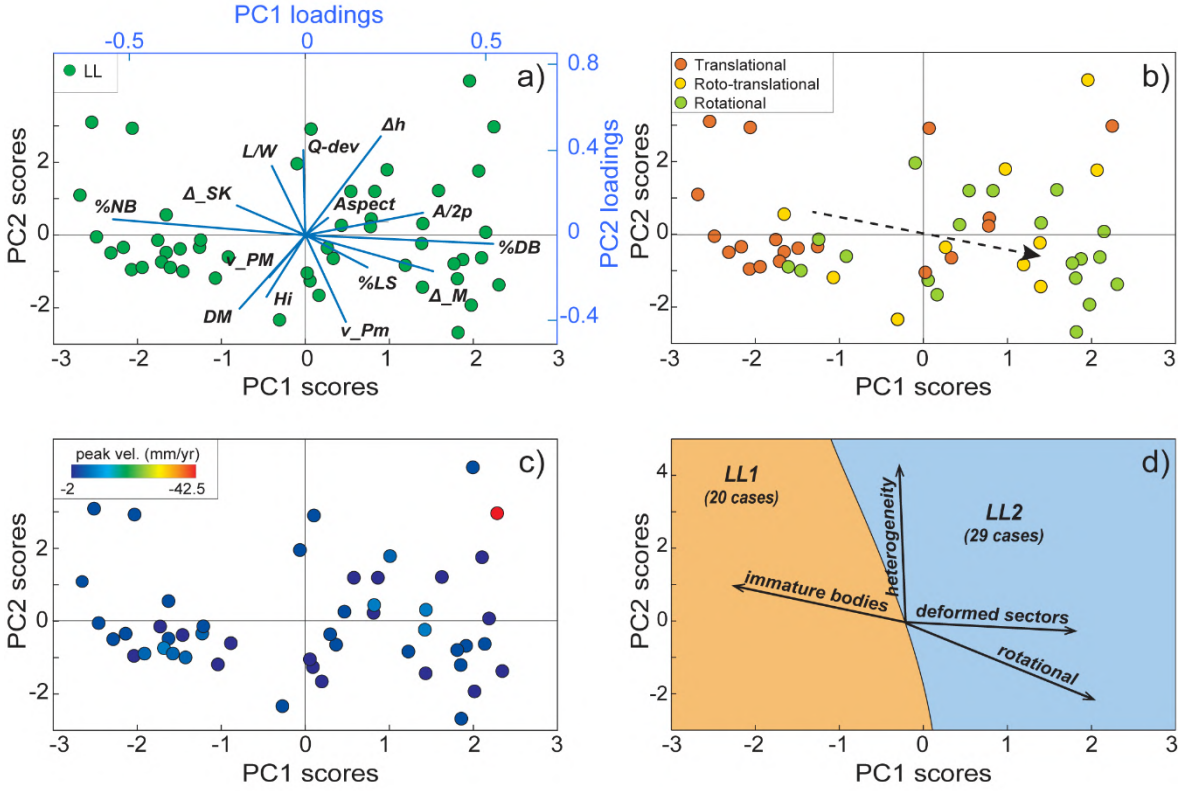


*Figure 4.14: MV4: combined PCA and cluster analysis for Large Landslides (LL) covered by InSAR data (49 cases). (a) PC1-PC2 biplot resulting from a PCA on morphometric, morpho-structural and InSAR-derived variables. (b) kinematics distribution in the PC1-PC2 plot showing a trend from rotational to translational style from the left to the right side. (c) Velocity distribution in the PC1-PC2 plot outlining an almost homogeneous velocity range with only an extreme value reaching -40mm/yr. (d) classification graph. Boundaries between groups are set according to quadratic discriminant analysis surfaces. Arrows cosrrespond to the direction of representative eigenvectors.*

#### 4.2.2.5 MV5: DSGSD and large landslides lacking InSAR data, proximity analysis

Since 42 out of 208 rock-slope deformation lack significant InSAR data coverage, they are not classified in the MV3 and MV4 analyses but only in MV2, based on morphometric and morpho-structural variables only.

A two-step proximity analysis is then performed to obtain a complete classification of all the mapped landslides. First, all the mapped landslides were classified in the three main groups extracted from MV2 (gm1, gm2, gm3; Figure 4.10) and displayed in a PC1-PC2 plot. Then, all landslides with InSAR data belonging to the different gm groups were further reclassified in terms of the style of activity classes resulting from MV3 and MV4 (Figure 4.12, Figure 4.14). Eventually, the 42 SAR-blind cases were reclassified through a proximity analysis considering the surrounding points (minimum Euclidean distance) and their class signature (Figure 4.15).

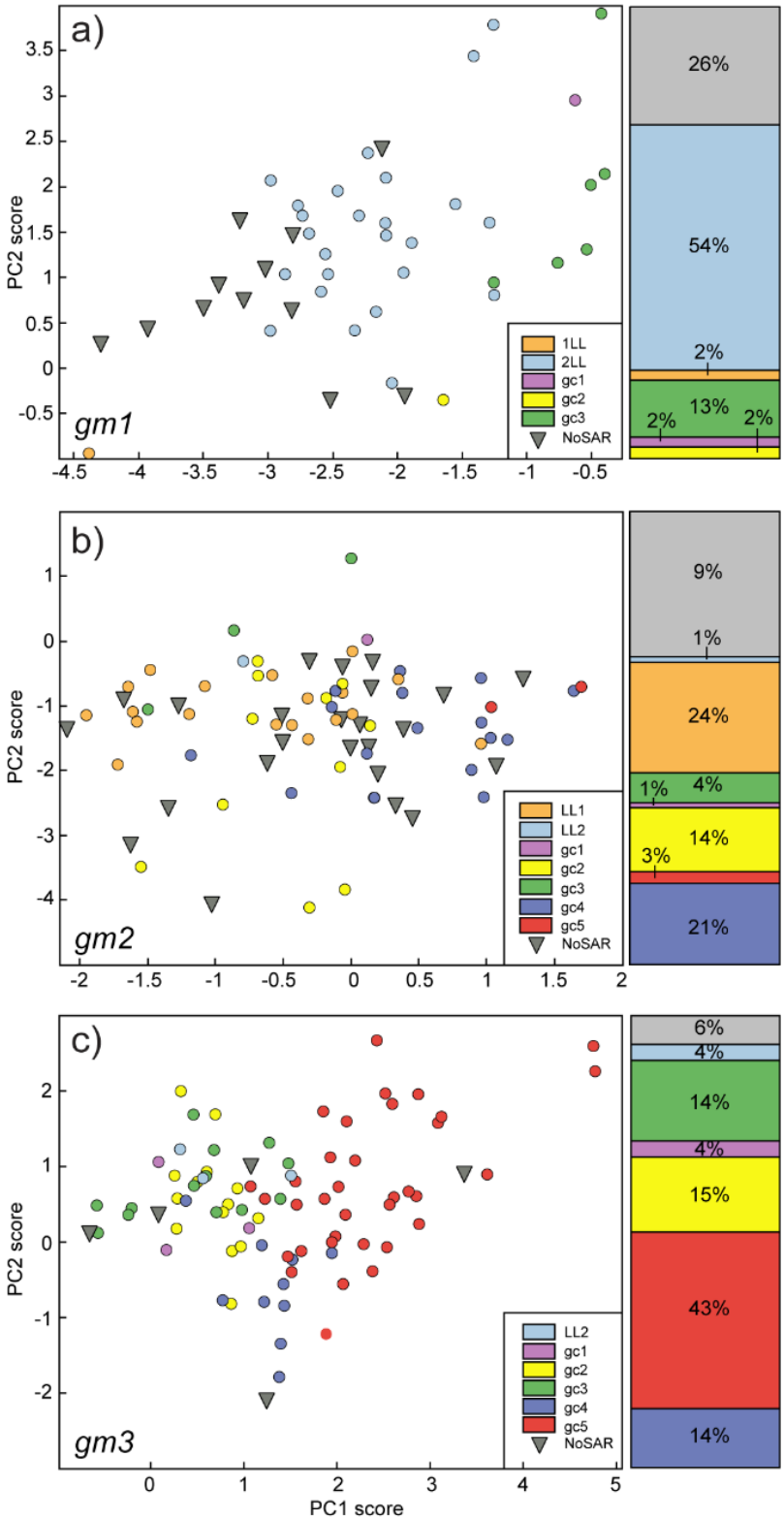


*Figure 4.15: MV5: proximity analysis on DSGSDs and large landslides not covered by InSAR data (42 cases). according to similarity criteria (Euclidean distance) with the other style of activity classes. (a) shows the distribution of SAR blind elements in gm1, (b) the distribution in gm2 and (c) the distribution in gm3. The stacked column indicates the percentage of each group inside gm1, gm2 and gm3.*

## 4.3 Final style of activity classification of slow rock slope deformations

A practical evaluation of the style of activity of slow rock-slope deformation for land planning, hazard assessment and engineering purposes must account for a suite of kinematic, morphometric and morpho-structural descriptors. Our multivariate statistical analysis is able to subdivide the studied inventory sample into 7 classes with fairly homogeneous styles of activity, even including cases for which InSAR data are unavailable to describe the present-day patterns of movement.

First, our results (MV1) outline clear differences between DSGSD and large landslide phenomena according to the considered variables. This is not obvious, because the distinction between these two classes of slope instability is debated and usually only relies on morphometric and morpho-structural criteria, including the affected relief and slope sectors, morpho-structural expression, and total accumulated strain (Crosta et al., 2013). On the other hand, the very similar magnitude-frequency scaling of hundreds of DSGSD and large landslides suggests that the two classes of phenomena belong to a continuous spectrum of slow rock slope deformations, where the diagnostic features used for their distinction are constrained by size (Agliardi et al., 2012). Interestingly, multivariate statistical analysis results in a sharp distinction in two groups, well-fitting the pre-classification into DSGSDs and large landslides (Figure 4.9) and mainly controlled by morphological features. More elongated shapes and high density of deformed nested bodies, testifying higher accumulated internal deformation, characterize large landslides with respect to DSGSDs (Figure 4.10). This suggests that DSGSDs and large landslides undergo different mechanisms and/or evolutionary stages and should be treated separately.

Multivariate statistical analyses, performed on DSGSD and large landslides separately (MV3 and MV4) and expanded through a similarity analysis to include SAR-blind landslides (MV5), led to the classification of the landslide inventory into seven style-of-activity classes, five for DSGSDs and two for large landslides. The distributions of the different variables in each group (Figure 4.16) demonstrate the impossibility to use single variables as reliable indicators of the style of activity of slow rock slope deformations.

Furthermore, the concept of "inactive" landslides implies a capability to correctly measure displacements at all sites, not guaranteed by InSAR techniques due to: a) the inability of radar sensors to illuminate unfavourably oriented slopes; b) the lack of coherence of interferograms in densely vegetated or debris covered slopes. Since we cannot be sure that SAR-blind landslides are not moving, to avoid underestimation of the related risks we dropped the concept of "inactive landslides" and classified all the cases in the seven style of activity classes.

Our classification (Table 10) provides an accurate mapping (Figure 4.17) of slow rock slope deformations with consistent style of activity. This is useful to identify critical phenomena to prioritize site-specific analyses, and to analyze the damage potential of slow rock slope deformations on specific classes of elements at risk, depending on the most important interaction factors (e.g. rate, volume, heterogeneity).

The class gc1 includes the fastest DSGSDs (5, all covered by InSAR data; Figure 4.16), typically affecting high relief slopes (>1200m) and characterized by dominant translational kinematics.

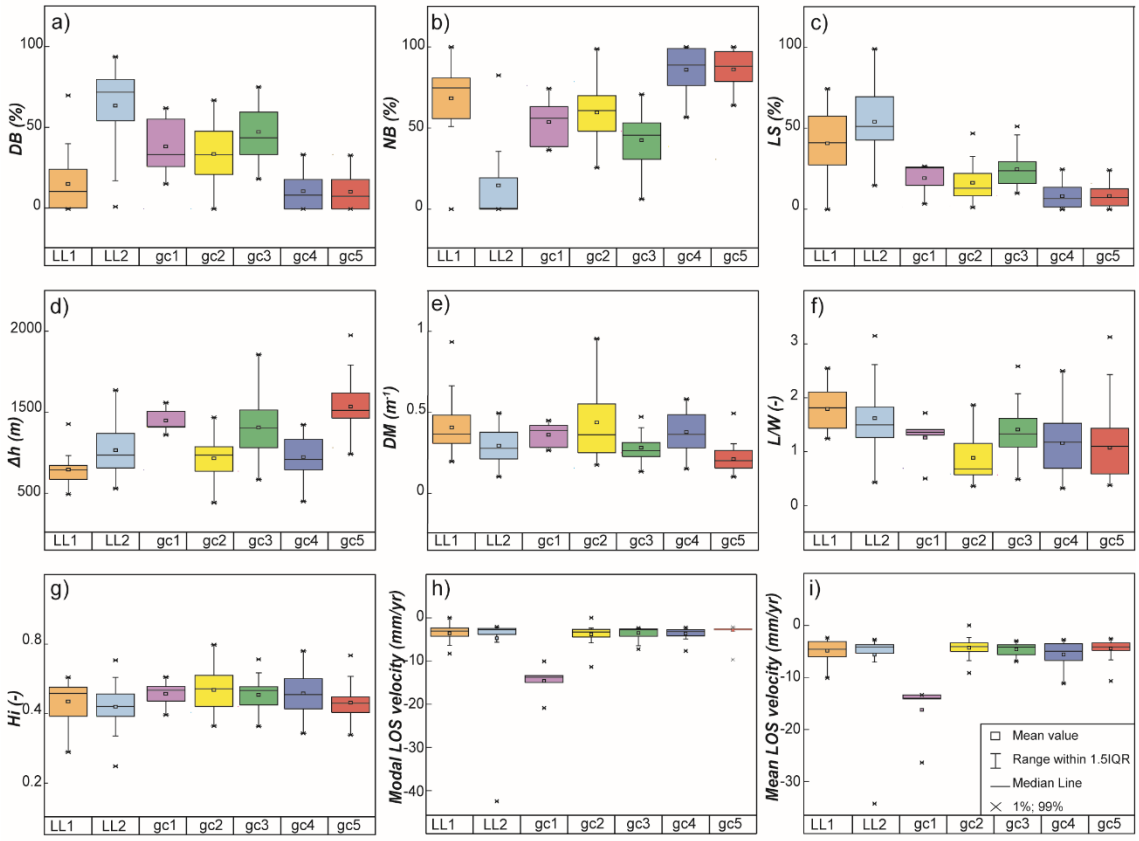


*Figure 4.16: Boxplots of the morphometric, morpho-structural and activity variables for each landslide group. (a) deformed nested landslide density (b) immature nested landslide density (c) landslide scarp sector density (d) relief (e) density of morpfostructures (f) shape factor (g) hypsometrical integral (h) modal LOS velocity (i) mean LOS velocity. Whisker lengths: upper and lower inner fences based on interquartile range (IQR)*

These DSGSDs evolve at modal rates up to 15-20 mm/yr and host deformed nested bodies that undergo faster differential evolution at displacement rates exceeding 25 mm/yr (Figure 4.16). This class includes the most active DSGSDs in Lombardia (i.e Corna Rossa, Agliardi et al. 2018, 2019; Saline, Agliardi et al. 2001; Mt. Mater, Crippa et al. 2020; respectively 11,10 and 3 Figure 4.17), that pose major risk to infrastructures (roadways, hydroelectric facilities and lifelines). These are the most important candidates for site-specific studies to quantify their potential for slow-to-fast evolution and catastrophic failure (Agliardi et al., 2020; Crosta et al., 2017).

The other classes include far slower landslides (i.e. modal and mean LOS velocities lower than 5-10 mm/yr) that cannot be distinguished in terms of displacement rates (Figure 4.16), but are characterized by different mechanisms and degrees of segmentation, internal damage and accumulated strain (Figure 4.16). Clusters gc2 (32 DSGSD, including 7 SAR-blind cases) and gc3 (21 DSGSD; Figure 4.17) include phenomena affecting middle-high relief

slopes and characterized by significant segmentation, but with different kinematics and internal deformation style. gc2 are dominantly translational and characterized by significant distributed damage (e.g. Bosco del Conte DSGSD; (Agliardi et al., 2009); Fuipiano DSGSD; (Forcella and Rossi 1984); respectively 8, 14 in Figure 4.17), while gc3 are dominantly rotational and segmented into deformed nested sectors (e.g. Masuccio DSGSD, De Finis et al., 2015; 6 in Figure 4.17). Although these DSGSDs are slow, their strong heterogeneity must be considered in practical engineering geological problems including: a) the definition of potential collapse scenarios, i.e. actually evolving nested volumes constrained by segmentation; b) the quantification of rock mass properties for stability modeling, strongly depending on internal damage; c) the prediction of damage to infrastructures, that is significantly complicated by differential displacements in heterogeneous landslide masses. Finally, classes gc4 (38 DSGSD, including 10 SAR-blind cases) and gc5 (40 DSGSD, including 2 SAR-blind cases) include slow-moving DSGSDs characterized by either dominant roto-translational (gc4; e.g. Lake Palù DSGSD (Frattini et al., 2013); 5 in Figure 4.17) or rotational kinematics (gc5; e.g. Albenza DSGSD; (Forcella, 1987) 13 in Figure 4.17). Both classes include phenomena with limited internal damage and segmentation into poorly deformed nested bodies (Figure 4.16).

Style of activity classes defined for large landslides, i.e. LL1 (32 large landslides, including 12 SAR-blind cases) and LL2 (40 large landslides, including 11 SAR-blind cases), differ according to morpho-structural characteristics that witness different geomorphological maturity and accumulated deformation (Figure 4.16). In particular, class LL1 (e.g. Mt. Solena; 9 in Figure 4.17) includes translational landslides affecting slopes with relatively low relief (Figure 4.16), characterized by limited scarp areas and segmented into immature nested masses, suggesting a limited accumulated strain. Instead, class LL2 (e.g. Piz Groppera; 4 in Figure 4.17) mainly includes roto-translational and rotational landslides, affecting high-relief slopes and characterized by large accumulated deformations.

*Table 10: Groups identified and the descriptive parameters of their style of activity: Kin= kinematics; DM= morpho-structural density; DB=density of deformed nested bodies; velocity is computed as the median value of all the PS; heterogeneity is evaluated considering the coefficient of quartile deviation (see section 3.4).*

| **Classes** | | **Kin** | **DM** | **DB** | **Median PS LOS vel (mm/yr)** | **Vel Heterogeneity** |
|---|---|---|---|---|---|---|
| **DSGSD** | **Gc1** | T | High | Medium | 13.5 | High |
| | **Gc2** | T | High | Medium | 4.4. | Low |
| | **Gc3** | R-RT | Medium | High | 3.9 | Low |
| | **Gc4** | T-RT | Medium | Low | 6.1 | High |
| | **Gc5** | R-RT | Low | Low | 3.7 | Medium |
| **Large Landslides** | **LL1** | T | High | Low | 4.5 | Low |
| | **LL2** | R-RT | Medium | High | 4.3 | Medium |

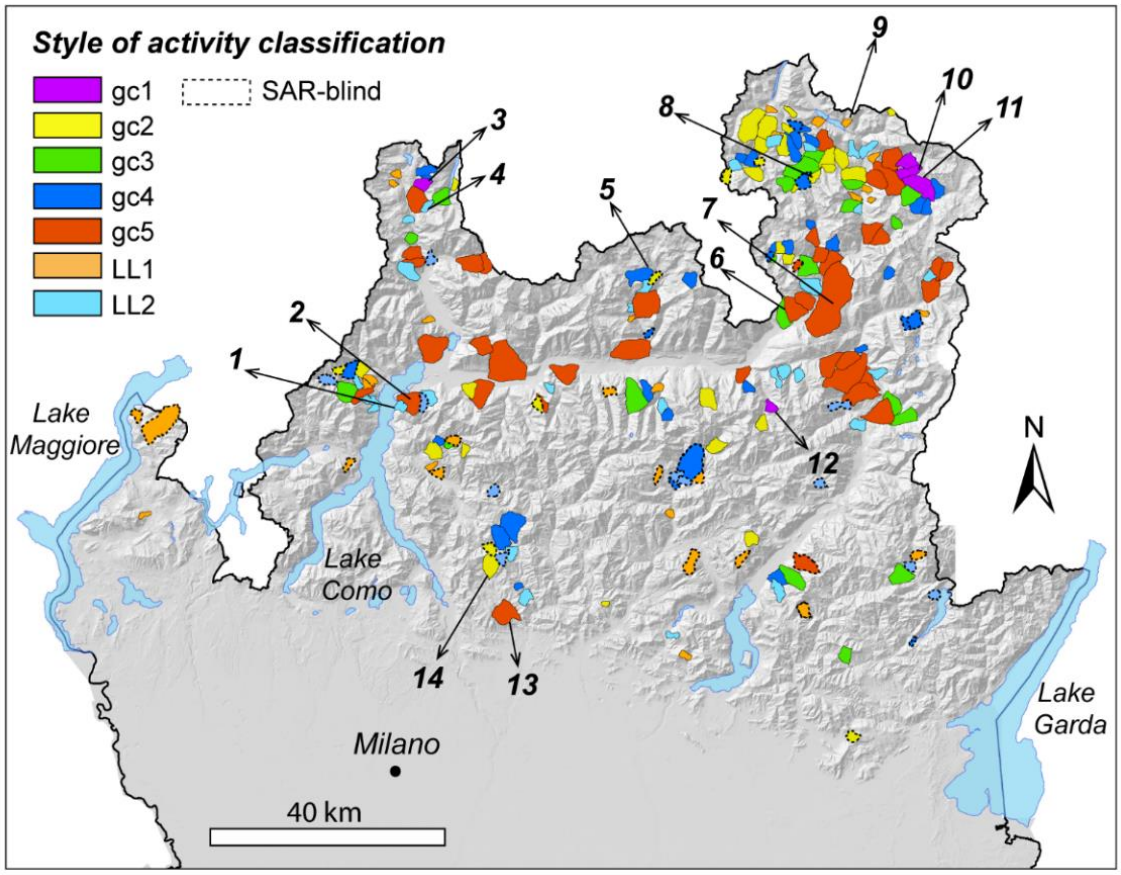


*Figure 4.17: Style of activity classification map of slow rock slope deformations in Lombardia. Mapped cases are classified in the seven group arising from the multivariate statistical analysis. Key to the case studies cited in the text: 1: Mt. Letè (Cancelli, 2017); 2: Mt Legnone DSGSD (Ambrosi and Crosta, 2006); 3: Mt. Mater DSGSD (Crippa et al., 2020); 4: Piz Groppera large landslide; 5: Lake Palù DSGSD (Frattini et al.2013); 6: Mt. Masuccio DSGSD (De Finis et al., 2015) 7: Padrio-Varadega DSGSD (Ambrosi and Crosta, 2006; Forcella, 1984; Frattini et al., 2013); 8: Bosco del Conte DSGSD (Agliardi et al., 2009); 9: Mt Solena large landslide; 10: Saline DSGSD (Agliardi et al., 2001; Frattini et al, 2018; Agliardi et al., 2018); 11: Corna Rossa DSGSD (Agliardi et al., 2018); 12: Belviso DSGSD; 13: Albenza(F Forcella, 1987); 14: Fuipiano DSGSD (Forcella and Rossi, 1987).*

# 5 Local Scale analysis

A regional-scale analysis is fundamental to achieve a first reconnaissance and characterization of the style of activity of slow rock slope deformations, useful for classification and hazard/risk assessment. Moreover, regional-scale classification is key for prioritization purposes: since a full site-specific characterization of a large number of giant slope deformation is usually practically unfeasible, detailed local-scale analysis must be focused on specific case studies recognized as significant or critical for practical application (i.e. interaction with specific elements at risk, relatively large displacement rates, need to identify scenarios for engineering modeling of potentially critical evolution). Local scale studies should be then targeted to the detailed reconstruction of the landslide mechanism and to highlight internal segmentation and differential evolution of different sectors, as well as heterogeneities and non-linearity of the temporal evolution of the phenomenon, e.g. seasonal or accelerating trends, indicative of advanced stages of progressive failure or hydro-mechanical rockslide differentiation (Riva et al., 2018; Agliardi et al., 2020; Crippa et al., 2020).

Despite the demonstrated effectiveness of PSI data in the regional-scale characterization of slow rock slope deformation activity, their application to local-scale analysis is limited by their point-like nature, hampering a spatially-distributed assessment of the complex and often segmented displacement field of slow rock slope deformations. Moreover, a fine detection of nonlinear or seasonal temporal patterns of very slow-moving landslides with PSI is also conditioned by linear velocity assumptions in the PSI technique (Ferretti, 2014), that introduces strong uncertainties in the characterization of complex temporal dynamics. For a sound local scale analysis, we used a targeted DInSAR approach, integrated with detailed field morpho-structural constraints and, where possible, with ground-based displacement measurements. Starting from raw Sentinel 1 SAR images, we produced *ad hoc* interferograms, aimed at tailoring the temporal baselines on the studied process rates and reducing atmospheric and snow-cover disturbances, in order to enhance the signals representative of very slow rock slope deformations. We applied this analysis approach to three DSGSDs belonging to the group gc1 identified in the regional scale study (section 4.3). These are the Corna Rossa, Mt. Mater, and Saline DSGSD (Figure 4.17). They are the fastest DSGSDs in Lombardia, are characterized by displacement rates up to some cm/yr, but by very different morpho-structural features, mechanisms and potential in a risk perspective. In particular:

- the Corna Rossa slope (Valfurva, central Italian Alps; Agliardi et al., 2019) is affected by an outstanding example of structurally controlled DSGSD, characterized by a very

segmented style of gravitational deformation, with strain partitioning in different sectors and along individual persistent fractures. Despite the huge involved mass and the significant displacement rates, this DSGSD has not been investigated or monitored in detail so far;

- Mt. Mater (Valle Spluga, central Italian Alps; Crippa et al., 2020) is affected by a DSGSD showing evidence of an evolutive trend of the entire slope, yet characterized by a strongly heterogeneous activity. Since this slope instability directly impends over the village and ski resort of Madesimo, since 2011 it has been a subject of investigation and monitoring activities by ARPA Lombardia (the Environmental Protection Agency of Regione Lombardia). However, the detailed mechanisms and style of activity of the DSGSD are still elusive;
- the Saline Ridge (Valfurva, central Italian Alps; Agliardi et al., 2001) is affected by a previously well-known DSGSD, that in its middle-lower sector hosts the active Ruinon rockslide, one of the most active landslides in Lombardia (Crosta et al., 2017). Although the Ruinon rockslide has been extensively monitored and modelled for Early Warning purposes since 1997, the style of activity of the DSGSD, its links with the Ruinon rockslide and evolutionary potential are still unknown.

## 5.1 Mechanisms and segmentation: Corna Rossa DSGSD

### 5.1.1 Geological and structural framework

The studied area is located on the right flank of the middle Valfurva (Upper Valtellina, Italian Central Alps), on the SW flank of Mt. Confinale; the highest peak of Valfurva at 3300 m.a.s.l.. The slope is located few kilometers south of the Zebrù Line, a steep north dipping fault separating the Campo Nappe from the overlying Ortler Nappe (Agliardi et al., 2001). Here the metamorphic rocks of the of the Campo Nappe (Austroalpine crystalline basement), crop out and extend between the Engadine Line to the W and the Pejo Line to the E (Agliardi et al., 2001). The slope was carved by fluvial and glacial erosion in pre-Permian metamorphics of the Bormio phyllite unite, including dominant phyllites and micashists. These consist of an aggregate of quartz + chlorite + sericite, with minor amounts of biotite, garnet and ilmenite, and record a polyphase tectono-metamorphic evolution during the Varisican and Alpine orogenesis (Figure 5.1.1 a; Conti et al., 1997; Florineth and Froitzheim, 1994; Gregnanin and Valle, 1995; Agliardi et al., 2001). A green schist facies retrogression overprints the whole tectono-metamorphic unit.

Minor pre-Permian and late alpine intrusive rocks, both acidic and basic, also occur in the phyllites, together with thick lenses of impure marbles, made of saccharoidal calcite or of calc-silicate with calcite + chlorite +white mica. Major marble outcrops show evidence of diffuse karst processes, favoring the formation of sinkholes along persistent fractures.

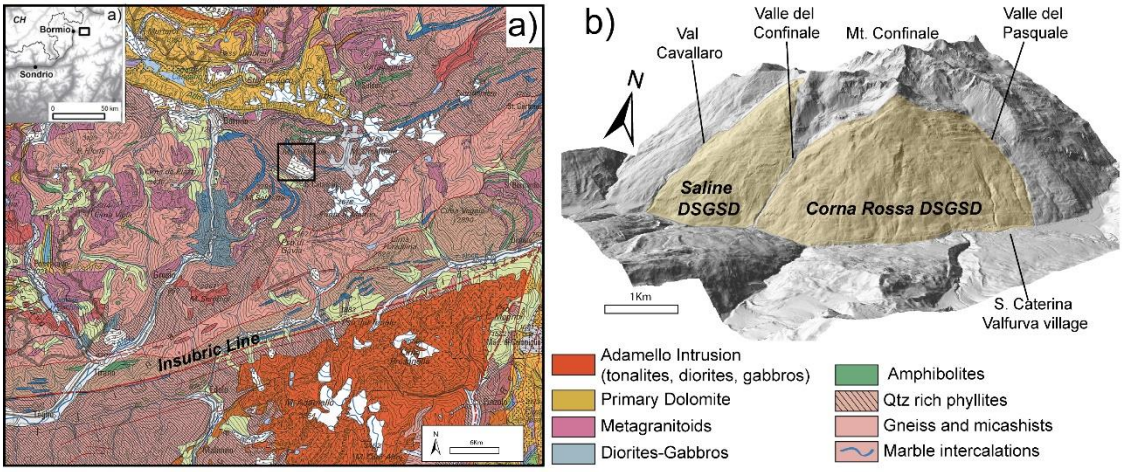


*Figure 5.1.1 :a) geological setting of Upper Valtellina (Geologische Karte der Schweiz 1:500000) b) DEM of Corna Rossa DSGSD (1m resolution).*

From the Variscan orogenesis on, four main deformational events affected this area. D1 phase produced S1 foliation, isoclinally folded and transposed by a successive Variscan D2 deformation phase (Gregnanin and Valle, 1995; Agliardi et al., 2001). The resulting S1+2 foliation has been deformed and crenulated by the alpine D3 deformation, resulting in polyharmonic asymmetrical and non-cylindrical F3 folds characterized by an axial plane moderately dipping to N-NE and with sub-horizontal NW±SE striking hinges (Agliardi et al., 2001).

Since Late Oligocene, brittle tectonic deformation stages affected the area, resulting in the development of different fracture systems recognizable from outcrop to regional scale (Figure 5.1.2). A swarm of WNW-ESE tectonic lineaments is aligned along Valfurva axis and is organized as dextral *en echelon* master fractures that terminate and partially overlap at the Corna Rossa Ridge (Figure 5.1.2 a).

The main master fracture starts in correspondence of Gembresca landslide, it bounds the upper sector of Ruinon rockslide and reaches the upper headscarp of Corna Rossa DSGSD delimiting its western border (Figure 5.1.2 UF). In the upper slope portion this master fracture is segmented and accommodates the movement of the DSGSD itself. A second branch of the master facture (Figure 5.1.2 LF) starts on the eastern sector at about 2400 m.a.s.l exending towards WSW and partially overlap with the UF segment through a complex series of gravitational shear and extensional zones up to 450 m deep.

Analysis of aerial photos (T.E.M.-Regione Lombardia, 1981, 1:20000 scale) and field surveys revealed the presence of several types of landform, suggesting a complex evolution of the area from the late Pleistocene on, especially as result of glacial and periglacial processes, gravitational deformation and surface erosion. All these processes acted together, imprinting the landscape during the Last Glacial Maximum and Lateglacial re-advances (Forcella and Orombelli, 1984).

Glacial deposits like outwash till and morains (Forcella and Orombelli, 1984) as well as permafrost-related landforms such as rock glaciers, protalus rampart and solifluction lobes are widespread on the slope testifying that the study area was affected by an intense glacial and postglacial evolution and that periglacial conditions persisted on the area after the deglaciation. Several moraines have been mapped from valley to the upper part of the slope. Best preserved forms are found between 2300 and 2700 m.a.s.l. and are ascribable, according to previous studies (Ivy-Ochs et al., 2008; Scotti et al., 2017) to Egesen stadials. Some of them are cut by morphostructures and set constraints on the activity of DSGSD relative to the deposition of glacial features.

Tongue shaped rock glaciers develop between 2300 and 3000 m a.s.l. extending downslope from talus cones. They are characterized by relict frontal lobes with no evidence of ice content. In the upper part of the slope striated surfaces and roches moutonée are still recognizable and well preserved.

The slope has high relief energy, ranging in elevation between 1700 and about 3300 m.a.s.l., with a maximum elevation difference of 1600 m and it is almost entirely affected by an active DSGSD system hosting Saline DSGSD (Agliardi et al., 2001) bounded by the Cavallaro and the Confinale valleys, and Corna Rossa DSGSD, bounded by the Confinale and the Pasquale valleys (Figure 5.1.1).

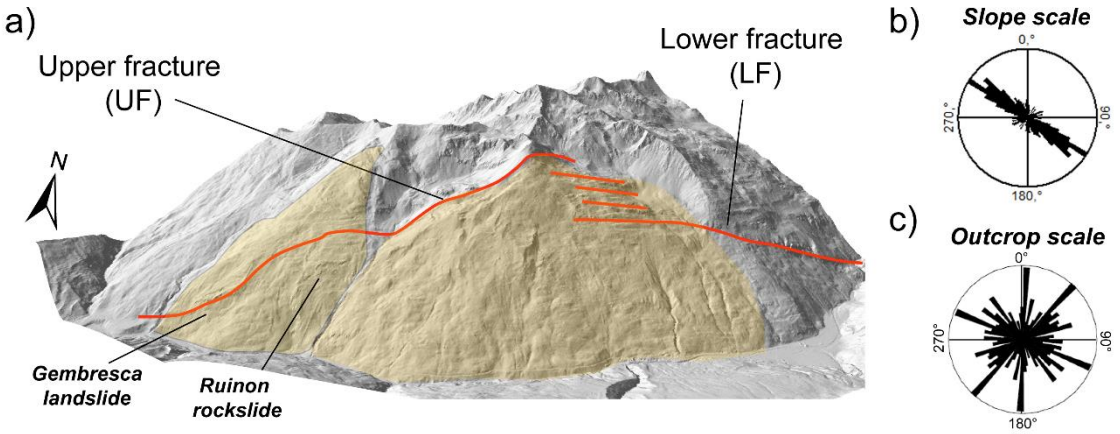


*Figure 5.1.2.: Main structural features on Corna Rossa slope. a) Master fracture cutting Mt. Confinal slope and bounding Corna Rossa DSGSD b) orientation of slope scale lineaments c) orientation of outcrop scale fractures.*

The stereoscopic analysis of T.E.M. aerial photos (Regione Lombardia T.E.M. series, 1981-83scale 1:20000) and LiDAR (1m resolution Figure 5.1.2 a) data allowed a first interpretation of DSGSD morphostructures that were classified as trenches, counterscarps and scarps (Figure 5.1.3). Detailed field surveys were also conducted to map in higher detailed the single morphostructures and clarify their structural associations.

At the mesoscale N-S, E-W, NNE-SSW and NNW-SSE lineaments control rock mass properties (Gatto and Scolari, 1974; Forcella et al., 1982; Agliardi et al., 2001). Close to this sheaf of lineaments, the uppermost ridge is split and lowered towards the Valley.

All these lineaments interplay in setting the limits and controlling the evolution of Corna Rossa DSGSD. Inherited non-persistent fractures, outline the occurrence a "gravitational transfer zone" within the DSGSD (Figure 5.1.2, Figure 5.1.3) which accommodates gravitational strain by dominant extension in the interaction zone between partially overlapping gravitational "faults" (dominant slip). This affects the mechanism, amount and rate of gravitational deformation in different slope sectors, with significant geohazard implications.

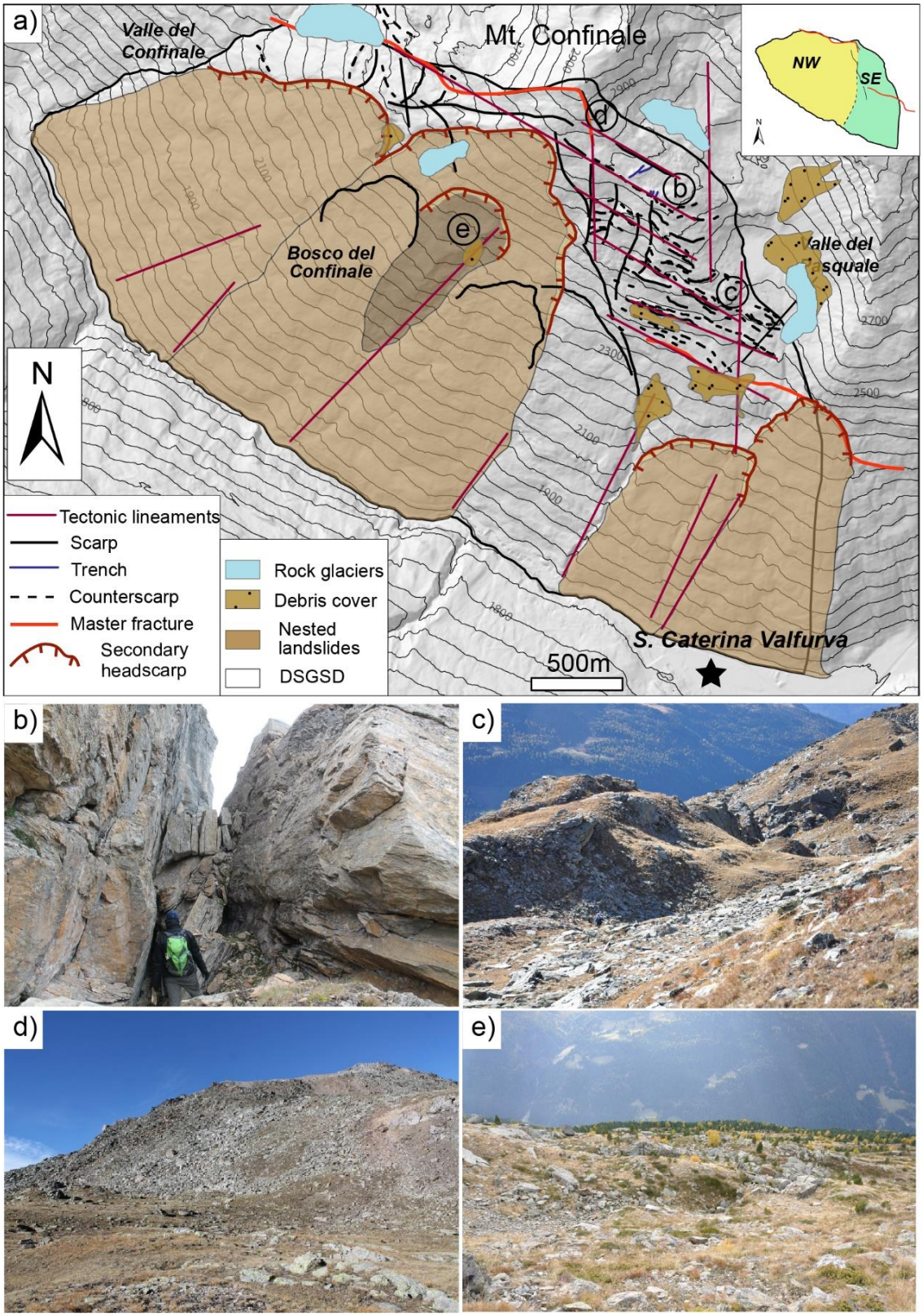


*Figure 5.1.3: Main features of Corna Rossa DSGSD. (**a**) Simplified map portraying the main morpho-structural features associated with DSGSD and nested large landslides. (**b**) trenches (**c**) Graben system affecting the SE slope sector (**d**) headscarp; (**e**) blocky expression of a nested landslide in the midslope sector.*

According to the structural features distribution, two main sectors (insert Figure 5.1.3 a) can be recognized: a western (NW) and eastern (SE) one, characterized by different superficial expressions that reflect a change in the deep kinematic behavior.

NW sector:

The uppermost part of the NW sector (insert in Figure 5.1.3 a) above 2500m.a.s.l has a strong structural control due to the presence of a swarm of WNW-ESE persistent scarps on which the main DSGSD headscarp is imposed. This latter extends for more than 2 km from Confinale valley towards east and it is characterized by a double crested ridge with vertical downthrow of about 50m.
Going downslope the ridge becomes less evident and a series of trenches and scarps cut the slope as WNW-ENE sub-vertical fractures, often filled with debris. Under 2200 m.a.s.l. a more and more thick vegetation cover (Bosco del Confinale) hides the morphostructures that locally still outcrop in a sporadic way.
Nested large rockslides, reaching up to the top, affect the entire slope sector, that is characterized by prevalent sliding mechanisms testified by scarps, extending up to the crest and as reported by kinematic profile in Figure 3.14 from which a compound behaviour is extracted.

SE sector:

From 2800 to 2200 m.a.s.l. this sector is dominated by gravitational spreading accommodated by a 200 m wide graben and hybrid semi-graben systems.
Going downslope from the uppermost main graben, an almost continuous system of synthetic and antithetic scarps and counterscarps trending WNW-ESE extends till 2450m. The highest counterscarps are characterized by bare rock outcrops and evident dip slip movement with vertical displacement reaching 3-4m. DSGSD counterscarps form continuous structures transecting the slope along WE-SE direction, and they are only locally interrupted by transversal trenches trending N-S and open down to several meters' depth. The outcropping basement in this sector appears crumbled and supplies coarse material that fill the depressions.
Structures progressively change towards valley from grabens and half-grabens to less evident and grassy scarps with small vertical displacement (~1m).

The transition between these two sectors is marked by the abrupt closing of the NW sector main scarp in correspondence of the graben system and by persistent scarps which are oriented towards NNW-SSE. These latter dismantle the external morphostructures of the graben system above 2500 m.a.s.l. dragging and reorienting the scarps and counterscarps towards the central sliding portion. CRE datings (Agliardi et al., 2019) on scarps and counterscarps in the two different sectors confirmed their progressive activation and eventual locking, shedding light on the role of different morphostructures in the activation of inner slope sectors.

Sampled counterscarps in this sector reveal an active deformation from the Lateglacialt which stopped in the Early Holocene. This sector is now only locally active with very low rate (~3-3.5mm/yr) (Agliardi et al., 2019).
The sliding sector on the contrary results active since Lateglacial and it is still undergoing rapid evolution with displacement reaching tens of mm/yr. CRE dating on the main headscarp in fact reveals a much younger age compared to the other structures (Agliardi et al., 2019).

### 5.1.2 Present day activity: targeted DInSAR processing

To capture the present-day mechanisms and activity of the DSGSD, we performed SAR Differential Interferometry (DInSAR) processing of over 100 Sentinel-1 descending radar images (track = 168; orbit azimuth $\delta = 8.99°$; mean LOS angle $\vartheta = 41.78°$).
Corna Rossa has mean slope ~28° and aspect orientation towards SW (Figure 5.1.4 a,b). This orientation is better caught by the descending LOS geometry of Sentinel 1 pass that senses the slope with medium high accuracy as reported by values of R index (Eq. 8, Figure 5.1.4 c) that remains almost equal over the entire slope. Therefore, despite the inevitable underestimation of the displacement vector on LOS direction, the percentage of sensed movement remains almost constant in each slope sector.

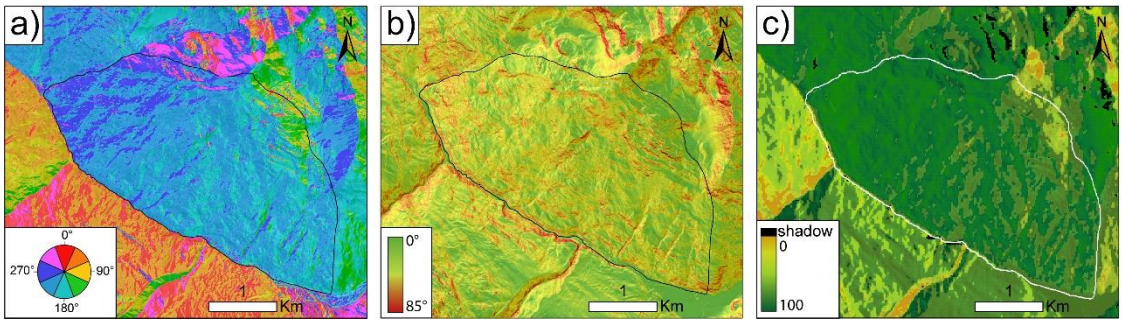


*Figure 5.1.4: Corna Rossa slope morphometry and S1 sensing detection. A) northerness b) slope c) R index.*

SqueeSAR data (Sentinel-1 descending, Figure 5.1.5) outline how the DSGSD is nowadays very active with displacement rates up to 48 mm/yr for the sliding sector and much lower velocities in the spreading one. However, despite the dense point distribution, a clear map of the internal segmentation and transition between the two sectors is still missing. To unravel the relations between them and extract a spatial distributed map of the ongoing displacement associated to the nested landslides inside the sliding one a DInSAR targeted approach should be preferred.

Starting from descending Sentinel-1 image pairs we thus computed multiple differential interferograms considering different temporal baselines, from the shortest available for Sentinel mission (6 days) to longer ones (seasonal, 1 year) to increase the DInSAR detection potential in the slowest sectors, as well as to mitigate the effects of snow cover (Figure 5.1.6 a) in winter periods and atmospheric artefacts (Figure 5.1.6 b). Heterogeneous surface displacements, high topographic elevations and gradients, vegetation, and snow cover during winter periods, act on the intrinsic limitations of SAR signal and affect the quality of DInSAR analysis. This may strongly limit the capability to retrieve accurate information on the spatial and temporal evolution of the DSGSD.

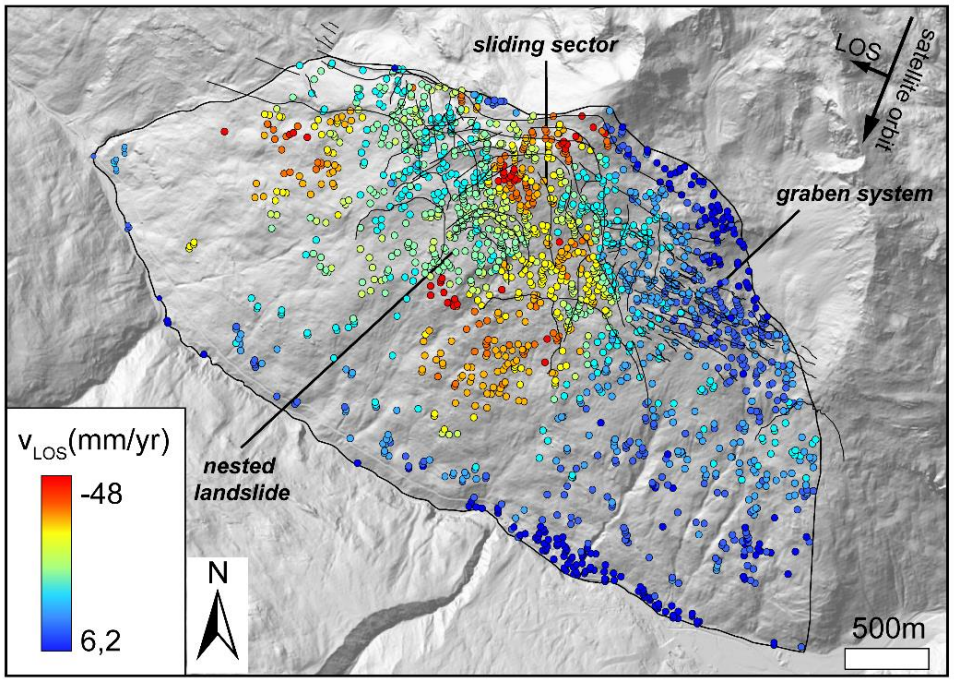


*Figure 5.1.5: SqueeSAR data on Corna Rossa DSGSD (Sentinel-1, descending).*

When exploiting DInSAR on Sentinel-1 images to investigate alpine DSGSD a typical scenario that we also found on Corna Rossa, is the following.

Interferograms with temporal baselines of days-weeks are strongly affected by atmospheric disturbances (Figure 5.1.6 b) due to the topographic variations between lower and higher portions of the slope (atmospheric phase screen APS; Jung et al., 2014). Even with accurate correction of APS, the DSGSD displacement signal (few tens of millimetres only) is very difficult to retrieve.

Interferograms with temporal baselines of several weeks-months have coherent signal mostly in the lower lands and above the tree line. Temporal baselines of several months-years further decrease signal coherence, which is preserved only when acquisitions are not affected by snow cover (Figure 5.1.6 a, winter periods, usually between end of October and beginning of June in the European Alps).

Due to the reasons above, the underlying parameters and quality of the interferograms deeply affect the final capability of advanced DInSAR products to capture the spatial and temporal aspects of the surface displacement patterns associated to complex, very slow rock slope deformation.

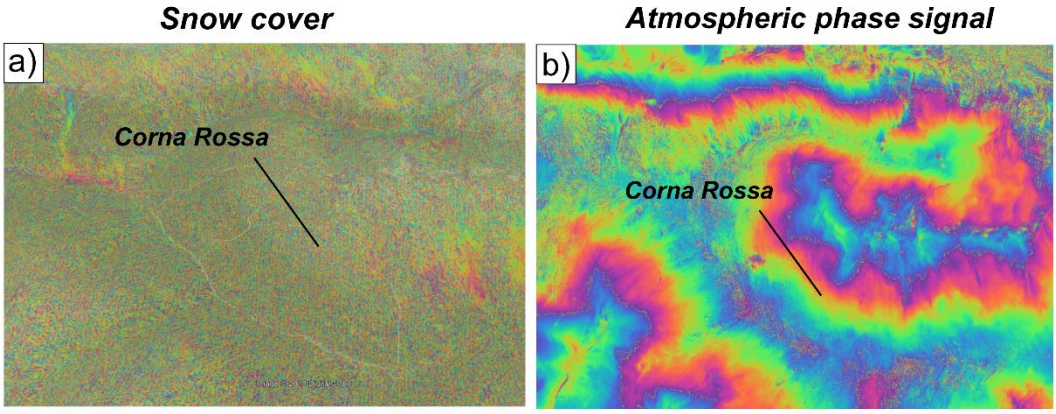


*Figure 5.1.6: decorrelation effect over Corna Rossa due to a) snow cover and b) atmospheric contribution*

Therefore, using the software SNAP (annex A) we processed available Sentinel-1 A/B radar images over Corna Rossa DSGSD slope in the 2015-2018 time period by considering only snow free data pairs (selected considering nivometric data from Oga Meteo Station and Landsat 8 (OLI) C1 images) with three temporal baselines:

1) S1 pairs spanning 6-12-24 days of S1 images acquired during the summer seasons. We mitigated the APS with empirical selection of snow free images and high coherence image pairs to analyse the short term response of the slope and possible heterogeneities also in the slowest slope sectors.
2) S1 pairs spanning June-October (hereafter, summer season pairs) and October-June (hereafter, across winter pairs). These analyses were targeted to identify potential non linearities in the temporal evolution of surface displacements.
3) All S1 pairs with temporal baseline spanning about 1-year (+/- 12 days). This dataset was aimed at identifying the displacement signal permanently affecting the area of study during the observation period. Each image was considered only once to produce independent interferograms spanning very similar time periods.

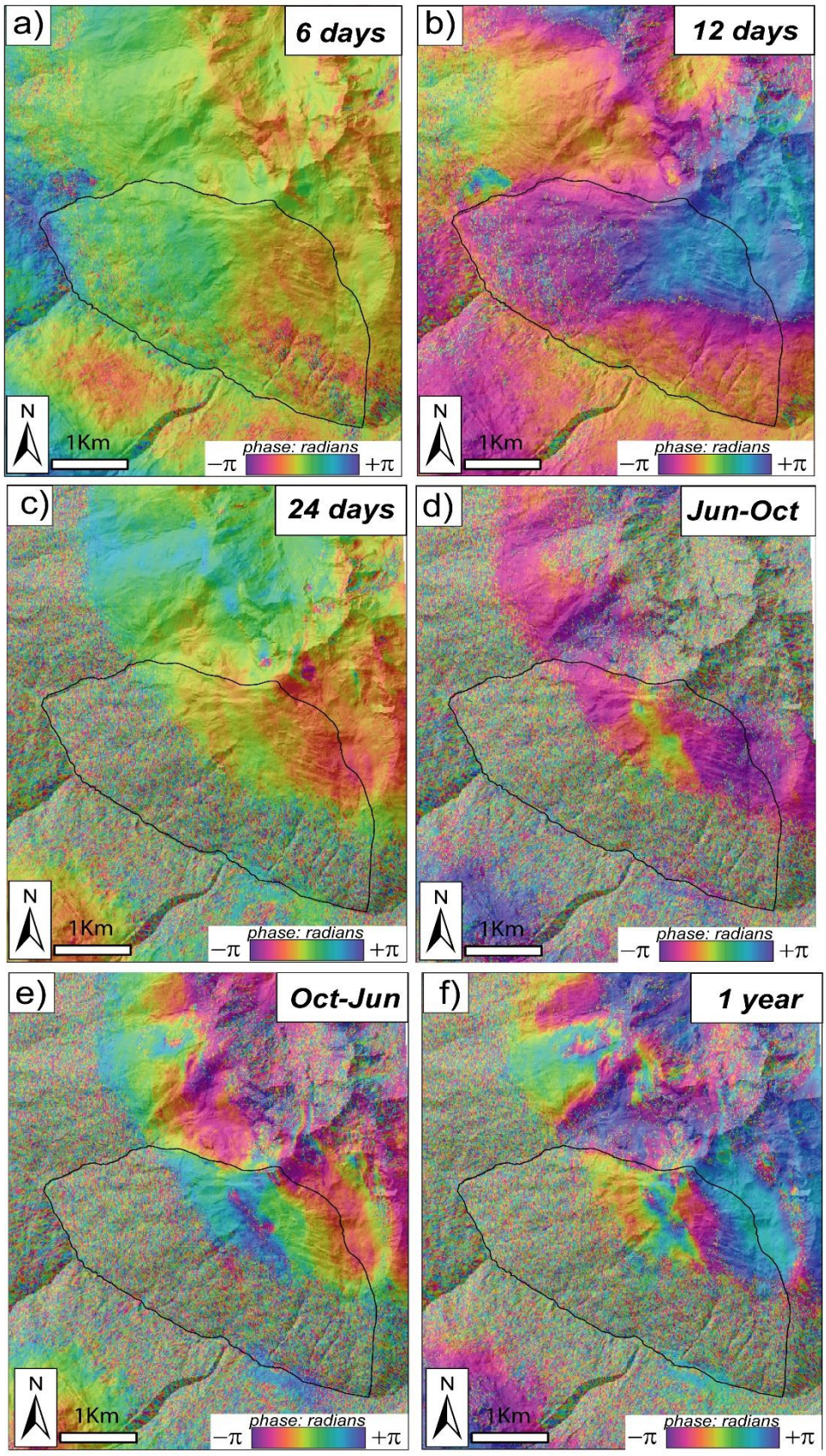


*Figure 5.1.7: Multi baseline DInSAR interferograms processed over Corna Rossa DSGSD. a) 6 days baseline products don't highlight clear slope partitioning since the DSGSD displacement rate is too low to be caught by short baseline; b) 12 day baseline behaves similar to 6 day one, with an increasing response of the upper slope sector and decreasing in coherence in the lower part as highlighted in c) 24 day baseline. d) Summer and e) winter interferograms show slope heterogeneities in the upper slope portion that become sharp in f) 1 year baseline interferogram where a clear displacement signal permanently affecting the area arise.*

Short temporal baseline interferograms

6-12-18 and 24-day interferograms (Figure 5.1.7 a, b, c, and Figure 5.1.8) were processed to identify those areas that lack coherence with increasing temporal baselines and show the possible presence of shallower (or deep) nested landslides with higher displacement rates.
The main issue related to these products is the strong APS (atmospheric phase screen) that often affects the images and hampers the slope investigation. We thus selected only those pairs with a good SNR ratio (lack of atmospheric fringes, temporal or spatial decorrelation) and analysed their response on the summer period (June-October) of 2017 though a moving window each 6 days.
The middle and lowest parts of the slope lose coherence with increasing temporal baselines because of the dense vegetation cover (i.e. conifer forest up to about 2300 m.a.s.l. in elevation). On the other hand, the upper portion remains coherent, but have low SNR ratio with almost homogeneous pattern at 6 days and outlines reliable slope heterogeneities only from 24 days on.

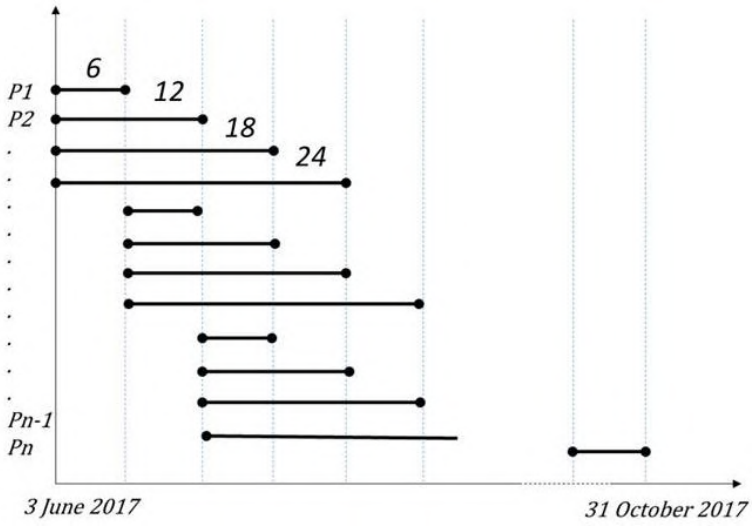


*Figure 5.1.8: Short baselines spanning the summer period of 2017.*

"Seasonal" interferograms

A total of 7 interferograms (Figure 5.1.9) were computed for the period 2015-2018 to investigate displacement patterns in snow-free periods of successive years, and outline possible differences between "summer" (Figure 5.1.7 d; June-October) and "across winter" (Figure 5.1.7 e October-June) periods. Also in this analysis, we used independent pairs to avoid that disturbances (i.e. strong atmospheric disturbance) on common images affect the results, and thus the final interpretation.

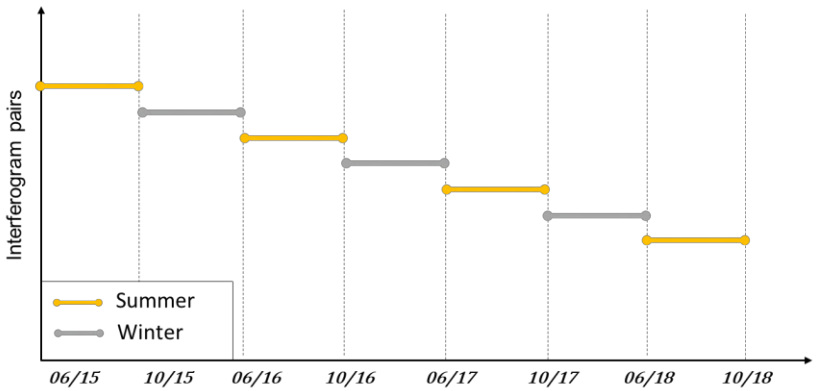


*Figure 5.1.9: Seasonal interferograms spanning the period Jun-Oct (summer period) and Oct-Jun (winter period) from 2015 to 2018.*

The results show strong deformation pattern on the upper portions of the Corna Rossa DSGSD (Figure 5.1.7 d, e), but as drawback there is no spatial evidence of landslides affecting the slope toe due to decorrelation caused by the presence of vegetation. Moreover, they also outline the presence of fringes that appear in the across winter periods, while summer interferograms show minor signals. The difference between the temporal windows considered for the seasonal interferogram cannot explain alone these differences. One potential explanation is that the majority of the surface displacement at Corna Rossa occurs during snow melt periods, as observed in other alpine DSGSD.

## 1-year interferograms

Stacking strategies are routinely employed in signal processing analyses to increase the SNR (Rocca, 2007). The hypothesis considered is that, starting from multiple samplings of the same signal, summation, average, or other statistical descriptors highlight the signal itself while random noise is minimized.

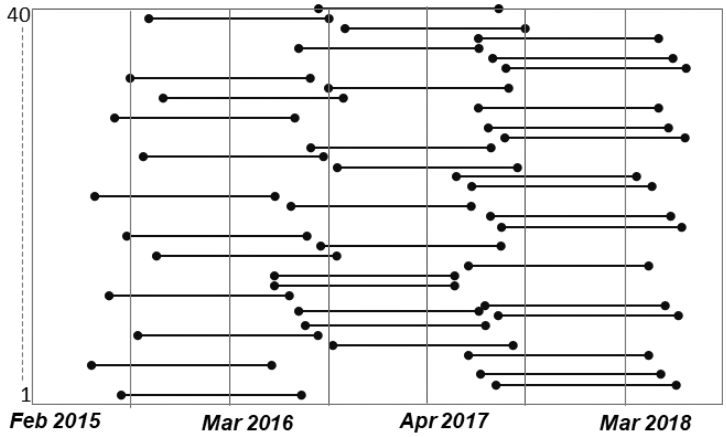


*Figure 5.1.10: 40 annual interferograms selected for the stacking approach..*

The standard approach is first to unwrap the interferograms and then proceed with the stacking. However, this implies also that if the unwrapping results are inaccurate due poor signal coherence and strong strain partitioning along slope (i.e. strong heterogeneity and segmentation), the stacking would be misleading. In addition, spatial aliasing due to sharp displacement heterogeneities and/or discontinuities between different kinematic domains (Manconi et al., 2018) can cause further errors.

As shown in Figure 5.1.7 f, the scenario at Corna Rossa when approaching 1-year summer interferograms indicates that the displacement fringes are discontinuous (cut) on the lower portions of the slope due to the presence of forest. In the upper slope portions the coherence is relatively high, however, spatial heterogeneities and discontinuities of the signal are clearly visible. Compared with standard stacking approaches, here we considered the wrapped interferograms (Figure 5.1.10) with the following steps.

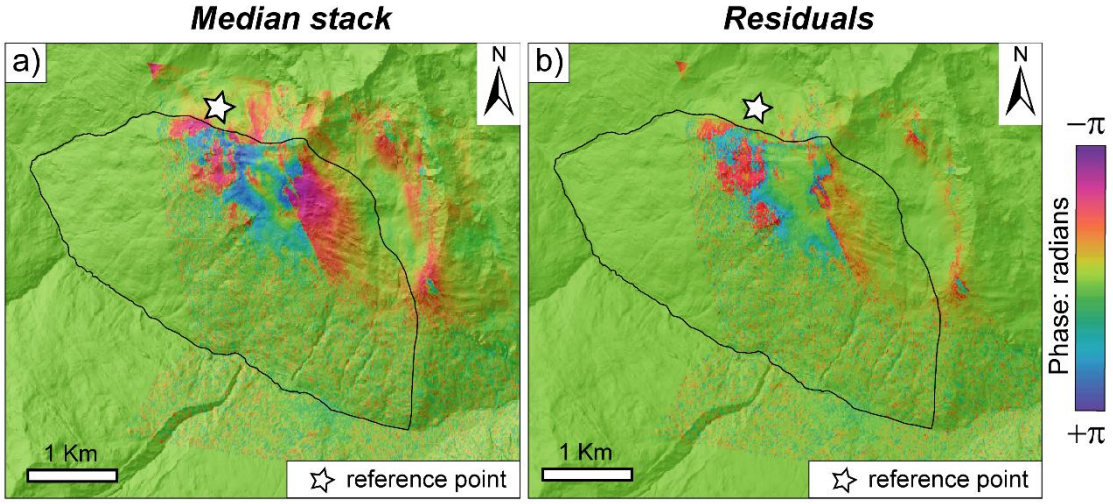


*Figure 5.1.11: Median residuals resulting from the stacking procedure of wrapped interferograms.*

We first co-registered (aligned) all independent interferograms by considering the oldest acquisition as master. Then we defined a point in the vicinity of the DSGSD as stable, based on geological considerations. Finally, we generated the stacked interferogram by computing the median (central value) in phase domain (Figure 5.1.11 a). The resulting stacked interferogram can be considered as a "model" representative of the background signal constantly affecting the area of interest. Median of the signal was here preferred to the average in the stacking approach in order to avoid extreme phase smoothing and preserve signal edges.

The stacking procedure is applied iteratively to the phase residuals (Figure 5.1.11 b; i.e., the new sequence obtained by subtracting the background signal to the initial interferograms), allowing the interpretation of additional spatial heterogeneities. Stacking results emphasize the permanent displacement signal (Figure 5.1.11 a, Figure 5.1.14 a) and the visualization of the residuals (Figure 5.1.11 b, Figure 5.1.14 b) provides a trace of the boundaries (i.e. partitioning) occurring between the NW and SE sectors, the location of inner nested landslides and highlight the presence of active scarps (Figure 5.1.14 a, b)

dissecting the slope and delimiting different nested phenomena. Approximate velocity values extracted from phase information attribute a median displacement rate around 16-20 mm/yr for the upper sliding portion and higher velocities for the nested landslides affecting the mid slope sliding sector. A sharp deformation change and velocity drop occurs in the transfer zone sector with displacement rates lower than 10 mm/yr.

### 5.1.3 Results: strain partitioning and segmented DSGSD activity

Through geomorphological and morpho-structural analysis of field, aerial and HRDEM data we identified main tectonic and morpho-structural lineaments and outlined the occurrence of a "gravitational transfer zone" within the DSGSD.
This setting strongly affects the mechanism and amount of gravitational deformation inside the slope also controlling the reactivation of the master fractures (Figure 5.1.12, Figure 5.1.13) by gravitational deformations with sharply different styles.
Targeted DInSAR processing shed light on the present day displacement pattern and provided detailed surface velocity and phase gradient maps highlighting different slope sectors characterized by different activity styles and abrupt deformation changes.
DInSAR analysis on annual interferograms, exploited through an original stacking approach (Figure 5.1.14), allowed to increase the SNR associated to long temporal baseline products and maximize the SAR information emphasizing the displacement signal associated to the DSGSD (Figure 5.1.14 a), also identifying potential spatial and temporal heterogeneities emerging both from 1 year and seasonal interferograms (Figure 5.1.14 b).
Our integrated results allow to answer two major questions about the state of activity and evolution history of such a complex DSGSD strongly controlled by structural features: 1) how non-persistent inherited structures can affect the long term evolution of different DSGSD sectors? 2) Which features are reactivated in different stage?
Structural mapping and detailed field analysis coupled with DInSAR analysis unraveled the key role of non-persistent inherited fractures (Figure 5.1.14) in the evolution of the DSGSD, which accommodates gravitational strain by dominant extension in the interaction zone between partially overlapping gravitational master fractures (Figure 5.1.14).
Their presence conditions the onset of the phenomenon, while their gravitational reactivation after LGM induces the formation of a "transfer zone" with stress increment around the tips of the two fracture segments (Figure 5.1.12 , Fossen and Rotevatn, 2016) and strain partitioning between dominant sliding (gravitational "faults") and dominant extension (fracture overlap) sectors (Figure 5.1.14).
The spacing between two fault tips has been related to the zone of stress reduction (Figure 5.1.12) that occurs around faults (Ackermann and Schlische, 1997; Cowie and Roberts, 2001; Soliva et al., 2006; Fossen and Rotevatn, 2016;). The stress drop in this region retards the fault growth into the region of overlapping faults and reduces the propagation rate producing a skewed displacement profile (Fossen and Rotevatn, 2016).

The in between overlap zone is characterized by mainly extension and hybrid reactivation of minor subparallel fractures (Figure 5.1.14, Figure 5.1.15 c) that develop between the two segments of the master fracture.

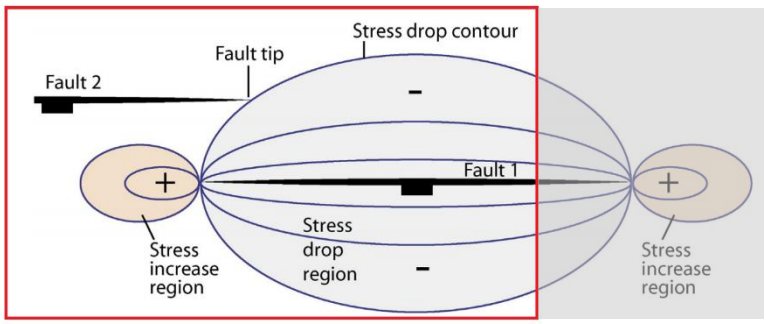


*Figure 5.1.12: Transfer zone in the overlapping sector between two fault segments (Fossen and Rotevatn, 2016).*

Preexisting brittle structures are here reactivated with dominant dip slip component that overprints a previous strike slip movement (Figure 5.1.13) and accommodates the extension creating a complex segmented sector of scarps and counterscarps whose movement arrested in the Holocene.

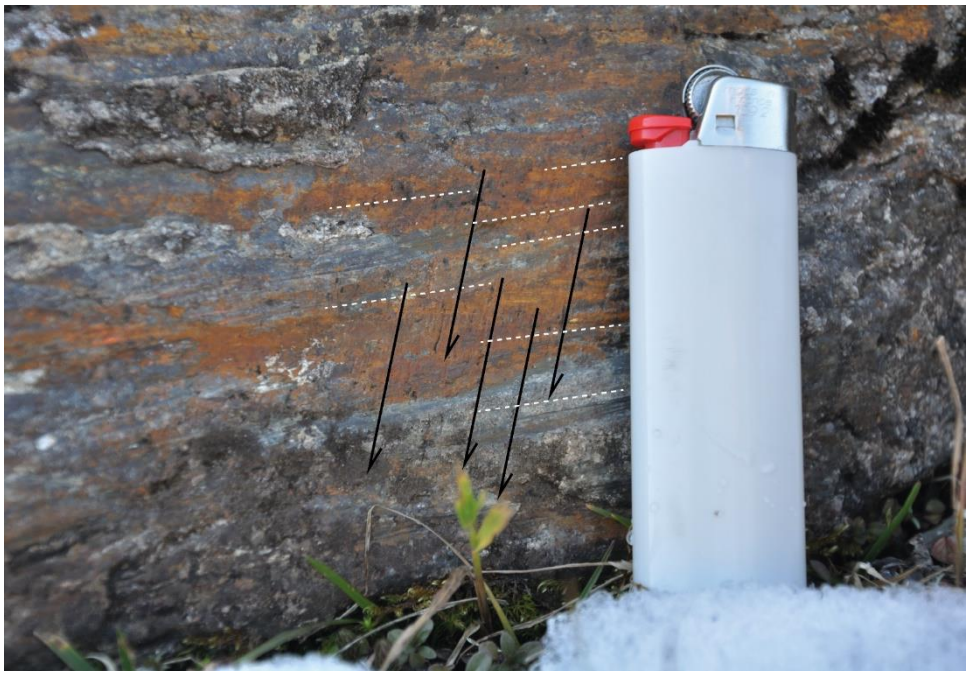

*Figure 5.1.13: Kinematic indicators referring to a strike slipe displacement component (white dashed lines) overprinted by new dip slip striations (black arrows).*

Only marginal features still display ongoing activity, but this may also be due to the dragging action of the central sliding sector which DInSAR analysis revealed to be constantly moving with high displacement rates up to 30mm/yr.

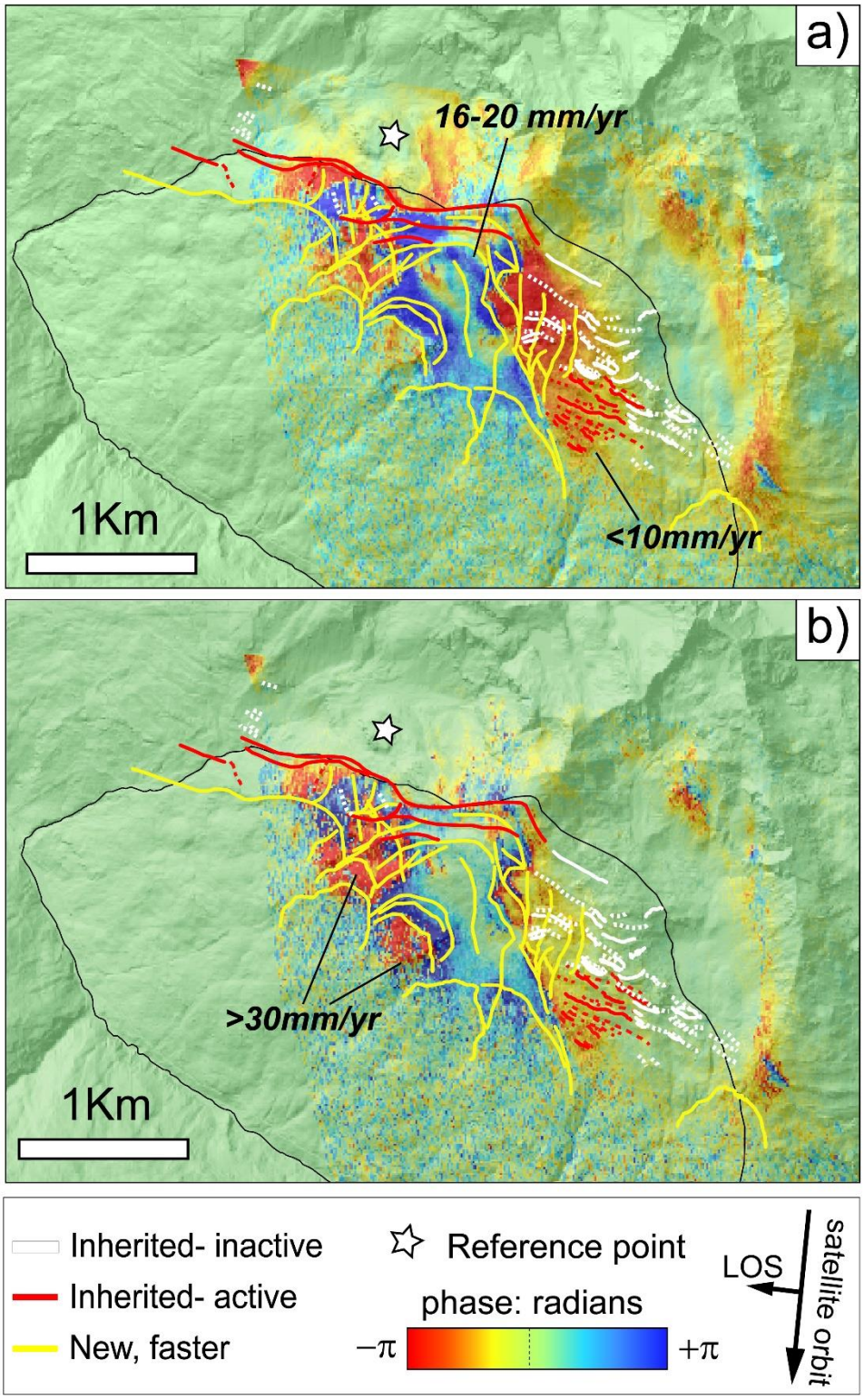


*Figure 5.1.14: Morpho-structures activation timing unravelled using DInSAR data. a) results of the median staking approach b) result of the stacking on the residuals.*

In the western sector, slope failure mechanisms are controlled by pure sliding testified by a series of scarps trending NW-SE and a kinematic profile (Figure 5.1.15 a) that reflects a

typical compound movement. Going to east on the contrary a more rototranslational kinematic is found along a middle slope transect (Figure 5.1.15 b).

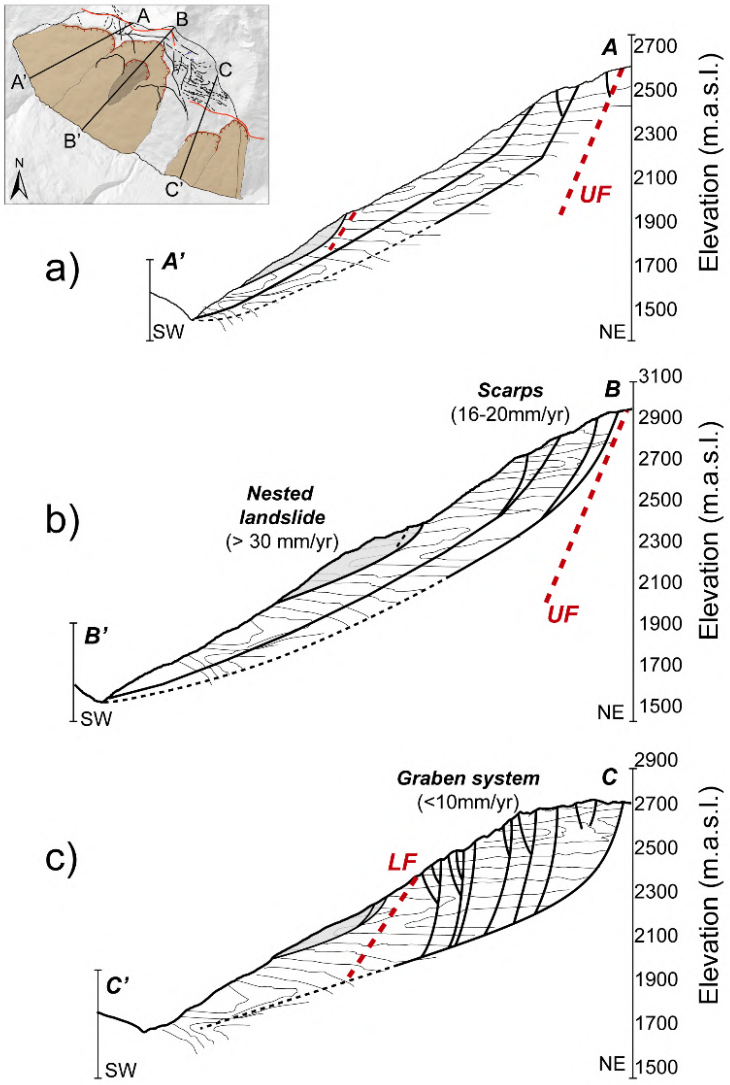


*Figure 5.1.15: Interpretative cross section of 3 representative sectors of Corna Rossa DSGSD.*

Preliminary CRE results (Agliardi et al., 2018; Agliardi et al., 2019) using both $^{10}$Be and $^{26}$Al cosmogenic nuclides suggest the DSGSD initiated in the Lateglacial through the development of graben and half-graben systems in the spreading sector. Its deformation had an early activation during the deglaciation and ceased in the Early Holocene, while the sliding sector is still undergoing progressive evolution at a constant velocity of tens of mm/yr. This latter is nowadays the most active slope portion as confirmed by radar LOS velocity and hosts giant segmented rockslides (Figure 5.1.2, Figure 5.1.15).
Our approach effectively unravels the complexity of strongly heterogeneous deep-seated landslides and identify key sectors in a geohazard management perspective.

Several possible scenarios can be depicted considering different sectors evolution (Figure 5.1.16) which also correspond to different collapse potential according to the involved rock mass volume and potential energy (e.g. suspended rock masses or leaning on the valley floor). Our considerations also set constraints to calibrate further numerical models that would result more effective if targeted on precise scenarios more than on the global complex phenomenon.

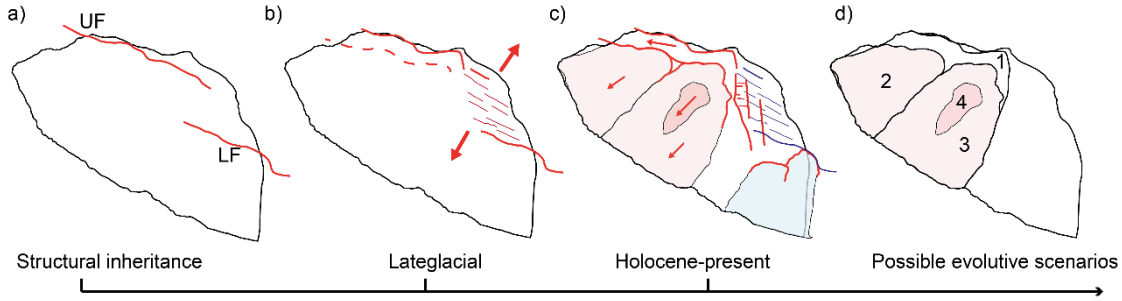


*Figure 5.1.16: Timeline of the slope evolution from inherited structures to their reactivation due to gravitational movement. A) inherited master fracture; b) activation of the spreading mechanism in the overlapping sector between the UF and the LF ; c) activation of the sliding portion and segmentation in different nested bodies; d) possible evolutive scenarios affecting different slope sectors.*

## 5.2 Heterogenous activity: Mt. Mater DSGSD

### 5.2.1 Geology and Geomorphology

The Mt. Mater western slope is located on the eastern flank of the upper Valle Spluga (Lombardia, Central Italian Alps) and impends directly over the Madesimo village and tourist resort. The high relief slope (1550 to 3000 m a.s.l.) ranges in inclination between 33° (< 2500 m a.s.l.) and 25° (> 2500 m a.s.l.). The slope is made of metamorphic rocks of the Suretta and Tambò Penninic nappes (Schmid et al., 2004), with dominant mica schist and paragneiss of the Stella-Timun complex (Suretta nappe) and limited outcrop of Mesozoic metasedimentary rocks at the slope toe, marking the contact with the underlying Tambò nappe(Figure 5.2.1).

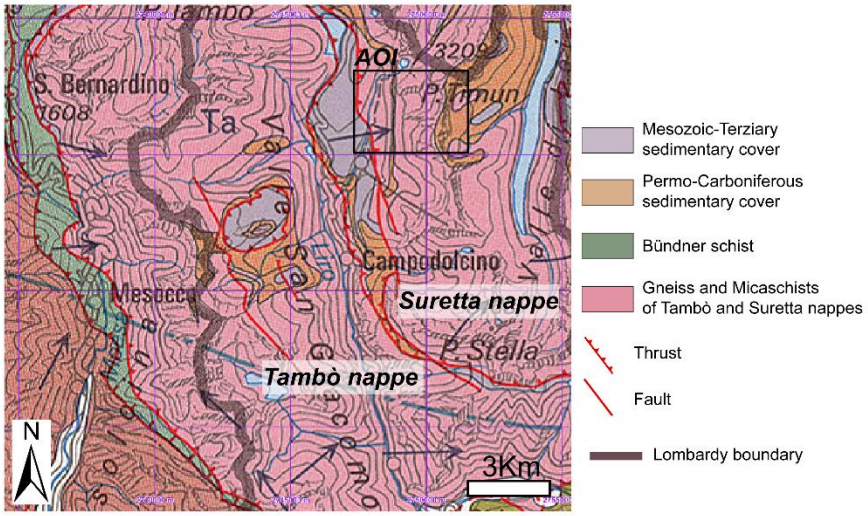


*Figure 5.2.1: Geological map of Vallespluga (Geologische Karte der Schweiz 1:500000).*

These rocks underwent a polyphase alpine tectono-metamorphic evolution with four main deformation stages since the Paleocene (Baudin et al., 1993; Marquer et al., 1996).

The first two stages involved the regional nappe structure and resulted in tight isoclinal folds associated with a pervasive foliation moderately dipping to the East. Locally, the third stage refolded previous structures with a subvertical N-verging axial plane (Marquer et al., 1996; Scheiber et al., 2012).

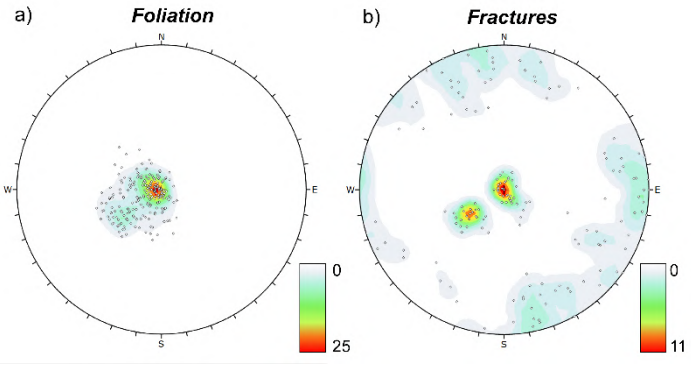


*Figure 5.2.2: Poles and density concentration of a) foliation and b) fractures on Mt. Mater slope.*

Ductile deformation in metamorphic environment plays and important role in the definition of the geomechanic rock properties since it influences: a) the mineralogical composition and structure (quartz Vs mica domains); b) the anisotropy (presence or lack of pervasive fabric); c) heterogeneities. In our case, the intense ductile deformation produces a foliation that is generally constant and dips inside the slope towards NE with a low angle (mean values 068/15) (Figure 5.2.2, Figure 5.2.3), thus resulting in a less favourable geometric control for the onset of sliding phenomena.

*Figure 5.2.3: Pervasive foliated micaschists on Mt. Mater slope.*

Later brittle deformation resulted in the development of NNW-SSE trending normal faults cutting nappe boundaries (Baudin et al., 1993) and in N-S and E-W trending master fractures. Tectonic strain and fabric are strongly heterogeneous due to the widespread occurrence of ductile shear zones, affecting the variability of rock strength and deformability in the brittle field.

The geomorphology of the upper Valle Spluga was strongly imprinted by Quaternary glaciations, especially by the Last Glacial Maximum (LGM; Bini *et al.*, 2009), that carved

steep slopes in basement rocks with local reliefs up to 1500 m. After post-LGM deglaciation, landscape development was controlled by Lateglacial glacier re-advances (Ivy-Ochs et al., 2008), testified by well-preserved glacial cirques, steps and moraine ridges below 2350 m a.s.l. (Figure 5.2.5). During and following Lateglacial, extensive periglacial processes strongly affected rock degradation, slope stability, and sediment redistribution, as testified by widespread scree deposits and intact rock glaciers above 2400 m a.s.l. (Scotti et al., 2013).

### 5.2.2 Gravitational Morpho-Structures

The post-glacial destabilization of the entire slope by means of deep-seated gravitational slope deformation (DSGSD) is testified by evident morpho-structural features (Agliardi et al., 2001;Agliardi et al., 2012), that affect the slope from the toe to the crest over an area exceeding 3 km$^2$. These features have been recognized, mapped and interpreted through a geological and geomorphological investigation of the area, integrating 1:5000 field surveys, aerial photo-interpretation (stereo-photo coverage; TEM 1981-83; ortho-photos: 2000, 2003, 2007, 2012, 2015) and high-resolution digital elevation models (5m resolution) (Figure 5.2.4).

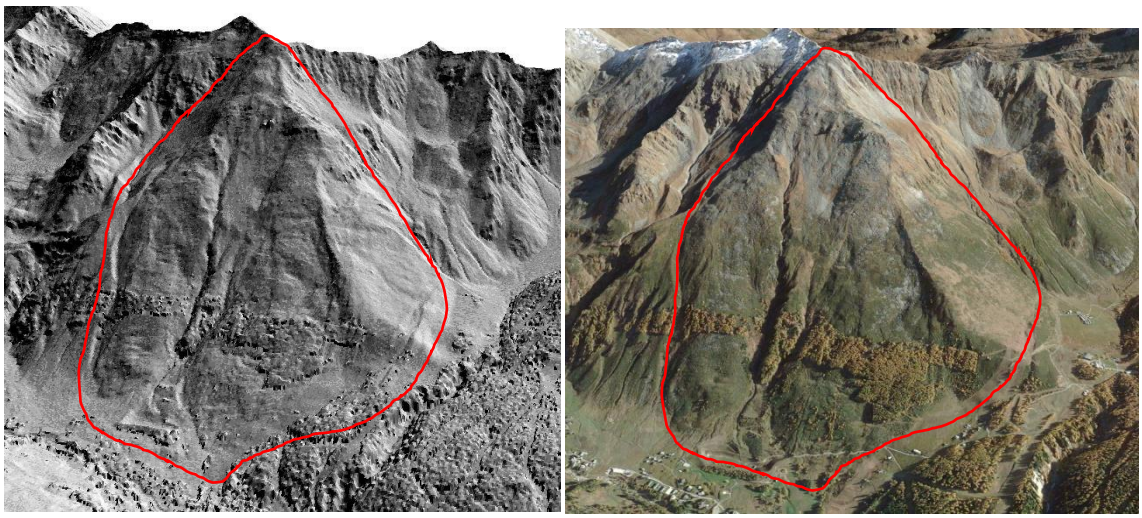

*Figure 5.2.4: DEM model (5m resolution) and ortophotofrom Google Earth of Mt Mater Slope.*

Above 2500 m a.s.l., these features include dominant scarps, suggesting limited or negligible rotational movements within the DSGSD mass. At 2900 m a.s.l., the slope is cut by a sharp triangular head scarp with a vertical downthrow of about 40 m (Figure 5.2.5 a). Laterally, the scarp trace can be followed continuously to the N and S, suggesting that the DSGSD is bounded by a relatively well-developed basal shear zone. Between 2900 and 2500 m a.s.l., the slope is cut by several steep persistent N-S trending scarps, structurally controlled by the main master fractures, which extend to the south crossing the ridge with the Val Groppera. Here, NE-SE trenches and NW-SE counterscarps with a maximum length of few tens of meters define a small gravitational graben (Figure 5.2.5 b). Moving downslope, shallower arcuate scarps mark the transition to two nested large landslides, affecting the slope between 2400 m a.s.l. to the toe (Figure 5.2.5). In these sectors, the structural control

exerted by the master fractures becomes less evident and rock masses are progressively more damaged and become almost entirely crushed at 1900-2000 m a.s.l behaving like a continuum.

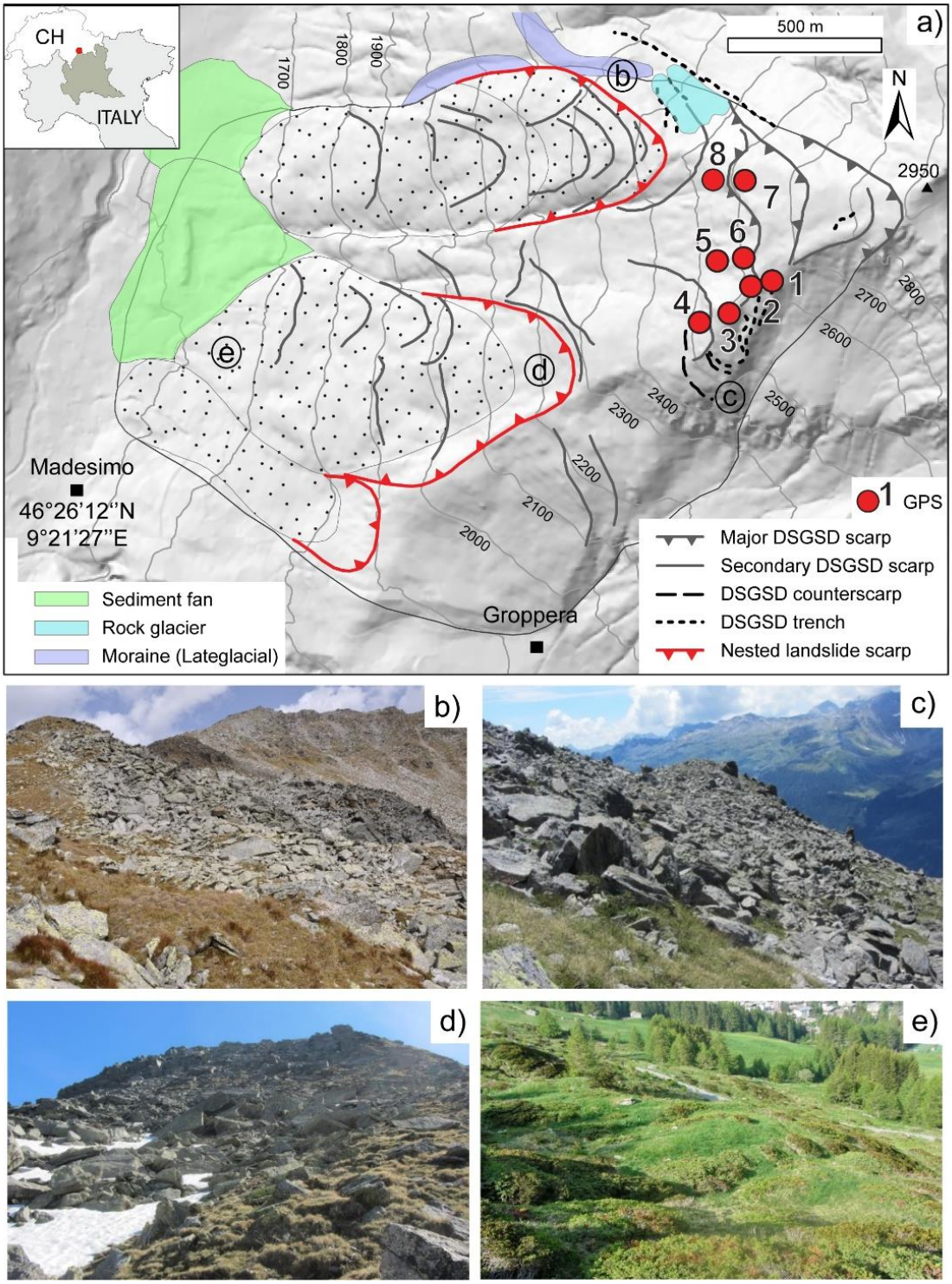


*Figure 5.2.5 Main features of the Mt. Mater deep-seated gravitational slope deformation (DSGSD). (**a**) Simplified map portraying the main morpho-structural features associated with DSGSD and nested large landslides. GPS benchmark locations are outlined. (**b**) tranches on the S side of the main DSGSD body; (**c**) main scarp of the northern nested landslide (cross-section in Figure 6); (**d**) damaged rock mass at the top of the southern nested landslide; (**e**) blocky accumulation at the southern nested landslide toe.*

Nested landslides are bounded by curve-shaped, highly fractured main scarps with vertical downthrow up to 20-25 m (Figure 5.2.5 c,d). Several secondary scarps occur between 2200 and 2450 m a.s.l. within the landslide masses, suggest their internal segmentation in sectors with different degrees of damage (Figure 5.2.5 a). Both the nested landslides have highly displaced toes, pushed out towards the valley floor through a series of slope-parallel lobes associated with debris sliding and a localized collapse of large landslide toes (Figure 5.2.5 e). The main scarp of the northern nested landslide partially dismantled a moraine ridge at about 2300 m a.s.l., while DSGSD morpho-structures interact with intact rock-glaciers. This suggests that large-scale rock-slope instability was active in different stages after the Lateglacial.

### 5.2.3 DInSAR analysis and ground based validation

We characterized the DSGSD using products of different spaceborne differential SAR interferometry (DInSAR) techniques. To analyze different aspects of the phenomenon, we used both point-like information from SqueeSAR™ data (2015–2017) and spatially distributed information from specially processed multi-temporal baseline interferograms (Crippa et al., 2020). We integrated this information with GPS ground measurements covering a period of 4 years from 2014 to 2019 (Figure 5.2.6) and compared the results with GB-InSAR information.

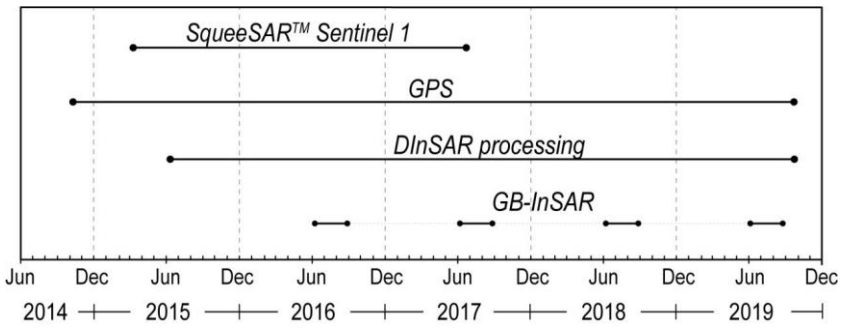


*Figure 5.2.6: Time windows and temporal baselines covered by remote sensing and monitoring data.*

#### 5.2.3.1 SqueeSAR™ Data

In order to test the potential of commercially available PSI data processed over large areas for the detailed characterization of a very slow rock slope deformation, we used SqueeSAR™ data (TRE Altamira; Figure 5.2.7 a,b). These were derived from Sentinel 1A/B SLC radar images (C-band, wavelength: 5.56 cm), acquired in TOPS Interferometric Wide swath (IW) mode (De Zan and Guarnieri, 2006) between March 2015 and July 2017 (revisit: 12 days, 6 days since March 2017; Annex table A-1 ) in both ascending (track = 15; orbit azimuth $\delta$=10.23°; mean LOS angle $\vartheta$ = 41.99°) and descending geometries (track = 168; $\delta$ = 8.99°; $\vartheta$ = 41.78°).

The Mt. Mater slope, facing to the W (mean aspect: 262°) with a mean slope gradient of 28°, is favorably oriented to the satellite LOS of descending orbits, able to catch slope movements with the highest sensitivity and without significant geometrical distortions.
To maximize the exploitation of SqueeSAR$^{TM}$ data (Figure 5.2.7), we integrated the information in a 2DInSAR analysis (Figure 5.2.7 c, Manzo et al., 2006; Dalla Via et al., 2012; Eriksen et al., 2017) and computed the components (Vv,Ve,τ) of the 2D displacement vector (T) on the vertical EW plane.

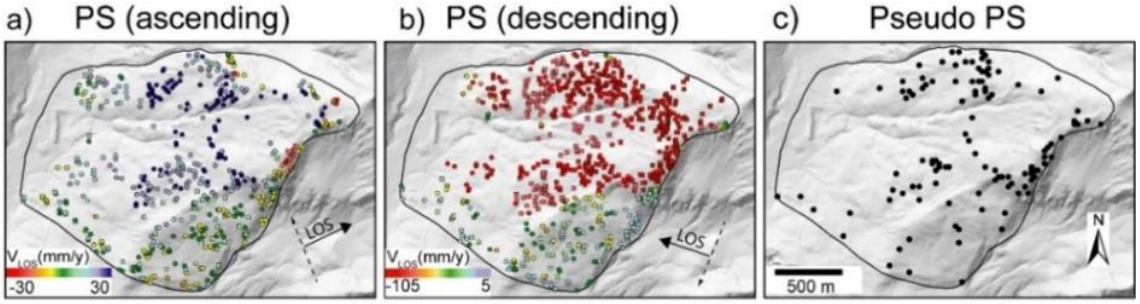


*Figure 5.2.7: Kinematics of the Mt. Mater DSGSD derived from SqueeSAR$^{TM}$ data analysis. (**a,b**) permanent (PS) and distributed scatterers (DS), classified by line-of-sight (LOS) displacement rate ($V_{LOS}$); (**c**) pseudo-PS derived by combining data from ascending and descending orbit.*

### 5.2.3.2 DInSAR Processing

To further investigate the spatial and temporal patterns and heterogeneities of DSGSD displacements, we used the software SNAP (ESA Sentinel Application Platform 7.0.0) to generate 61 interferograms with increasing temporal baselines, ranging from 24 days to 1 year in the period between June 2016 and October 2019 (Figure 5.2.7). Shorter baseline interferograms (6,12 days) have been discarded because they are only able to capture fast displacements of scree deposits or periglacial features. To reduce speckle noise and better outline phase signatures in the interferograms, we applied multi-looking factors of 1 (azimuth) and 4 (range) and phase filtering techniques (Goldstein phase filtering, Goldstein and Werner, 1998)). For those interferograms with good signal to noise ratio and high coherence, we obtained phase-unwrapped displacement maps using the minimum cost flow algorithm (MCF, Costantini, 1998) implemented in the SNAPHU software plugin (Chen and Zebker, 2000).

Short temporal baseline (24-day) interferograms are frequently affected by atmospheric disturbances in the early June and September-October periods, due to the association of sharp topography and daily temperature variations (Figure 5.2.8). Thus, they were carefully selected to avoid submitting misleading information to the unwrapping procedure.

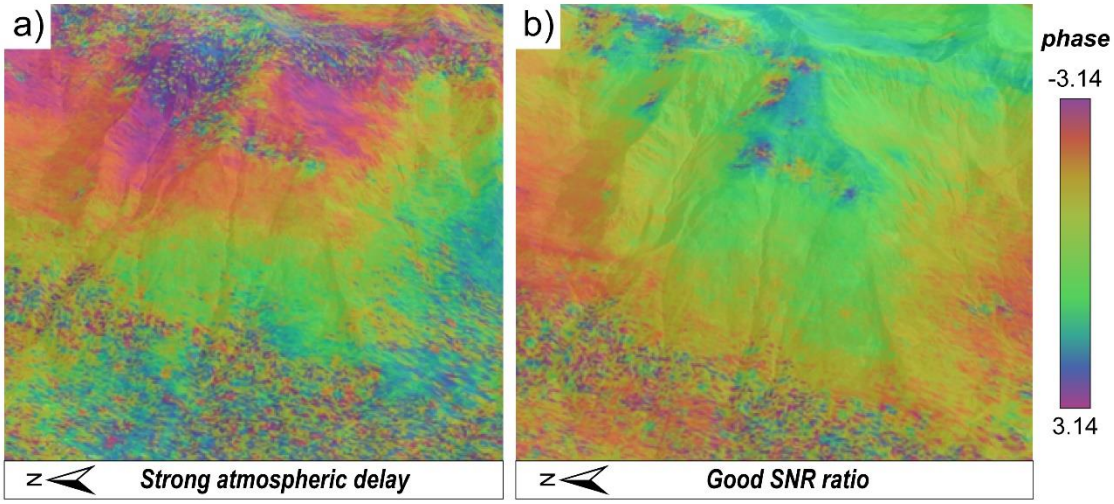


*Figure 5.2.8: 24 days interferogram with a) strong atmospheric contribution highlighted by the presence of bands b) a good SNR in which different phase values are recognized in the upper slope portion and in the lower sector.*

Using GACOS (Generic Atmospheric Correction Online Service (Yu et al., 2017, 2018; Figure 5.2.9) we also attempted an atmospheric correction to reduce the phase delay on short baseline interferograms. However, the scale of the atmospheric models is insufficient to explain local disturbances and the corrected result in general differed by the original displacement maps only in the range of submillimeter values. We mitigated the atmospheric phase signal according to key observations. Those image pairs that presented characteristic signals of atmospheric phase delay such as strong decorrelation effects or the repetition of regular fringes associated to thermal and atmospheric stratification were discarded from the analysis (Figure 5.2.8 a).We only kept the interferograms with highest signal to noise ration and high coherence (>0.4) in the scene and where the displacement signal clearly arose from the background noise (Figure 5.2.8 b).

Seasonal interferograms with temporal baselines of several months were processed considering snow cover occurrence from nivometric data (Campodolcino Meteo Station) and Landsat 8 (OLI) C1 images. Suitable pairs of snow-free images were selected to generate interferograms representative of displacements accumulated from June to October (hereafter summer interferograms) and from October to June (hereafter snow cover period interferograms).

Finally, annual interferograms were targeted to outline persistent (pluri-annual) displacement signals. We considered pairs of images with temporal baseline spanning 1-year (± 6 days), rolling over the period June 2016-October 2019.

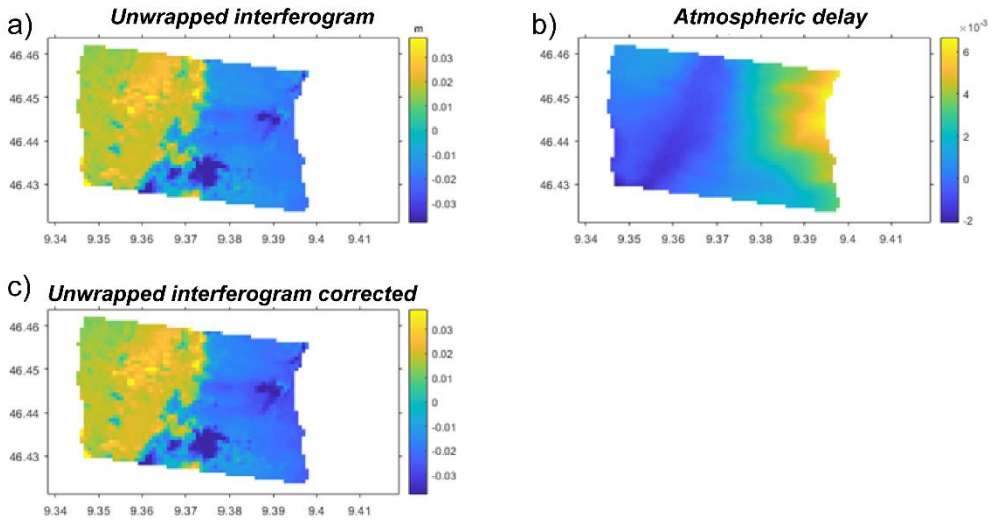


*Figure 5.2.9: GACOS correction. a) input unwrapped interferogram; b) atmospheric delay model computed over the interferogram period; c) result of the interferometric correction.*

### 5.2.3.3 GPS Data

We considered 8 GPS benchmarks (operated by ARPA Lombardia), installed in the upper sector of the slope above 2500 m.a.s.l. (Figure 5.2.5). Periodical differential GNSS measurements (about 3 surveys per year), carried out using double-frequency GNSS Leica GS09 receivers, started in October 2014 for station 3 and in June 2015 for the other ones. Considering instrumentation specifications and the distance to the master control station (~1.5 km), measurements are affected by a static (post-processed) horizontal standard error of 3–5 mm + 0.5 ppm and a vertical one of 6–10 mm + 1 ppm. No further corrections have been applied for environmental sources of error affecting measurements in field conditions.

### 5.2.3.4 GB-InSAR

Ground-Based Synthetic Aperture Radar (GB-InSAR) systems uses radar sensors based on the synthetic aperture radar (SAR) technique, similar to that used on satellites but implemented in a ground-based platform. The system adopted for Mt. Mater is provided by LisaLAB srl (Figure 5.2.10). It acquires in Ku band (λ=2.5-1.67cm) both in continuous and in periodic mode in the time intervals identified in Figure 5.2.6.
The radar is located on the opposite valley flank respect to Mt. Mater at a distance of almost 4Km. Range resolution is approximately of 1.5m while azimuthal one ranges between 5.8 and 11.6 m respectively at 4 km and 2 km of distance (Figure 5.2.10). “Periodical check” campaigns are conducted usually over short term periods (few days-1 week) with continuous

acquisition every 10 minutes (in average). Long term analysis are also conducted correlating the date acquired in different campaign with monthly distance.

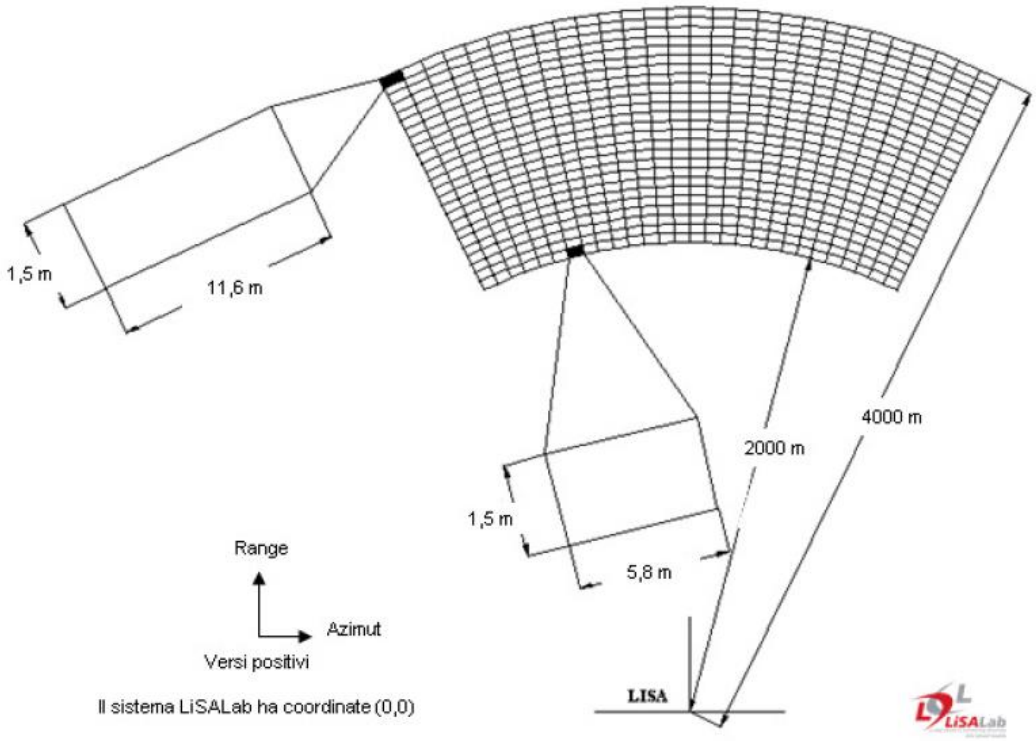


*Figure 5.2.10: Resolution grid of GBInSAR LiSALab adopted in the study of Mt. Mater DSGSD.*

### 5.2.4 Results

We characterized the global kinematics (i.e. sliding mechanism) of the Mt. Mater DSGSD by exploiting the available SqueeSAR™ dataset based on Sentinel-1 radar images (Figure 5.2.7 ,b), from which we derived the products of 2D displacement rate vector decomposition (2DInSAR, Figure 5.2.11).

For Mt. Mater, our results indicate an average $\tau$ value of about 30° over the slope, while higher values (around 80°) can be detected only close to the steep DSGSD upper scarps and to the headscarps of nested large landslides. These values and their spatial distribution provide robust insights into the global kinematics of the DSGSD. This is characterized by dominant translational sliding, with rotational sliding components associated with the head sectors of the nested large landslides mapped in the field (Figure 5.2.5, Figure 5.2.11).

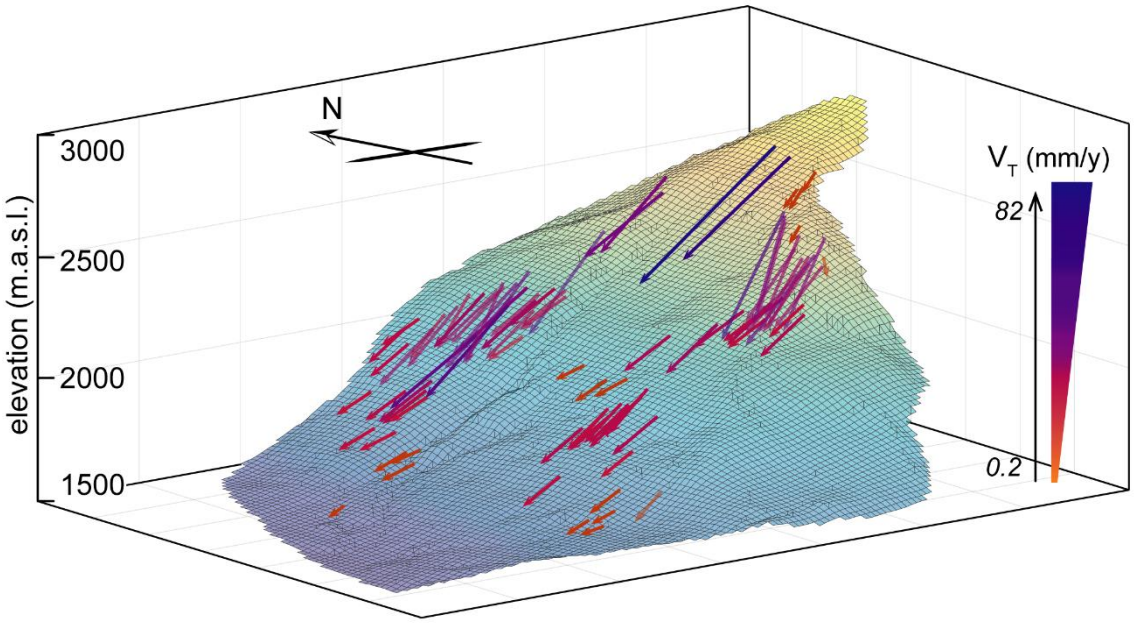


*Figure 5.2.11: 3Dvisualization of the 2D total displacement vector T, derived by the 2D decomposition of LOS velocitiesat pseudo-PS locations. Vector color and length are classified by T vector velocity ($V_T$).*

$V_T$ values (Figure 5.2.11) are generally higher in the upper DSGSD sectors, reaching 80 mm/year above the curved scarp at around 2600 m a.s.l. (Figure 5.2.5 a) and testifying the ongoing active deformation of the entire slope. At and above the head sectors of the two nested large landslides, $V_T$ values range between 30 and 45 mm/year (head of northern landslide; Figure 5.2.5 a,b) and 25–30 mm/year (above the head of southern landslide; Figure 5.2.5 c,d). Displacement rates fade to 1-5 mm/year moving towards the slope toe, where landslide materials become more crushed and crumpled and/or the true displacement vector may significantly deviate from the radar line-of-sight.

However, the sparse nature of these data hampers a sound interpretation of the spatial pattern of measured displacements with respect to the scale (i.e. shallow vs deep-seated) and heterogeneity of slope failure mechanisms characteristic of different slope sectors. Thus, to better investigate displacement patterns along the slope, we analyzed the multi-temporal interferograms generated through targeted DInSAR processing across the period June 2016-October 2019 (Figure 5.2.12). In all the processed interferograms, a low coherence area ($<$0.4) due to patchy vegetation and thermal stratification of the valley air, hampers the possibility to detect deformations close to the slope toe. This effect becomes more severe when increasing the temporal baseline from 24 days to 1-year, in which, the low coherence sector extends up to the middle slope sector because of increasing temporal decorrelation. Interferograms with a baseline shorter than 24 days (i.e. 6, 12 days) do not show significant displacements, except for localized superficial debris covers or periglacial forms. From 24 days on, a triangular-shaped moving sector emerges from an almost homogeneous ground displacement signal (Figure 5.2.12 a).

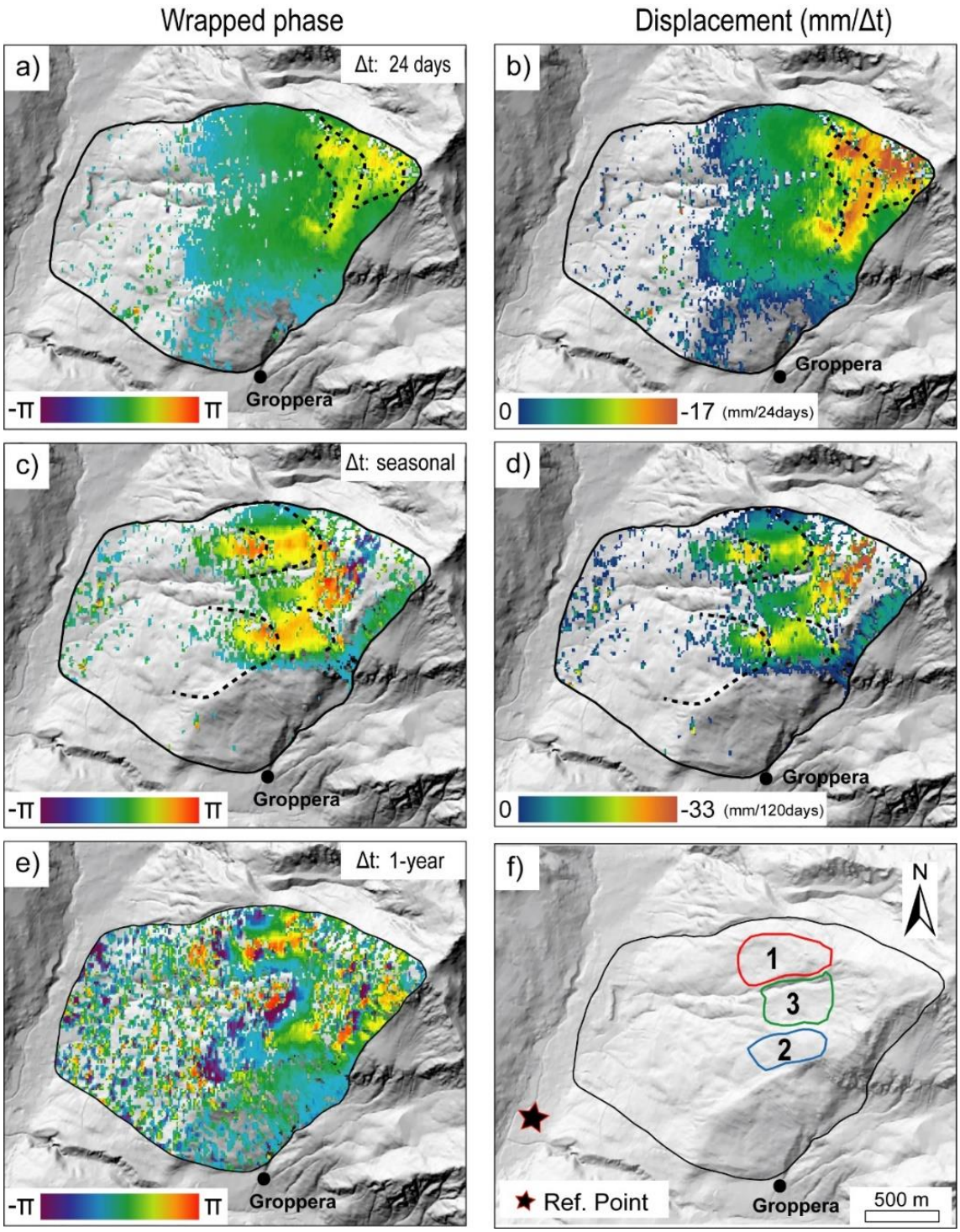


*Figure 5.2.12: Examples of interferograms and displacement maps obtained by DInSAR with different temporal baselines (images: Sentinel-1 (Track 66, descending). Left column: wrapped phase interferograms with increasing temporal baseline: (**a**) 24 days (2-26 Jul 2017); (**c**) seasonal (June-October 2019); (**e**) 1-year (2018-2019). Right column: (**b**) and (**d**) unwrapped phase converted to displacements (mm). The unwrapped results for the 1-year interferogram were affected by a high noise level and unreliable values, and for reason are omitted; (**f**) sectors 1, 2 and 3, representative of the activity of northern and southern nested landslide heads and the background DSGSD, respectively. 24-days and seasonal wrapped and unwrapped interferograms are masked where the phase coherence of the filtered interferogram is. < 0.4 and displacement >0. On 1-year interferograms pixels with coherence <0.3 are masked out. The reference point used for phase to displacement conversion is shown.*

It extends between the N-S curvilinear scarp trending at 2500 m a.s.l. and the DSGSD headscarp at 2900 m a.s.l. (Figure 5.2.5) and is made of damaged rock with extensive debris cover and periglacial features. This is the fastest slope sector, as it always decorrelates in longer baseline interferograms and is characterized by average displacement rates of 10 mm/month (Figure 5.2.12 b).

These values are consistent with data provided by GPS benchmarks, all located within the upper slope sector between 2500 and 2650 m a.s.l. (Figure 5.2.5 a). As few GPS measurements were carried out during each year, for this comparison we referred to displacement rates averaged over the entire time span covered by GPS (2015 to 2019), which were projected along the descending Sentinel-1 satellite LOS.

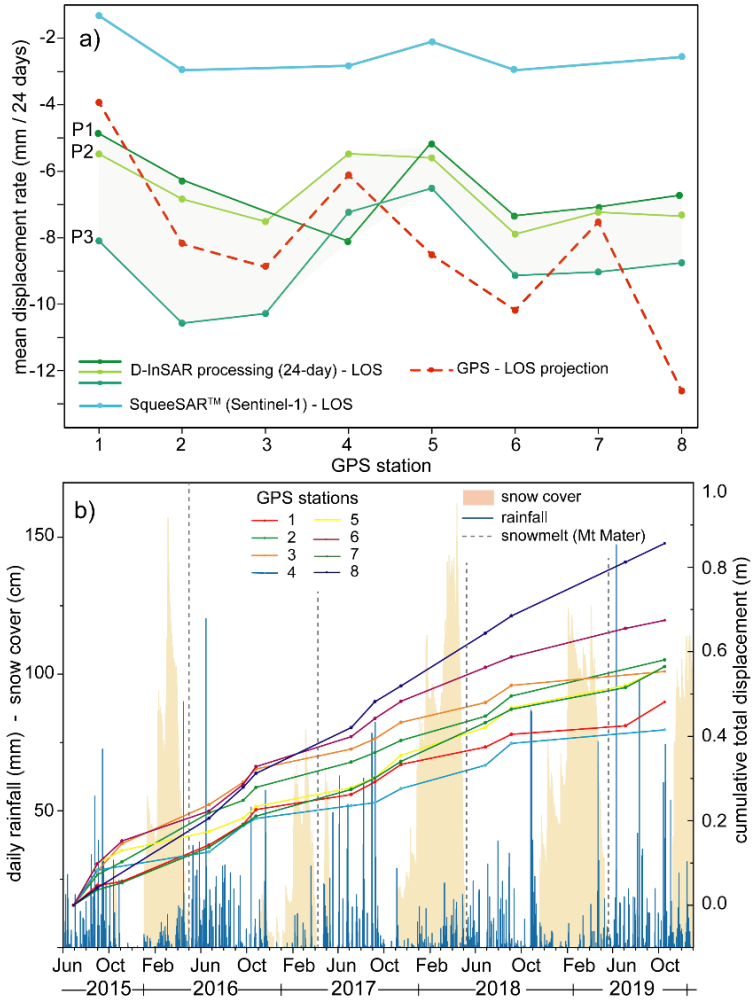


*Figure 5.2.13: Spatial and temporal trends of activity from GPS and DInSAR data. (**a**) spatial trends of displacement rates derived from SqueeSAR™, DInSAR and GPS data, extracted at GPS benchmark locations and scaled to a 24-day period. SqueeSAR™ data were processed over a 2-year acquisition period; GPS displacement rates are derived from cumulative displacements averaged over the 4-year observation period and projected along the Sentinel-1 LOS; DInSAR displacement rates were extracted from three unwrapped 24-day interferograms (P1: 14/06/2017-14/07/2017; P2: 02/07/2017-26/07/2017; P3: 12/09/2017-06/10/2017) ; (**b**) time series of cumulative GPS 3D displacements compared to daily rainfall and snow cover (data: ARPA Lombardia).*

GPS data show evident seasonal trends, characterized by increased displacement rates in the early summer-autumn period (June to October) as an effect of combined snowmelt and rainfall (Figure 5.2.13 a). In fact, due to the high elevation (2800 m a.s.l.), snowmelt in this sector usually starts around the end of May, later than usually observed at the valley floor. In the snowmelt period, major portions of the slopes are still covered by snow, hampering DInSAR processing (Ferretti et al., 2011; Wasowski and Bovenga, 2014; Bovenga et al., 2018) and accurate quantification of snowmelt contributions to displacements.
Seasonal interferograms (Figure 5.2.12 c) with longer temporal baselines clearly highlight continuous displacement fields, corresponding with: a) localized deformation along the major DSGSD scarps at 2600 m and 2700 m a.s.l. (Figure 5.2.5 and Figure 5.2.12 d), occurring at rates of several millimeters per seasonal cycle. This signal is very different from that of shallow debris movement detected in 24-day interferograms (Figure 5.2.12 b) and reflects deep-seated slow deformations; b) displacements of the head and internal sectors of the northern nested landslide below 2400 m a.s.l. (Figure 5.2.5, Figure 5.2.12 d), at rates up to 5 mm/month depending on the period (Figure 5.2.14) movements up to 3–4 mm/month (Figure 5.2.14) of the southern nested landside head at 2100 m a.s.l. and the strongly segmented above sector, up to a neat curved scarp at 2500 m a.s.l. (Figure 5.2.5, Figure 5.2.12d).
DInSAR-derived displacement maps report for these sectors velocities ranging from a mean value of 1.5 to 4 mm/month, depending on the considered seasonal period (Figure 5.2.14).

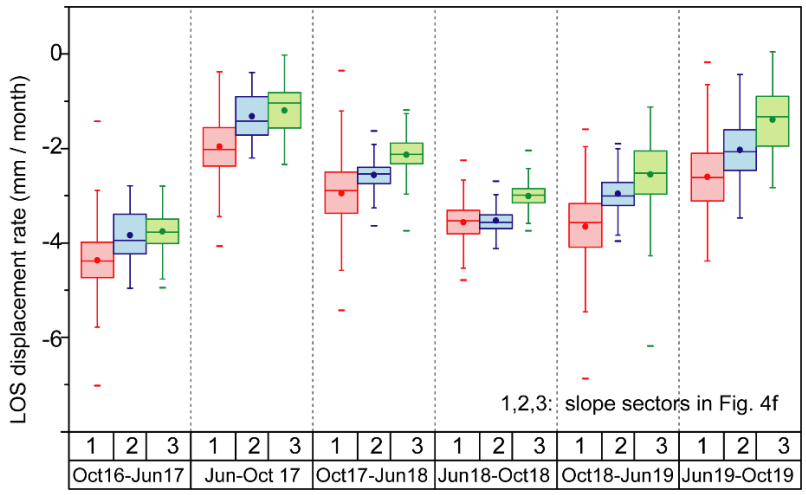


*Figure 5.2.14: Seasonal response of slope sectors. Distributions of LOS displacement rates extracted from seasonal interferograms (Jun-Oct and Oct-Jun) for the 3 sectors highlighted in Figure 4f. Whisker lengths: upper and lower inner fences based on interquartile range (IQR).*

This suggests a differential seasonal response also for the middle slope sector, with variable trends conditioned by the snowmelt timing and rainfall input in the across winter and springtime.
To better constrain this observation, we selected three slope sectors (Figure 5.2.12 f) corresponding to the nested landslides heads and above scarps (sectors 1 and 2) and the area in between (sector 3). We compared displacement rate distributions between the three

sectors during consecutive seasonal periods, from 2016 to 2019. Boxplots in Figure 5.2.14 show that displacement rates change seasonally in response to the magnitude and timing of different hydrological inputs, with variable trends through the considered years. In 2016–2017, when snowmelt started early in April (Figure 5.2.13 b), displacement rates recorded across the snow cover periods (Oct-Jun; about 4 mm/month) were higher than in the summer period (Jun-Oct; about 1.5 mm/month).

An opposite behavior is observed for 2017-2018. In this case, snowmelt occurred later Figure 5.2.13 b) and its contribution is recorded by the summer interferogram, with larger displacement rates between June and October (Figure 5.2.14). In the 2018-2019 period, despite late snowmelt (May; Figure 5.2.13), abundant rainfall during autumn and spring triggered an anticipated acceleration, with mean LOS displacement rates of about 3.5 mm/month. While consistently reflecting seasonal changes, displacement rates in the three considered sectors confirm a sharp internal segmentation of the DSGSD. The northern nested landslide (sector 1) is always faster than the southern one (sector 2) and both are faster than sector 3, which is interpreted as representative of the background DSGSD activity.

Because of the low signal to noise ratio and poor coherence, we could not derive reliable unwrapped displacement maps from 1-year interferograms. However, wrapped phase maps (Figure 5.2.12 e) still provide valuable information on the persistent, pluri-annual displacement signal of the DSGSD. In fact, two fringe cycles are evident in the nested landslide sectors and a coherent signal turns out between them in the central part, corresponding to the previously identified sector 3. Such signal unlikely results from shallow movements in the debris cover, which would decorrelate with such a long temporal baseline.

### 5.2.4.1 Comparison between spaceborne DInSAR and GB-InSAR

We compared the results provided by out DInSAR processing to GB-InSAR measurements (Figure 5.2.15) acquired from 2017 to 2019 in the period June-October.

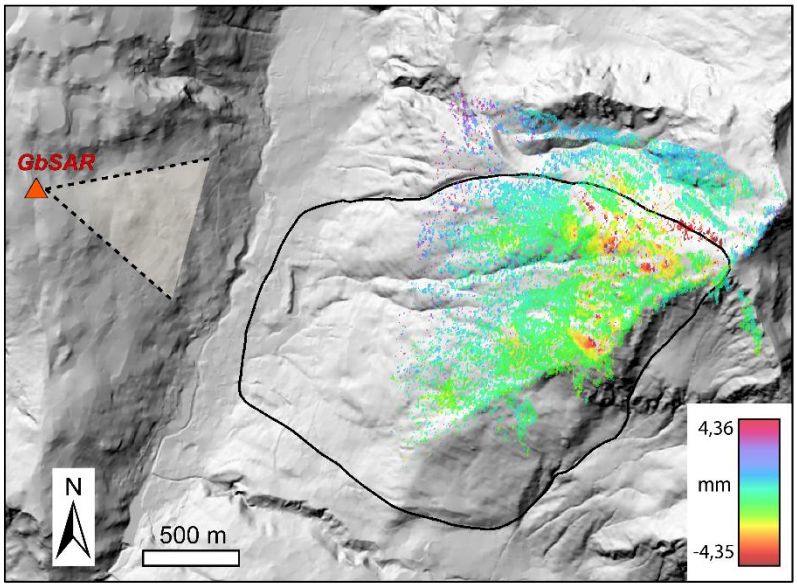


*Figure 5.2.15: GB-InSAR position and sensing area on Mt. Mater Slope.*

To this aim, we extracted two longitudinal slope profiles (AA') and (BB') crossing the two main nested landslides (Figure 5.2.16 a, b) from about 2400 to 2000 m.a.s.l. and plotted LOS velocity values both from Sentinel-1 and GB-InSAR interferograms considering values within a lateral buffer of 15m on each side from the profile trace.
To refine DInSAR products we attempted to remove as much atmospheric component as possible applying GACOS correction on selected Sentinel 1 interferograms (Figure 5.2.16). When possible, we selected Sentinel-1 images covering the same period of GB-InSAR Jul-Sept acquisition campaigns (i.e. processing Sentinel interferograms over 3 months from July to Septermber), but in the case of low quality computed interferograms we kept the results of the seasonal interferograms closer to those same campaigns (i.e. seasonal interferograms from June to October). Velocity values were then rescaled on the number of span days and expressed as velocity (mm) per week.
GB-InSAR and DInSAR trends result comparable (Figure 5.2.16) but they show an almost constant velocity shift in each period within a maximum range of 0.5 mm/7dd (Figure 5.2.16 e). This shift is not completely ascribable to atmospheric contribution since even removing the atmospheric delay from the unwrapped displacement, we can't gain a complete overlap of the two curves.

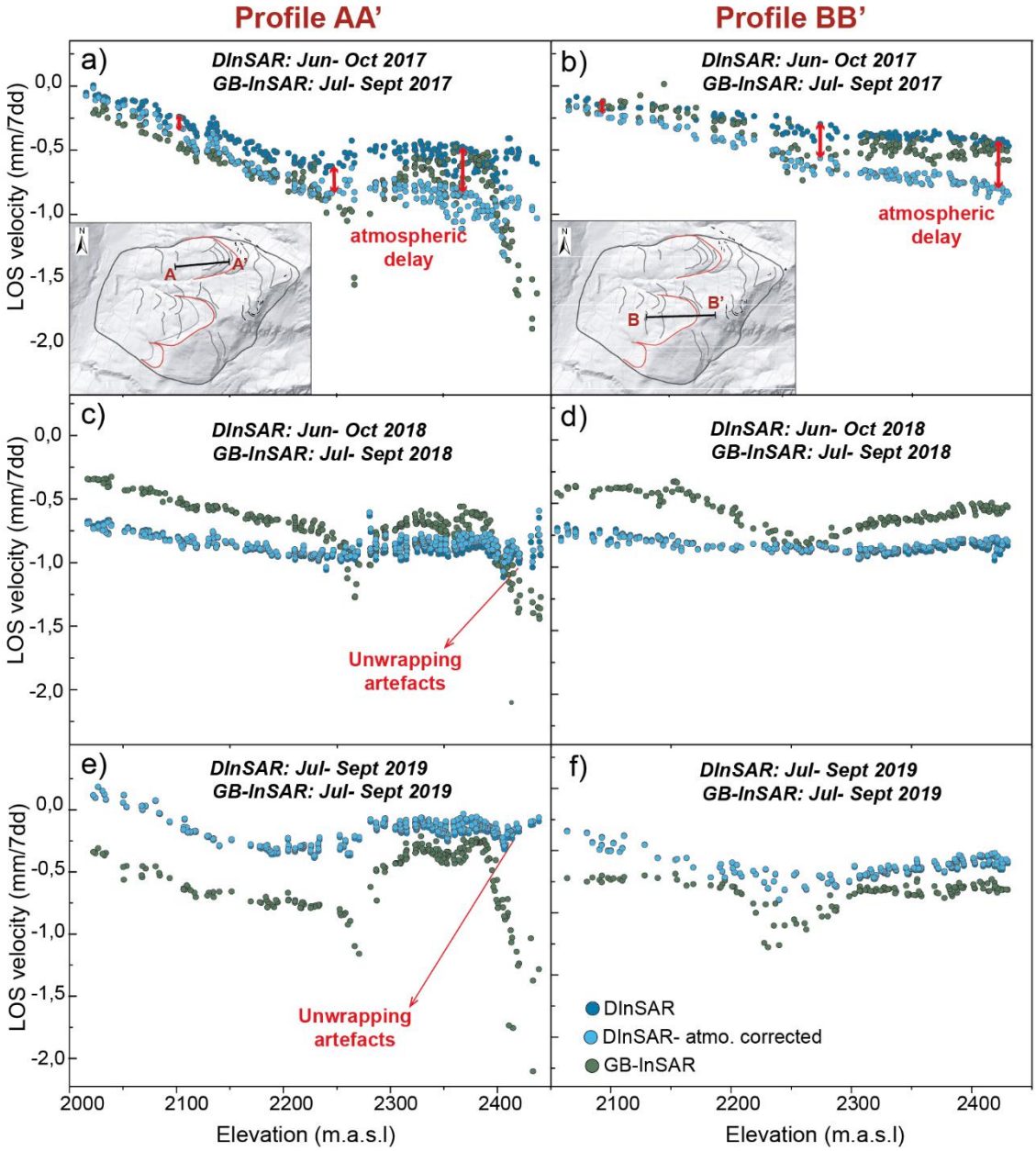


*Figure 5.2.16: Comparison between GB-InSAR, DInSAR and DInSAR values corrected for the atmospheric contribution. Profiles are extracted along the two nested landslides. AA' corresponds to the northern nested landslide, BB' to the southern one.*

This difference should therefore be due to other factors, including:

- the difference in LOS direction acquisition: GB-InSAR has a variable LOS changing from a minimum of 9° to a maximum of 15°, while Sentinel 1 senses the scene with an angle of 35°. Because of the different inclination of the LOS, the two sensors also capture differential components of the real movement: Sentinel-1 better catches vertical displacement components, while GB-InSAR is more sensitive to sliding movements.
- errors in the unwrapping step: some points that result in the GB-InSAR profile as high velocity points appear "rolled" in the DInSAR one because of unwrappimg artefacts;

- local atmospheric effects that are only partially compensated and are differentially corrected in the GB-InSAR (through a statistical approach) and DInSAR processing (subtraction of a delay model);
- the different acquisition temporal baseline.

Despite these discrepancies both the DInSAR and GB-InSAR profiles show local negative velocity peaks corresponding to active scarps inside the two nested landslide (e.g. 2400 m.a.s.l. scarp sector in the AA' profile and 2250 m.a.s.l. headscarp sector in the BB' profile). This demonstrates that a targeted spaceborne DInSAR analysis approach allows to minimize noise effects and extract reliable displacement rates in the order of few millimetres, especially on those slope that are favourably oriented towards the satellite LOS.

### 5.2.5 Discussion

Successful slope-scale DInSAR applications have been presented in the literature for slow-moving landslides characterized by displacement rates far exceeding 5 cm/year and relatively homogeneous displacement fields (Handwerger et al., 2013; Schlögel et al., 2015; Kos et al., 2016; Manconi et al., 2018). Slower movements typical of DSGSD (Agliardi et al., 2012; Frattini et al., 2018) are close to the limits of detection of DInSAR, moreover atmospheric and snow-cover disturbances strongly affect the quality of remote sensing products. Although persistent-scatterers interferometry (PSI) techniques proved their ability to measure displacement rates of a few mm/year for coherent targets (Wasowski and Bovenga, 2014; Frattini et al., 2018;) due to their point-like nature, they often fail at capturing a complete picture of the spatial variability associated to slope failure mechanisms. Our study shows that integrating field morpho-structural observations, remote sensing data from different InSAR techniques and ground-based monitoring allows a successful detail-scale investigation of heterogeneous, very slow-moving rock slope deformations.

In the first stage, we exploited PSI data to retrieve a sound interpretation of the global kinematics of the DSGSD (Figure 5.2.11). However, these data have a point-like, sparse nature, making them unsuitable to capture the spatial heterogeneity of the phenomenon. Moreover, SqueeSAR™ data processed over large areas are usually unable to account for the temporal patterns of activity of individual very slow-moving DSGSD and the site-specific atmospheric and snow cover disturbances, which greatly affect the local signal to noise ratio. Thus, we adopted a targeted DInSAR processing approach integrating multi-temporal baseline interferograms (2016-2019) constrained by detailed field morpho-structural observations and GPS data to unravel the deformation patterns and trends of activity in a spatially distributed fashion (Figure 5.2.12).

DInSAR processing, specifically designed on the spatial and temporal scales of slope processes associated with DSGSD, provides data consistent with ground-based GPS and GB-InSAR measurements. As the ability of GPS to measure very small displacements is limited by several error sources such as satellite coverage, temperature changes, and ground dilation for each GPS benchmark we considered displacement rates averaged over the entire 4-year measurement period. Despite smoothing non-linearities of the GPS time series, this

reduces the errors associated with individual measurements and provides a consistent figure of persistent displacement rates. GPS and DInSAR displacement rates consistently settle within about ±2 mm/24 days, according to the specific 24-day period covered by interferograms. Despite keeping the same spatial trend of DInSAR products obtained with targeted temporal baselines, SqueeSAR™ data processed over large areas (Ferretti et al., 2011) always underestimate displacement rates (Figure 5.2.13 a). This might be caused by reduced spatial coherence (quality) of the interferograms included in the SqueeSAR™ analysis (mainly associated with long temporal baselines considered and/or the occurrence of relatively large spatial/ temporal phase gradients), which might result in underestimations of local surface velocities (Manconi et al., 2018).

Selecting image pairs covering different temporal windows (i.e., 24-days, seasonal, annual) allows us to maximize the sensor detection capability for complex phenomena, extracting slope displacement rates, that in the studied case range between more than -15 mm/month and less than -3.5 mm/month. These very different values are typical of associated slope instability processes acting on different scales (e.g., shallow vs deep-seated sliding, nested landslides). Failing to discriminate among these different processes can lead to a misleading interpretation of the overall slope instability mechanisms with major impacts on the assessment of risk components (e.g., scenario volumes, intensity), that can be strongly over- or underestimated. Moreover, 24-day and seasonal interferograms effectively highlighted active sectors characterized by different spatial patterns and rates of displacements.

Combining mapping and morpho-structural information with remote sensing constraints on kinematic and spatial segmentation of the slope, we were able to provide an interpretative geological model of Mt. Mater slope (cross-section in Figure 5.2.17), even without the support of investigations. Different morpho-structures and their associations are witnesses of different deformation mechanisms and provide a first insight into the kinematic behaviour of the landslide. We mapped several orders of persistent scarps that dissect the slope from the edge to the toe and only a few minor counterscarps that cut the southern border of the DSGSD towards the Groppera valley. This morpho-structural assemblage suggests a translational sliding mechanism characterized by synthetic structures developing at different depth levels and bounding discrete sectors. Field surveys and aerial photo interpretation revealed that the slope deformation is sliced by secondary large landslides, nested at different depths within the main DSGSD. These are characterized by rotational movements in the head sectors, where the highest vertical displacements are recorded, and by a variable amount of internal damage. The presence of nested sectors reflects a deep complexity of slope deformation mechanisms, controlled by multiple shear zones almost parallel to the slope profile (Figure 5.2.17).

While 1-year interferograms provide a picture of long-term background DSGSD displacement signals, the combined analysis of seasonal interferograms and GPS data outline a sensitivity of the different slope sectors to hydrological forcing. Displacement rates in the middle-upper slope are dominantly sensitive to snowmelt, modulated by spring rainfall depending on the relative timing and magnitude of the two contributions. This induces differential responses across the snow cover period and the summer season. The large

landslides nested in the main DSGSD mass exhibit similar styles of activity but deform at displacement rates higher than the background signal of the DSGSD.
This may be due to the development of different shear zones at shallower depth from the toe to the top and their different degree of evolution that condition the response of the relative slope sectors to hydrological inputs.

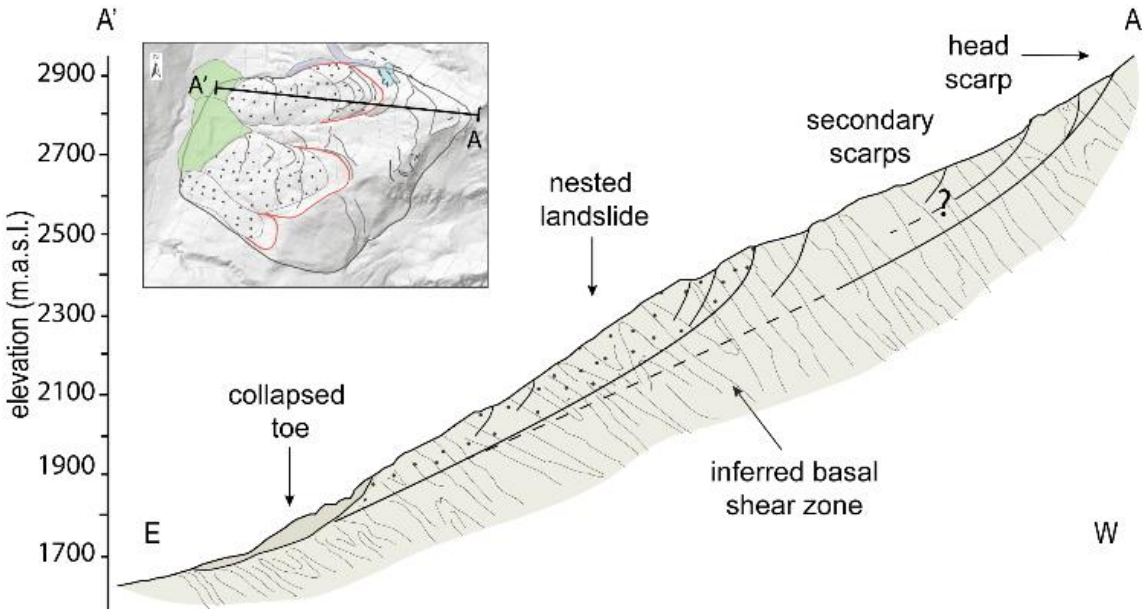


*Figure 5.2.17: Interpretative cross-section across the northern sector of the Mt. Mater slope. DSGSD morpho-structures, basal shear zones and nested landslides are reconstructed from field evidence and interpretation of DInSAR displacement patterns. Cross-section trace is shown in the inset.*

Our approach, that can be applied also to other slow rock deformations in different geological and geomorphological settings, proved to supply key information (i.e. internal segmentation, style of activity, forcing) required to define reference scenarios for risk analysis and mitigation of a widespread, yet challenging class of slope instabilities.

## 5.3 Sensitivity to hydrological trigger: Saline DSGSD

### 5.3.1 Geology and Geomorphology

The Saline Ridge DSGSD develops on the right side of Valfurva and, together with Corna Rossa DSGSD, it defines the Confinale sakung (section 5.1.1 and Figure 5.1.1).
The slope instability affects the entire NW side of Mt. Confinale from 1400 to 2900 m.a.s.l. (Figure 5.3.1 a) and it is characterized by the same geological background presented in section 5.1.1 for Corna Rossa case study.
The slope is made of pluri-deformed phyllites and micaschists that, since late Oligocene, were affected by several brittle deformation stages which led to the formation of persistent fracture systems (Figure 5.3.2, Figure 5.3.3) recognisable both at the slope and outcrop scale. Four main sets of structures have been mapped along slope (Agliardi et al., 2001): these comprise fractures, including joints and faults, from steeply dipping to subvertical trending WNW-ESE or SSW, NE-SW striking joints and steep normal faults, N-S oriented fractures and minor E-W trending fractures.
The geomorphological setting of the study area is typical of the Alpine environment of this sector of the axial Central Alps, where glaciers carved the valleys during the Last Glacial Maximum (LGM) and strongly reshaped the valley flanks. Clear evidence of glacial erosion are recognizable in frequent cirques in the upper portions of tributaries valleys (i.e. Valle del Confinale), connected to the main Valfurva by different orders of glacial steps, striated rock surfaces and roches moutunées. Widespread slope deposits, including till, rock glaciers and talus, cover the slope (Catasta and Smiraglia, 1978). Debris and glacial deposits mantle extended portion of the slope with lithologies outcropping in the upper portion of the valley and here transported by Valfurva glacier. Many glacial deposits, post LGM, are reshaped by slope dynamics and appear as patchy covers. Similarly, also rock glaciers, both in Cavallaro and Confinale valleys, are cut by DSGSD morpho-structures and allow to set constraints on the age of the gravitational deformation (Agliardi et al., 2001).

### 5.3.2 DSGSD morphostructures

The Saline DSGSD is clearly bounded by a huge headscarp (Figure 5.3.1 a, c) and by a continuous lateral scarp that defines a deep oblique slope deformation. At the top of the slope, a NNE-SSW trending scarp delimits a triangular facet that display a maximum downward displacement 140m (Agliardi et al., 2001). Nowadays, the main scarp is extensively covered by scree deposits and accompanied by a swarm of curved listric counterscarps, that outline a local active wedge accommodating a rotational component of DSGSD displacement in the uppermost slope sector (Agliardi et al., 2001; Riva, 2017).

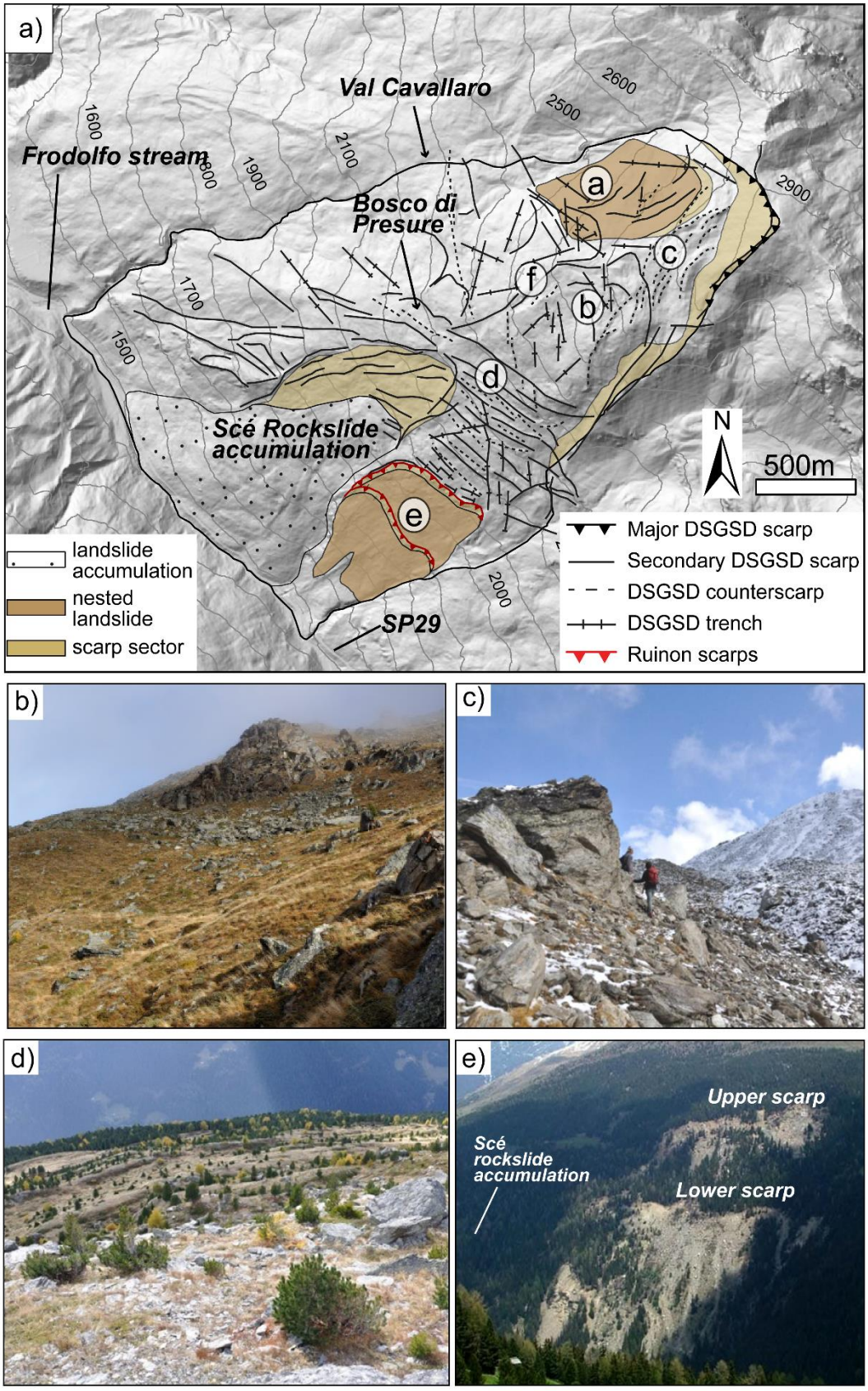


*Figure 5.3.1: Main features of the Saline DSGSD (**a**) Simplified map portraying the main morpho-structural features associated with DSGSD and nested landslides (**b**) nested and highly deformed DSGSD sector; (**c**) counterscarps cutting the upper eastern side of the DSGSD; (**d**) half graben systems with associated scarps and counterscarps; (e) Ruinon rockslide and Scé rockslide accumulation hidden by vegetation.*

Steep scarps and counterscarps also dissect a rockslide block moving towards Val Cavallaro at a significant displacement rate (Figure 5.3.1 a label a, Figure 5.3.2)
NE-SW trending structures (Figure 5.3.1 a, label f).mainly consisting of rectilinear scarps, divide the upper mid slope sector in two different portions displaying different degree of activity and morpho-structural evidences. The WNW side is cut by several orders of scarps and trenches with minor evidences of an intense past activity, while on the ESE side a nested highly deformed sector is found (Figure 5.3.1 a label b, Figure 5.3.1 b, Figure 5.3.2). It is bounded by an arcuate steep scarp at the top and dissected by several trenches differently oriented. Below it, a thick swarm of WNW-ESE trending scarps and counterscarps (Figure 5.3.1 a label d, Figure 5.3.1 d, Figure 5.3.2) testifies a gravitational reactivation of inherited fractures.

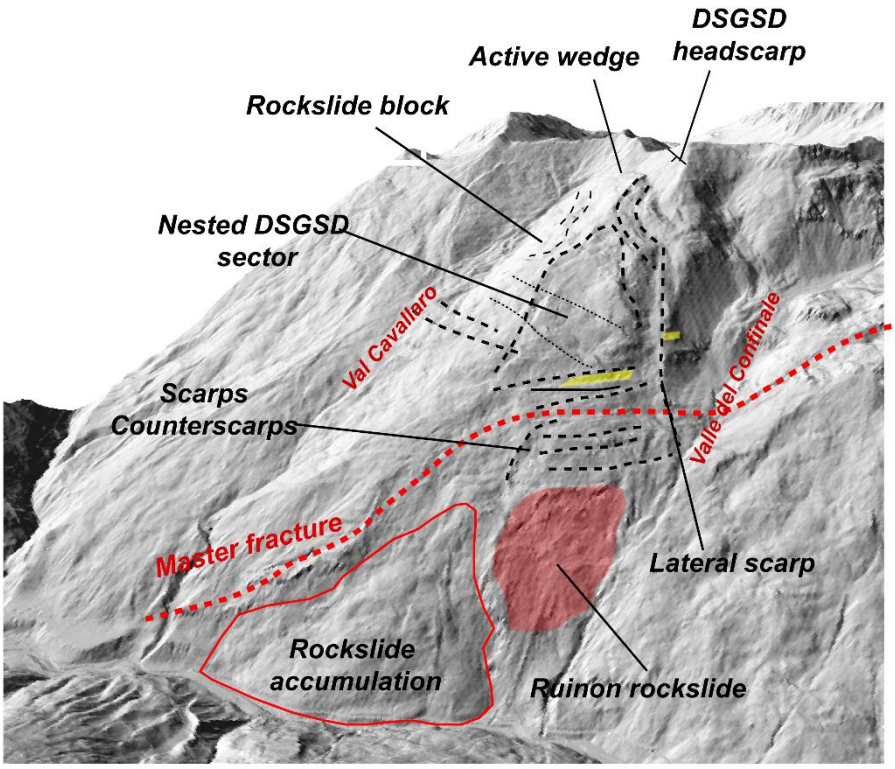


*Figure 5.3.2: 3D view of the Saline DSGSD (Lidar, 1m) and main morphostructures.*

These are arranged in half graben-like asymmetric systems up to 20- 30 m wide. Open cracks are here filled with blocky debris and show an average accumulated downthrow of 20 m. Going downslope these features progressively fade into convex trenches with strong evidence of activity until 2100 m.a.s.l where the active Ruinon rockslide (Figure 5.3.1 a label e, Figure 5.3.1 e, Figure 5.3.2) occurs (Agliardi et al., 2001; Crosta et al., 2017).
This rockslide is strongly influenced by inherited structural features and it is controlled in its upper part by the same tectonic lineament (master fracture in Figure 5.3.2) that extends from the valley floor to Corna Rossa ridge defining its upper headscarp (Crosta and Agliardi, 2003a; Crosta et al., 2017; Agliardi et al., 2018; Agliardi et al., 2019). Ruinon is further characterized by two major scarps: the upper scarp (2100 m a.s.l.), exposes disturbed rock masses and is affected by rock falls, while the lower scarp (1950 m a.s.l.), involves crushed

rock mass and a thick debris cover that induce shallower instabilities like debris slides and debris flows (Crosta et al., 2017)

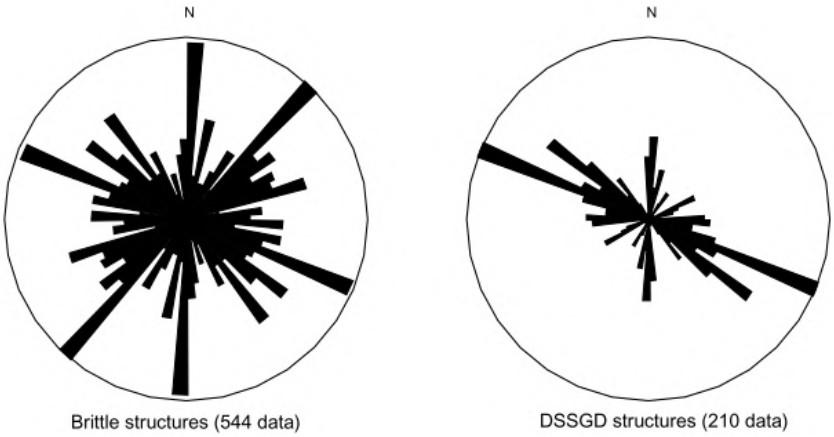


*Figure 5.3.3: Stereoplots of (a) brittle tectonic features and (b) DSGSD structures affecting the slope.*

Ruinon poses a major hazard for the huge involved volumes (estimated in up to 15Mm$^3$) and its rapid movement, with displacement rates upt to m/yr in its most active sectors (lower sectors). Boreholes and site investigations reveal shear zones localized at 30 to 70m in depth (Crosta and Zanchi, 2000; Agliardi et al., 2001; Crosta and Agliardi, 2003a; Casagli et al., 2010;) possibly daylighting at about 1700 m.a.s.l. In case of catastrophic failure, the collapsed rock mass would strike out SP29, the only road connecting the upper Valfurva with the main Valley and dam the Frodolfo river, possibly inducing debris flows and floods. Relict rockslide accumulations covered by vegetation (e.g. Bosco di Presure and Scé rockslide accumulation, Figure 5.3.2) and ESE trending trenches right above the upper rockslide scarp suggest a link between the rockslide activity and the main DSGSD in which it evolves through a progressive failure that affect the entire slope. However, this hypothesis can only be confirmed by analyzing with high accuracy the state of activity of the entire slope, since if the Ruinon rockslide is carefully monitored by ground measurements and GB-InSAR, the above DSGSD sector lack of such detailed monitoring networks.

Previous studies (Crosta et al., 2003, 2017; Casagli et al., 2010; Riva, 2017) have outlined a long-term evolution of the rock slope instability and a retrogression of the Ruinon rockslide up to 2200 m a.s.l., in a slope sector with high rock mass damage. Also considering the retrogressive sector, the total volume of the rockslide reaches 20 Mm$^3$.

Geotechnical site investigations have been carried out from 1988 and include 14 boreholes, equipped with inclinometers, extensometers and piezometers. Surface investigations comprising optical targets, 17 GPS points and a GB-InSAR system (from 2006) are also operating providing detailed surface maps of the unstable rockslide mass with high spatial resolution and temporal sampling.

Ruinon rockslide is highly sensitive to external inputs and its displacement rates consequently vary in intensity and delay. Major displacements are recorded during rainy periods while in the dry and cold seasons, the rockslide slowly creeps in most of the sectors,

with the slower movements recorded in the uppermost rocky sector. Snowmelt contributes to local displacements in absence of rainfall, while the coupling of the two contributions can result in extreme accelerations (especially of the debris cover in the lower sector) and cumulative displacements.

### 5.3.3 Style of activity of Saline DSGSD

Despite the Saline DSGSD has been extensively investigated in the field and by numerical modelling (Agliardi et al., 2001) and the sector surrounding the Ruinon rockslide has been subjected to geotechnical site investigations and forecasting oriented monitoring activities (Crosta and Agliardi, 2003a; Casagli et al., 2010; Crosta et al., 2017), a complete understanding on the mechanisms, style of activity and evolution of the whole DSGSD is elusive and some questions are still open. These mainly concern the activity trend of the DSGSD and its relation with Ruinon rockslide evolution. To unravel these issues and find out possible links between their evolutive patterns, it is of primary importance to characterize the style of activity of the DSGSD integrating the field evidence with spatial distributed and temporal analysis. To this aim, we applied targeted DInSAR analysis to catch possible slope heterogeneities and potential progressive evolutive trends of the main DSGSD main mass, with particular focus on the sector right above Ruinon rockslide.
SqueeSAR™ data (Figure 5.3.4) provide the general displacement rate of the global phenomenon revealing velocities higher than 25mm/yr, but fail in capturing spatial and temporal heterogeneities. In addition, because of its high velocity, only few PS are found on Ruinon rockslide which displacement rate can be captured only by short revisiting time (6

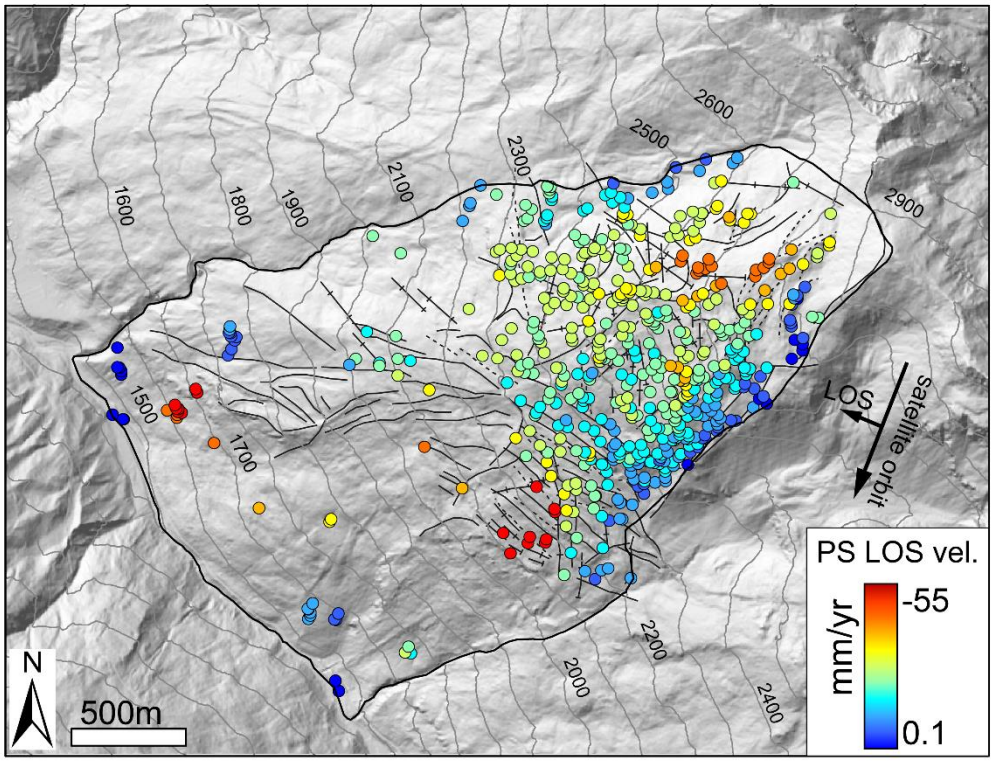


*Figure 5.3.4: SqueeSAR™ dataset (Sentinel-1 descending geometry) covering Saline DSGSD.*

days Sentinel 1) while it is almost lost using longer periods (24 days Radarsat, 35 days ERS).

### 5.3.4 Spatial distribution of activity

Also for Saline DSGSD, targeted DInSAR processing was focused to select the most suitable baseline to highlight slope heterogeneities in a spatial distributed fashion, providing a map of the ongoing displacement patterns.
We used SAR images acquired by Sentinel-1 A/B SLC in TOPS Interferometric Wide swath (IW) mode in descending geometry (track = 168; orbit azimuth $\delta = 8.99°$; mean LOS angle $\vartheta = 41.78°$) from June 2015 to October 2019. For the processing we used the software SNAP (ESA Sentinel Application Platform 7.0.0). Displacement maps (mm) were also extracted unwrapping the processed interferograms through SNAPHU plugin (annex A).
Explorative short baseline interferograms (6 days) and 17 interferograms with increasing temporal baselines from seasonal (summer Jun-Oct and across winter period Oct-Jun) were processed to investigate slope dynamics and potential heterogeneities (Figure 5.3.5).
Short baseline (6 days) interferograms, clearly outline the displacement associated to the presence of Ruinon rockslide Upper Scarp and retrogression areas (Figure 5.3.6 a), but fail in capturing the movement of its lowest sector (m/yr) below the Lower Scarp.

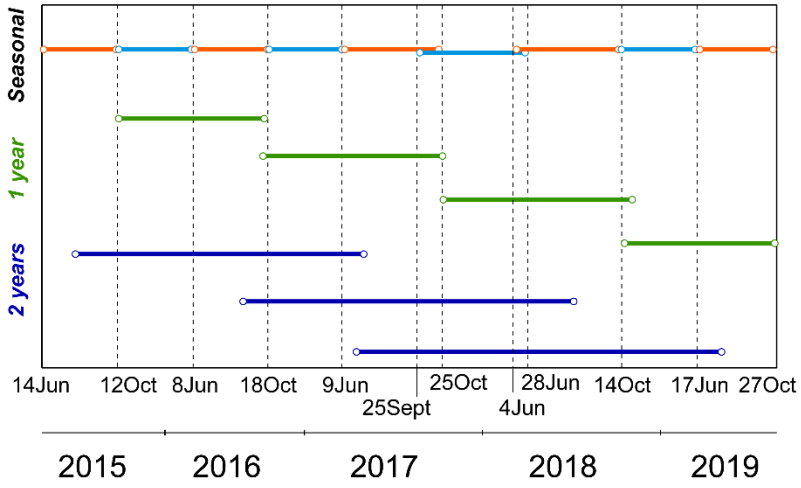


*Figure 5.3.5: Seasonal, annual and biannual interferograms processed over Saline area (Sentinel-1, descending, track 168).*

An almost coherent signal derives from the upper rockslide portion, while the lowest one, that is covered by debris and undergoes very fast evolution with shallower instabilities, decorrelates even in such short periods. The DSGSD main mass on the contrary doesn't display any evident velocity changes in correspondence of active morphostructures keeping an almost homogeneous phase signature (Figure 5.3.6 a).
First signals of the upper DSGSD movement arise from seasonal interferograms (Figure 5.3.6 a, summer: June-October and Figure 5.3.6 b snow cover period: October-June) while the rest of the slope becomes affected by general temporal decorrelation because of the

vegetation cover as usually expected when generating interferograms with long temporal baselines. Similarly, Ruinon, that moves several cm/season, can't be anymore identified because it exceeds the velocity of ambiguity threshold that can be detected.

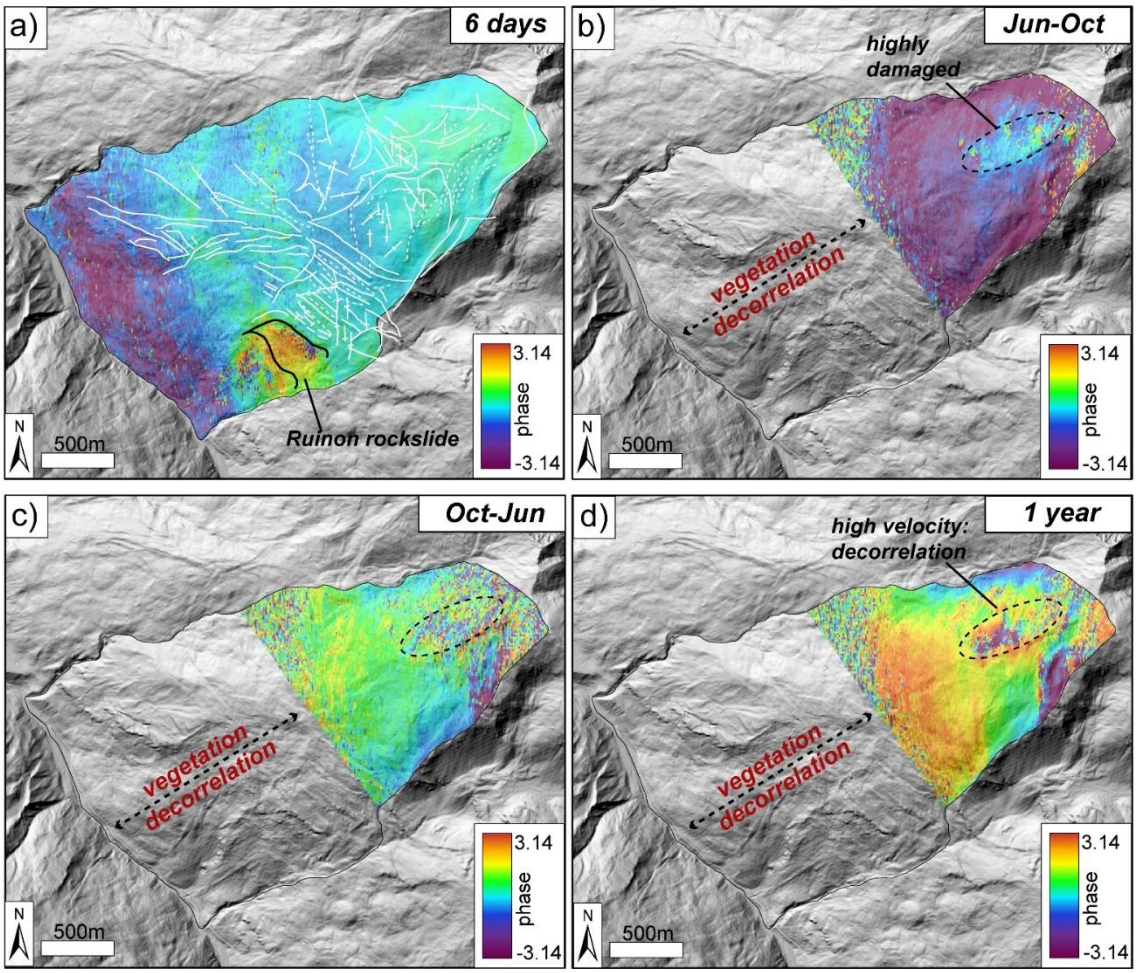


*Figure 5.3.6: Multi baseline interferograms processed over Sentinel DSGSD area. a) short baseline interferograms (6days) outline the presence of Ruinon rockslide and its partition in 2 main sectors with different displacement rate. The lowest sector is covered by debris and evolves faster than the upper one thus resulting decorrelated even a t 6 days. Longer baseline b) summer i (Jun-Oct) and c) across winter interferograms present complete decorrelation in the lowest slope sector but keep a coherent signal in the upper DSGSD portion in which a fast sliding wedge is identified. d) 1-year baseline interferograms still present good coherence values but don't highlight an evident slope segmentation, except for the active wedge that lose coherence.*

Seasonal interferograms also show how the active rockslide block (label a in Figure 5.3.1) highly damaged and crushed evolves faster than the main DSGSD (Figure 5.3.6 b, c), with a sliding movement constrained by several orders of scarps towards Val Cavallaro.
Clear fringes can't be detected, but phase changes seem to point out a major deformation of this latter sector in the across winter period rather than in the summer season because of the increasing decorrelation in the Oct-Jun period. A major response also comes from the counterscarps bounding the SE side of the DSGSD, but a quantification of their displacement rate is made difficult by the lack of closed and clear fringes.
Except for these sectors, the slope seems to deform homogeneously without sharp variations or presence of segmented sectors, as in the case of Corna Rossa DSGSD.

We thus generated interferograms with longer temporal baseline to 1 and 2 years to further confirm this observation, but reaching a critical SNR due to the increasing spatial and temporal decorrelation.

1-year interferograms are still unable to outline evident spatial differences in the activity of the upper DSGSD sector, but confirms the presence of the active rockslide block and of the headscarp sector (label c in Figure 5.3.1). The nested SE sector (label b in Figure 5.3.1 and) that over the long term has accumulated significantly higher internal deformation with respect to surrounding according to field evidence, doesn't show evidence of differential activity in the interferograms, suggesting that the entire slope sector is presently moving at the same rate.

To support this observation and investigate the annual response of the slope, we considered 5 representative areas (Figure 5.3.7), for which we sampled the velocity values (mm/yr) at each pixel of the annual interferograms of four consecutive years.

The five sectors were selected as follows:

- Sector1: corresponds to the evolved and highly deformed SE sector delimited by a sharp arcuate scarp and dissected by evident morphostructures (trenches and scarps), testifying a past intense activity.
- Sector 2: corresponds to the extensional area associated to semi graben system formed by thick swarm of WNE-ESE trending structure. This sector is right above Ruinon rockslide and might be more influenced by its activity.
- Sector 3: corresponds to the rockslide block highly deformed and crushed that slides towards Val Cavallaro.
- Sector 4: located close to sector 1 from which it is separated by a major ENE-WSW trending scarp.
- Sector 5: on the WNW side in a slope portion cut by scarps and trenches but displaying minor evidences of past evolution than sector 1.

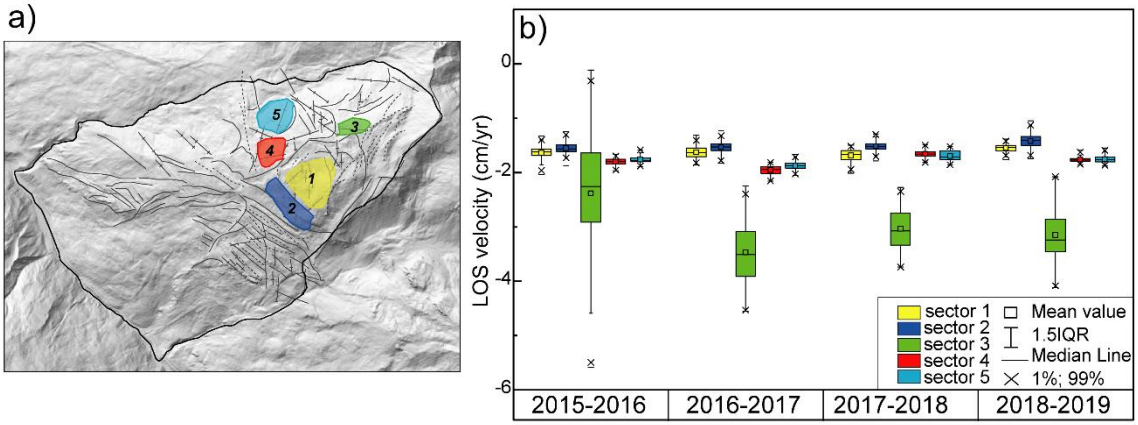


*Figure 5.3.7: Analysis of annual velocity trends of representative slope sectors. a) Representative sectors selected along slope; b) annual displacement rate associated with each sector.*

Sector 3, despite being the smallest one, clearly results the most active in all the considered periods and the one with a highest velocity variability. This may also be due to the noise

contribution and unwrapping uncertainties affecting the upper sliding wedge on long baselines as well as to the blocky and highly damaged structure that induces high variability in the values.

As general trend, all the five sectors have a more or less constant annual velocity (from 1.7 to 2cm/yr for sectors 1,2,4 and 5; from 2 to 3.5 cm/yr for sector 3), but a relative velocity variability seems to arise between sector 1 and 2, that always keep lower displacement rates (1.6-1.7cm/yr), and sector 4 and 5 that display slightly higher displacement rates (1.7-1.9 cm/yr). This observation isn't straightforward because, at first glance, from phase maps no clear heterogeneity can be found between these slope portions or can be linked to corresponding morphostructures.

We thus pushed further the analysis, by generating interferograms with considering an even longer temporal baseline covering 2 years (Figure 5.3.8) to enhance the possible spatial heterogeneities in the activities of the two adjoining slope sectors, A and B in Figure 5.3.8 c. 2-year wrapped interferograms emphasize the different phase signature of the two sectors (Figure 5.3.8 a). In addition, we computed a median stack both on the wrapped (Figure 5.3.8 b) and unwrapped (Figure 5.3.8 b, c) product to highlight the background signal constantly affecting the slope. Slightly different velocity rates are found for the two sectors with a mean difference of almost 16% (Figure 5.3.8 d).

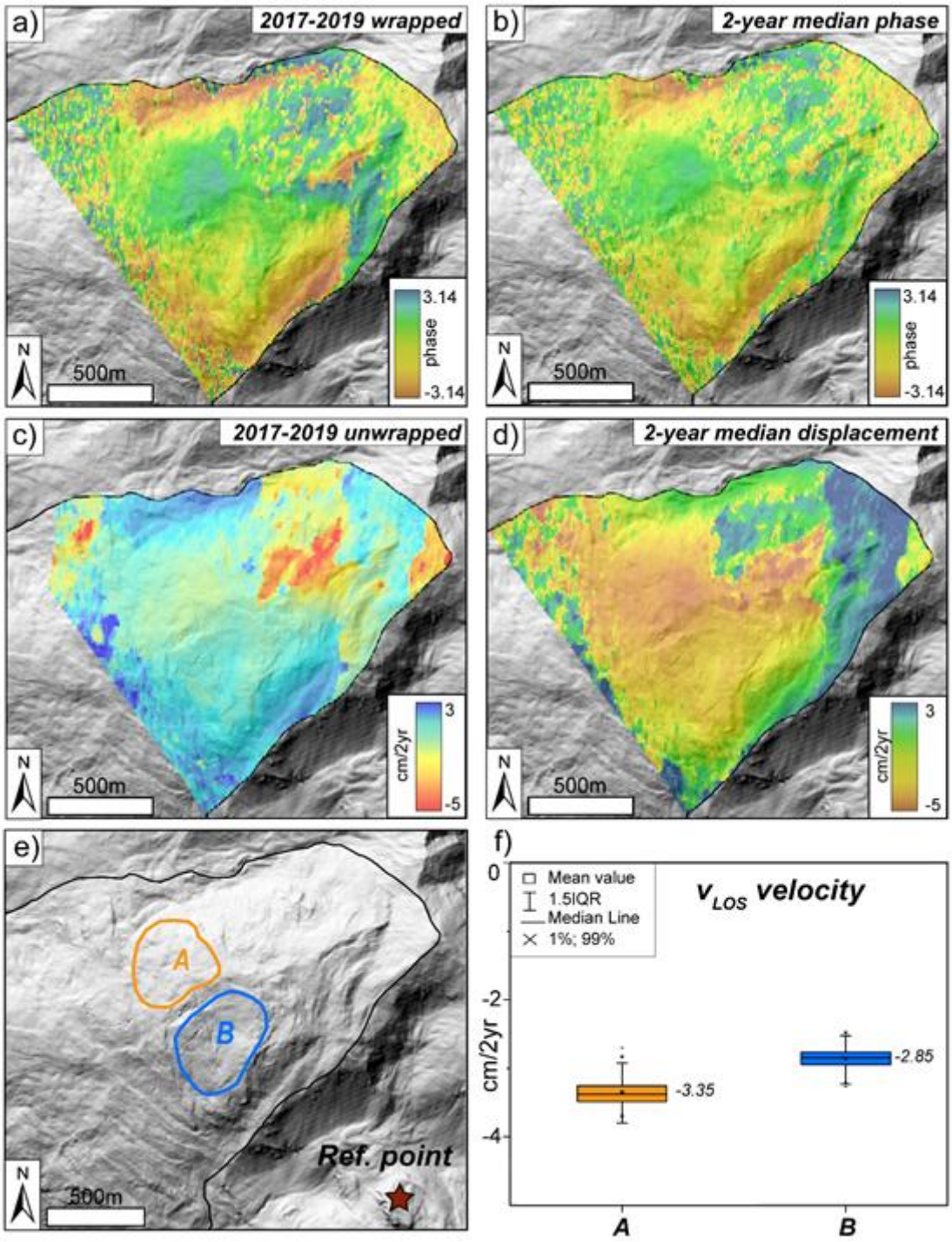


*Figure 5.3.8:Analysis of slope segmentation through biannual interferograms processing a) Wrapped 2-year baseline (2017-2019) interferogram; b) median stack computed over the wrapped 2-year baseline interferograms (2015-2017/ 2016-2018/2017-2019); c) unwrapped 2 year interferogram (2017-2019); d) stacking on the 2-year baseline interferograms (2015-2017/ 2016-2018/2017-2019); e) distinct slope sectors with high coherence considered in the analysis f) corresponding boxplots of LOS velocity values extracted from the median stack on the 2-years unwrapped products.*

However, because of the convex morphology of the ridge, that has a sharp aspect change from the NW (A) to the SE (B) side from a mean value of 285° for sector A to 243° for sector B (Figure 5.3.9 a), the observed velocity variability may be due to the different LOS sensibility towards the slope more than real displacement heterogeneities.

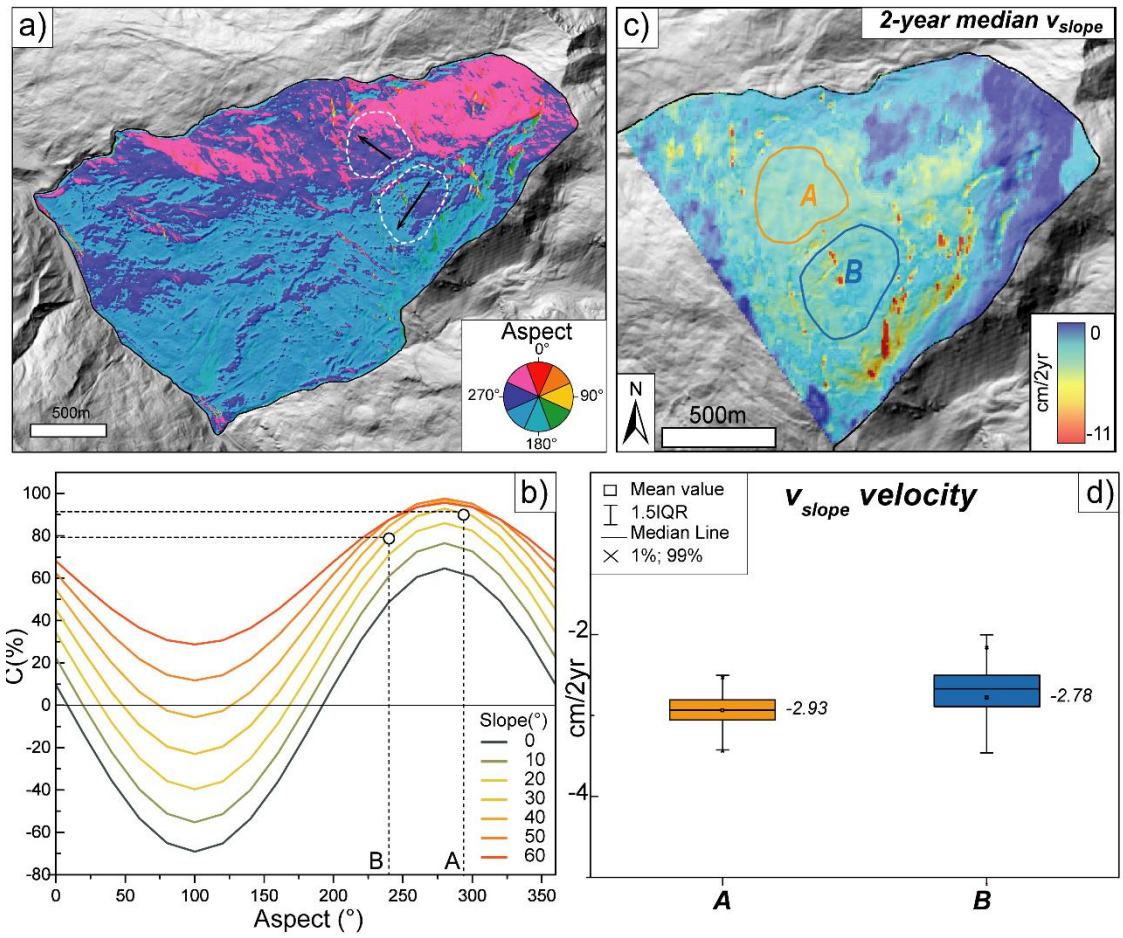


*Figure 5.3.9: velocity correction for slope orientation. a) Northerness map. Saline ridge has a peculiar slope orientation with abrupt change of northerness from the NW sector to the SE. white circles correspond to A and B sectors while white arrows indicate the direction of movement along the steepest slope direction; b) difference in C value (percentage of measured displacement vector) corresponding to the A and B sectors; c) map of along slope velocity computed as $v_{LOS}/C$; d) boxplots of $v_{SLOPE}$ velocities extracted for the two slope sectors.*

As discussed in section 2.2.7, different combination of slope, aspect and LOS inclination lead to different sensing sensibility. In our case, considering a mean slope value of 30°, we can give a first quantification of the movement registered by Sentinel 1 (descending geometry) considering the curves in Figure 5.3.9 b. The two sectors are well sensed by the sensor, having a C index higher than 75%, but their relative displacement vector is measured with a 15% difference. We investigated this possibility correcting the LOS velocity values for the orientation bias projecting the values along slope (see section 2.2.7) (Notti et al., 2012). This is a reasonable assumption for Saline DSGSD since the global kinematics is mainly translational (Agliardi et al., 2001) and thus the along slope projected value are still

representative of the ongoing displacement style. For each pixel we computed the C value and extracted $v_{slope}$ value dividing the LOS velocity by the so computed C index. To avoid overestimation of the projected velocity we excluded C values between -0.2 and 0.2.
What we observe is that median $v_{slope}$ map appears smoother than $v_{LOS}$ one and the signal between section A and B is mitigated (Figure 5.3.9 c). Also the difference between the mean velocities of the two sectors is reduced from 16% to 5% (Figure 5.3.9 d). Therefore, also considering 2-year interferograms, there isn't an evident displacement variation between the 2 sectors and the great differential deformation of the nested sector (SE) can't be linked to the actual displacement rate, but it is produced by a long term strain accumulation. In this case spaceborne InSAR (band C) results thus ineffective in capturing small differential displacement rates or non-linear trends in the range of sumbmillimetric differences over 2 years for complex phenomena like DSGSDs in alpine environment.

### 5.3.5 Temporal trends of activity

Detailed analysis have been done on Ruinon rockslide to unravel its response to precipitations and snowmelt (Crosta et al., 2017), while the activity, temporal trends and relationships with hydrological forcing of the main DSGSD mass has never been analysed.
Thus, we analysed the temporal trends and relationships between seasonal DSGSD activity and external hydrological triggers (i.e. precipitations and snowmelt) considering the amount of rain and snowfall as well as an approximate index of the snowmelt. The evaluation of precipitation and snowfall contribution on large landslides is fundamental in the definition of their displacement trend. According to the landslide kinematics and depth, seasonal accelerations can be observed related to snow melting periods or prolonged precipitations (deep recharge). Displacements are in fact generally triggered by hydrologic inputs and a correlation between groundwater level oscillations and slope movements has been extensively observed (Angeli et al., 1996; Butterfield, 2000; Corominas et al., 2005; Lollino et al., 2006; Helmstetter and Garambois, 2010). Since Saline DSGSD is an extremely deep slow rock slope deformation, in the analysis we took into account both the precipitations and snowmelt triggers considering long cumulative time ranges (month- season).
Precipitations, snow cover and temperature data (ARPA Lombardia) comes from Confinale Station, ~2300 m.a.s.l.. They cover the period 2012-2019 and were acquired with daily measurement with a time interval of 10 minutes. Starting from these, we computed the cumulative monthly precipitation value (mm) and the mean daily snowcover depth (mm). To highlight the total precipitation contribution in each "interferometric season" (i.e. summer Jun-Oct, across winter Oct-Jun) covered by DInSAR analysis, we then computed the cumulative precipitation value over each period (mm/season).
Snowmelt was quantified starting from the snow water equivalent (SWE, Bavera 2008; Bavera and De Michele 2009) parameter, that indicates the water column that would result from the instantaneous melt of the snow pack. SWE is defined as the product between the snow depth and density ($\rho_s$). We computed snow density using the equation proposed by Bavera (2008):

$$\rho_s = 0.038\, z + 0.649\, D - 1.434\, l + 145.030 \ (\mathrm{Kg/m^3}) \qquad \textit{Eq. 33}$$

where:

z= elevation above sea level (m)

D= age of the snow pack as number of days after 1st September

l= local slope (°)

The snow water equivalent (SWE≥0) is then defined as:

$$SWE = \frac{\rho_s}{\rho_w} H_s \qquad \textit{Eq. 34}$$

where

$H_s$= snow depth (m)

$\rho_s$= snow density (200÷650 $\mathrm{Kg/m^3}$) estimated using Eq. *33*

$\rho_w$= water density (1000$\mathrm{Kg/m^3}$)

Several factors interplay in determining the quantity of water deriving from a specific snow pack. First of all, snow compaction results in a primary density uncertainty, then also evapotranspiration affects the precise measure of the real water content.

We computed the SWE starting from temperature and snow height data and applied a correction for the evapotranspiration evaluated according to Turc formula of effective monthly evapotranspiration (ETR):

$$ETR = \frac{P}{\sqrt{0.9 + \frac{P^2}{L^2}}} \qquad \textit{Eq. 35}$$

where:

P= total monthly precipitation (snow+rainfall)

T=mean monthly temperature (°C)

$L = 300 + 15T + 0.05T^3$

Since the ETR (Eq. 35) is a monthly quantification of evapotranspiration, we divided its value by 30 to retrieve and approximate daily factor.

However, comparing SWE and SWE-ETR curves (Figure 5.3.10), it results how evapotranspiration affects the SWE measure only for max 13% and it can't be further refined for the contribution of soil, vegetation and liquid precipitation. So, we didn't consider the influence of ETR in order to avoid introducing further uncertainties, but the gross SWE values, to be intended as the maximum amount of water deriving from the snowpack melt without ETR and compaction loss.

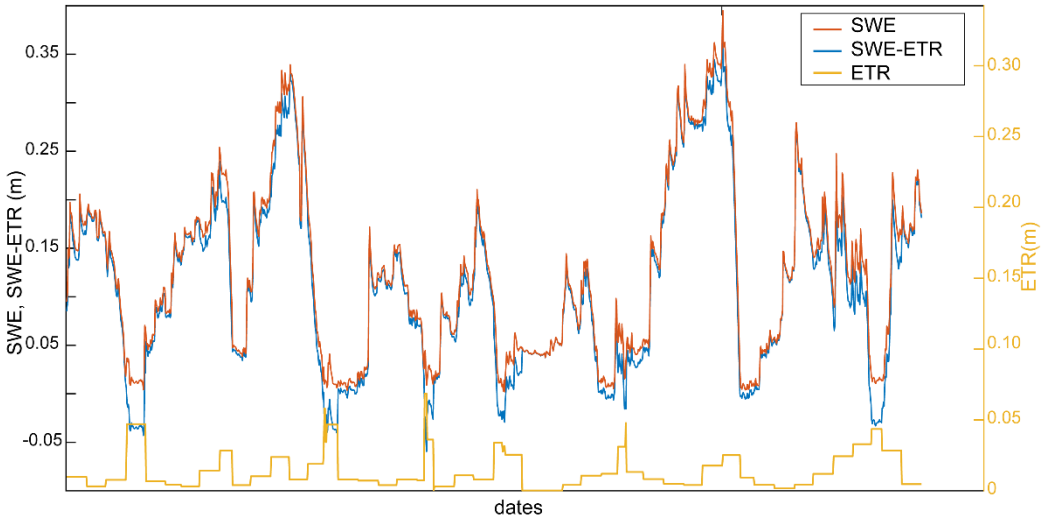


*Figure 5.3.10: Curves representing the SWE (snow water equivalent), the ETR (evapotranspiration) and SWE corrected value (SWE-ETR) for each sampling date.*

To retrieve an indicator of the water coming from each snowmelt occurrence we considered the negative increment of the SWE curve (i.e .$SWE_{(i)}$ –$SWE_{(i-1)}$) corresponding to the snowmelt contribution for each date and computed their cumulative value over the winter season.

We compared this information with velocity values extracted for the 5 slope sectors previously identified (Figure 5.3.7 a) considering the summer (Jun-Oct) and across winter (Oct-Jun) interferograms.

A variable response of slope sectors to hydrological inputs clearly arise in each season, but a constant periodic trend between summer and across winter period can't be assessed. The DSGSD therefore presents a sensitivity to external factors and, despite an almost constant mean annual displacement rate (Figure 5.3.7 b) it has hydrological induced variations (Figure 5.3.11 a).

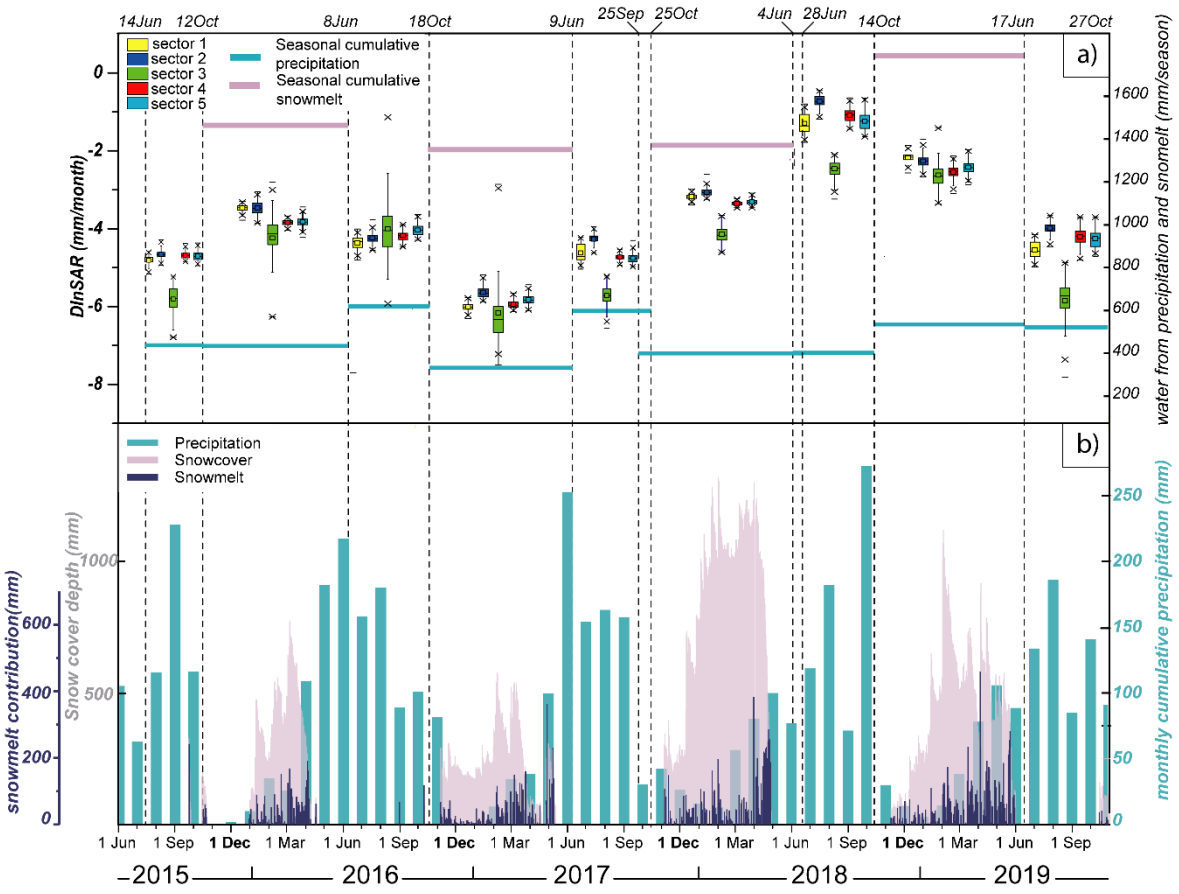


*Figure 5.3.11: graph reporting the different hydrological inputs on Saline DSGSD. a) monthly displacement rates for 5 sectors on the main DSGSD body and cumulative amount of water for each interferometric season (i.e. summer, Jun-Oct and across winter, Oct-jun) Whisker lengths: upper and lower inner fences based on interquartile range (IQR). b) Snowcover depth, monthly cumulative precipitation and snowmelt contribution computed as decumulative values from SWE curve.*

A comparison between the seasonal trends of precipitation, snowmelt and averaged displacement rates in different slope sectors shows that DSGSD activity is characterized by a clear seasonal trend. Nevertheless, DSGSD seasonal accelerations and decelerations are not in phase with climatic seasons but display a shift with temporal wavelength up to 2 years. This shif may suggest an influence of hydrological inputs on the deep behavior of the DSGSD, but with a very complex relation between displacement rates and forcing factors.
The relationships among average displacement rates in the considered DSGSD sectors, precipitations and snowmelt is better explained by scatterplots linking the hydrological input in specific periods with the relative slope velocity (Figure 5.3.12). In fact:

- considering the across winter period, there seems to be no correlation between the amount of snowmelt and the increasing of displacement rate (Figure 5.3.12 a). This might be explained by a delayed response of the slope to its contribution. In addition the lowest (2018-19) and the highest (2016-17) across winter velocity values occur in periods respectively characterized by a previous dry (2018) and rainy (2016) summer.
- considering the mean velocity value in summer periods (Jun-Oct), this increases with higher precipitations according to a threshold effect with an increment up to 45-50mm/yr of $v_{LOS}$ velocity for cumulative precipitation values higher than 400-450mm on

the considered period (Figure 5.3.12 b). Displacement rates over the threshold display variable values according to the considered sector and year, but without a clear defined trend.

- Summing the contribution of cumulative precipitation of each summer period with the snowmelt contribution of the previous across winter period, the mean summer velocity increases with higher total hydrological forcing (Figure 5.3.12 c). Also in this case, it is difficult to highlight a clear trend or main differences between the years with the highest velocities, but a sharp increment from 2018 (the driest year) outcomes.

The combined information from Figure 5.3.12 b and graph c suggests that seasonal precipitations represent the major controlling factor on the complex seasonal response of the DSGSD. Nevertheless, since the seasonal variability seems to have a "wavelength" longer than the analyzed period, other observations from different sources and sensors (e.g. GB-InSAR) should be integrated to retrieve the long term seasonal trend of the DSGSD.

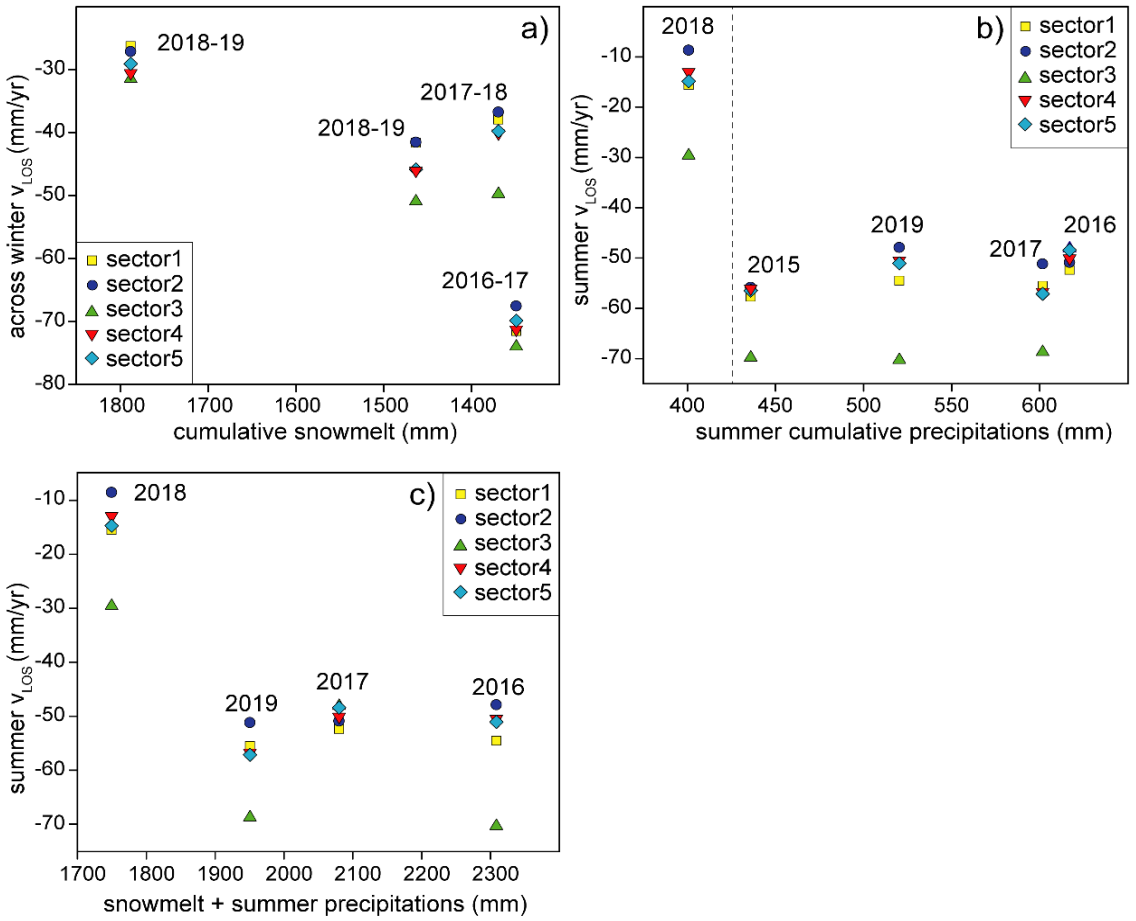


*Figure 5.3.12: scatterplot displaying relations between the displacement rate of each sector and the hydrological input contribution. a) across winter velocity (Oct-Jun) Vs cumulative snowmelt contribution; b) summer velocity (Jun-Oct) Vs summer cumulative precipitations (i.e. mainly rainfall); c) summer velocity Vs total hydrological input during the summer season, including the snowmelt input from the previous winter period.*

The combined observation of measurements from spaceborne InSAR and GB-InSAR, having different wavelength, LOS direction and accuracy to small displacement rates would in fact improve and validate the temporal trend of activity of the DSGSD and its relation to hydrological triggers.

### 5.3.6 Discussion

Saline DSGSD is one of the most active slow rock slope deformation in Lombardia with displacement rates of 15 and 20 mm/yr (Sentinel-1 descending SqueeSAR$^{TM}$ dataset), strongly increasing in the sector above the Ruinon rockslide.
As we made for the Corna Rossa and Mt. Mater DSGSDs, for the Saline DSGSD we adopted a targeted DInSAR to perform a site specific, spatially continuous analysis of the spatial and temporal aspects of the DSGSD activity, highlight relevant heterogeneities and achieve a better understanding on the possible roles of hydrological triggers in the evolution of the DSGSD.
Although SqueeSAR$^{TM}$ datasets performed over large areas (TRE Altamira) provide a dense PS and DS coverage over the slope (~145 PS/Km$^2$), they proved ineffective for a detailed local scale analysis. This is not only due to their point like nature but, as pointed out for Mt. Mater DSGSD, because their mean velocity values often underestimate the displacement rate along slope. This becomes clear when considering the annual velocity distribution of different slope sectors (1,2,4 and 5), extracted from DInSAR unwrapped interferograms and the corresponding PS values (Figure 5.3.13). Sector 3 was excluded from this analysis because it corresponds to an active and fast wedge which causes uncertainties in the unwrapping procedure of 1-year interferograms thus resulting in less reliable displacement rates.
From Figure 5.3.13, PS data always display lower values that all the other boxplots, which report the velocity range of slope sectors in different years. Moreover, since the PSI algorithm (Ferretti, 2001) adopts a linear velocity estimation, they result unsuitable to detect non-linear movements and slight slope heterogeneities or a possible seasonality.
Explorative DInSAR analysis at different temporal baselines (6 days, seasonal, 1 year) revealed a spatial slope heterogeneity, as also suggested by different morpho-structural association and degree of evolution of nested sectors, which however results less evident than on Corna Rossa DSGSD. In this latter, segmentation was strongly structural controlled by the partially overlapping master fracture and it sharply emerged from seasonal and even shorter interferograms. Saline ridge on the contrary, displays a major activity segmentation in the lowest slope portion where Ruinon rockslide develops, but a less evident heterogeneity for the main DSGSD.
6 days baseline interferograms only show the presence of Ruinon rockslide (when atmospheric disturbances aren't impeding), but don't display any heterogeneities in the upper slope portion, that seems to behave as a homogeneous body.
Longer baselines interferograms start to show the presence of an active wedge at the top of the slope (sector 3) and possible segmentation corresponding to sectors A and B. These two

are separated by NE-SW persistent scarps and lay on two sides of the ridge with different aspect orientation, but with similar mean slope inclination of about 30°.

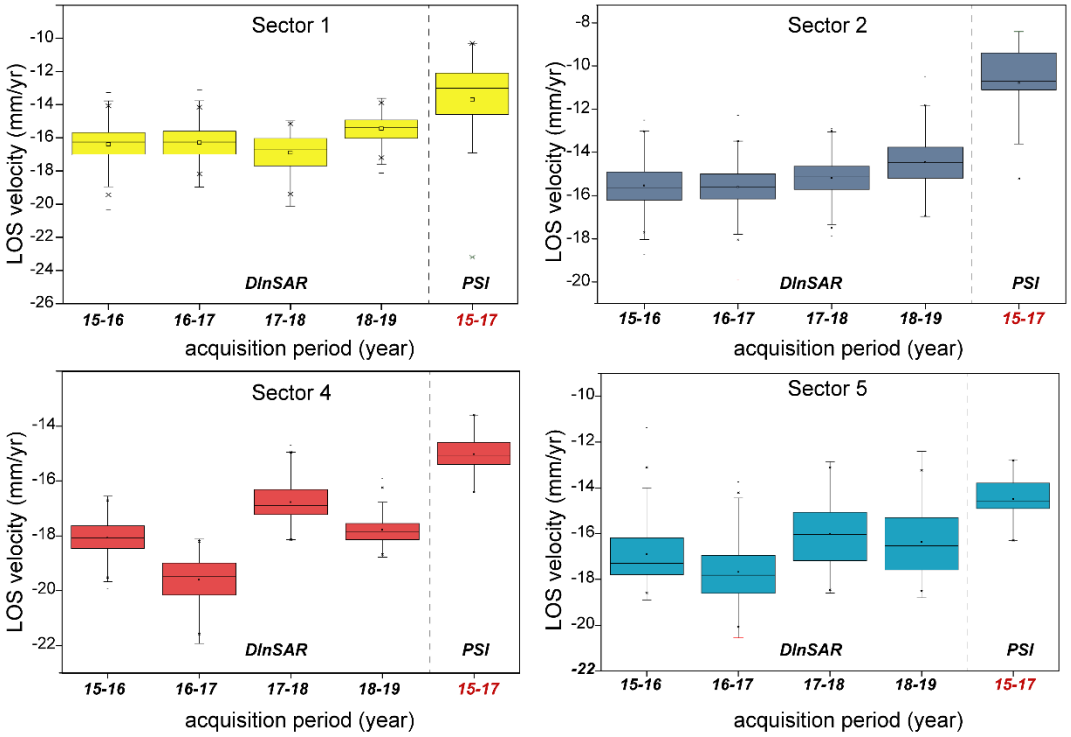


*Figure 5.3.13: boxplots reporting the annual velocity of each slope sector compared with relative PS values distribution. PS boxplot always erports a slowr velocity rate than the others. Whisker lengths: upper and lower inner fences based on interquartile range (IQR).*

From field and DEM analysis, sector B results much more evolved than sector A with sharp curvilinear bounding scarps that, going downslope, are associated to counterscarps arranged in an asymmetrical graben system. Despite the evident morpho-structural difference, seasonal and annual interferograms don't display visible variations between the two and attribute to sector A (less evolved) higher displacement rates than sector B (more evolved and right above Ruinon rockslide). This may be due to velocity differences that are still too small to be caught at 1 year and also influenced by LOS sensibility to different slope orientations. Two-year median stack on both wrapped and unwrapped products in fact highlights a difference between A and B sector, but projecting the velocity along slope (thus reducing the orientation bias) the velocity change is reduced and becomes almost negligible. So, according to these observations, the slope heterogeneity is not linked to the actual displacement rate, but is the result of a long term strain accumulation expressed by sharp morpho-structural features and concave slope of sector B, which strong deformation should be addressed to a past intense activity rather than a present day one.
Temporal heterogeneities expressed by differences in seasonal response also outcome considering summer and across winter periods (Figure 5.3.11).

A recurrent response of the slope to different amount of hydrological inputs (rainfall+ snowmelt) is difficult to be assessed, but a long wavelength seasonality (exceeding the year) clearly arises. In particular, our analysis points out how rainfall contribution mainly influences the velocity trends of the DSGSD with a major response over a threshold value of cumulative summer precipitations of 450mm.
However, only using spaceborne InSAR data we couldn't identify progressive non-linear trends associated to the DSGSD, which would correspond to an advanced stage of progressive failure towards tertiary creep. This response has instead been found on Ruinon rockslide, which is completely differentiated, and shows an extreme seasonality.

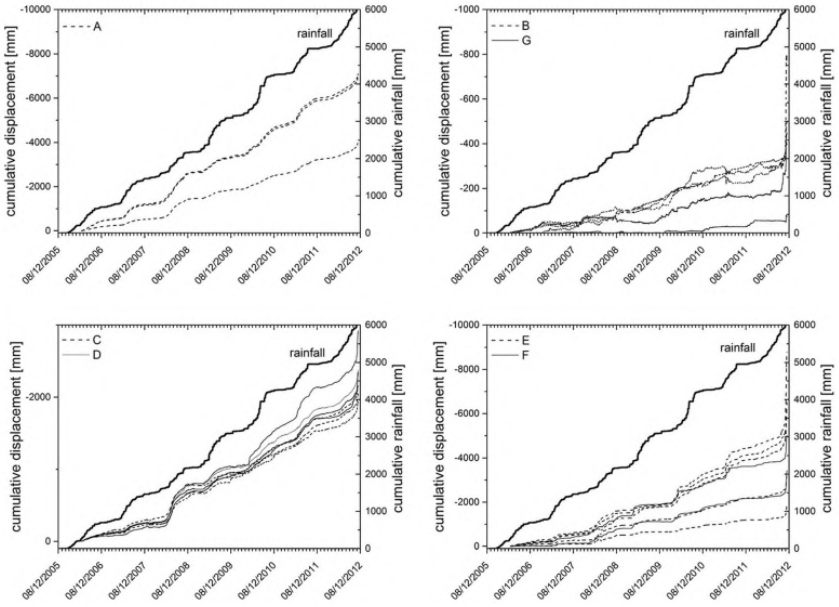


*Figure 5.3.14: displacements recorded on Ruinon rockslides with cumulative displacements following cumulative rainfall trends on long, annual and short term. Curves correspond to different sectors in which Ruinon rockslide has been discretized (Crosta et al., 2017).*

Displacements are recorded during rainy periods (late summer–early fall), with cumulative displacements following cumulative rainfall trends on long, annual and short term while in the dry and cold seasons, the rockslide slowly creeps in most of the sectors (Crosta et al., 2017).
Despite a progressive trend from DSGSD to rockslide can't be assessed considering only satellite DInSAR data, the evidence of a seasonal response and the sharp morpho-structural features that mark the transition between the creeping main body and the sliding rockslide suggest that the DSGSD is a well evolved phenomenon and it developed in a complex and inter connected framework of long-term damage with Ruinon rockslide. Further analysis with different sensors (i.e. GB-InSAR) covering longer periods and with higher spatial resolution could be useful to highlight more in detail slow slope responses and displacement rates variability and explain if DSGSD behaviour can help anticipating rockslide risks.

# 6 General discussion

Slow rock slope deformations (deep seated gravitational slope deformations and large landslides) are widely diffused in the European Alps as well as in other mountain ranges. They evolve over thousands of years by progressive failure processes, resulting in slow movements impacting infrastructures and possibly accelerating until catastrophic collapse of entire slope sectors. The complexity of these phenomena, related to progressive failure processes developing over long period and time-variable hydro-mechanical coupling mirrored by a complex creep behaviour (Crosta et al., 2017; Riva et al., 2018; Agliardi et al., 2020)makes difficult to predict their interaction with elements at risk and anticipate their possible evolution towards catastrophic failure. Furthermore, these huge landslides are usually characterized by complex styles of activity associated to slope sectors with different kinematics, strain partitioning into morpho/structural features and different displacement rates. A robust and complete characterization of their style of activity is thus required in a risk management perspective both at the regional and local scale.

On the regional scale, main goals include performing a screening of ongoing slow rock slope deformations and providing a sound, fast and cost-effective characterization and classification of their activity and kinematics to support land planning, risk analyses and prioritization of detailed local-scale studies aimed at granting safety and infrastructure integrity.

For relevant cases outlined by the regional screening, local scale analyses are intended to supply information on the internal segmentation, style of activity and long term temporal trends, which are required to define possible scenarios for risk analysis and provide constraints for engineering modeling.

In this methodological perspective, main challenges are related to the complexity of the studied phenomena mainly due to the huge involved volumes, heterogeneous displacements in space and time and the uncertainties on the depth, geometry and textural maturity basal shear zones, hardly reached by geo geotechnical and geophysical site investigations. Moreover, the low amounts and rates of surface displacements associated to these phenomena, as well as their size and spatial complexity, limit the use of traditional ground-based and sub-surface monitoring techniques.

Thus, our capability to detect and measure slow rock slope deformations mainly relies on remote sensing applications, as spaceborne radar interferometry that as proved to be a powerful tool to characterize landslides at local and regional scales. Nevertheless, the application of this technique to very slow rock slope deformations in alpine environments (displacement rates $< 5$ cm/year) remains challenging, mainly due to low signal to noise

ratio, atmospheric disturbances, snow cover effects, and complexities resulting from heterogeneous displacement trends.

In this context, this PhD project has been targeted to (1) evaluate the suitability, advantages and limitations of the use of DInSAR to characterize large very slow rock slope deformations, and develop approaches to maximize its potential; (2) characterize the kinematics, style and rate of activity of large slow-moving landslides (DSGSDs and LL) in Lombardia (Central Italin Alps) by innovative and objective approaches; (3) perform an objective identification of sub-areas with different behaviour (e.g. rockslides) nested inside large slow-moving areas; (4) redefinition of the "style of activity" of slow rock slope deformations to account for their internal complexity and state of activity integrating different aspects (displacement rate, segmentation/heterogeneity, kinematics, internal damage and accumulated strain); (5) develop analysis tool, workflows and a best practice for the analysis of local-scales studies and phenomena.
On the regional scale, we exploited PS-InSAR™ and SqueeSAR™ commercial products (TRE Altamira), processed over the alpine sectors of Lombardia region, to develop a novel approach for the characterization and classification of slow rock-slope deformations according to their style of activity, with support of an original geomorphological mapping, performed on an inventory of 208 slow rock slope deformations. As the surface morphological and morpho-structural characteristics of mapped landslides mirror their deep geometry and mechanisms, a preliminary study of the geological background and the surface morphostructures is fundamental to gain a first insight in the activity, kinematics and segmentations of these complex phenomena.
We showed that the commonly used 1D $v_{LOS}$ analysis is ineffective in describing the landslide kinematics, which can be resolved using a multi-geometry approach (2DInSAR). Our analyses suggest that the best geometric indicator to characterize both the local and global kinematics of large slope deformations is the dip angle of the 2D displacement vector ($\tau$) and the related $\Delta$ value ($\tau$-dip of the slope). The statistical distribution of these descriptors within landslide areas can be used to provide an objective assessment of slope kinematics both at the local scale, through vector fields and profile extraction, and regional scale, through a machine learning implementation approach.
Our analysis benefits from both deterministic and statistical components. The deterministic component consists of original routines in Matlab™ and GIS, that allow quantifying the internal segmentation, heterogeneity, kinematics and representative displacement rates of each mapped landslide through a refined post-processing of PS-InSAR™ and SqueeSAR™ data, validated using geomorphological mapping. These routines can be used as stand-alone tools (see section 3), and provide indexes that, together with morphometric and morpho-structural variables, feed a multivariate statistical analysis aimed at classifying the mapped landslides in groups with consistently different style of activity.
In this perspective, our research at the regional scale obtained the following main results:

- new semi-automated, objective methods and tools to characterize the internal segmentation and kinematics of slow rock slope deformations. These methods, readily

applicable to other datasets, effectively highlight the phenomena subjected to a certain degree of segmentation, with the presence of internal nested bodies that can potentially evolve into faster landslides, and their global kinematics;

- a statistically-based evidence that DSGSD and large landslides are characterized by different mechanisms and/or evolutionary stages, with different associated morphological features that testify higher accumulated internal deformation for large landslides with respect to DSGSD;
- a statistically-based classification of rock-slope deformations based on their style of activity, including the contributions of displacement rate, segmentation, kinematics and internal damage. This is intended to support regional scale landplanning and the prioritization of detailed site-specific mapping, monitoring and modeling studies, required to understand and manage the risks posed by slow rock slope deformations.

The final product of our regional scale analysis is a dataset classification into seven synthetic "styke of activity groups" of all the 208 mapped slow rock slope deformations in Lombardia according to their style of activity. Each group outlines the principal factors interplaying in the definition of their main critical aspects (higher displacement rates, kinemtics), spatial complexity and interaction with elements at risk (slow but heterogeneous movements affecting sensitive infrastructures), degree of internal damage and the possible indicators of a long term evolutive curve (degree of strain accumulations, morpho-structural expression, presence of nested bodies). This result provides useful information for site-specific characterization of individual landslides towards the definition of their hazard and future evolution in terms of unstable scenarios (volumes), mechanisms of interaction with elements at risk (homogeneous vs heterogeneous, slow vs fast displacements) and predisposition to collapse.

Starting from this classification we selected 3 critical case studies emerging from the regional analysis: Corna Rossa, Mt. Mater and Saline DSGSDs, with peculiar issues and interacting with sensitive elements, in order to analyse their style of activity in an applied perspective. Despite PSI data are very useful for a regional, first-order characterization of slope activity and allow to retrieve its kinematics, due to their point like nature they often fail to capture spatial segmentation, temporal trends and associated mechanisms resulting ineffective for site-specific applications. Moreover, comparisons with site specific results and ground-based measurements demonstrate that PS datasets, processed over large areas and commonly used by the scientific and technical landslide communities, often underestimates slope displacement rates. PSI processing chain is in fact based on a stack of several images (multi interferogram method) that often includes snow covered scenes and atmospheric disturbances which, if not corrected, reduce the already weak "very slow movement" signal. In addition, the mean displacement rate of each PS is referred to a "fictitious" temporal baseline that depends on the number and on the total acquisition periods spanned by the considered SAR images, thus mixing up signals coming from a wide range of processes specifically detectable on different temporal baselines (i.e. periglacial movement, slow slope deformation etc.).

In site-specific studies, such problems can be overcome by targeting DInSAR analysis to catch specific features and representative spatial-temporal scales of very slow rock slope deformations (months, years), by integrating during the analysis stages: a) DInSAR processing over multiple temporal baselines; b) detailed field morpho-structural constraints; c) ground-based displacement measurements; d) absolute datings.

DInSAR processing, targeted on multiple temporal baselines, allows to successfully unravel the mechanisms and temporal trends of activity of slow slope deformations.

To investigate the main issues outlined for the 3 case studies: mechanisms and segmentation of Corna Rossa DSGSD, heterogenous activity of Mt. Mater DSGSD, temporal trends of Saline DSGSD, we analysed for each one the slope response emerging from interferograms generated with different temporal baselines (from the minimum Sentinel 1 revisiting time, i.e. 6days, to 2 years). In the analysis we selected ad hoc temporal baselines providing a major information and high SN, excluding the snow covered periods and the interferograms with a strong APS.

The selection of different baselines strongly affects the type of process detected, that must be always characterized before conducting systematic analyses. For examples, debris or periglacial features, having higher velocities, emerge from short temporal baseline interferograms while slower displacement rates arise on longer periods. This further suggests that site specific analysis only based on PSI datasets, derived from multi-interferogram stacks not targeted on specific temporal baselines, often provides information mixing different processes and biased by the length of the overall processing period, the original SAR images used, the considered "stable" reference point and the correction applied to remove atmospheric contribution. To reach a complete description of local case studies detailed field mapping data, ground truthing measurements (GSP) and absolute datings should be always integrated (where available). These provide clues on the long term displacement trend of the considered deformations setting constraints to their onset and possible evolutive trend.

A bare application of DInSAR techniques and products to the study of slow rock slope deformation is in fact ineffective to complete a detailed study of such complex phenomena. This is both due to the limits of the technique itself that, despite the considered band (C, L) and revisiting time, can't completely measure the 3D displacement vector on the ground and is always biased by topographic orientation and specific morphometric conditions (geometrical distortions). Therefore, despite the proven potential of DInSAR technique, an a priori knowledge of the study area and its main characteristics is necessary to complete the derived information, calibrate the analysis and avoid misinterpretating its results.

On the contrary, targeted DInSAR analysis allows us to unravel slope segmentation associated to the presence of highly deforming nested landslides, as in the case of Mt. Mater case study, or major structural features, as for Corna Rossa DSGSD, identifying slope sectors more prone to a rapid evolution.

In the analyses, we adopted an original stacking procedure to further increase the SNR along slope, emphasizing the background displacement signal constantly affecting the slope and distinguished by residual velocity contributions corresponding to local heterogeneities. Our

results highlight how persistent features and active morphostructures influence the strain partitioning along slope delimiting slope portions with differential kinematics and degree of activity. These observations are strategic in the definition of evolutionary scenarios for engineering modelling, risk analysis and collapse forecasting studies.

We further exploited targeted DInSAR products to unravel temporal response of the slope and investigated a possible seasonality or non-linearity of their displacement trends.

Seasonal interferograms (summer and across winter periods) revealed for all the three case studies a different response of the DSGSD in the summer and across winter periods thus supporting a sensitivity of the phenomenon to hydrological inputs.

A recurrent response of the slope to different amount of hydrological inputs (rainfall+ snowmelt) is generally difficult to be assessed, but, as highlighted for Mt. Mater and Saline DSGSD, seasonal variations and a long wavelength seasonality clearly arises. This response is more evident for nested shallower phenomena (i.e. active and differentiated Ruinon rockslide, uppermost slope portion on Mt. Mater) but also emerges for the main DSGSD body. Therefore, despite the huge involved volumes and ill-defined basal shear zones, the analysed case studies all present a sensitivity to external forcing depicting complex evolutive scenarios in a geohazard management perspective.

# 7 Concluding remarks

We deeply investigated the advantages and main limitations of space borne radar interferometry in the analysis and classification of slow rock slope deformations exploiting PSI, SqueeSAR and DInSAR products to unravel the spatial and temporal heterogeneities of these complex phenomena through an objective and multiscale approach constrained by geological evidences.

Starting from the state of art we tested classical analytical methods and propose specific targeted analysis implemented in original Matlab$^{TM}$ tools and workflows to gather a detailed knowledge of the style of activity of slow rock slope deformations in the alpine environment of Lombardia.

Our study allowed to retrieve a complete regional scale classification of the mapped phenomena also taking into account their spatial complexity, kinematic style and morpho-structural expression. Furthermore, targeted local scale analysis revealed how slow rock slope deformations are actually active landslides and may also be sensitive to hydrological inputs. This poses major implications to forecast possible differentiation into nested and more active roscksslides, which represent an important geo-hazard in relation to the deformation of sensitive structures and infrastructures.

Our approach can be easily applied to different landslide datasets and provides an objective and cost-effective support to both regional-scale hazard assessment and site-specific studies.

We further point out how a blind use of DinSAR products can result in misleading information on the nature and evolutive style of slow rock slope deformations and their interpretation should be always preceded by a background geological and morpho-structural knowledge of the cases of study.

Moreover, spaceborne InSAR resulted ineffective in highlighting progressive trends for very slow movements and the application of DInSAR in the investigation of non linear velocity trends in slow rock slope deformations remains and an open topic to be explored. The integration with mapping and field data, as well as information coming from different sources and techniques (i.e. ground truthing measurements, absolute datings, GB-InSAR information etc.), is thus a fundamental step for a reliable assessment of the ongoing deformation and allows to catch the long term and complex behaviour of slow rock slope deformations also under an engineering point of view.

# Annex

## A. Sentinel-1 interferometric processing chain (SNAP)

### 1. Download Sentinel 1 SAR images

Sentinel-1 is an imaging radar mission providing C-band SAR images free available on the Copernicus open access hub website (https://scihub.copernicus.eu/).
The Sentinel-1 mission includes a two- satellites constellation Sentinel-1A and Sentinel-1B, with identical sun-synchronous near polar orbit 180° apart and at an altitude of almost 700 km. Sentinel-1A was launched on 3rd April 2014 and Sentinel-1B on 25th April 2016. Now, working in tandem, they are able to cover the same area of Earth's surface every 6 days.
Sentinel-1 senses the scene according to 4 main modes in single (HH, VV) (WV mode) and dual polarization (HV,VH) (for the others modes).
Acquisition modes (Figure A.1) include :

1. Stripmap (SM)
2. Interferometric Wide swath (IW)
3. Extra-Wide swath (EW)
4. Wave (WV)

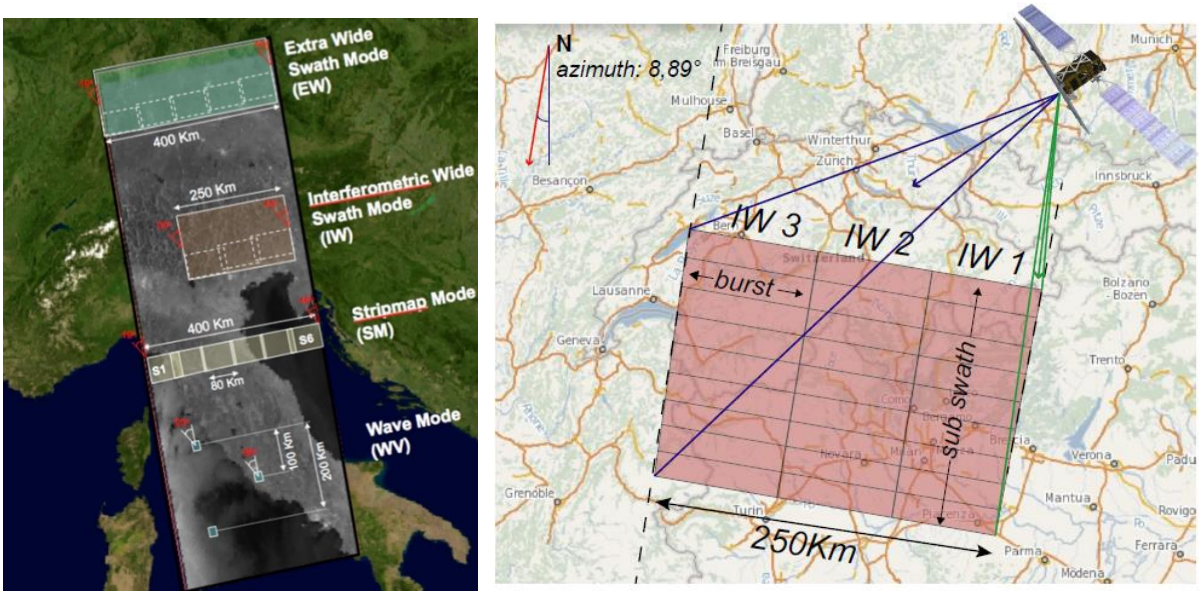


*Figure A.1: Sentinel 1 acquisition modes (image from https://sentinel.esa.int/web/sentinel/user-guides/sentinel-1-sar/revisit-and-coverage) and IW swath organization.*

Sentinel 1 primarily operates over land in Interferometric Wide (IW) mode, sensing scenes over a 250 km wide "swath" (corresponding to the sensor ground range), further divided in 3 "subswaths" and "bursts" (resolution range x azimuth 5mx20m) using Terrain Observation Progressive Scanning SAR (TOPSAR) technique.
ESA distributes products at three different processing levels:

1. Raw Level-0 data
2. Processed Level-1 Single Look Complex (SLC: each image pixel is represented by a complex value and contains both amplitude and phase information) and Ground Range Detected (GRD) Level-1 data with multi-looked intensity only
3. Level-2 Ocean (OCN) data for geophysical parameters of the ocean

For our analyses we used S1-A/B IW SLC images.

*In the download page select: the sensing period, the type of product, the satellite and the relative orbit number that covers the AOI. Then select "search".*

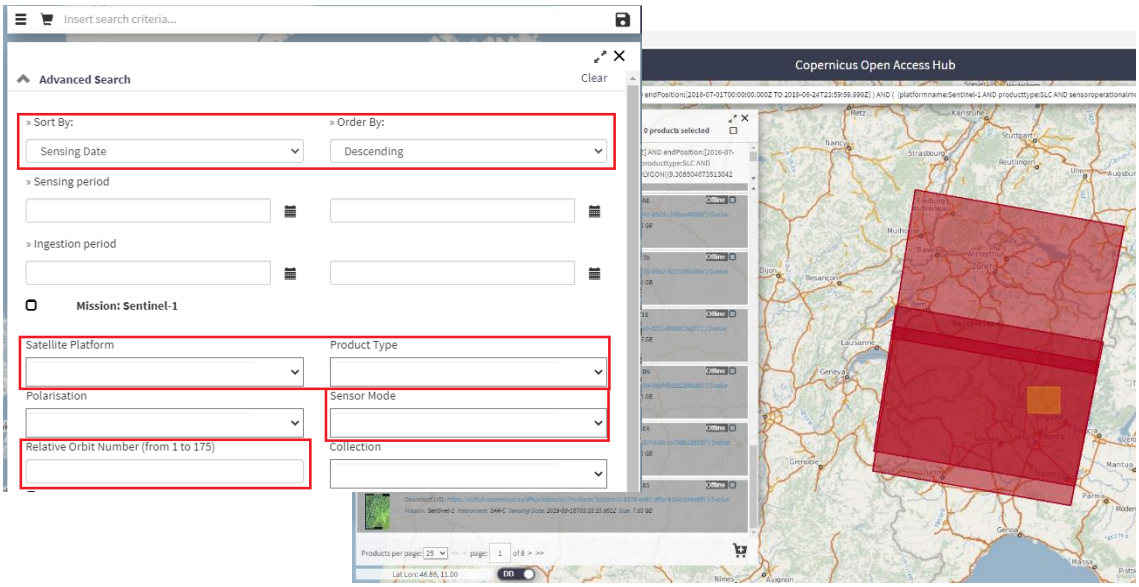


*Figure A.2: Copernicus scihub download page.*

A list of images appears on the left side of the webpage (Figure A.2). Those displayed with the label "offline" have to be requested and it usually takes from some hours to some days to have the products available. The others already available can be downloaded as zip files. The long name of the folder contains all the information of the product:

*Table 6:Sentinel 1 product name specifications*

| mmm | bb | tttr | lfpp | yyyymmdd thhmmss | yyyymmdd thhmmss | oooo | dddd | cccc | .safe |
|---|---|---|---|---|---|---|---|---|---|
| MMM | | | | Mission identifier: S1A, S1B | | | | | |
| BB | | | | Mode/IW-EW-WV | | | | | |
| TTTR | | | | Product Type: SLC, GRD, OCN | | | | | |
| LFPP | | | | Processing level (1,2), Product class (A,S), Polarization (SH,SV,DH,DV) | | | | | |
| YYYYMMDDTHHMMSS | | | | Start date/time: year, month, day, hour, minutes, seconds | | | | | |
| YYYYMMDDTHHMMSS | | | | Start date/time: year, month, day, hour, minutes, seconds | | | | | |
| OOOO | | | | Absolute orbit number | | | | | |
| DDDD | | | | Mission data-take ID | | | | | |
| CCCC | | | | Product unique ID | | | | | |
| .safe | | | | Product file extension | | | | | |

## 2. SNAP: interferometric processing

SNAP (Sentinel Application Platform) is an open source architecture for ESA Toolboxes ideal for Earth Observation processing and analysis exploiting Satellite images.
The Sentinel-1 Toolbox (S1TBX) can be downloaded from the *Science Toolbox Exploitation Platform (STEP: http://step.esa.int/main/download/snap-download/)*. It consists of a collection of processing tools intended to handle data from ESA SAR missions including SENTINEL-1, ERS-1 & 2 and ENVISAT, as well as data from ALOS PALSAR, TerraSAR-X, COSMO-SkyMed and RADARSAT-2. This Toolbox is being developed for ESA by SkyWatch in partnership with DLR, Brockmann Consult and OceanDataLab.

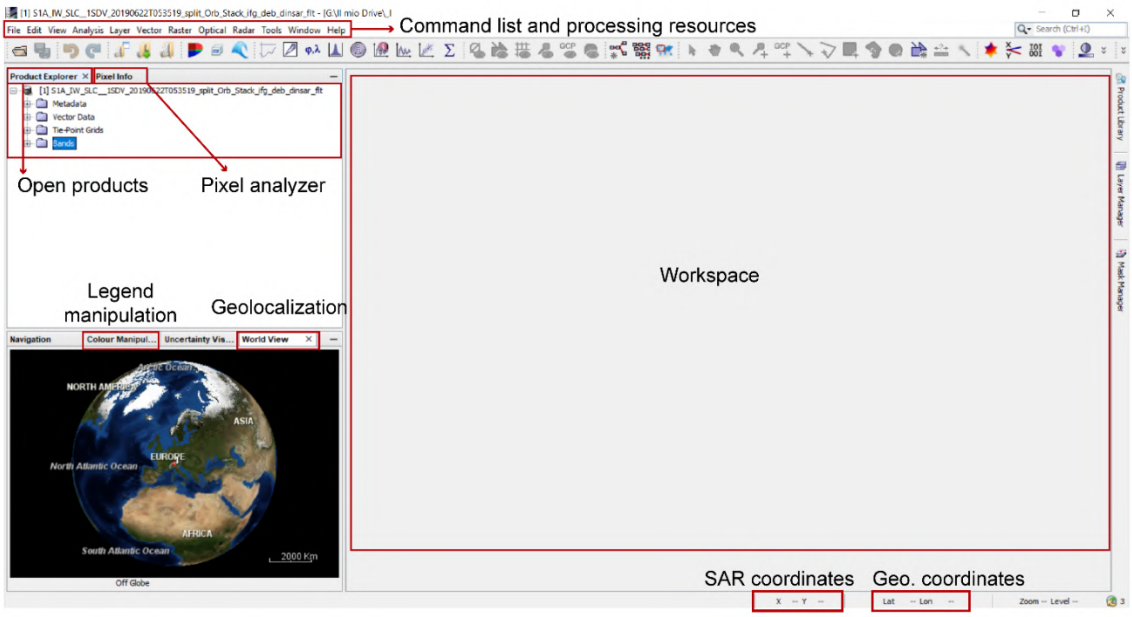


*Figure A.3:SNAP main window.*

The following tutorial allows performing the basic interferometric processing workflow with Sentinel-1 Interferometric Wide Swath products in SNAP (Figure A.3) from the upload of the SAR images to the processing of a DInSAR wrapped interferogram. The unwrapping procedure is processed in SNAP too, provided that an external software plugin, SNAPHU (statistical cost network-flow algorithm for phase unwrapping), is installed.

- Open SAR products

*Drag and drop the downloades zip folders containing the SAR images in the product explorer window (Figure A.4) or use the open product button in the top toolbar and browse for the location of the downloaded data. Select the zip files and press open product.*

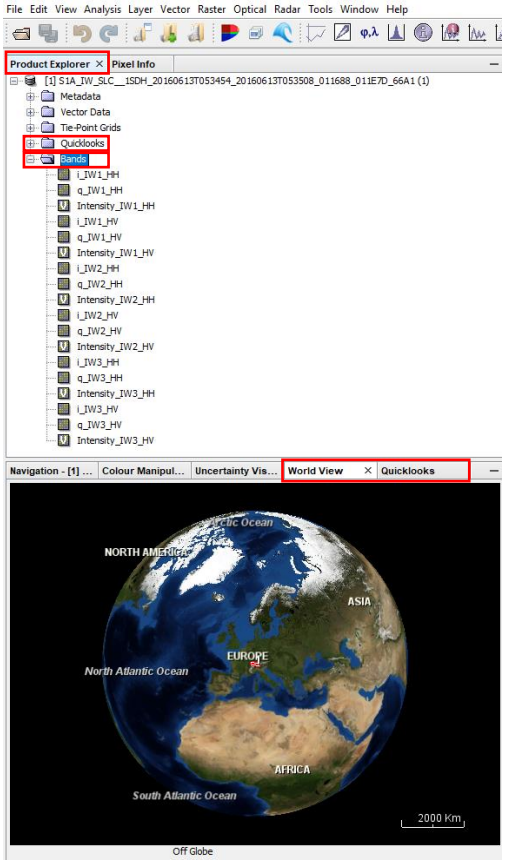


*Figure A.4:Opening product step.*

The products are displayed in the Product Explorer Panel. Each Sentinel-1 product consists of 5 subfolders containing Metadata, Vector Data, Tie-Point Grids, Quicklooks and Bands. The Band folder comprises the actual raster data, organized by polarization and subswath. For SLC data, bands contain the real (i) and imaginary (q) parts of the complex data and the intensity (=amplitude) band for each polarization (Figure A.4).
As each subswath covers a wide area, it is not advised to open the bands at this stage, but the geolocalization of the swath can be checked in the bottom *world view panel*. Another way to visualize the product without opening the single bands is to double click on the Quicklooks folder and open an RGB colour representation of the dataset (Figure A.4)

- Tops split

To consider only the area of interest in the interferometric processing, thus reducing the computational time and the memory usage, it is advised to split the subswath considering only the bursts that cover the AOI (Figure A.5).

*Radar → Sentinel-1 TOPS → S-1TOPS Split*

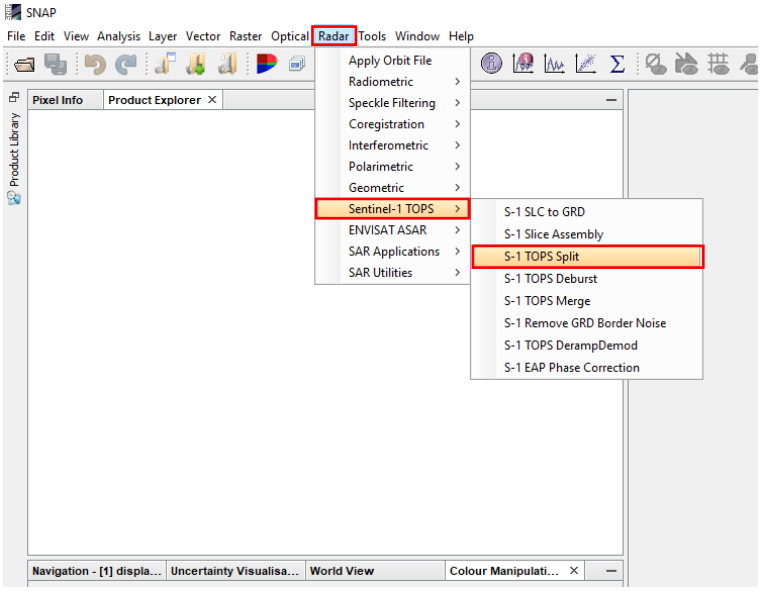


*Figure A.5:TOPS split.*

*In the S-1 TOPS Split moving window select under I/O parameters tab the file to be split and the saving folder.*

*In the Processing parameters tab select the subswath covering the AOI (zoom in the preview window to see better) and select the VV polarization. Then reduce the number of bursts by dragging the grey triangles towards the middle* (Figure A.6).

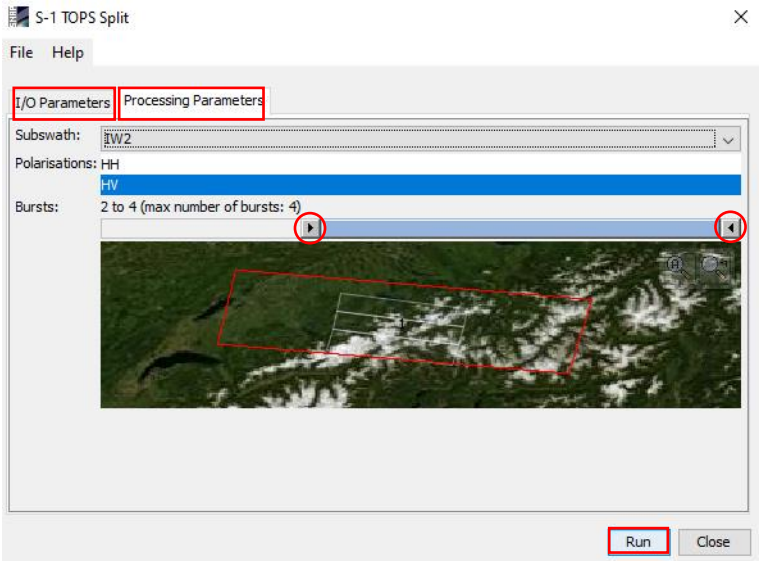


*Figure A.6: split tool parameters*

*Press Run* and repeat the step for the second S1 image. SNAP saves the products adding the suffix "split" to the original name. For the sake of simplicity and an easier visualization, it is advised to shorten part of the original name to make it clear.
Note: Sentinel-1A and Sentinel-1B may have shifted extents, and thus different bursts must be considered for the same AOI.

- Apply orbit file

Precise orbit files aren't directly associated to the image data, but they are delivered by the European Space Agency within 20 days after the acquisition as separate files. SNAP automatically search and download them. Applying orbit file is an optional step, but it maximizes the geolocation quality by using accurate satellite position and velocity information.
*Radar → Apply orbit file*

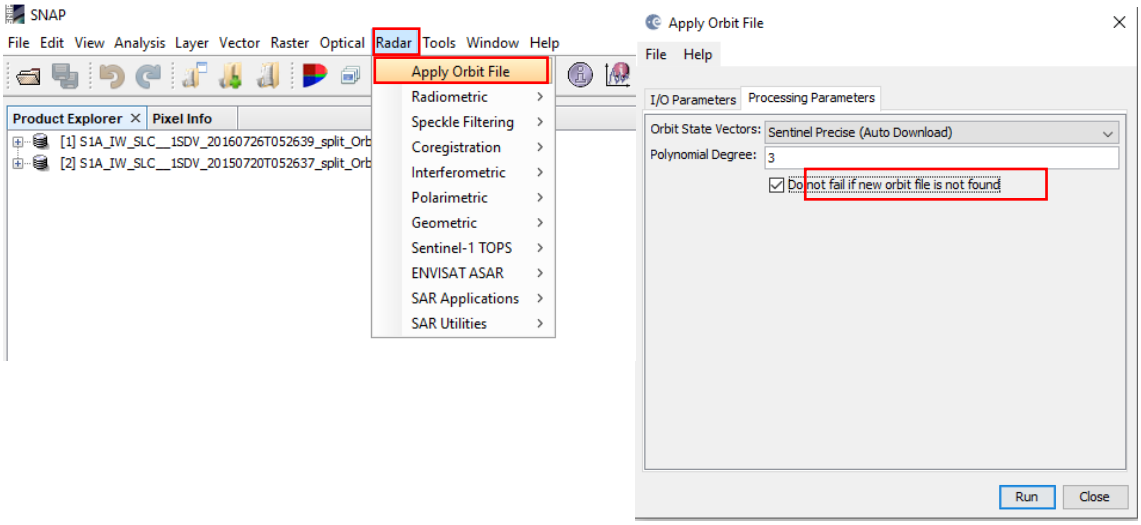


*Figure A.6:Apply orbit file.*

*In the I/O parameters tab select the split files and the saving folder.In the Processing parameters tab check the "Do not fail if new orbit is not found" box.* The default setting "*Sentinel Precise*" in the orbit state vectors dropdown menu does not need to be changed (Figure A.7).
*Execute the operator for both split products* generated in step 2.SNAP saves the product appending the suffix "_Orb" to the previous "_split" file name.

- Coregister the images into a stack

The coregistration step aligns the two images (master and slave) (Figure A.8) using the orbits parameters and a digital elevation model that can be uploaded or directly chosen in SNAP. The slave image pixels are moved to overlap the corresponding ones on the master image with a sub-pixel accuracy. This ensures that each ground target contributes to the same pixel in both the master and the 'slave' image.

*Radar → Coregistration → Sentinel-1 TOPS Coregistration → S-1 Back Geocoding*

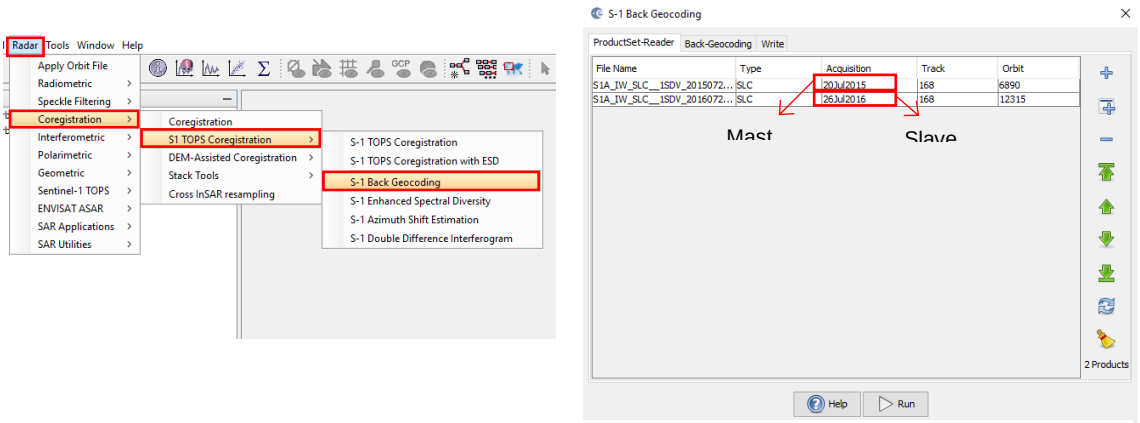


*Figure A.8:Coregistration: S-1 Back Geocoding.*

*In the ProductSet-Reader menu add the master and slave images (ending with "_split_orb") to the table. The master must come before the slave* (Figure A.8). *In the Back Geocoding tab choose the most suitable DEM selecting from the dropdown menu*_(Figure A.9). In our analysis we always selected the SRTM 1Sec HGT (AutoDownload) but other options are available, as well as the upload of an external DEM. Once selected the DEM it must be kept the same in the all the other processing steps.

*DEM resampling Method* and *Resampling Type* respectively refers to the interpolation method used to obtain elevation values from the original DEM file and pixel values from the source image. The default settings (Bilinear interpolation) are generally preferred if specific changes are not necessarily required.

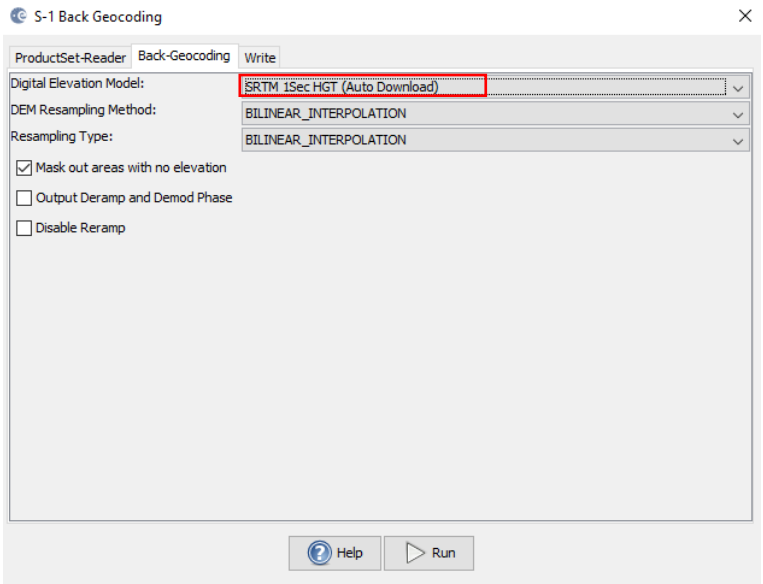


*Figure A.9: Coregistration: DEM and advanced settings selection.*

*Check the Mask out areas with no elevation box* to avoid artefacts and remove areas with no elevation attribute (ocean or not covered by DEM pixels).
*Output Deramp* and *Demod Phase* are not recommended to be checked as they work with deramping and demodulation phase bands. The *Disable Deramp* box doesn't have to be selected if the stacking will be used to generate an interferogram (Figure A.9)
*Press Run to complete the operation*. The final stacked product will be saved with suffix "_Stack".
*To verify that stack was successfully computed right click on the stack file displayed in the Produc Explorer window and select "open RGB image window".* The channel corresponds to the master image, the green one to the slave (Figure A.10). *Press OK to display the result*. If the stack succeded the product will be a yellowish image with only few green or red borders where the image stacking wasn't fulfilled (Figure A.10).

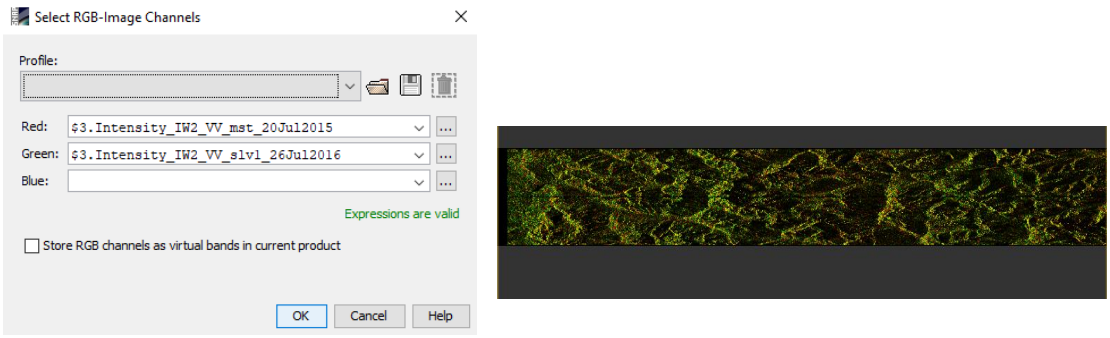


*Figure A.10: Visualisation of the stack result.*

Note: the SRTM is not global available and some areas lie outside its coverage. Check at the following link if the AOI is covered: https://www2.jpl.nasa.gov/srtm/coverage.html.

- Interferogram formation

The amplitude of master and slave images is multiplied while their respective phases are differenced to form the interferogram.
*Radar → Interferometric → Products → Interferogram Formation*
*In the I/O parameters tab select the "_stack" file and the saving folder.*
In the *Processing Parameters* be sure that (Figure A.11):

- the "*Subtract flat earth phase"* is checked: the flat-earth phase is the contribution due to the curvature of the reference surface. It is estimated considering the orbital and metadata information and subtracted from the interferogram. The program automatically computes the flat earth phase in a number of control points within the SAR image and then interpolates them using a polynomial function. The default setting of polynomial degree, number of points and orbit interpolation degree are in general sufficient to model the reference phase for a 100x100Km wide SAR scene with a good smoothing over the area.
- The "*coherence estimation*" is included: this produces a coherence band in the output calculated on a window of 10x3 pixels (default setting) in range/azimuth direction.

The box "*Subtract topographic phase*" (Figure A.11Figure A.11:Interferogram formation.) should not be checked if the expected result of the workflow is the Derivation of a Digital Elevation Model. Otherwise, if the final product is aimed at detecting the surface displacement it should be checked to remove the topographic influence from the interferogram. In our analysis we didn't check the "Subtract topographic phase" at this stage but in the following step with the command "*Topographic phase removal*" (point 7). *Press Run to conclude the operation*. The final product is saved with the suffix "_ifg".

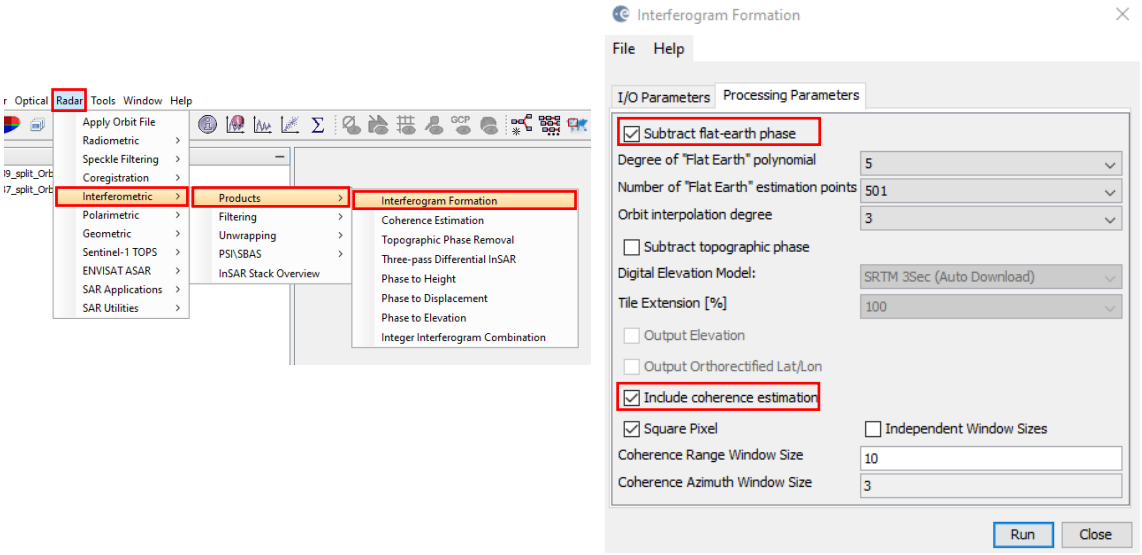


*Figure A.11:Interferogram formation.*

- Tops deburst

The deburst operation joins the bursts into a single image (Figure A.12).

*Radar → Sentinel-1 TOPS → S-1 TOPS Deburst*

No further parameters have to be selected in this step except for the input file "_ifg" and the saving folder directory.

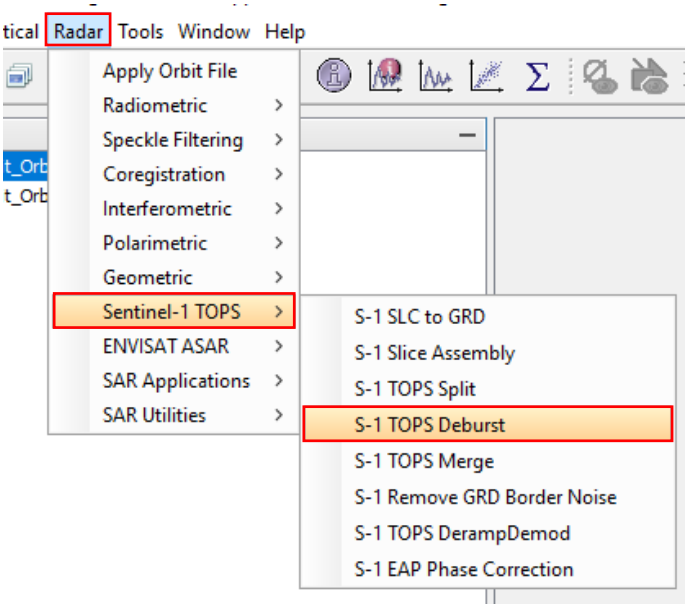


*Figure A.12:S-1 TOPS Deburst.*

- Topographic phase removal

The topographic phase contribution is here removed from the interferogram using a known DEM (that must be the same as the one used in point 4 for the coregistration step). Topographic Phase Removal operator simulates an interferogram based on the reference DEM and subtract it from the processed interferogram (Figure A.13).
Radar → Interferometric → Products → Topographic Phase Removal

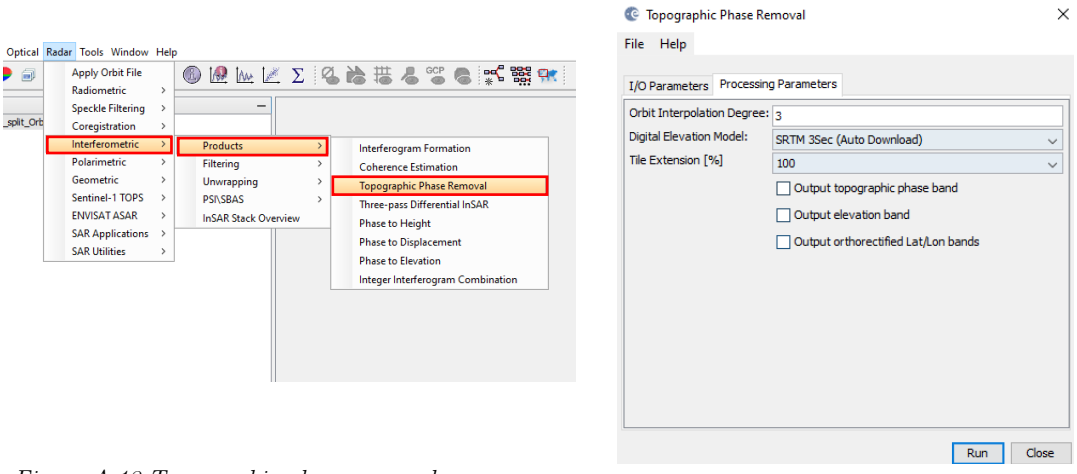


*Figure A.13:Topographic phase removal.*

*In the Processing Parameters tab, the reference Dem must be selected and a separated band showing the simulated topographic phase component based on the DEM can be included in the final product.* The "*Tile extension (%)*" is an optimization parameter. It defines the extension of tile for DEM simulation (optimization parameter). The other default parameters (i.e. orbit interpolation degree) can be kept as by default.

- Optional step: multilooking

Interferometric phase can be affected by several sources of noise. To increase the S/N ratio and highlight the phase signatures in the interferogram the multilook correction can be applied (Figure A.14). Multilook reduces speckle noise in SAR images by averaging adjacent pixels and produces square pixels (~12x12m for S1), but as drawback causes a loss in resolution.Multilooking is thus not advised for the extraction of permanent scatterers products.

Radar → SAR Utilities → Multilooking

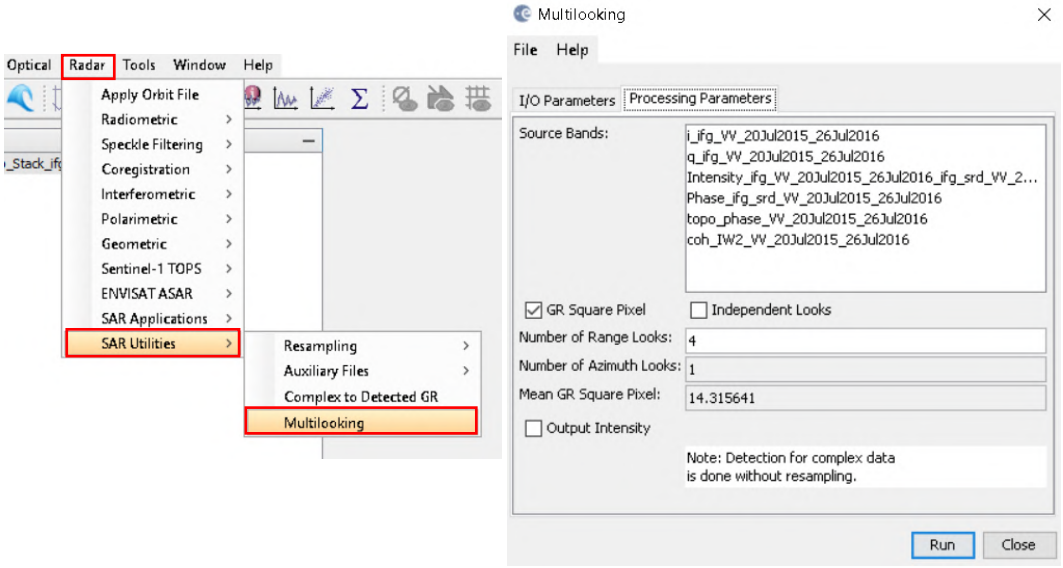


*Figure A.14:Multilooking.*

*In the Processing Parameters tab leave all the Source Bands unselected, by default all of them will be selected in the processing.* If the *GR Square Pixel* is checked the range and azimuth spacing are approximately the same in the multilooked image. During the multilooking step a SLC radar image is divided in different looks (=groups of signal samples in the SAR processor) characterized by different frequencies. The different looks are then averaged.

If the Indipendent Look is selected, the number of range looks and the number of azimuth looks are selected independently by the user, otherwise they are authomatically set by default (4:1).

*Run to complete the process*. The product is saved with the suffix "_ML".

- Phase filtering

An additional filtering step can be applied to further improve the interferometric phase. A common filter is the Goldstein filter which uses a Fast Fourier Transformation (FFT) to enhance the signal-to-noise ratio of the image (Figure A.15).

Radar → Interferometric → Filtering → Goldstein Phase Filtering

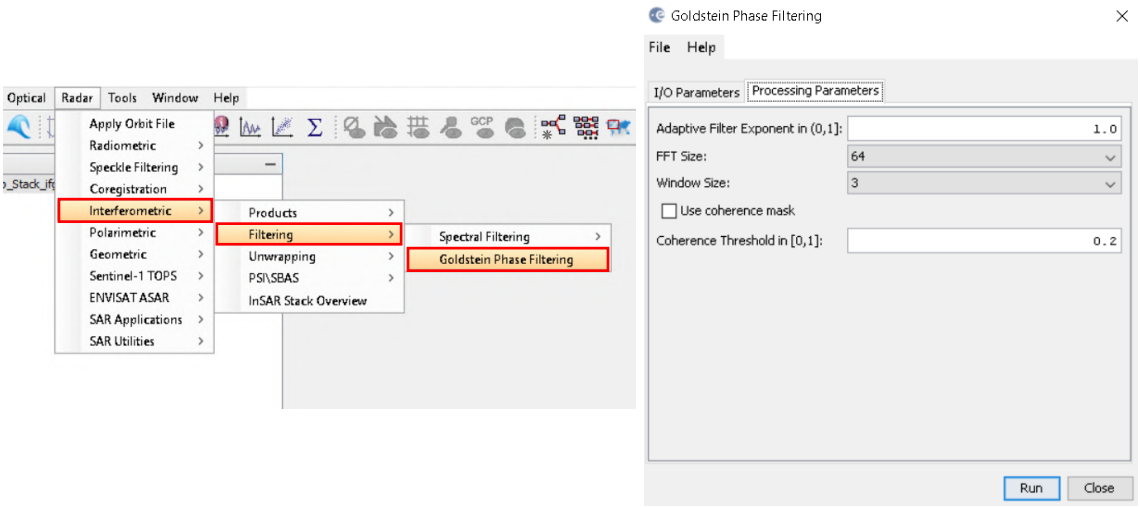


*Figure A.15:Goldstein Phase Filtering.*

*Leave all the parameters as default in the Processing Parameters tab.* The *Adaptive Filter Exponent* has a value between (0,1]. The larger the value the stronger the filtering, the default value is set to 1.

*Press run to complete the filtering step*. The final product is saved as "_flt".

- Terrain correction

Due to topographical variations of a scene and the tilt of the satellite sensor (viewing angle ≠0), distances can be distorted in the SAR images.

To reproject the data into a geographic coordinate system and make the interferogram easily accessible, the phase image must be corrected through a DEM-based geocoding step (Figure A.16).

If the interferogram has to be further unwrapped, this step must be skipped and performed later, otherwise it is useful to geocode and visualize the final product.

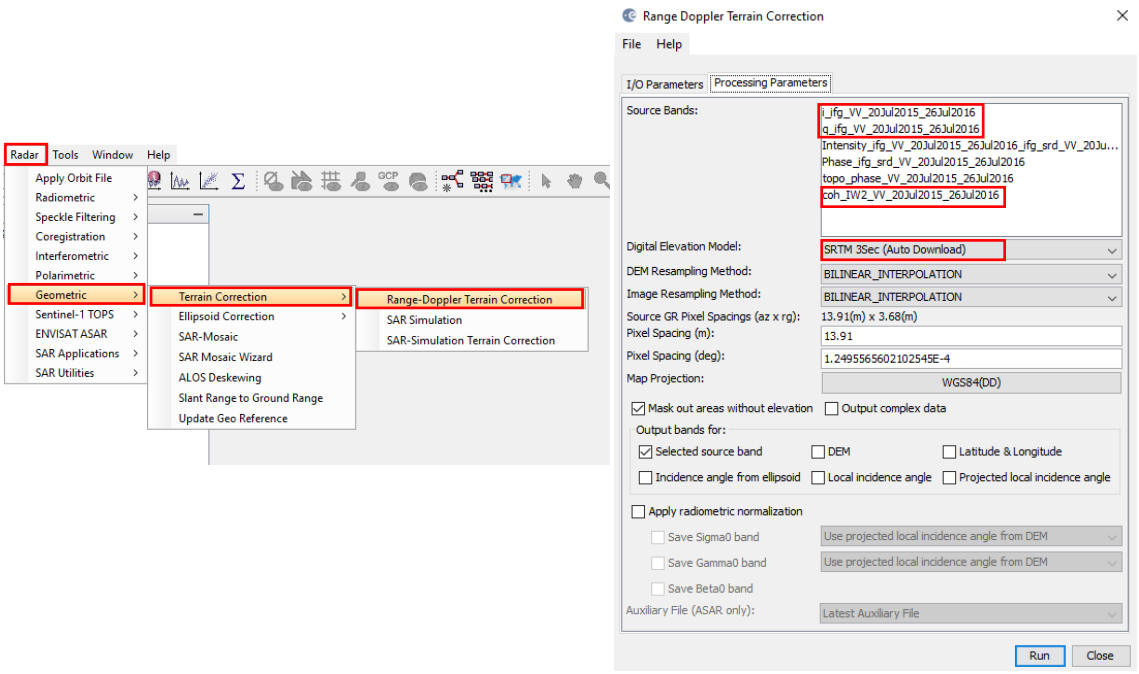


*Figure A.16:Terrain correction.*

Radar → Terrain Correction → Range Doppler Terrain Correction

In the *I/O Parameters* tab select the "_flt" file and the saving directory. In the *Processing Parameters* tab select as *Source Band* the real(i) and imagery(q) bands and the coherence band (Figure A.16) or leave all the bands unselected to have all of them considered.

In the dropdown menu of *Digital Elevation Model* choose the DEM used in the previous step. *Pixel spacing* (i.e. the distance on the ground for a pixel in the range and azimuth directions between the center of each pixel) can be changed as well. The output *Map Projection* can be changed and the interferogram saved in different coordinates systems. Additional bands can be exported (ie. DEM, incident angle etc.).

Press Run to conclude. The product will be renamed with the suffix "_TC".

- Export the product

The so processed phase interferogram can be displayed in the workspace window double clicking on the *Phase* file in the band folder. As the interferogram is in phase, it is suggested to rescale the colormap between $-\pi$ and $\pi$ in the colour manipulation tab. The "_TC" interferogram is now projected in geographical coordinates and Lat-Lon values are displayed in the lower right corner (Figure A.17).

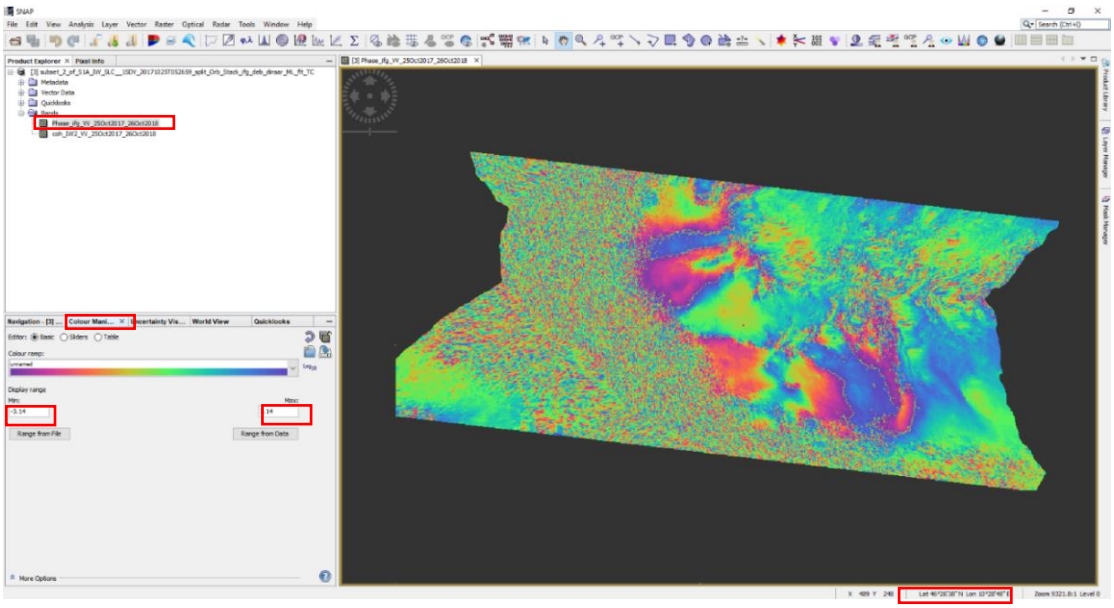

*Figure A.17: colour manipulation and product export.*

Lat-Lon coordinates are shown also before the _TC correction, however as they are not exacted before the terrain correction step, they are estimated based on the image's extent and it is thus quite common that the location (Lat-Lon values) of single pixels doesn't coincide between the two visualization.

*The interferogram can be exported in several formats: to choose the desired one, clic on the workspace and then go to: File → Export. It can be also exported as KMZ file: to do so right click on the workspace and select "Export view as Google earth KMZ".*

## 3. Phase unwrapping: SNAPHU

To extract the displacement map from an interferogram, it is necessary to unwrap the phase and convert its values from radians to metric scale. This step can be run in SNAP using the unwrapping plugin SNAPHU.

Snaphu is a statistical-cost network-flow algorithm for phase unwrapping (C W Chen & Zebker, 2003) that computes the most likely unwrapped solution given the input interferogram.

It can be installed in SNAP from: *Tools → Plugins →Available Plugins → SNAPHU unwrapping.*

- Create a subset

The first requirement to unwrap an interferogram is to consider the product not geocoded (*_split_orb_stack_ifg_deb_dinsar_ML_flt*) (point 10) and clip only the AOI to reduce the computational time.

To create a subset two ways are possible:

1. *Zoom on the "_flt" phase product to select the AOI. Right click in the workspace window and select spatial subset from view. Press OK*. All the bands associated to the interferogram (intensity, coherence etc.) will be extracted in the subset (Figure A.18).
2. *Go to* Raster → subset. The same panel will appear, but to clip the scene it is necessary to insert the SAR or geographic coordinates of a rectangle bounding the AOI (Figure A.18Figure A.18:Spatial subset.). *Press OK*.

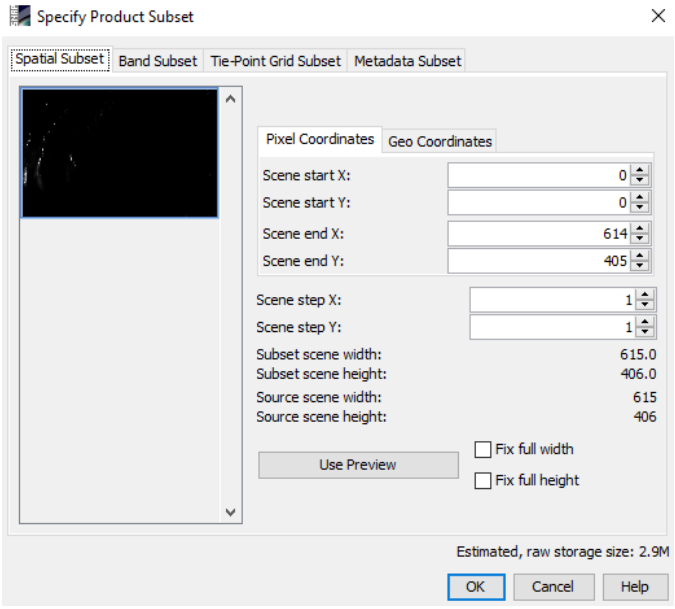


*Figure A.18:Spatial subset.*

The subset will be displayed in the Product Explorer Panel (Figure A.19), but it is necessary to save it in the directory folder: right click on the product → save product as.

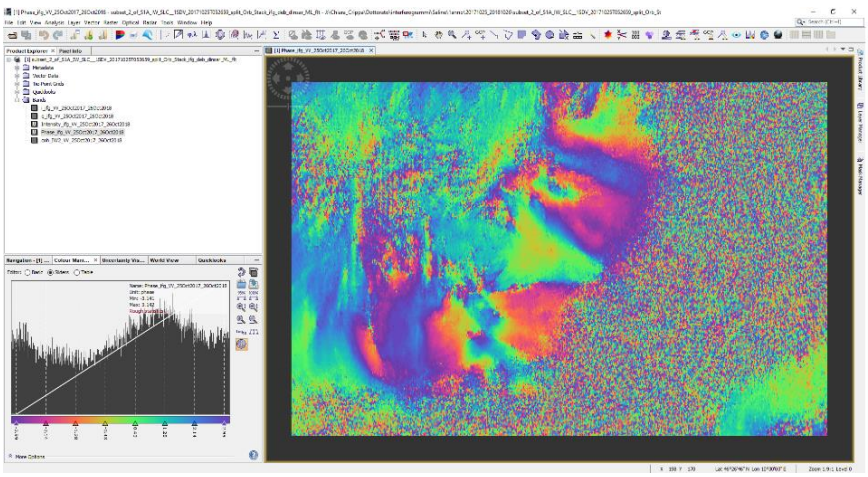

*Figure A.19:Subset visualization.*

- Unwrapping: export

This step is aimed at preparing the product for the unwrapping procedure making the bands compatible for SNAPHU processing and store the files in a proper "container" file (Figure A.20).

*Radar → Interferometric → Unwrapping →Snaphu Export*

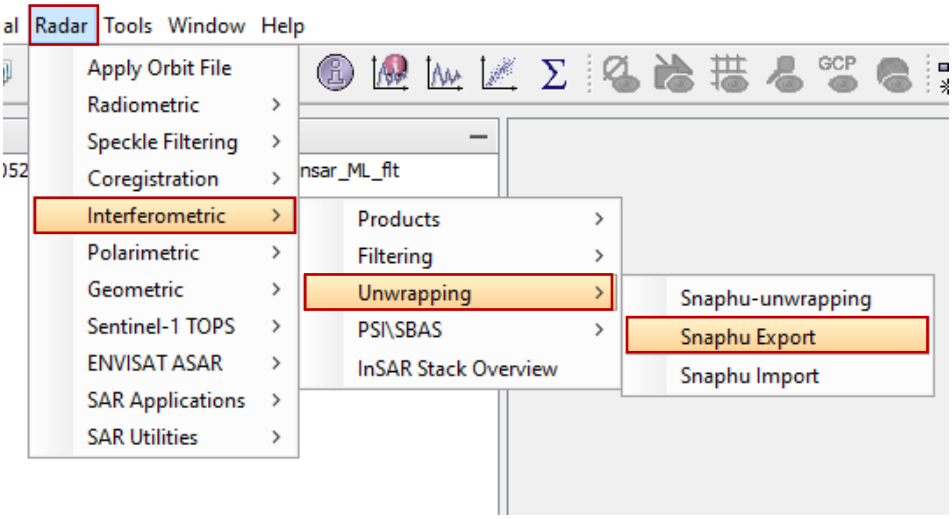


*Figure A.20:SNAPHU export.*

*In the "Read" tab select the subset target product. In the "SnaphuExport" tab (*Figure A.21*) fill the fields as follows:*

- *Target folder:* It is advised to create a separate folder in the main saving directory where all the interferogram files are stored (i.e."snaphu_export").
- *Statistical-cost mode:* select DEFO for deformation mapping.
- *Initial method:* Two unwrapping methods are proposed. MCF (minimum cost flow) and MST (minimum spanning tree). We adopted the MCF (Mario Costantini, 1998) method. This algorithm is suggested for those scenes with several low coherence area as it tends to reduce the phase jumps associated to these sectors and scatter the deriving error.
- *Number of tile Rows and Coloums:* Since the unwrapping process can be *computationally intensive* large interferograms can be split in tiles processed (unwrapped) in parallel. However, possible boundary effects may cause problems in the tiles combination and as consequence the complete result will be more affected by errors. If the interferogram (subset) is not too big it is suggested to use a single tile (Number of tile Rows and Coloums=1).
- *Number of processors:* it is the number of concurrent processing threads. To speed up the unwrapping increase the number of processors.
- *Row and column overlap:* overlap in pixels between neighboring tiles.
- *Tile cost threshold:* larger cost threshold implies smaller regions. It is safer, but more expensive computationally.

Once set all the parameters *press Run.*

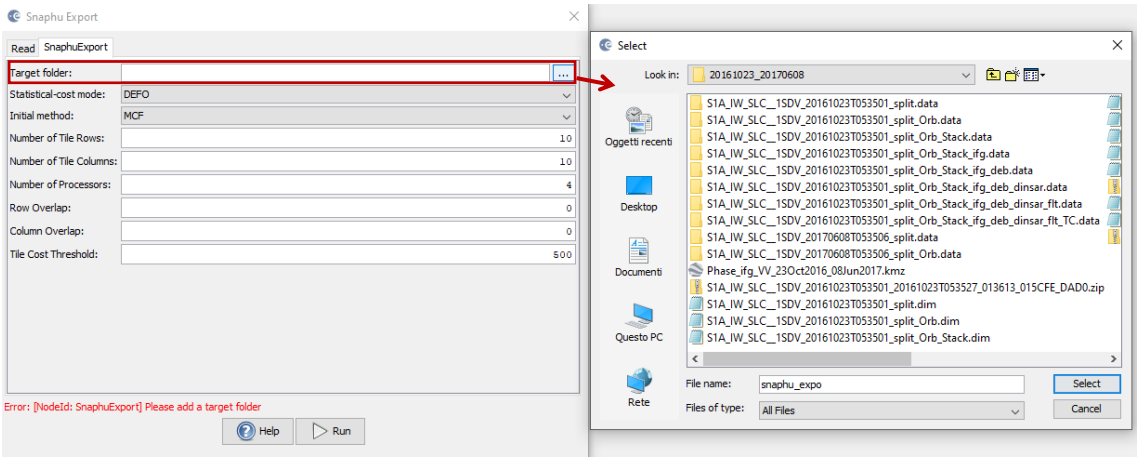


*Figure A.21:Snaphu export parameters.*

- Unwrapping

Open the files stored in the snaphu_export folder (Figure A.22).
*Radar* → *Interferometric* → *Unwrapping* → *Snaphu-unwrapping*

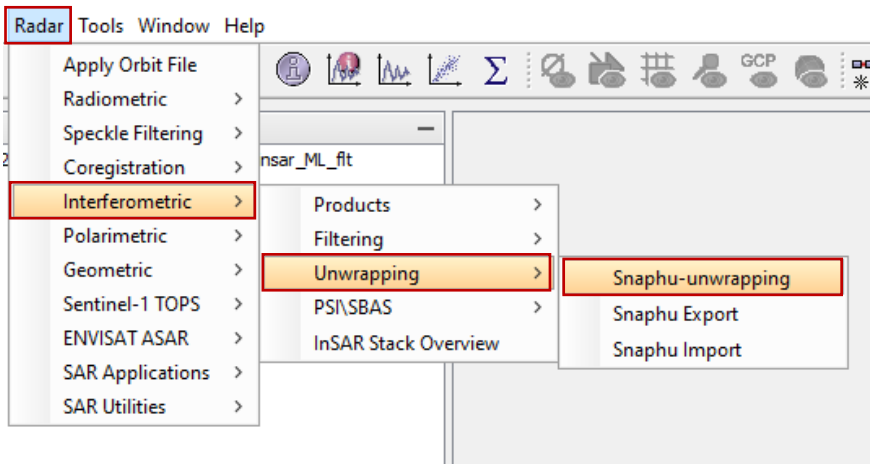


*Figure A.22: Snaphu unwrapping.*

Files are stored in the same folder containing the input files (and snaphu.conf) and are prefixed with UnwPhase. There is a header file (.hdr) and an image file (.img)
In the *I/O parameters* tab select as *Source Product* the .hdr file saved in the snaphu_expo folder previously created (Figure A.23).

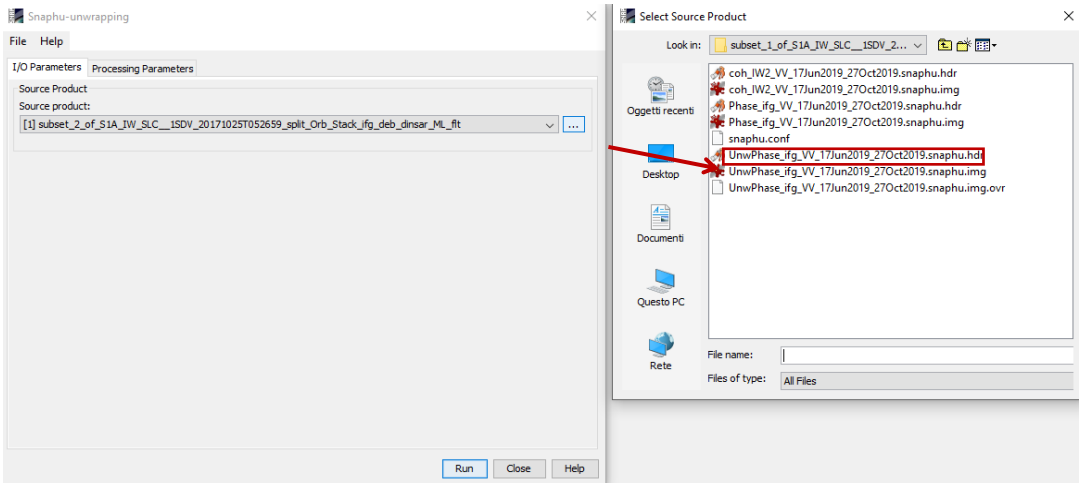


*Figure A.23: I/O Parameters.*

In the *Processing Parameter* tab select the output folder that must coincide with the folder containing the snaphu- export files (Figure A.24).
Press *Run*. The final result appears as "Output Product" in the Product Explorer panel, if this file doesn't appear the process failed.

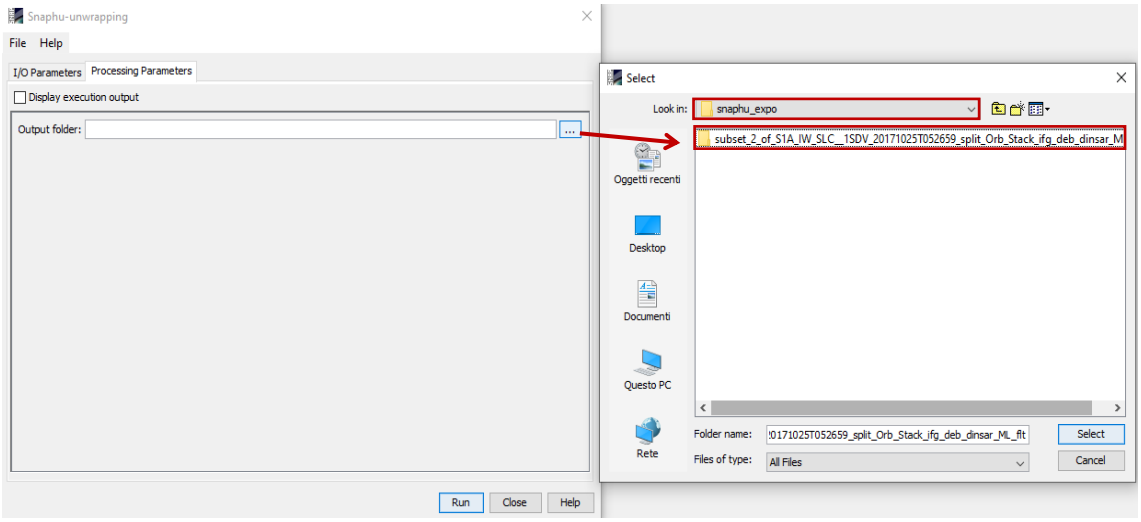


*Figure A.24: Output folder selection.*

- Unwrapping: import

In this step the results from SNAPHU processing (point 14) are imported, and the interferometric product containing the unwrapped phase band and the metadata of the source interferometric product is built (Figure A.25).
*Radar → Interferometric → Unwrapping → Snaphu Import*
In the Snaphu import panel complete the fields as follows:

- In the Snaphu Import panel select in the *1-Read-Phase-tab* the initial interferogram product "subset_XXX_flt".

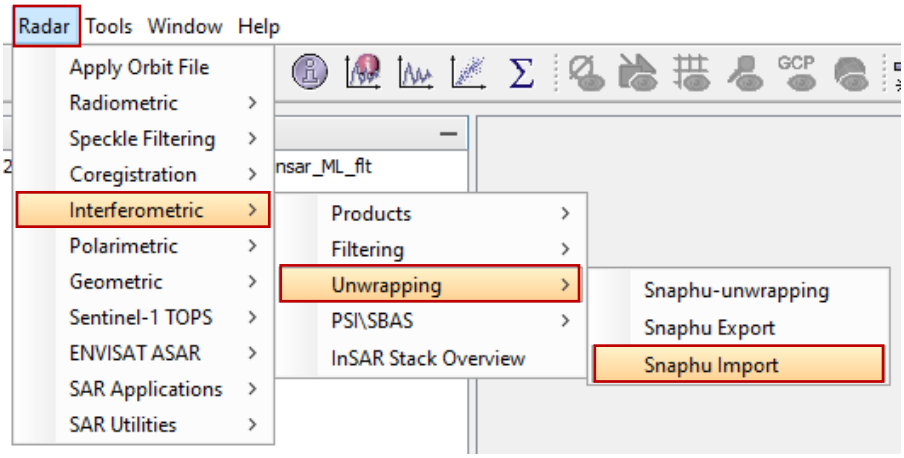


*Figure A.25: Snaphu Import.*

- In the *2-Read-Unwrapped-Phase* navigate to the Snaphu export folder and select the *"UnwPhase_XXX.hdr"* file (Figure A.26Figure A.26: import the unwrapped phase.).
- In the *3-Snaphu-Import* check the "*Do NOT save Wrapped interferogram in the target product*" option. This will generate a product without including all the other bands from the source interferogram. If it remains unchecked all the source bands will be kept in the output.
- In the *4-Write* tab save the product adding the suffix "_unw" to the displayed name and select the saving directory folder.

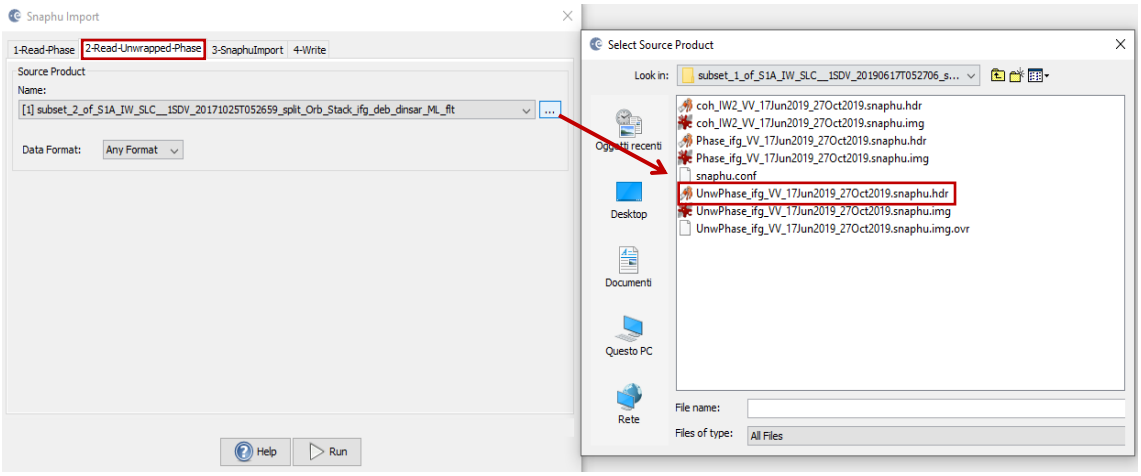


*Figure A.26: import the unwrapped phase.*

*Press Run* to conclude the operation. The final product will be displayed in the Product Reader Window (Figure A.27). The unwrapped phase band is stored in the bands folder.

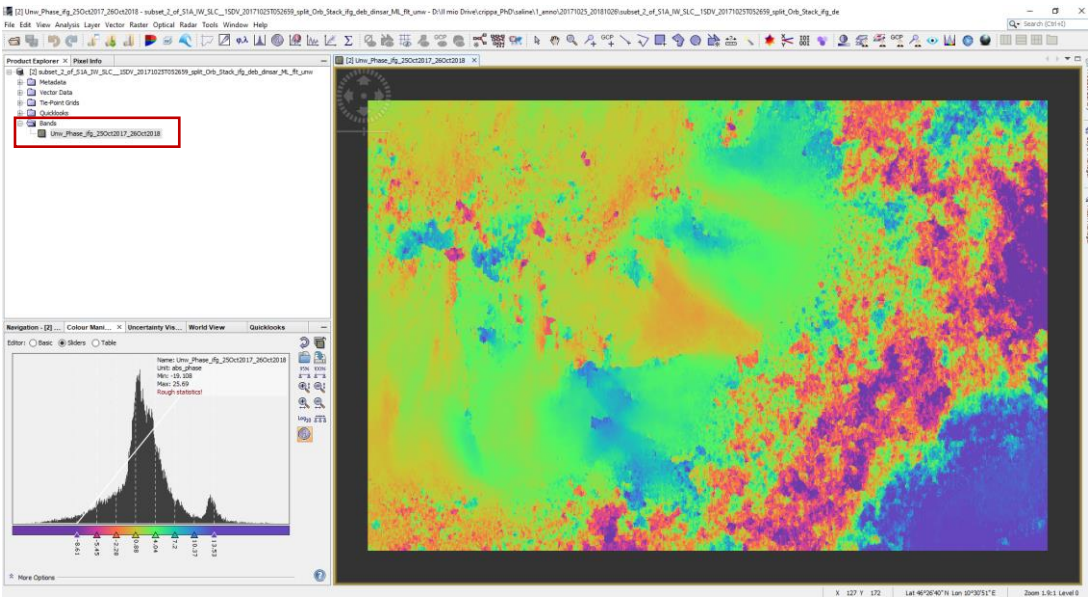

*Figure A.27:Unwrapped phase visualization.*

- Phase to displacement conversion

The unwrapped product is still in phase. To convert it from phase to a displacement map go to (Figure A.28):

*Radar* → *Interferometric* → *Products* → *Phase to Displacement*

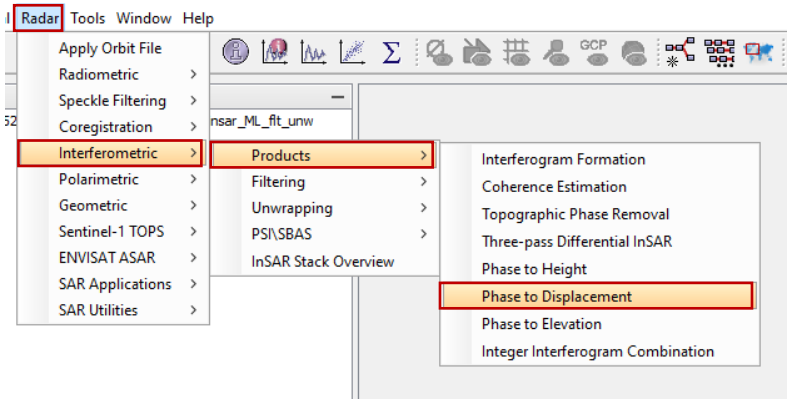


*Figure A.28:Phase to displacement.*

In the opening panel select the unwrapped phase product, the saving directory and press *Run* to conclude the processing.

The displacement map is saved with the suffix "_disp".

- Correction for a stable point

Once extracted the deformation map in metric scale, it has to be corrected rescaling all the values to a known stable point (0 displacement) on the ground.

As SAR image is distorted respect to the real geographical setting, it is not straightforward to recognize homologous points between the interferogram scene and the topography. It is

thus suggested to rectify the interferogram with the command "*terrain correction*" as explained in point 10.
Once reprojected the displacement map, Lat-Lon coordinates (displayed in the bottom right corner) can be used to identify the selected stable point in the scene. Set the pointer on the reference Lat-Lon coordinates in the workspace and in the the "Pixel Info" window check the corresponding displacement value (Figure A.29).

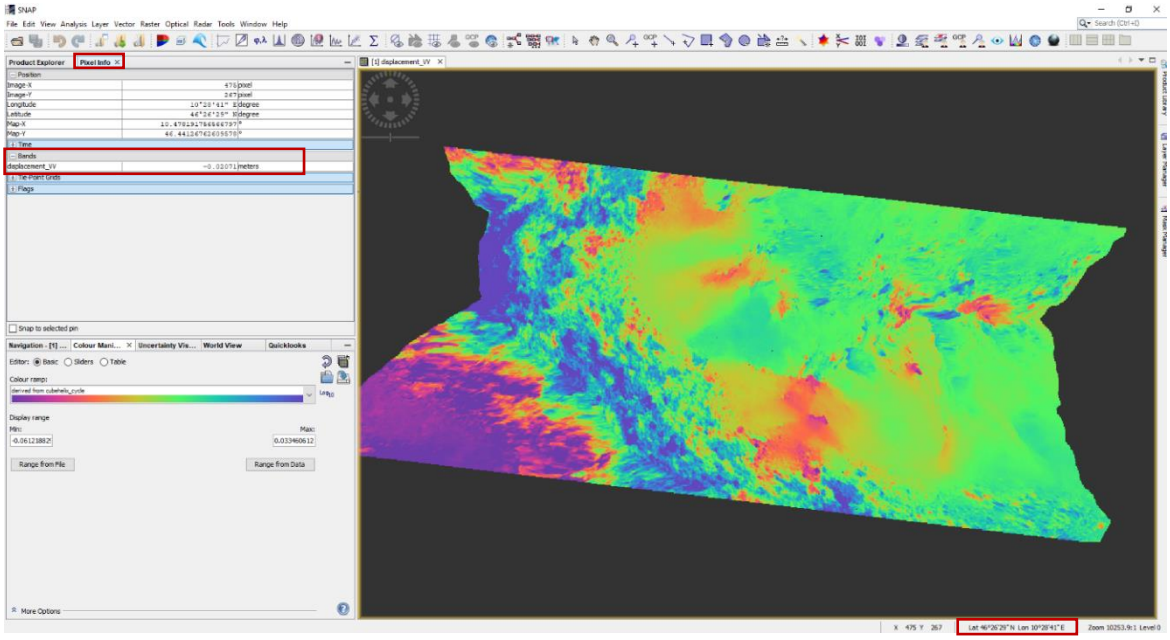

*Figure A.29: Pixel values identification.*

This value has to be subtracted or added to all the other pixels to rescale the displacement map. This can be easily done in: *Raster* → *Band Maths*
In the Band Maths panel select the displacement map in the dropdown menu and choose a new name to save the product (Figure A.30) (i.e. "XXX_disp_corr" for displacement correction). Then press *Edit Expression* (Figure A.30).

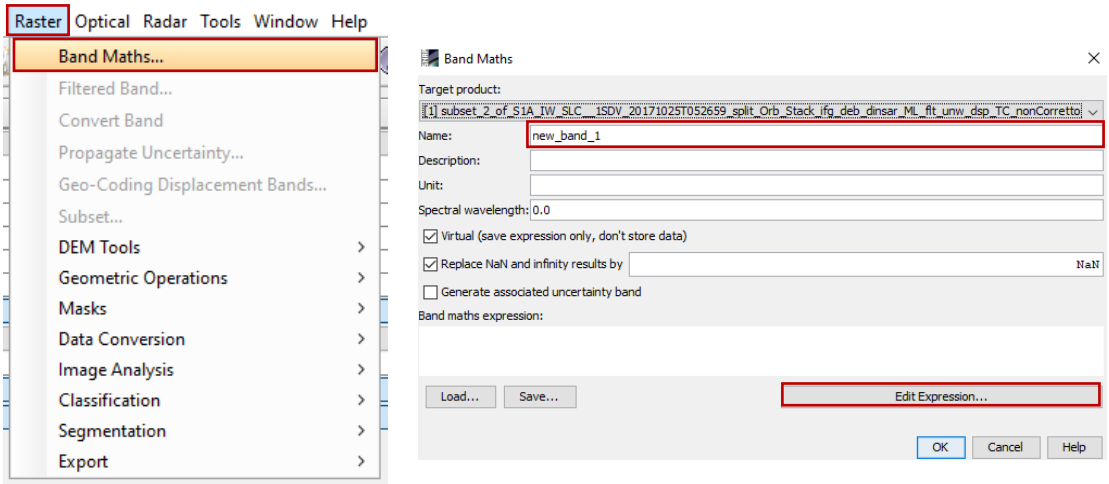


*Figure A.30: Band Maths.*

In the Band Maths Expression Editor panel set up the expression to correct the displacement: click on the displacement product displayed in "*Data sources*" and add or subtract the displacement value extracted for the reference point (Figure A.31).

$$disp\_corr = d_{original} - d_{reference\ point} \qquad if\ d_{reference\ point} > 0$$
$$disp\_corr = d_{original} + d_{reference\ point} \qquad if\ d_{reference\ point} < 0$$

With $d = displacement\ value$

*Then press OK to conclude the process*.

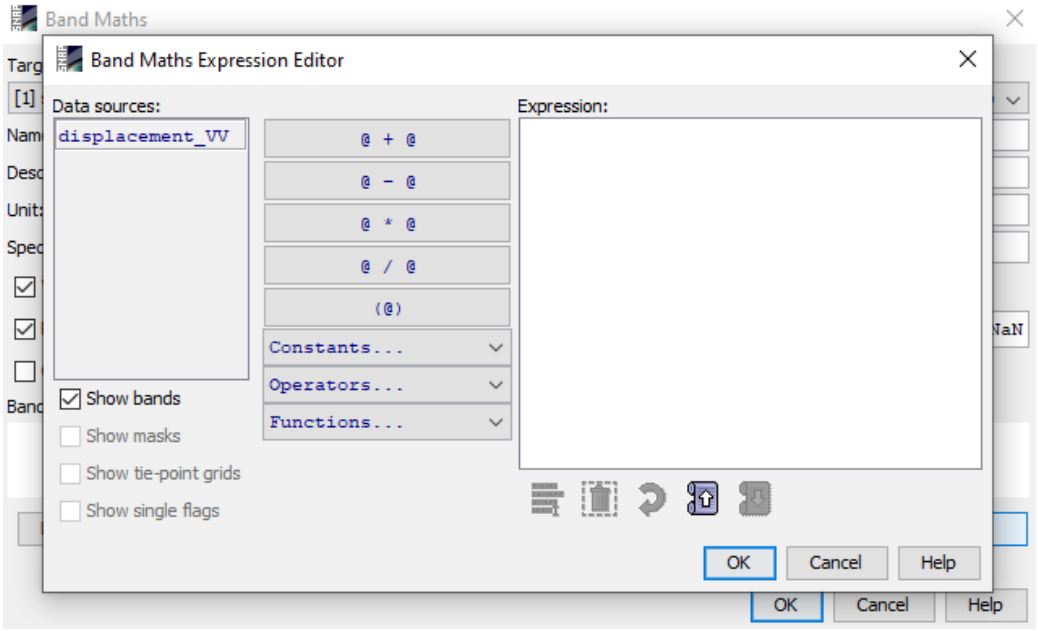


*Figure A.31:Band Maths Expression Editor.*

Useful readings and tutorials for processing in SNAP:

- SENTINEL-1 SAR User Guide Introduction:
- Sentinel-1 Toolbox: Stripmap Interferometry Tutorial (Braun & Veci, 2015)
- ESA Sentinel Online
- Science Toolbox Exploitation Platform (STEP)
- Sentinel Toolboxes website http://step.esa.int/main/doc/tutorials/
- The SAR handbook (Flores et al., 2019)

*TableA 1: Interferograms processed over Mater DSGSD from Sentinel-1 SLC images*

| Geometry | Master (date) | Slave (date) | Bt (days) [1] | $B_{perp}$ (m) [1] |
|---|---|---|---|---|
| Descending | 24/08/2016 | 17/09/2016 | 24 | 66.66 |
| Descending | 17/09/2016 | 11/10/2016 | 24 | 21.18 |
| Descending | 8/06/2017 | 2/07/2017 | 24 | 129.86 |
| Descending | 2/07/2017 | 26/07/2017 | 24 | 23.71 |
| Descending | 26/07/2017 | 19/08/2017 | 24 | 20.05 |
| Descending | 19/08/2017 | 12/09/2017 | 24 | 6.07 |
| Descending | 12/09/2017 | 6/10/2017 | 24 | 49.59 |
| Descending | 6/10/2017 | 30/10/2017 | 24 | 30.37 |
| Descending | 9/06/2018 | 3/07/2018 | 24 | 70.97 |
| Descending | 3/07/2018 | 27/07/2018 | 24 | 13.88 |
| Descending | 27/07/2018 | 20/08/2018 | 24 | 54.43 |
| Descending | 20/08/2018 | 13/09/2018 | 24 | 44.89 |
| Descending | 13/09/2018 | 7/10/2018 | 24 | 65.18 |
| Descending | 7/10/2018 | 31/10/2018 | 24 | 46.84 |
| Descending | 16/06/2019 | 10/07/2019 | 24 | 82.77 |
| Descending | 10/07/2019 | 3/08/2019 | 24 | 12.09 |
| Descending | 3/08/2019 | 27/08/2019 | 24 | 20.38 |
| Descending | 27/08/2019 | 20/09/2019 | 24 | 13.92 |
| Descending | 20/09/2019 | 14/10/2019 | 24 | 49.20 |
| Descending | 1/06/2016 | 23/10/2016 | 144 | 66.56 |
| Descending | 8/06/2017 | 30/10/2017 | 144 | 69.97 |
| Descending | 9/06/2018 | 19/10/2018 | 132 | 46.55 |
| Descending | 22/06/2019 | 20/10/2019 | 120 | 16.66 |
| Descending | 23/10/2016 | 8/06/2017 | 228 | 116.63 |
| Descending | 30/10/2017 | 15/06/2018 | 228 | 25 |
| Descending | 19/10/2018 | 16/06/2019 | 240 | 70.99 |
| Descending | 7/07/2016 | 2/07/2017 | 360 | 96.12 |
| Descending | 19/07/2016 | 20/07/2017 | 366 | 9.85 |
| Descending | 12/08/2016 | 13/08/2017 | 366 | 12.19 |
| Descending | 24/08/2016 | 25/08/2017 | 366 | 47.60 |
| Descending | 5/09/2016 | 6/09/2017 | 366 | 20.24 |
| Descending | 17/09/2016 | 18/09/2017 | 366 | 37.68 |
| Descending | 29/09/2016 | 30/09/2017 | 366 | 55.62 |
| Descending | 11/10/2016 | 12/10/2017 | 366 | 55.62 |
| Descending | 23/10/2016 | 24/10/2017 | 366 | 75.24 |
| Descending | 8/06/2017 | 9/06/2018 | 366 | 127.72 |
| Descending | 20/06/2017 | 21/06/2018 | 366 | 106.73 |
| Descending | 2/07/2017 | 3/07/2018 | 366 | 73.08 |
| Descending | 20/07/2017 | 21/07/2018 | 366 | 53.36 |
| Descending | 1/08/2017 | 2/08/2018 | 366 | 37.21 |
| Descending | 13/08/2017 | 14/08/2018 | 366 | 43.81 |
| Descending | 19/08/2017 | 20/08/2018 | 366 | 43.81 |
| Descending | 25/08/2017 | 26/08/2018 | 366 | 19.11 |
| Descending | 6/09/2017 | 7/09/2018 | 366 | 38.19 |
| Descending | 18/9/2017 | 19/09/2018 | 366 | 22.61 |
| Descending | 24/09/2017 | 25/09/2018 | 366 | 22.61 |
| Descending | 6/10/2017 | 7/10/2018 | 366 | 28.63 |
| Descending | 18/10/2017 | 19/10/2019 | 366 | 22.96 |
| Descending | 24/10/2017 | 25/10/2018 | 366 | 12.77 |
| Descending | 30/10/2017 | 31/10/2018 | 366 | 10.50 |
| Descending | 15/06/2018 | 16/06/2019 | 366 | 35.68 |
| Descending | 27/06/2018 | 28/06/2019 | 360 | 107.83 |
| Descending | 9/07/2018 | 10/07/2019 | 366 | 22.53 |

| | | | | |
|---|---|---|---|---|
| Descending | 21/07/2018 | 22/07/2019 | 366 | 22.69 |
| Descending | 2/08/2018 | 3/08/2019 | 366 | 34.42 |
| Descending | 14/08/2018 | 15/08/2019 | 366 | 74.15 |
| Descending | 26/08/2018 | 27/08/2019 | 366 | 29.28 |
| Descending | 7/09/2018 | 8/09/2019 | 366 | 55.55 |
| Descending | 19/09/2018 | 20/09/2019 | 366 | 2.51 |
| Descending | 7/10/2018 | 8/10/2019 | 366 | 101.60 |
| Descending | 19/10/2018 | 20/10/2019 | 366 | 57.07 |

*Table_ A 2: List of SAR images used in the interferogram processing over Saline ridge and Corna Rossa*

| Date | Sat | Track | Date | Sat | Track |
|---|---|---|---|---|---|
| 02/06/2015 | SNT | 168 | 20/08/2017 | SNT | 168 |
| 08/06/2015 | SNT | 168 | 26/08/2017 | SNT | 168 |
| 14/06/2015 | SNT | 168 | 01/09/2017 | SNT | 168 |
| 14/06/2015 | SNT | 168 | 27/06/2017 | SNT | 168 |
| 08/07/2015 | SNT | 168 | 03/07/2017 | SNT | 168 |
| 20/07/2015 | SNT | 168 | 07/09/2017 | SNT | 168 |
| 01/08/2015 | SNT | 168 | 13/09/2017 | SNT | 168 |
| 13/08/2015 | SNT | 168 | 19/09/2017 | SNT | 168 |
| 25/08/2015 | SNT | 168 | 20/09/2017 | SNT | 168 |
| 06/09/2015 | SNT | 168 | 25/09/2017 | SNT | 168 |
| 18/09/2015 | SNT | 168 | 01/10/2017 | SNT | 168 |
| 30/09/2015 | SNT | 168 | 07/10/2017 | SNT | 168 |
| 12/10/2015 | SNT | 168 | 13/10/2017 | SNT | 168 |
| 24/10/2015 | SNT | 168 | 25/10/2017 | SNT | 168 |
| 02/06/2016 | SNT | 168 | 31/10/2017 | SNT | 168 |
| 08/06/2016 | SNT | 168 | 04/06/2018 | SNT | 168 |
| 14/07/2016 | SNT | 168 | 16/06/2018 | SNT | 168 |
| 26/07/2016 | SNT | 168 | 28/06/2018 | SNT | 168 |
| 07/08/2016 | SNT | 168 | 02/07/2018 | SNT | 168 |
| 19/08/2016 | SNT | 168 | 04/07/2018 | SNT | 168 |
| 31/08/2016 | SNT | 168 | 10/07/2018 | SNT | 168 |
| 12/09/2016 | SNT | 168 | 16/07/2018 | SNT | 168 |
| 24/09/2016 | SNT | 168 | 28/07/2018 | SNT | 168 |
| 24/09/2016 | SNT | 168 | 09/08/2018 | SNT | 168 |
| 06/10/2016 | SNT | 168 | 10/08/2018 | SNT | 168 |
| 18/10/2016 | SNT | 168 | 15/08/2018 | SNT | 168 |
| 18/10/2016 | SNT | 168 | 21/08/2018 | SNT | 168 |
| 30/10/2016 | SNT | 168 | 27/08/2018 | SNT | 168 |
| 09/06/2017 | SNT | 168 | 02/09/2018 | SNT | 168 |
| 15/06/2017 | SNT | 168 | 08/09/2018 | SNT | 168 |
| 21/06/2017 | SNT | 168 | 14/09/2018 | SNT | 168 |
| 02/06/2015 | SNT | 168 | 26/09/2018 | SNT | 168 |
| 08/06/2015 | SNT | 168 | 14/10/2018 | SNT | 168 |
| 14/06/2015 | SNT | 168 | 14/10/2018 | SNT | 168 |
| 14/06/2015 | SNT | 168 | 17/06/2019 | SNT | 168 |
| 08/07/2015 | SNT | 168 | 01/07/2019 | SNT | 168 |
| 20/07/2015 | SNT | 168 | 27/10/2019 | SNT | 168 |
| 27/06/2017 | SNT | 168 | | | |
| 03/07/2017 | SNT | 168 | | | |
| 09/07/2017 | SNT | 168 | | | |
| 09/07/2017 | SNT | 168 | | | |
| 09/07/2017 | SNT | 168 | | | |
| 15/07/2017 | SNT | 168 | | | |
| 16/07/2017 | SNT | 168 | | | |
| 21/07/2017 | SNT | 168 | | | |
| 27/07/2017 | SNT | 168 | | | |
| 02/08/2017 | SNT | 168 | | | |
| 08/08/2017 | SNT | 168 | | | |
| 14/08/2017 | SNT | 168 | | | |

*Table_ A 3: List of images- SqueeSAR ascending dataset*

| Date | Sat | Track | Date | Sat | Track |
|---|---|---|---|---|---|
| 23/03/2015 | SNT | 15 | 06/03/2017 | SNT | 15 |
| 04/04/2015 | SNT | 15 | 12/03/2017 | SNT | 15 |
| 16/04/2015 | SNT | 15 | 18/03/2017 | SNT | 15 |
| 28/04/2015 | SNT | 15 | 24/03/2017 | SNT | 15 |
| 10/05/2015 | SNT | 15 | 30/03/2017 | SNT | 15 |
| 22/05/2015 | SNT | 15 | 05/04/2017 | SNT | 15 |
| 03/06/2015 | SNT | 15 | 11/04/2017 | SNT | 15 |
| 15/06/2015 | SNT | 15 | 17/04/2017 | SNT | 15 |
| 27/06/2015 | SNT | 15 | 23/04/2017 | SNT | 15 |
| 09/07/2015 | SNT | 15 | 29/04/2017 | SNT | 15 |
| 21/07/2015 | SNT | 15 | 05/05/2017 | SNT | 15 |
| 02/08/2015 | SNT | 15 | 11/05/2017 | SNT | 15 |
| 14/08/2015 | SNT | 15 | 23/05/2017 | SNT | 15 |
| 26/08/2015 | SNT | 15 | 29/05/2017 | SNT | 15 |
| 07/09/2015 | SNT | 15 | 04/06/2017 | SNT | 15 |
| 19/09/2015 | SNT | 15 | 10/06/2017 | SNT | 15 |
| 01/10/2015 | SNT | 15 | 22/06/2017 | SNT | 15 |
| 13/10/2015 | SNT | 15 | | | |
| 25/10/2015 | SNT | 15 | | | |
| 06/11/2015 | SNT | 15 | | | |
| 18/11/2015 | SNT | 15 | | | |
| 30/11/2015 | SNT | 15 | | | |
| 12/12/2015 | SNT | 15 | | | |
| 24/12/2015 | SNT | 15 | | | |
| 17/11/2016 | SNT | 15 | | | |
| 29/01/2016 | SNT | 15 | | | |
| 05/03/2016 | SNT | 15 | | | |
| 17/03/2016 | SNT | 15 | | | |
| 29/03/2016 | SNT | 15 | | | |
| 10/04/2016 | SNT | 15 | | | |
| 22/04/2016 | SNT | 15 | | | |
| 04/05/2016 | SNT | 15 | | | |
| 16/05/2016 | SNT | 15 | | | |
| 28/05/2016 | SNT | 15 | | | |
| 09/06/2016 | SNT | 15 | | | |
| 15/07/2016 | SNT | 15 | | | |
| 27/07/2016 | SNT | 15 | | | |
| 08/08/2016 | SNT | 15 | | | |
| 01/09/2016 | SNT | 15 | | | |
| 13/09/2016 | SNT | 15 | | | |
| 25/09/2016 | SNT | 15 | | | |
| 07/10/2016 | SNT | 15 | | | |
| 19/10/2016 | SNT | 15 | | | |
| 31/10/2016 | SNT | 15 | | | |
| 12/11/2016 | SNT | 15 | | | |
| 24/11/2016 | SNT | 15 | | | |
| 06/12/2016 | SNT | 15 | | | |
| 18/12/2016 | SNT | 15 | | | |
| 30/12/2016 | SNT | 15 | | | |
| 11/10/2017 | SNT | 15 | | | |
| 23/01/2017 | SNT | 15 | | | |
| 04/02/2017 | SNT | 15 | | | |
| 16/02/2017 | SNT | 15 | | | |
| 28/02/2017 | SNT | 15 | | | |

*Table_ A 4: List of images- SqueeSAR descending dataset*

| Date | Sat | Track | Date | Sat | Track |
|---|---|---|---|---|---|
| 22/03/2015 | SNT | 168 | 29/12/2016 | SNT | 168 |
| 15/04/2015 | SNT | 168 | 10/01/2017 | SNT | 168 |
| 27/04/2015 | SNT | 168 | 03/02/2017 | SNT | 168 |
| 09/05/2015 | SNT | 168 | 15/02/2017 | SNT | 168 |
| 21/05/2015 | SNT | 168 | 27/02/2017 | SNT | 168 |
| 02/06/2015 | SNT | 168 | 11/03/2017 | SNT | 168 |
| 14/06/2015 | SNT | 168 | 17/03/2017 | SNT | 168 |
| 26/06/2015 | SNT | 168 | 23/03/2017 | SNT | 168 |
| 08/07/2015 | SNT | 168 | 29/03/2017 | SNT | 168 |
| 20/07/2015 | SNT | 168 | 04/04/2017 | SNT | 168 |
| 01/08/2015 | SNT | 168 | 10/04/2017 | SNT | 168 |
| 13/08/2015 | SNT | 168 | 16/04/2017 | SNT | 168 |
| 25/08/2015 | SNT | 168 | 22/04/2017 | SNT | 168 |
| 06/09/2015 | SNT | 168 | 28/04/2017 | SNT | 168 |
| 18/09/2015 | SNT | 168 | 04/05/2017 | SNT | 168 |
| 30/09/2015 | SNT | 168 | 10/05/2017 | SNT | 168 |
| 12/10/2015 | SNT | 168 | 16/05/2017 | SNT | 168 |
| 24/10/2015 | SNT | 168 | 22/05/2017 | SNT | 168 |
| 05/11/2015 | SNT | 168 | 28/05/2017 | SNT | 168 |
| 17/11/2015 | SNT | 168 | 03/06/2017 | SNT | 168 |
| 29/11/2015 | SNT | 168 | 09/06/2017 | SNT | 168 |
| 23/12/2015 | SNT | 168 | 15/06/2017 | SNT | 168 |
| 04/10/2016 | SNT | 168 | 21/06/2017 | SNT | 168 |
| 28/01/2016 | SNT | 168 | 27/06/2017 | SNT | 168 |
| 09/02/2015 | SNT | 168 | 03/07/2017 | SNT | 168 |
| 21/02/2016 | SNT | 168 | | | |
| 04/03/2016 | SNT | 168 | | | |
| 16/03/2016 | SNT | 168 | | | |
| 09/04/2016 | SNT | 168 | | | |
| 21/04/2016 | SNT | 168 | | | |
| 03/05/2016 | SNT | 168 | | | |
| 15/05/2016 | SNT | 168 | | | |
| 27/05/2016 | SNT | 168 | | | |
| 08/06/2016 | SNT | 168 | | | |
| 14/07/2016 | SNT | 168 | | | |
| 26/07/2016 | SNT | 168 | | | |
| 07/08/2016 | SNT | 168 | | | |
| 19/08/2016 | SNT | 168 | | | |
| 31/08/2016 | SNT | 168 | | | |
| 12/09/2016 | SNT | 168 | | | |
| 24/09/2016 | SNT | 168 | | | |
| 30/09/2016 | SNT | 168 | | | |
| 06/10/2016 | SNT | 168 | | | |
| 18/10/2016 | SNT | 168 | | | |
| 30/10/2016 | SNT | 168 | | | |
| 11/11/2016 | SNT | 168 | | | |
| 23/11/2016 | SNT | 168 | | | |
| 05/12/2016 | SNT | 168 | | | |
| 17/12/2016 | SNT | 168 | | | |

# C. Pseudo PS distribution for kinematic assessment

Examples of PseudoPS distribution and morphostructural mapping of linear features on some slow rock slope deformations with different kinematics.

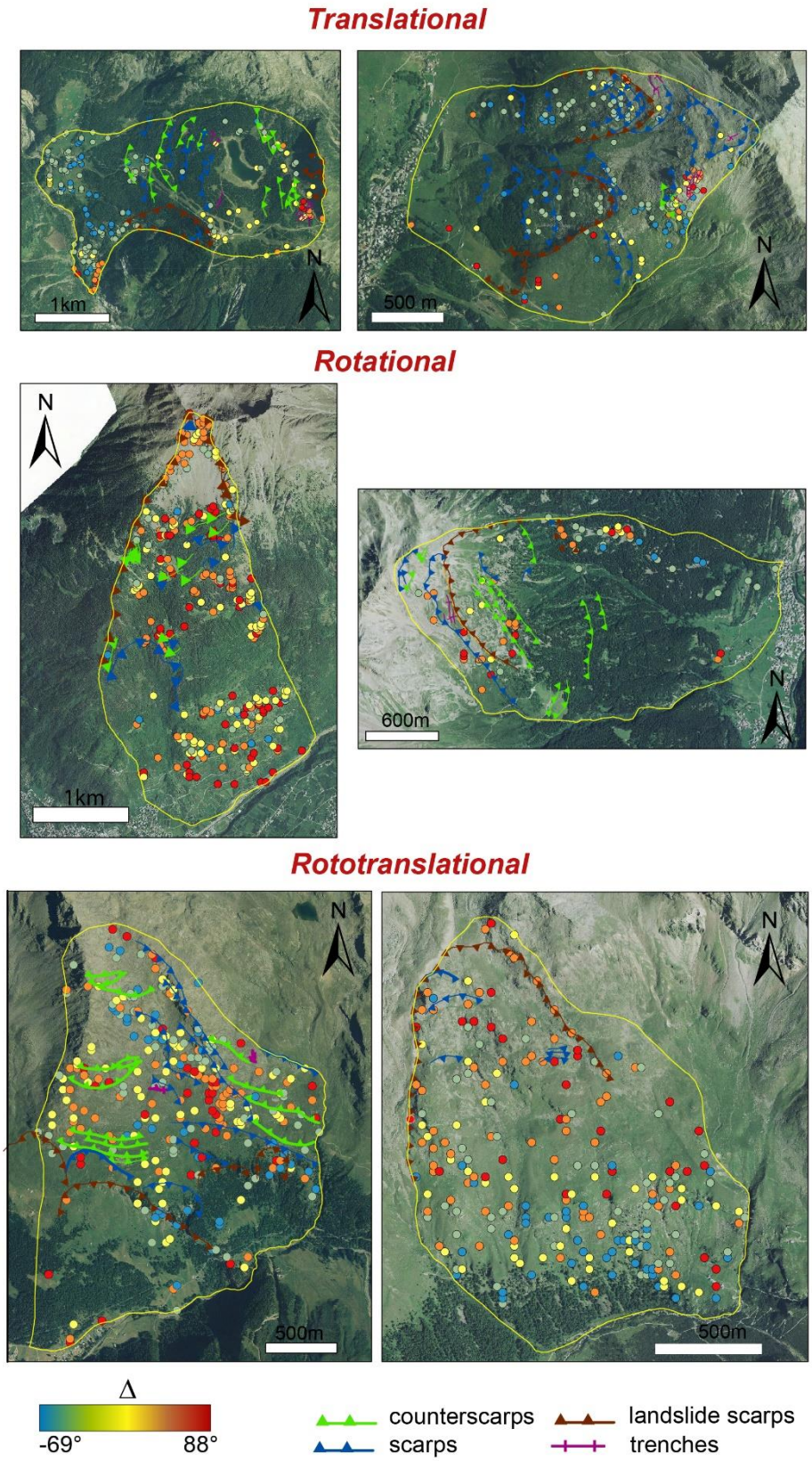

# D. Active PS and Pseudo PS abundance

Number of active PS (-2 >LOSvel (mm/yr) >+2) and Pseudo PS in the mapped slow rock slope deformations. Analaysis robustness is strongly influenced by PS and Pseudo PS abundance.

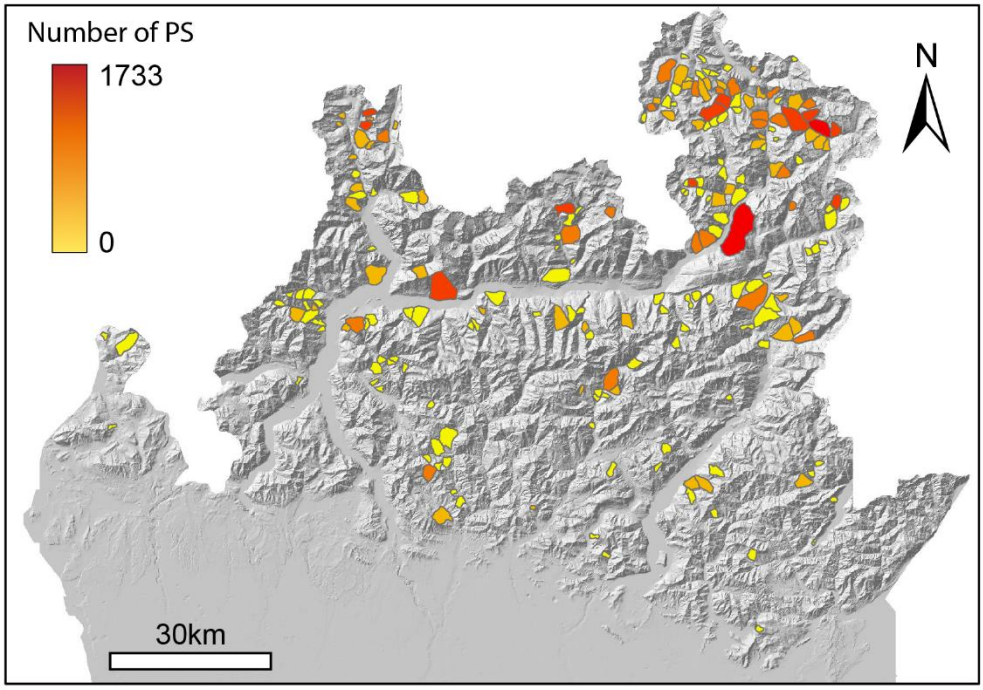


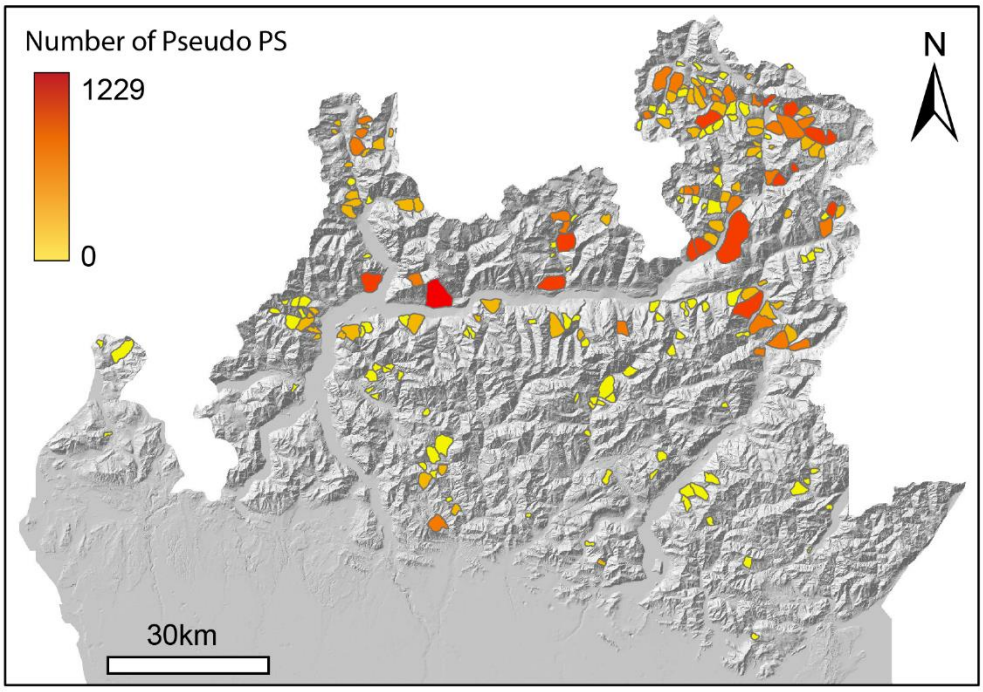

# Acknowledgments

I express sincere gratitude to my supervisor Prof. Federico Agliardi for his constant support of my PhD study and research and his coaching during these years.
I deeply thank all the engineering and structural geology group of Bicocca for the precious help and collaboration and Marco Previtali (Zic) for his patience, tips-and-tricks with Matlab programming.
I thank Dr. Andrea Manconi for his teaching and guidance through the InSAR world and for the fruitful discussions on the potentials and limitations of InSAR applications.

# Research funding and collaborations

This research was partially funded by Fondazione Cariplo, Grant 2016-0757 Slow2Fast to F. Agliardi, which provided a four-month grant from July2018 to October 2018. The abroad period in collaboration with ETH Zurich was funded by The Swiss-European Mobility Program and the Exchange mobility EXTRA UE program which provided a three-month grant each from September 2018 to December 2018.

# References


Ackermann, R. V., & Schlische, R. W. (1997). Anticlustering of small normal faults around larger faults. Geology, 25(12), 1127–1130. https://doi.org/10.1130/0091-7613(1997)025<1127:AOSNFA>2.3.CO;2

Ager, T. P. (2013). An introduction to synthetic aperture radar imaging. Oceanography, 26(2), 20–33.

Agliardi, F., Crosta, G. B., & Zanchi, A. (2001). Structural constraints on deep-seated slope deformation kinematics. Engineering Geology, 59(1–2), 83–102. https://doi.org/10.1016/S0013-7952(00)00066-1

Agliardi, F., Crosta, G. B., Zanchi, A., & Ravazzi, C. (2009). Onset and timing of deep-seated gravitational slope deformations in the eastern Alps, Italy. Geomorphology, 103(1), 113–129. https://doi.org/10.1016/j.geomorph.2007.09.015

Agliardi, F., Zanchi, A., & Crosta, G. B. (2009). Tectonic vs. gravitational morphostructures in the central Eastern Alps (Italy): Constraints on the recent evolution of the mountain range. Tectonophysics, 474(1–2), 250–270. https://doi.org/10.1016/j.tecto.2009.02.019

Agliardi, F., Crosta, G. B., & Frattini, P. (2012). Slow rock-slope deformation. In Landslides: Types, mechanisms and modeling (p. 207). Cambridge University Press. https://doi.org/10.1017/cbo9780511740367.019

Agliardi, F., Crosta, G. B., Frattini, P., & Malusà, M. G. (2013). Giant non-catastrophic landslides and the long-term exhumation of the European Alps. Earth and Planetary Science Letters, 365, 263–274. https://doi.org/10.1016/j.epsl.2013.01.030

Agliardi, F., Spreafico, M. C., Zanchetta, S., Castellanza, R., Asnaghi, R., Paternoster, J., Crippa, C., & Crosta, G. (2018). Gravitational transfer zones influence DSGSD mechanisms and activity. EGUGA, 13819.

Agliardi, F., Crippa, C., Spreafico, M. C., Manconi, A., Bourlès, D., Braucher, R., Cola, G., & Zanchetta, S. (2019). Strain partitioning and heterogeneous evolution in a giant slope deformation revealed by InSAR, dating and modelling. Geophysical Research Abstracts, 21.

Agliardi, F., Riva, F., Barbarano, M., Zanchetta, S., Scotti, R., & Zanchi, A. (2019). Effects of tectonic structures and long-term seismicity on paraglacial giant slope deformations: Piz Dora (Switzerland). Engineering Geology, 263, 105353. https://doi.org/10.1016/j.enggeo.2019.105353

Agliardi, F., Scuderi, M. M., Fusi, N., & Collettini, C. (2020). Slow-to-fast transition of giant creeping rockslides modulated by undrained loading in basal shear zones. Nature Communications, 11(1), 1–11. https://doi.org/10.1038/s41467-020-15093-3

Allievi, J., Ambrosi, C., Ceriani, M., Colesanti, C., Crosta, G. B., Ferretti, A., & Fossati, D. (2003). Monitoring slow mass movements with the Permanent Scatterers technique. IGARSS 2003. 2003 IEEE International Geoscience and Remote Sensing Symposium. Proceedings (IEEE Cat. No. 03CH37477), 1, 215–217.

Ambrosi, C., & Crosta, G. B. (2006). Large sackung along major tectonic features in the Central Italian Alps. Engineering Geology, 83(1–3), 183–200. https://doi.org/10.1016/j.enggeo.2005.06.031

Amitrano, D., & Helmstetter, A. (2006). Brittle creep, damage, and time to failure in rocks. Journal of Geophysical Research: Solid Earth, 111(11), 1–17. https://doi.org/10.1029/2005JB004252

Angeli, M.-G., Gasparetto, P., Menotti, R. M., Pasuto, A., & Silvano, S. (1996). A visco-plastic model for slope analysis applied to a mudslide in Cortina d'Ampezzo, Italy. Quarterly Journal of Engineering Geology and Hydrogeology, 29(3), 233–240.

Arora, P., & Varshney, S. (2016). Analysis of K-Means and K-Medoids Algorithm For Big Data. Procedia - Procedia Computer Science, 78(December 2015), 507–512. https://doi.org/10.1016/j.procs.2016.02.095

Aslan, G., Foumelis, M., Raucoules, D., De Michele, M., Bernardie, S., & Cakir, Z. (2020). Landslide mapping and monitoring using persistent scatterer interferometry (PSI) technique in the French alps. Remote Sensing, 12(8). https://doi.org/10.3390/RS12081305

Audemard, F. A., Beck, C., & Carrillo, E. (2010). Deep-seated gravitational slope deformations along the active Boconó Fault in the central portion of the Mérida Andes, western Venezuela. Geomorphology. https://doi.org/10.1016/j.geomorph.2010.04.020

Augustinus, P. C. (1995). Glacial valley cross-profile development: the influence of in situ rock stress and rock mass strength, with examples from the Southern Alps, New Zealand. Geomorphology, 14(2), 87–97. https://doi.org/10.1016/0169-555X(95)00050-X

Badger, T. C. (2002). Fracturing within anticlines and its kinematic control on slope stability. Environmental and Engineering Geoscience, 8(1), 19–33.

Ballabio, D., & Consonni, V. (2013). Classification tools in chemistry. Part 1: Linear models. PLS-DA. Analytical Methods, 5(16), 3790–3798. https://doi.org/10.1039/c3ay40582f

Ballabio, D. (2015). A MATLAB toolbox for Principal Component Analysis and unsupervised exploration of data structure. Chemometrics and Intelligent Laboratory Systems, 149, 1–9. https://doi.org/10.1016/j.chemolab.2015.10.003

Bamler, R., & Just, D. (1993). Phase statistics and decorrelation in SAR interferograms. Proceedings of IGARSS'93-IEEE International Geoscience and Remote Sensing Symposium, 980–984.

Barboux, C., Delaloye, R., & Lambiel, C. (2014). Inventorying slope movements in an Alpine environment using DInSAR. Earth Surface Processes and Landforms, 39(15), 2087–2099.

Barla, G., Antolini, F., Barla, M., Mensi, E., & Piovano, G. (2010). Monitoring of the Beauregard landslide (Aosta Valley, Italy) using advanced and conventional techniques. Engineering Geology, 116(3–4), 218–235.

Baudin, T., Marquer, D., & Persoz, F. (1993). Basement-cover relationships in the Tambo nappe (Central Alps, Switzerland): geometry, structure and kinematics. Journal of Structural Geology, 15(3–5), 543–553. https://doi.org/10.1016/0191-8141(93)90147-3

Bavera, D. (2008). Water availability in mountain regions: estimation of Snow Water Equivalent using ground data and MODIS® images. Ph. D. dissertation in Hydraulic Engineering, Politecnico di Milano.

Bavera, Davide, & De Michele, C. (2009). Snow water equivalent estimation in the Mallero basin using snow gauge data and MODIS images and fieldwork validation. Hydrological Processes: An International Journal, 23(14), 1961–1972. https://doi.org/10.1002/hyp

Bechor, N. B. D., & Zebker, H. A. (2006). Measuring two-dimensional movements using a single InSAR pair. Geophysical Research Letters, 33(16), 1–5. https://doi.org/10.1029/2006GL026883

Berardino, P., Fornaro, G., Lanari, R., & Sansosti, E. (2002). A new algorithm for surface deformation monitoring based on small baseline differential SAR interferograms. IEEE Transactions on Geoscience and Remote Sensing, 40(11), 2375–2383. https://doi.org/10.1109/TGRS.2002.803792

Bini, A., Buoncristiani, J.-F., Couterrand, S., Ellwanger, D., Felber, M., Florineth, D., Graf, H. R., Keller, O., Kelly, M., Schlüchter, C., & Schoeneich, P. (2009). Die Schweiz während des letzteiszeitlichen Maximums (LGM). In Bundesamt für Landestopographie, swisstopo. Bundesamt fuïr Landestopografie.

Bonora, N., & Esposito, L. (2011). Transient creep modeling based on the dependence of the activation energy on the internal stress. 120–125.

Bouvet, A., Mermoz, S., Ballère, M., Koleck, T., & Le Toan, T. (2018). Use of the SAR shadowing effect for deforestation detection with Sentinel-1 time series. Remote Sensing, 10(8). https://doi.org/10.3390/rs10081250

Bovenga, F., Belmonte, A., Refice, A., Pasquariello, G., Nutricato, R., Nitti, D. O., & Chiaradia, M. T. (2018). Performance analysis of satellite missions for multi-temporal SAR interferometry. Sensors (Switzerland). https://doi.org/10.3390/s18051359

Bovis, M. J. (1990). Rock-slope deformation at Affliction Creek, southern Coast Mountains, British Columbia. Canadian Journal of Earth Sciences, 27(2), 243–254. https://doi.org/10.1139/e90-024

Bovis, M. J. (2013). Sackung. In Geological Society of America Bulletin (Vol. 93, Issue 8, pp. 881–882). https://doi.org/10.1007/978-1-4020-4399-4_305

Braathen, A., Blikra, L. H., Berg, S. S., & Karlsen, F. (2004). Rock-slope failures in Norway; type, geometry, deformation mechanisms and stability. Norsk Geologisk Tidsskrift, 84(1), 67–88.

Brantut, N., Heap, M. J., Baud, P., & Meredith, P. G. (2014). Rate-and strain-dependent brittle deformation of rocks. Journal of Geophysical Research: Solid Earth, 119(3), 1818–1836.

Braun, A., & Veci, L. (2015). Sentinel-1 Toolbox Interferometry Tutorial. May 2014, 1–20. http://www.ggki.hu/~banyai/S1TBX/S1TBX Stripmap Interferometry with Sentinel-1 Tutorial.pdf

Broadbent, C. D., & Zavodni, Z. M. (1982). Influence of rock structure on stability. Stability in Surface Mining. Society of Mining Engineers.

Brocklehurst, S. H., & Whipple, K. X. (2004). Hypsometry of glaciated landscapes. Earth Surface Processes and Landforms, 29(7), 907–926. https://doi.org/10.1002/esp.1083

Brückl, E., Brunner, F. K., & Kraus, K. (2006). Kinematics of a deep-seated landslide derived from photogrammetric, GPS and geophysical data. Engineering Geology, 88(3–4), 149–159. https://doi.org/10.1016/j.enggeo.2006.09.004

Brückl, E., Brunner, F. K., Lang, E., Mertl, S., Müller, M., & Stary, U. (2013). The Gradenbach Observatory-monitoring deep-seated gravitational slope deformation by geodetic, hydrological, and seismological methods. Landslides, 10(6), 815–829. https://doi.org/10.1007/s10346-013-0417-1

Budge, M. (2011). "EE 710-ST: Radar Waveforms & Signal Processing - Synthetic Aperture Radar: Part 1. 3, 1–13. http://www.ece.uah.edu/courses/material/EE710-Merv/SARPart1_11-revised.pdf

Butterfield, R. (2000). A dynamic model of shallow slope motion driven by fluctuating ground water levels. Landslides in Research, Theory and Practice: Proceedings of the 8th International Symposium on Landslides Held in Cardiff on 26–30 June 2000, 1–203.

Carballo, G. F., & Fieguth, P. W. (2000). Unwrapping. 38(5), 2192–2201.

Carlà, T., Intrieri, E., Raspini, F., Bardi, F., Farina, P., Ferretti, A., Colombo, D., Novali, F., & Casagli, N. (2019). Author Correction: Perspectives on the prediction of catastrophic slope failures from satellite InSAR (Scientific Reports, (2019), 9, 1, (14137), 10.1038/s41598-019-50792-y). Scientific Reports, 9(1), 1–9. https://doi.org/10.1038/s41598-019-55024-x

Casagli, N., Catani, F., Del Ventisette, C., & Luzi, G. (2010). Monitoring, prediction, and early warning using ground-based radar interferometry. Landslides, 7(3), 291–301. https://doi.org/10.1007/s10346-010-0215-y

Catasta, G., & Smiraglia, C. (1978). Il versante della Reit (bassa Valfurva). Bormio (SO).

Ceriani, M., & Fossati, D. (2006). Inventario dei Fenomeni Franosi in Lombardia Regione Lombardia. DG Protezione Civile, Programma Delle Ricerche Strategiche (Inventory of Landslides in Lombardy Region.

Chan, Y. K., & Koo, V. C. (2008). An introduction to Synthetic Aperture Radar (SAR). Progress In Electromagnetics Research B, 2, 27–60. https://doi.org/10.2528/pierb07110101

Chen, C. W., & Zebker, H. A. (2000). Network approaches to two-dimensional phase unwrapping: intractability and two new algorithms. Journal of the Optical Society of America A. https://doi.org/10.1364/josaa.17.000401

Chen, C W, & Zebker, A. H. (2003). SNAPHU: statisticalcost, network-flow algorithm for phase unwrapping. Retrieved April, 27, 2016.

Chen, X., Sun, Q., & Hu, J. (2018). Generation of complete SAR geometric distortion maps based on DEM and neighbor gradient algorithm. Applied Sciences (Switzerland), 10(11), 1–14. https://doi.org/10.3390/app8112206

Chigira, M. (1992). Long-term gravitational deformation of rocks by mass rock creep. Engineering Geology, 32(3), 157–184. https://doi.org/10.1016/0013-7952(92)90043-X

Cigna, F., Bateson, L. B., Jordan, C. J., & Dashwood, C. (2014). Simulating SAR geometric distortions and predicting Persistent Scatterer densities for ERS-1/2 and ENVISAT C-band SAR and InSAR applications: Nationwide feasibility assessment to monitor the landmass of Great Britain with SAR imagery. Remote Sensing of Environment, 152, 441–466. https://doi.org/10.1016/j.rse.2014.06.025

Colesanti, C., Ferretti, A., Novali, F., Prati, C., & Rocca, F. (2003). SAR monitoring of progressive and seasonal ground deformation using the permanent scatterers technique. IEEE Transactions on Geoscience and Remote Sensing, 41(7 PART I), 1685–1701. https://doi.org/10.1109/TGRS.2003.813278

Colesanti, C., Ferretti, A., Prati, C., & Rocca, F. (2003). Monitoring landslides and tectonic motions with the Permanent Scatterers Technique. Engineering Geology. https://doi.org/10.1016/S0013-7952(02)00195-3

Colesanti, C., & Wasowski, J. (2006). Investigating landslides with space-borne Synthetic Aperture Radar (SAR) interferometry. Engineering Geology, 88(3–4), 173–199. https://doi.org/10.1016/j.enggeo.2006.09.013

Conti, M. A., Mariotti, N., Nicosia, U., & Pittau, P. (1997). Succession of selected bioevents in the continental Permian of the Southern Alps (Italy): improvements in intrabasinal and interregional correlations. World and regional geology, 51–65.

Corominas, J., Moya, J., Ledesma, A., Lloret, A., & Gili, J. A. (2005). Prediction of ground displacements and velocities from groundwater level changes at the Vallcebre landslide (Eastern Pyrenees, Spain). Landslides, 2(2), 83–96.

Cowie, P. A., & Roberts, G. P. (2001). Constraining slip rates and spacings for active normal faults. Journal of Structural Geology, 23(12), 1901–1915. https://doi.org/10.1016/S0191-8141(01)00036-0

Crescenti, U., Dramis, F., & Sorriso-Valvo, M. (1994). Deep-seated gravitational slope deformations and large-scale landslides in Italy. Dipartimento di scienze, storia dell'architettura e restauro.

Crippa, C., Franzosi, F., Zonca, M., Manconi, A., Crosta, G. B., Dei Cas, L., Agliardi, F., Cas, L. D., & Agliardi, F. (2020). Unraveling Spatial and Temporal Heterogeneities of Very Slow Rock-Slope Deformations with Targeted DInSAR Analyses. Remote Sensing, 12(8), 1329. https://doi.org/10.3390/rs12081329

Crosta, Giovanni Battista. (1996). Landslide, spreading, deep seated gravitational deformation: analysis, examples, problems and proposals. Geografia Fisica e Dinamica Quaternaria, 19, 297–313.

Crosta, G.B., & Zanchi, A. (2000). Deep seated slope deformations: huge, extraordinary, enigmatic phenomena. Landslides in Research, Theory and Practice: Proceedings of the 8th International Symposium on Landslides Held in Cardiff on 26–30 June 2000, 1–351.

Crosta, G. B., & Agliardi, F. (2003a). Failure forecast for large rock slides by surface displacement measurements. Canadian Geotechnical Journal, 40(1), 176–191. https://doi.org/10.1139/t02-085

Crosta, G B, & Agliardi, F. (2003b). Natural Hazards and Earth System Sciences A methodology for physically based rockfall hazard assessment. Natural Hazards and Earth System Sciences, 3, 407–422.

Crosta, G. B., Imposimato, S., & Roddeman, D. G. (2003). Numerical modelling of large landslides stability and runout. Natural Hazards and Earth System Science, 3(6), 523–538. https://doi.org/10.5194/nhess-3-523-2003

Crosta, G. B., di Prisco, C., Frattini, P., Frigerio, G., Castellanza, R., & Agliardi, F. (2013). Chasing a complete understanding of the triggering mechanisms of a large rapidly evolving rockslide. Landslides, 11(5), 747–764. https://doi.org/10.1007/s10346-013-0433-1

Crosta, G. B., Frattini, P., & Agliardi, F. (2013). Deep seated gravitational slope deformations in the European Alps. Tectonophysics, 605, 13–33. https://doi.org/10.1016/j.tecto.2013.04.028

Crosta, G. B., Agliardi, F., Rivolta, C., Alberti, S., & Dei Cas, L. (2017). Long-term evolution and early warning strategies for complex rockslides by real-time monitoring. Landslides. https://doi.org/10.1007/s10346-017-0817-8

Cruden, D. M., & Varnes, D. J. (1996). Landslides: investigation and mitigation. Chapter 3-Landslide types and processes. Transportation Research Board Special Report, 247.

Dai, K., Peng, J., Zhang, Q., Wang, Z., Qu, T., He, C., Li, D., Liu, J., Li, Z., Xu, Q., Burgmann, R., Milledge, D. G., Tomas, R., Fan, X., Zhao, C., & Liu, X. (2020). Entering the Era of Earth Observation-Based Landslide Warning Systems: A Novel and Exciting Framework. IEEE Geoscience and Remote Sensing Magazine, 8(1), 136–153. https://doi.org/10.1109/MGRS.2019.2954395

Dalla Via, G., Crosetto, M., & Crippa, B. (2012). Resolving vertical and east-west horizontal motion from differential interferometric synthetic aperture radar: The L'Aquila earthquake. Journal of Geophysical Research: Solid Earth. https://doi.org/10.1029/2011JB008689

Dawson, E. M., Roth, W. H., & Drescher, A. (1999). Slope stability analysis by strength reduction. Geotechnique, 49(6), 835–840.

De Finis, E., Gattinoni, P., & Scesi, L. (2015). The genesis of the anomalous Sernio Fan, Valtellina, Northern Italy. International Journal of Civil and Environmental Engineering, 9(10), 1309–1315.

De Zan, F., & Guarnieri, A. M. (2006). TOPSAR: Terrain observation by progressive scans. IEEE Transactions on Geoscience and Remote Sensing. https://doi.org/10.1109/TGRS.2006.873853

Desio, A. (1961). Geological features of the reservoirs and of the dam foundation rocks. Association of Italian Electric Producer and Utility Companies (Ed.) Dams for Hydroelectric Power in Italy. Unpublished.

Ding, X., Li, Z., Zhu, J., Feng, G., & Long, J. (2008). Atmospheric effects on InSAR measurements and their mitigation. Sensors, 8(9), 5426–5448.

Dramis, F., & Sorriso-Valvo, M. (1994). Deep-seated gravitational slope deformations, related landslides and tectonics. Engineering Geology, 38(3–4), 231–243.

Durville, J. L. (1992). Study of mechanisms and modeling of large slope movements. Bull. Int. Assoc. Eng. Geol, 45(1), 23–40.

Eberhardt, E., Stead, D., & Coggan, J. S. (2004). Numerical analysis of initiation and progressive failure in natural rock slopes-the 1991 Randa rockslide. International Journal of Rock Mechanics and Mining Sciences, 41(1), 69–87. https://doi.org/10.1016/S1365-1609(03)00076-5

Emery, J. J. (1978). Simulation of slope creep. In Developments in Geotechnical Engineering (Vol. 14, Issue PA, pp. 669–691). Elsevier. https://doi.org/10.1016/B978-0-444-41507-3.50027-1

Eriksen, H. Ø. (2013). Slope displacement patterns observed using satellite InSAR data in the Storfjord-Kåfjord-Lyngen region, Troms, Master thesis, University of Tromsø, Tromsø, Norway. May, 138. https://doi.org/http://hdl.handle.net/10037/5240

Eriksen, H. Ø. (2017). Combining Satellite and Terrestrial Interferometric Radar Data to Investigate Surface Displacement in the Storfjord and Kåfjord Area, Northern Norway. April.

Eriksen, H. Ø., Lauknes, T. R., Larsen, Y., Corner, G. D., Bergh, S. G., Dehls, J., & Kierulf, H. P. (2017). Visualizing and interpreting surface displacement patterns on unstable slopes using multi-geometry satellite SAR interferometry (2D InSAR). Remote Sensing of Environment, 191, 297–312. https://doi.org/10.1016/j.rse.2016.12.024

Fattahi, H., & Amelung, F. (2014). InSAR uncertainty due to orbital errors. Geophysical Journal International, 199(1), 549–560.

Ferretti, A., Prati, C., & Rocca, F. (2000). Nonlinear subsidence rate estimation using permanent scatterers in differential SAR interferometry. IEEE Transactions on Geoscience and Remote Sensing, 38(5 I), 2202–2212. https://doi.org/10.1109/36.868878

Ferretti, A., Prati, C., & Rocca, F. (2001). Permanent scatterers in SAR interferometry. IEEE Transactions on Geoscience and Remote Sensing, 39(1), 8–20. https://doi.org/10.1109/36.898661

Ferretti, A., Monti-guarnieri, A., Prati, C., & Rocca, F. (2007). InSAR Principles : Guidelines for SAR Interferometry Processing and Interpretation (Issue February).

Ferretti, A., Fumagalli, A., Novali, F., Prati, C., Rocca, F., & Rucci, A. (2011). A new algorithm for processing interferometric data-stacks: SqueeSAR. IEEE Transactions on Geoscience and Remote Sensing. https://doi.org/10.1109/TGRS.2011.2124465

Ferretti, A. (2014). Satellite InSAR data: reservoir monitoring from space. EAGE publications.

Fisher, R. A. (1936). the Use of Multiple Measurements in Taxonomic Problems. Annals of Eugenics, 7(2), 179–188. https://doi.org/10.1111/j.1469-1809.1936.tb02137.x

Flores, A., Herndon, K., Thapa, R., & Cherrington, E. (2019). SAR Handbook: Comprehensive Methodologies for Forest Monitoring and Biomass Estimation. THE SAR HANDBOOK Comprehensive Methodologies for Forest Monitoring and Biomass Estimation, 1–307. https://doi.org/10.25966/nr2c-s697

Florineth, D., & Froitzheim, N. (1994). Transition from continental to oceanic basement in the Tasna nappe (Engadine window, Graubunden, Switzerland): evidence for early Cretaceous opening of the Valais Ocean. Schweizerische Mineralogische Und Petrographische Mitteilungen, 74(3), 437–448.

Forcella, F, Gallazzi, D., Montrasio, A., & Notarpietro, A. (1982). Note illustrative relative

all'evoluzione neotettonica dei Fogli 6–Passo dello Spluga, 7–Pizzo Bernina, 8–Bormio, 17–Chiavenna, 18–Sondrio, 19–Tirano. Contributi Alla Realizzazione Della Carta Neotettonica d'Italia. Progetto Finalizzato Geodinamica, 513, 239–288.

Forcella, F. (1984). The Sackung between Mount Padrio and Mount Varadega, Central Alps, Italy : a remarkable example of slope gravitational tectonics. Méditerranée, 51, 81–92. https://doi.org/10.3406/medit.1984.2237

Forcella, F. (1987). La deformazione di versante del M. Albenza. Bollettino Della Società Geologica Italiana, 106(2), 273–280.

Forcella, F, & Rossi, P. M. (1987). Le deformosioni di versante presenti nel territorio di Fuipiano Imagna (Prealpi bergamasche). Bollettino Della Società Geologica Italiana, 106(2), 281–291.

Forcella, F., & Orombelli, G. (1984). Holocene slope deformations in Valfurva, central Alps, Italy. Geografia Fisica e Dinamica Quaternaria, 7, 41–48.

Forcella, F., & Orombelli, Gi. (1984). Holocene slope deformations in Valfurva, Central Alps, Italy. Geografia Fisica e Dinamica Quaternaria, 7(2), 41–48.

Fossen, H., & Rotevatn, A. (2016). Fault linkage and relay structures in extensional settings-A review. Earth-Science Reviews, 154, 14–28. https://doi.org/10.1016/j.earscirev.2015.11.014

Frattini, P., Crosta, G. B., & Allievi, J. (2013). Damage to buildings in large slope rock instabilities monitored with the PSinSAR$^{TM}$ technique. Remote Sensing, 5(10), 4753–4773. https://doi.org/10.3390/rs5104753

Frattini, P., Crosta, G. B., Rossini, M., & Allievi, J. (2018). Activity and kinematic behaviour of deep-seated landslides from PS-InSAR displacement rate measurements. Landslides, September 2017, 1–18. https://doi.org/10.1007/s10346-017-0940-6

Gabriel, A. K., Goldstein, R. M., & Zebker, H. A. (1989a). Mapping small elevation changes over large areas: differential radar interferometry. Journal of Geophysical Research, 94(B7), 9183–9191. https://doi.org/10.1029/JB094iB07p09183

Gabriel, A. K., Goldstein, R. M., & Zebker, H. A. (1989b). Mapping small elevation changes over large areas: differential radar interferometry. Journal of Geophysical Research. https://doi.org/10.1029/JB094iB07p09183

Gatto, G. O., & Scolari, A. (1974). La tettonica tardiva del ciclo orogenetico alpino nell'Alto Adige occidentale e regioni limitrofe. Bollettino Della Società Geologica Italiana, 93, 1211–1231.

Gignoux, M., & Barbier, R. (1955). Géologie des barrages et des aménagements hydrauliques.

Gischig, V., Preisig, G., & Eberhardt, E. (2016). Numerical investigation of seismically induced rock mass fatigue as a mechanism contributing to the progressive failure of deep-seated landslides. Rock Mechanics and Rock Engineering, 49(6), 2457–2478. https://doi.org/10.1007/s00603-015-0821-z

Goldstein, R. M., Zebker, H. A., & Werner, C. L. (1988). Satellite radar interferometry: Two-dimensional phase unwrapping. Radio Science, 23(4), 713–720.

Goldstein, R. M., & Werner, C. L. (1998). Radar interferogram filtering for geophysical applications. Geophysical Research Letters. https://doi.org/10.1029/1998GL900033

Gosse, J. C., & Phillips, F. M. (2001). Terrestrial in situ cosmogenic nuclides:theory and application. Quaternary Science Reviews, 20, 1475–1560. https://doi.org/10.1016/S0277-3791(00)00171-2

Grämiger, L. M., Moore, J. R., Gischig, V. S., Ivy-Ochs, S., & Loew, S. (2017). Beyond debuttressing: Mechanics of paraglacial rock slope damage during repeat glacial cycles. Journal of Geophysical Research: Earth Surface, 122(4), 1004–1036. https://doi.org/10.1002/2016JF003967

Gregnanin, A., & Valle, M. (1995). Deformation and metamorphism in the Austroalpine Oetztal-Stubai Complex (Part II); Early-Alpine evolution in basement and cover. Bollettino Della Societa Geologica Italiana, 114(2), 393–409.

Guglielmi, Y., Cappa, F., & Binet, S. (2005). Coupling between hydrogeology and deformation of mountainous rock slopes: Insights from La Clapière area (southern Alps, France). Comptes Rendus - Geoscience, 337(13), 1154–1163. https://doi.org/10.1016/j.crte.2005.04.016

Hammah, R. E., Yacoub, T., Corkum, B., & Curran, J. H. (2008). The practical modelling of discontinuous rock masses with finite element analysis. The 42nd US Rock Mechanics Symposium (USRMS).

Handwerger, A. L., Roering, J. J., & Schmidt, D. A. (2013). Controls on the seasonal deformation of slow-moving landslides. Earth and Planetary Science Letters. https://doi.org/10.1016/j.epsl.2013.06.047

Hanssen, R. F. (2001). Radar interferometry: data interpretation and error analysis (Vol. 2). Springer Science & Business Media.

Helmstetter, A., & Garambois, S. (2010). Seismic monitoring of Séchilienne rockslide (French Alps): Analysis of seismic signals and their correlation with rainfalls. Journal of Geophysical Research: Earth Surface, 115(F3).

Henderson, I. H. C., Lauknes, T. R., Osmundsen, P. T., Dehls, J., Larsen, Y., & Redfield, T. F. (2011). A structural, geomorphological and InSAR study of an active rock slope failure development. Geological Society, London, Special Publications, 351(1), 185–199. https://doi.org/10.1144/SP351.10

Hermanns, R. L, Blikra, L. H., Anda, E., Saintot, A., Dahle, H., Oppikofer, T., Fischer, L., Bunkholt, H., Böhme, M., & Dehls, J. F. (2013). Systematic mapping of large unstable rock slopes in Norway. In Landslide science and practice (pp. 29–34). Springer.

Hermanns, R.L, & Longva, O. (2012). Rapid rock-slope failures. Landslides: Types, Mechanisms and Modeling, 59–70.

Hippolyte, J. C., Brocard, G., Tardy, M., Nicoud, G., Bourlès, D., Braucher, R., Ménard, G., & Souffaché, B. (2006). The recent fault scarps of the Western Alps (France): Tectonic surface ruptures or gravitational sackung scarps? A combined mapping, geomorphic, levelling, and 10Be dating approach. Tectonophysics, 418(3–4), 255–276. https://doi.org/10.1016/j.tecto.2006.02.009

Hippolyte, J. C., Bourlès, D., Léanni, L., Braucher, R., Chauvet, F., & Lebatard, A. E. (2012). 10Be ages reveal >12ka of gravitational movement in a major sackung of the Western Alps (France). Geomorphology, 171–172(OCTOBER 2012), 139–153. https://doi.org/10.1016/j.geomorph.2012.05.013

Humair, F., Pedrazzini, A., Epard, J.-L., Froese, C. R., & Jaboyedoff, M. (2013). Structural characterization of Turtle Mountain anticline (Alberta, Canada) and impact on rock slope failure. Tectonophysics, 605, 133–148.

Hutchinson, J. N. (1968). Mass movement. Encyclopedia of Geomorphology, 688–695.

Irwin, K., Braun, A., Fotopoulos, G., Roth, A., & Wessel, B. (2018). Assessing single-polarization and dual-polarization TerraSAR-X data for surface water monitoring. Remote Sensing, 10(6). https://doi.org/10.3390/rs10060949

Ivy-Ochs, S., Kerschner, H., Reuther, A., Preusser, F., Heine, K., Maisch, M., Kubik, P. W., & Schlüchter, C. (2008). Chronology of the last glacial cycle in the European Alps. Journal of Quaternary Science. https://doi.org/10.1002/jqs.1202

Jaboyedoff, M., Oppikofer, T., Abellán, A., Derron, M.-H., Loye, A., Metzger, R., & Pedrazzini, A. (2012). Use of LIDAR in landslide investigations: a review. Natural Hazards, 61(1), 5–28.

Jaboyedoff, M., Penna, I., Pedrazzini, A., Baroň, I., & Crosta, G. B. (2013). An introductory review on gravitational-deformation induced structures, fabrics and modeling. Tectonophysics, 605, 1–12. https://doi.org/10.1016/j.tecto.2013.06.027

Jarman, D., & Ballantyne, C. K. (2002). Beinn Fhada, Kintail: An example of large-scale paraglacial rock slope deformation. Scottish Geographical Journal, 118(1), 59–68. https://doi.org/10.1080/00369220218737136

Jin, X., & Han, J. (2010). K-Medoids Clustering BT - Encyclopedia of Machine Learning (C. Sammut & G. I. Webb (eds.); pp. 564–565). Springer US. https://doi.org/10.1007/978-0-387-30164-8_426

Jolliffe, I. T., & Cadima, J. (2016). Principal component analysis: a review and recent developments. Philosophical Transactions of the Royal Society A: Mathematical, Physical and Engineering Sciences, 374(2065), 20150202.

Joughin, L. R., Kwok, R., & Fahnestock, M. A. (1998). Interferometric estimation of three-dimensional ice-flow using ascending and descending passes. IEEE Transactions on Geoscience and Remote Sensing, 36(1), 25–37. https://doi.org/10.1109/36.655315

Jung, J., Kim, D. J., & Park, S. E. (2014). Correction of atmospheric phase screen in time series InSAR using WRF model for monitoring volcanic activities. IEEE Transactions on Geoscience and Remote Sensing, 52(5), 2678–2689. https://doi.org/10.1109/TGRS.2013.2264532

Kaufman, L. R., & Rousseeuw, P. (1990). PJ (1990) Finding groups in data: An introduction to cluster analysis. Hoboken NJ John Wiley & Sons Inc, 725.

Kos, A., Amann, F., Strozzi, T., Delaloye, R., von Ruette, J., & Springman, S. (2016). Contemporary glacier retreat triggers a rapid landslide response, Great Aletsch Glacier, Switzerland. Geophysical Research Letters, 43(24), 12,466-12,474. https://doi.org/10.1002/2016GL071708

Lauknes, T. R., Shanker, A. P., Dehls, J. F., Zebker, H. A., Henderson, I. H. C., & Larsen, Y. (2010). Remote Sensing of Environment Detailed rockslide mapping in northern Norway with small baseline and persistent scatterer interferometric SAR time series methods. Remote Sensing of Environment, 114(9), 2097–2109. https://doi.org/10.1016/j.rse.2010.04.015

Le Roux, O., Schwartz, S., Gamond, J. F., Jongmans, D., Bourles, D., Braucher, R., Mahaney, W., Carcaillet, J., & Leanni, L. (2009). CRE dating on the head scarp of a major landslide (Séchilienne, French Alps), age constraints on Holocene kinematics. Earth and Planetary Science Letters, 280(1–4), 236–245.

Lebuis, J., Robert, J.-M., & Rissmann, P. (1983). Regional mapping of landslide hazard in Quebec. Rapport-Statens Geotekniska Institut, 17, 205–262.

Lenti, L., & Martino, S. (2013). A parametric numerical study of the interaction between seismic waves and landslides for the evaluation of the susceptibility to seismically induced displacements. Bulletin of the Seismological Society of America, 103(1), 33–56. https://doi.org/10.1785/0120120019

Li, Z. (2005). Modeling atmospheric effects on repeat-pass InSAR measurements. Hong Kong Polytechnic University (Hong Kong).

Li, Z. W., Ding, X. L., Huang, C., Zou, Z. R., & Chen, Y. L. (2007). Atmospheric effects on repeat-pass InSAR measurements over Shanghai region. Journal of Atmospheric and Solar-Terrestrial Physics, 69(12), 1344–1356.

Lillesand, T. M., Kiefer, R. W., & Chipman, J. (1987). Remote sensing and image processing. John Wiley & Sons, New York.

Lin, C. W., Tseng, C. M., Tseng, Y. H., Fei, L. Y., Hsieh, Y. C., & Tarolli, P. (2013). Recognition of large scale deep-seated landslides in forest areas of Taiwan using high resolution topography. Journal of Asian Earth Sciences, 62, 389–400. https://doi.org/10.1016/j.jseaes.2012.10.022

Lockner, D. (1993). Room temperature creep in saturated granite. Journal of Geophysical Research, 98(B1), 475–487. https://doi.org/10.1029/92JB01828

Lollino, G., Arattano, M., Allasia, P., & Giordan, D. (2006). Time response of a landslide to meteorological events.

Lyons, S., & Sandwell, D. (2003). Fault creep along the southern San Andreas from interferometric synthetic aperture radar, permanent scatterers, and stacking. Journal of Geophysical Research: Solid Earth, 108(B1).

Ma, G., Zhao, Q., Wang, Q., & Liu, M. (2018). On the effects of inSAR temporal decorrelation and its implications for land cover classification: The case of the ocean-reclaimed lands of the Shanghai megacity. Sensors (Switzerland), 18(9), 1–19. https://doi.org/10.3390/s18092939

Mahr, T. (1977). Deep—Reaching gravitational deformations of high mountain slopes. Bulletin of the International Association of Engineering Geology-Bulletin de l'Association Internationale de Géologie de l'Ingénieur, 16(1), 121–127.

Malamud, B. D., Turcotte, D. L., Guzzetti, F., & Reichenbach, P. (2004). Landslide inventories and their statistical properties. Earth Surface Processes and Landforms, 29(6), 687–711.

Manconi, A. (2019). Technical note: Limitations on the use of space borne differential SAR interferometry for systematic monitoring and failure forecast of alpine landslides. EarthArXiv, 1–20. https://doi.org/10.31223/osf.io/3nmqj

Manconi, A., Kourkouli, P., Caduff, R., Strozzi, T., & Loew, S. (2018). Monitoring surface deformation over a failing rock slope with the ESA sentinels: Insights from Moosfluh instability, Swiss Alps. Remote Sensing. https://doi.org/10.3390/rs10050672

Mansour, Z., Miloud, B., Donzé, F., Soraya, R., & Abderahmane, H. (2015). Morphometric analysis of landslides in the Ouarsenis area (west Algeria): implications for establishing a relationship between tectonic, geomorphologic, and hydraulic indexes. Arabian Journal of Geosciences, 8(9), 6465–6482. https://doi.org/10.1007/s12517-014-1711-5

Manzo, M., Ricciardi, G. P. P., Casu, F., Ventura, G., Zeni, G., Borgström, S., Berardino, P., Del Gaudio, C., & Lanari, R. (2006). Surface deformation analysis in the Ischia Island (Italy) based on spaceborne radar interferometry. Journal of Volcanology and Geothermal Research, 151(4), 399–416. https://doi.org/10.1016/j.jvolgeores.2005.09.010

Mario Costantini, T. (1998). A novel phase unwrapping method based on network programming. IEEE Transactions on Geoscience and Remote Sensing. https://doi.org/10.1109/36.673674

Marquer, D., Challandes, N., & Baudin, T. (1996). Shear zone patterns and strain distribution at the scale of a Penninic nappe: The Suretta nappe (Eastern Swiss Alps). Journal of Structural Geology. https://doi.org/10.1016/S0191-8141(96)80009-5

Massart, D. L. (1983). The interpretation of analytical chemical data by the use of cluster analysis.

Mccandless, S. W. W., & Jackson, C. R. (1978). Chapter 1 . Principles of Synthetic Aperture Radar. SAR Marine User's Manual, 1–23.

Meisina, C., Zucca, F., Notti, D., Colombo, A., Cucchi, A., Savio, G., Giannico, C., & Bianchi, M. (2008). Geological interpretation of PSInSAR Data at regional scale. Sensors. https://doi.org/10.3390/s8117469

Monserrat, O., Crosetto, M., & Luzi, G. (2014). A review of ground-based SAR interferometry for deformation measurement. ISPRS Journal of Photogrammetry and Remote Sensing, 93, 40–48.

Montrasio, A., Bigioggero, B., Maino, A., Cirese, E., & Tacchia, D. (1990). Carta geologica della Lombardia: scala 1: 250.000. Istituto poligrafico e zecca dello stato.

Nappo, N., Peduto, D., Mavrouli, O., van Westen, C. J., & Gullà, G. (2019). Slow-moving landslides interacting with the road network: Analysis of damage using ancillary data, in situ surveys and multi-source monitoring data. Engineering Geology, 260, 105244.

Nemcok, A. (1972). Gravitational slope deformation in high mountains. Proc. 24th, Int. Geol. Congr., Motreal, 1972, 132–141.

Nemčok, A., Pašek, J., & Rybář, J. (1972). Classification of landslides and other mass movements. Rock Mechanics Felsmechanik Mécanique Des Roches, 4(2), 71–78. https://doi.org/10.1007/BF01239137

Notti, Davide, Davalillo, J. C., Herrera, G., Mora, O., & Ferrata, V. (2010). Assessment of the performance of X-band satellite radar data for landslide mapping and monitoring: Upper Tena Valley case study. Natural Hazards and Earth System Sciences, 10(9), 1865. https://doi.org/10.5194/nhess-10-1865-2010

Notti, D, Meisina, C., Zucca, F., & Colombo, A. (2012). Models To Predict Persistent Scatterers Data Distribution and Their Capacity To Register Movement Along the Slope. Proceedings of FRINGE 2011, 2011(January), 19–23. https://earth.esa.int/documents/10174/1573056/Models_predict_persistent_scatterers_data_distribution.pdf

Notti, Davide, Herrera, G., Bianchini, S., Meisina, C., García-Davalillo, J. C., & Zucca, F. (2014). A methodology for improving landslide PSI data analysis. International Journal of Remote Sensing. https://doi.org/10.1080/01431161.2014.889864

Oppikofer, T., Nordahl, B., Bunkholt, H., Nicolaisen, M., Jarna, A., Iversen, S., Hermanns, R. L., Böhme, M., & Yugsi Molina, F. X. (2015). Database and online map service on unstable rock slopes in Norway - From data perpetuation to public information. Geomorphology, 249, 69–81. https://doi.org/10.1016/j.geomorph.2015.08.005

Pan, W., Shen, X., & Liu, B. (2013). Cluster analysis: Unsupervised learning via supervised learning with a non-convex penalty. Journal of Machine Learning Research, 14, 1865–1889.

Pánek, T. (2015). Recent progress in landslide dating: A global overview. Progress in Physical Geography, 39(2), 168–198. https://doi.org/10.1177/0309133314550671

Pánek, T., & Klimeš, J. (2016). Temporal behavior of deep-seated gravitational slope deformations: A review. Earth-Science Reviews, 156, 14–38. https://doi.org/10.1016/j.earscirev.2016.02.007

Pedrazzini, A., Humair, F., Jaboyedoff, M., & Tonini, M. (2016). Characterisation and spatial distribution of gravitational slope deformation in the Upper Rhone catchment (Western Swiss Alps). Landslides, 13(2), 259–277. https://doi.org/10.1007/s10346-015-0562-9

Peduto, D., Ferlisi, S., Nicodemo, G., Reale, D., Pisciotta, G., & Gullà, G. (2017). Empirical fragility and vulnerability curves for buildings exposed to slow-moving landslides at medium and large scales. Landslides, 14(6), 1993–2007.

Pepe, A., & Calò, F. (2017). A review of interferometric synthetic aperture RADAR (InSAR) multi-track approaches for the retrieval of Earth's Surface displacements. Applied Sciences (Switzerland), 7(12). https://doi.org/10.3390/app7121264

Plank, S., Singer, J., Minet, C., & Thuro, K. (2012). Pre-survey suitability evaluation of the differential synthetic aperture radar interferometry method for landslide monitoring. International Journal of Remote Sensing, 33(20), 6623–6637. https://doi.org/10.1080/01431161.2012.693646

Poisel, R., & Eppensteiner, W. (1988). A contribution to the systematics of rock mass movements. International Symposium on Landslides. 5, 1353–1357.

Qiu, Z., Yue, J., Wang, X., & Yue, S. (2016). Spaceborne sar imaging algorithm for coherence optimized. PloS One, 11(2), e0148823.

Rabus, B., & Pichierri, M. (2018). A new InSAR phase demodulation technique developed for a typical example of a complex, multi-lobed landslide displacement field, Fels Glacier Slide, Alaska. Remote Sensing, 10(7). https://doi.org/10.3390/rs10070995

Radbruch-Hall, D. H., Varnes, D. J., & Savage, W. Z. (1976). Gravitational spreading of steep-sided ridges ("sackung") in Western United States. Bulletin of the International Association of Engineering Geology, 13(1), 23–35. https://doi.org/10.1007/BF02634754

Radbruch-Hall, D., Varnes, D. J., & Colton, R. B. (1977). Gravitational spreading of steep-sided ridges ("Sackung") in Colorado. Journal of Research of the US Geological Survey, 5(3), 359–363.

Radbruch-Hall, D. H. (1978). Gravitational creep of rock masses on slopes. In Developments in Geotechnical Engineering (Vol. 14, pp. 607–657). Elsevier.

Riahi, A., Hammah, E. R., & Curran, J. H. (2010). Limits of applicability of the finite element explicit joint model in the analysis of jointed rock problems. 44th US Rock Mechanics Symposium and 5th US-Canada Rock Mechanics Symposium.

Richards, J. A. (2009). Remote sensing with imaging radar (Vol. 1). Springer.

Richards, M. A., Scheer, J. A., & Holm, W. A. (2010). Principles of modern radar: Basic principles. In Principles of Modern Radar: Basic Principles. https://doi.org/10.1049/sbra021e

Riva F.(2017). Damage-Based Long-Term Modelling of Paraglacial To Postglacial Evolution of Alpine Rock Slopes. 267.

Riva, F., Agliardi, F., Amitrano, D., & Crosta, G. B. (2018). Damage-Based Time-Dependent Modeling of Paraglacial to Postglacial Progressive Failure of Large Rock Slopes. Journal of Geophysical Research: Earth Surface. https://doi.org/10.1002/2017JF004423

Rocca, F. (2007). Modeling interferogram stacks. IEEE Transactions on Geoscience and Remote Sensing, 45(10), 3289–3299. https://doi.org/10.1109/TGRS.2007.902286

Rosi, Ascanio, Agostini, A., Tofani, V., & Casagli, N. (2014). A Procedure to map subsidence at the regional scale using the persistent scatterer interferometry (PSI) technique. Remote Sensing, 6(11), 10510–10522. https://doi.org/10.3390/rs61110510

Rosi, A., Tofani, V., Tanteri, L., Tacconi Stefanelli, C., Agostini, A., Catani, F., & Casagli, N. (2018). The new landslide inventory of Tuscany (Italy) updated with PS-InSAR: geomorphological features and landslide distribution. Landslides, 15(1), 5–19. https://doi.org/10.1007/s10346-017-0861-4

Rott, H. (2009). Advances in interferometric synthetic aperture radar (InSAR) in earth system science. Progress in Physical Geography, 33(6), 769–791.

Sabins, F. F. (1997). Remote Sensing and Principles and Image Interpretation. W.H. Freeman and Co.

Sandwell, D. T., & Price, E. J. (1998). Phase gradient approach to stacking interferograms. Journal of Geophysical Research: Solid Earth, 103(B12), 30183–30204.

Sarmap, S. A. (2009). Synthetic Aperture Radar and SARscape: SAR Guidebook. Sarmap SA: Purasca, Switzerland, 274.

Saroli, M., Stramondo, S., Moro, M., & Doumaz, F. (2005). Movements detection of deep seated gravitational slope deformations by means of InSAR data and photogeological interpretation: northern Sicily case study. Terra Nova, 17(1), 35–43.

Savage, W. Z., & Varnes, D. J. (1987). Mechanics of gravitational spreading of steep-sided ridges («sackung»). Bulletin of the International Association of Engineering Geology-Bulletin de l'Association Internationale de Géologie de l'Ingénieur, 35(1), 31–36.

Scheer, J. A., & Holm, W. A. (2010). Introduction and radar overview. In Principles of Modern Radar: Basic Principles (pp. 3–58). https://doi.org/10.1049/sbra021e_ch1

Scheiber, T., Pfiffner, O. A., & Schreurs, G. (2012). Strain accumulation during basal accretion in continental collision - A case study from the Suretta nappe (eastern Swiss Alps). Tectonophysics. https://doi.org/10.1016/j.tecto.2012.03.009

Schlögel, R., Doubre, C., Malet, J. P., & Masson, F. (2015). Landslide deformation monitoring with ALOS/PALSAR imagery: A D-InSAR geomorphological interpretation method. Geomorphology, 231, 314–330. https://doi.org/10.1016/j.geomorph.2014.11.031

Schmid, S. M., Fügenschuh, B., Kissling, E., & Schuster, R. (2004). Tectonic map and overall architecture of the Alpine orogen. Eclogae Geologicae Helvetiae. https://doi.org/10.1007/s00015-004-1113-x

Schwartz, S., Gamond, J. F., Jongmans, D., Leroux, O., Bourlès, D., Braucher, R., & Carcaillet, J. (2009). High spatial resolution CRE dating on the head scarp of a major landslide (S. EGUGA, 2149.

Scotti, R., Brardinoni, F., Alberti, S., Frattini, P., & Crosta, G. B. (2013). A regional inventory of rock glaciers and protalus ramparts in the central Italian Alps. Geomorphology. https://doi.org/10.1016/j.geomorph.2012.12.028

Scotti, R., Brardinoni, F., Crosta, G. B., Cola, G., & Mair, V. (2017). Time constraints for post-LGM landscape response to deglaciation in Val Viola, Central Italian Alps. Quaternary Science Reviews, 177, 10–33. https://doi.org/10.1016/j.quascirev.2017.10.011

Sibson, R. (1981). A brief description of natural neighbour interpolation. Interpreting Multivariate Data.

Sireci, O. (2005). Training Course on Weather Radar Systems. module C(September).

Skempton, A. W., & Hutchinson, J. (1969). Stability of natural slopes and embankment foundations. Soil Mech & Fdn Eng Conf Proc/Mexico/.

Small, D. (1998). Generation of Digital Elevation Models through Spaceborne SAR Interferometry. Department of Geography, Ph.D., 168. http://www.geo.uzh.ch/fileadmin/files/content/abteilungen/rsl1/Publications/PhD_Theses/1998_DavidSmall.pdf

Soliva, R., Benedicto, A., & Maerten, L. (2006). Spacing and linkage of confined normal faults: Importance of mechanical thickness. Journal of Geophysical Research: Solid Earth, 111(1), 1–17. https://doi.org/10.1029/2004JB003507

Sorriso-Valvo, M. (1979). Trench features on steep-sided ridges of Aspromonte, Calabria (Italy). Proc. Polish-Italian Seminar on Superficial Mass Movement, 98–109.

Sorriso-Valvo, Marino. (1995). Considerazioni sul limite tra deformazione gravitativa pronfonda di versante e frana. Memorie Della Società Geologica Italiana, 50, 179–185.

Stark, C. P., & Hovius, N. (2001). The characterization of landslide size distributions. Geophysical Research Letters, 28(6), 1091–1094.

Stead, D., & Wolter, A. (2015). A critical review of rock slope failure mechanisms: The importance of structural geology. Journal of Structural Geology, 74, 1–23. https://doi.org/10.1016/j.jsg.2015.02.002

Sternai, P., Herman, F., Fox, M. R., & Castelltort, S. (2011). Hypsometric analysis to identify spatially variable glacial erosion. Journal of Geophysical Research: Earth Surface, 116(3), 1–17. https://doi.org/10.1029/2010JF001823

Sternai, P., Herman, F., Champagnac, J.-D., Fox, M., Salcher, B., & Willett, S. D. (2012). Pre-glacial topography of the European Alps. Geology, 40(12), 1067–1070.

Strozzi, T., Wegmuller, U., Werner, C., & Wiesmann, A. (2000). Measurement of slow uniform surface displacement with mm/year accuracy. IGARSS 2000. IEEE 2000 International Geoscience and Remote Sensing Symposium. Taking the Pulse of the Planet: The Role of Remote Sensing in Managing the Environment. Proceedings (Cat. No. 00CH37120), 5, 2239–2241.

Swisstopo. (2005). Geologische Karte der Schweiz 1: 500′ 000.

Tabor, R. W. (1971). Origin of ridge-top depressions by large-scale creep in the Olympic Mountains, Washington. Bulletin of the Geological Society of America, 82(7), 1811–1822. https://doi.org/10.1130/0016-7606(1971)82[1811:OORDBL]2.0.CO;2

Ter-Stepanian, G. I., & Goldstein, M. N. (1969). Multi-storied landslides and strength of soft clays. Intl Conf Soil Mech & Fdn Eng Proc.

Terzaghi, K. (1953). Some miscellaneous notes on creep: 3rd Internat. Conf. Soil Mechanics and Found. Eng. Proc, 3, 205–206.

Terzaghi, Karl. (1962). Stability of steep slopes on hard unweathered rock. Geotechnique, 12(4), 251–270.

Tessari, G., Floris, M., & Pasquali, P. (2017). Phase and amplitude analyses of SAR data for landslide detection and monitoring in non-urban areas located in the North-Eastern Italian pre-Alps. Environmental Earth Sciences, 76(2), 1–11. https://doi.org/10.1007/s12665-017-6403-5

Turkish State Meteorological Service. (2005). Training Course on Weather Radar Systems. module C(September), 55. https://www.wmo.int/pages/prog/www/IMOP/publications/IOM-88_TM-Radars/IOM-88_Module-A.pdf

Tzouvaras, M., Danezis, C., & Hadjimitsis, D. G. (2020). Differential SAR interferometry using sentinel-1 imagery-limitations in monitoring fast moving landslides: The case study of Cyprus. Geosciences (Switzerland), 10(6), 1–26. https://doi.org/10.3390/geosciences10060236

Ulaby, F. T., Moore, R. K., & Fung, A. K. (1986). Microwave remote sensing: Active and passive. Volume 3-From theory to applications.

Van Zyl, J., & Kim, Y. (2011). Synthetic Aperture Radar (SAR) Imaging Basics. Synthetic Aperture Radar Polarimetry, 1–22. https://doi.org/10.1002/9781118116104.ch1

Varnes, D. J. (1978). Slope movement types and processes. Special Report, 176, 11–33.

Varnes, D. J., Radbruch-Hall, D. H., & Savage, W. Z. (1989). Topographic and structural conditions in areas of gravitational spreading of ridges in the western United States. United States Geological Survey, Professional Paper;(USA), 1496.

Wasowski, J., & Bovenga, F. (2014). Investigating landslides and unstable slopes with satellite Multi Temporal Interferometry: Current issues and future perspectives. In Engineering Geology. https://doi.org/10.1016/j.enggeo.2014.03.003

Weike, L., & Goulin, L. (2012). A new method of weighted choice in InSAR Least Squares unwrapping. Geodesy and Geodynamics, 3(1), 39–43. https://doi.org/10.3724/sp.j.1246.2012.00039

Wempen, J. M., & McCarter, M. K. (2017). Comparison of L-band and X-band differential interferometric synthetic aperture radar for mine subsidence monitoring in central Utah. International Journal of Mining Science and Technology, 27(1), 159–163. https://doi.org/10.1016/j.ijmst.2016.11.012

Wolter, A., Gischig, V., Stead, D., & Clague, J. J. (2016). Investigation of geomorphic and seismic effects on the 1959 Madison Canyon, Montana, landslide using an integrated field, engineering geomorphology mapping, and numerical modelling approach. Rock Mechanics and Rock Engineering, 49(6), 2479–2501. https://doi.org/10.1007/s00603-015-0889-5

Wright, T., Parsons, B., & Fielding, E. (2001). the North Anatolian interferometry Fault by satellite radar. Geophysical Research Letters, 28(10), 2117–2120. https://doi.org/10.1029/2000GL012850

Yu, C., Li, Z., & Penna, N. T. (2018). Interferometric synthetic aperture radar atmospheric correction using a GPS-based iterative tropospheric decomposition model. Remote Sensing of Environment, 204(August 2017), 109–121. https://doi.org/10.1016/j.rse.2017.10.038

Yu, C., Penna, N. T., & Li, Z. (2017). Generation of real-time mode high-resolution water vapor fields from GPS observations. Journal of Geophysical Research, 122(3), 2008–2025. https://doi.org/10.1002/2016JD025753

Zebker, A., Rosen, P. A., & Hensley, S. (1997). Atmospheric effects in interferometric synthetic aperture radar surface deformation and topographic maps. JOURNAL OF GEOPHYSICAL RESEARCH, 102, 7547–7563.

Zebker, H. A., Rosen, P. A., Goldstein, R. M., Gabriel, A., & Werner, C. L. (1994). On the derivation of coseismic displacement fields using differential radar interferometry: The Landers earthquake. Journal of Geophysical Research: Solid Earth, 99(B10), 19617–19634.

Zerathe, S., Lebourg, T., Braucher, R., & Bourlès, D. (2014). Mid-Holocene cluster of large-scale landslides revealed in the Southwestern Alps by36Cl dating. Insight on an Alpine-scale landslide activity. Quaternary Science Reviews, 90(July), 106–127. https://doi.org/10.1016/j.quascirev.2014.02.015

Zischinsky, U. (1966). On the deformation of high slopes. 1st ISRM Congress.